L.E.A.F.

Low-Emission Aircraft Family

AE3200: Design Synthesis Exercise

Tutor: Pieter-Jan Proesmans
Coaches: Direnc Atmaca and Federico Taruffi

Group 14:

Carlos Orce López	5746132	Marius Michaud	5912857
Viktor Nikolov	5937574	Lisa van den Berg	5733960
Toine van Wassenaar	5803136	Lindsay Landman	5682770
Seán McCarthy	6001726	Kacper Montewka	5927846
Nathan Overvelde	5718279	Daan Vlasblom	6028551

Delft University of Technology

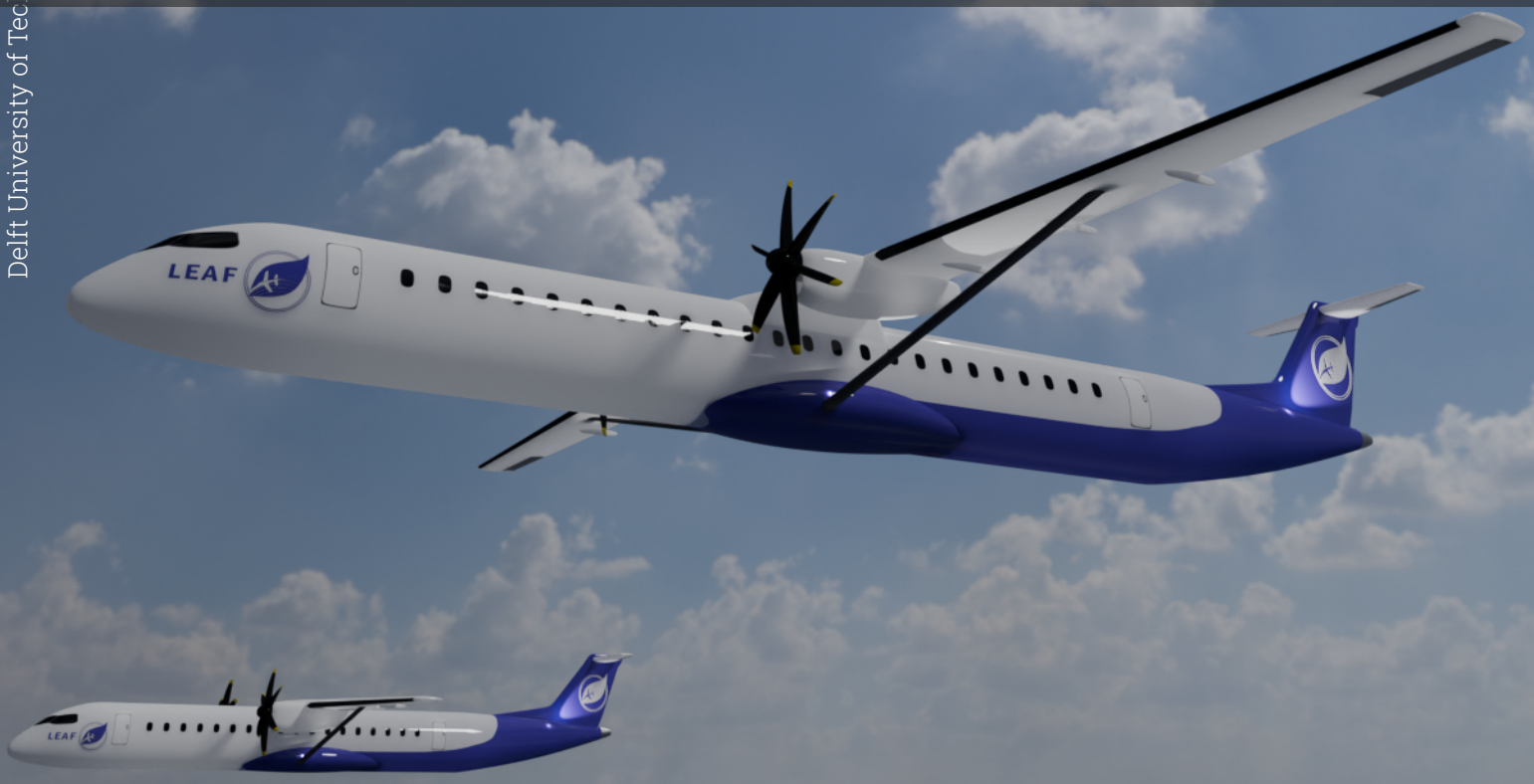

TU Delft

This page is intentionally left blank.

Executive overview

Author: Lindsay, Marius

Context

LEAF (Low-Emission Aircraft Family) is an on-going project in response to the following:

Mission N,'eed Statement:
Reduce climate impact of regional commercial aviation, while preserving operational flexibility for airlines with diverse range and payload needs.

This is achieved with the scope of the project defined in the following statement:

Project Objective Statement:
Design a commercial aircraft family consisting of a minimum of two high-commonality, low-emission members, covering regional missions, by ten students in ten weeks.

Previous conclusions

As was stated earlier, this report builds upon several other reports, where literature review, market analyses, trade-offs and preliminary designs were performed. It was chosen to power a strut-braced wing with a hydrogen combustion open-fan engine. To meet family requirements, it was decided to make two family variants: LEAF-A and LEAF-B, with the former carrying 84 passengers up to 1,500 km and the latter carrying 58 passengers up to 1,300 km. With regard to the wing structure, propulsion system, empennage, landing gear and certain fuselage sections, it was ensured that these systems are identical between each of the family variants.

Subsystem trade-offs

Prior to the detailed design, several further trade-offs are performed. This includes a critical decision on propulsion architecture. Given the high amount of technical design risk associated with open-fan architecture, in combination with hydrogen combustion technology, it is decided to retrograde to turboprop architecture while conserving a platform for engine upgrades in future versions. Further trade-offs are performed on airfoil selection, HLD architecture, and airframe material choices. The NACA $63-415$ was selected for its high lift-to-drag ratio and excellent thickness-to-chord ratio (moment relief). High lift devices are unique per family variant in order to prevent unnecessary oversizing of the wing planform for each of the family variants. Hence, LEAF-B benefits from a simple flap and slat system while LEAF-A requires a more complex Fowler flap and slat system. Airframe materials are selected according to a balance of their recyclability, cost and strength properties.

Sizing for commonality

The second level sizing of the aircraft focuses on the sizing of aircraft systems, which is done by following Roskam and Torenbeek's methods. Scissor plots allow the CG excursion to be computed for a variety of wing positions. The smallest possible tail is selected which satisfies controllability and stability requirements for both variants, which is used on both variants for commonality. However, this requires the tail positioning to differ between the variants, making the tail length for LEAF-A larger than LEAF-B.

Next, landing gear is positioned relative to the wing in order to achieve a common wing-fuselage connection, whilst ensuring clearance angle constraints and nose gear load are sufficient. The nose gear is constantly positioned relative to the aircraft's nose. This methodology allows for load paths to be consistent between variants without significant structural redesigns.

Strut-Braced Wing Design

Given that the airfoil is chosen, the internal forces of the wing are assessed. The strut is the most critical part of the wing, and therefore has to be investigated in more detail. The strut twist is varied to change lift distribution along the strut and make the total lift distribution resemble an elliptical lift distribution. As a result, most of the strut generates negative lift to offset the peak lift of the main wing. The strut and wing structure are sized based on the loads, where the strut provides significant bending relief. The final wing with the high lift device configuration can be seen in Figure 1.

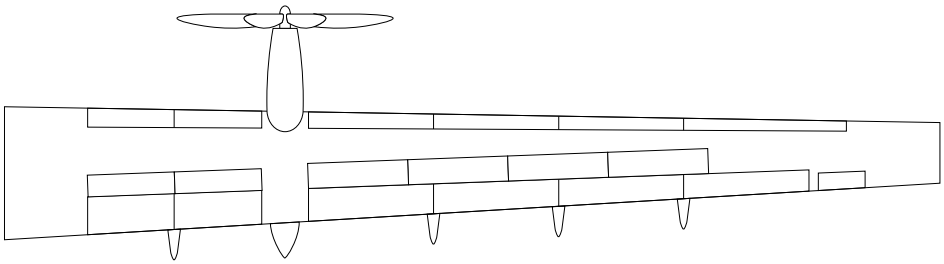

Figure 1: Final Wing Planform Design with LE and TE HLD's shown.

Novel Technologies Design

The fuselage design process consists of combining all load cases, including the particular extra loads around the wing-fuselage connection, and defining parameters for skin, frames, stringers, and longitudinal beams. It is concluded that the aircraft will be produced out of Al-2050 2198-T851, which results in an overall mass of just under 2500 kg. For reference, a typical aluminum shell would have resulted in a net mass of 400 extra kilograms.

After this, the tank and propulsion are designed in detail. The hydrogen is stored in liquid form in a single non-integral tank fitted in the tailcone, which is shown in Figure 2. It is sized to contain enough fuel for the entire mission, including loiter and diversion. The same tank is used for both family variants for commonality purposes.

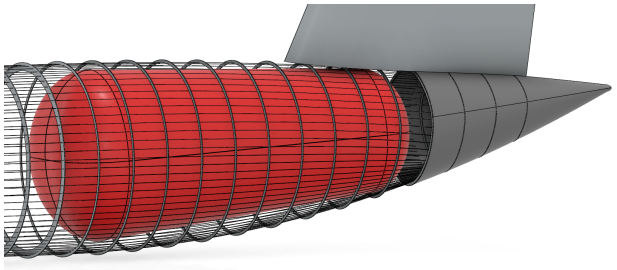

Figure 2: Placement of the aft tank in the tailcone of the aircraft. Identical for both LEAF variants.

Because liquid hydrogen is stored cryogenically, heat leaking through the tank wall boils off the liquid and raises the internal pressure during flight. To keep this within limits, the tank is insulated and has a venting system to release pressure if necessary. The pressure build-up is modelled over the mission, and venting is only required on extended missions, from the end of diversion cruise onward.

The propulsion system is a turboprop, which has a gas turbine core. This core is sized by calculating parameters at the inlet, compressor, combustor, turbine, and heat exchanger. The process is iterated until air mass flow converges. The propeller design then mainly focuses on the design of the six blades. The blade geometry is computed utilizing Blade Element Momentum Theory, which subdivides the blade into 2D slices. Parameters such as twist and sweep are calculated, and the chord distribution is determined with a differential evolution algorithm.

Final Design

The aircraft family design is performed in an non-linear iterative process until convergence is achieved in a cost function. It tracks the sequential values of key design parameters for variant A, the typically constraining variant. A sensitivity study on the effect of cruise altitude on block fuel concludes that block fuel marginally decreases when flying an extra six to seven thousand feet from FL250.

Cost

The direct operating cost is calculated to estimate the cost of flying missions with the aircraft. It focuses on the maintenance, depreciation, fees, financing and flying (crew, fuel) cost. The total DOC in USD per nautical

mile is 15.74 for LEAF-A, and 15.44 for LEAF-B. Next, the DOC is transformed into the cost per available seat kilometre for the aircraft. This is constrained by a stakeholder requirement to 115% of the E190 CASK on the same respective mission. LEAF-A costs around 76.5% of the E190 on the same mission, about 10.1 USD cents per ASK. LEAF-B is 113.4% of the E190, with 14.4 USD cents per ASK.

Another cost part is the return on investment. This is assessed by looking at the development, production, and operational cost of the entire project. This estimates a profit per aircraft of 2.2 million USD, which yields a return of investment of 5 percent. A list price of 46 million USD per aircraft is assumed (based on ERJ175) with development costs of the E-jet and Bombardier CRJ series multiplied by a novel technology factor. Since the market share is critical for profitability, a sensitivity analysis shows that the break-even market share is 17%.

Operations

Operations requirements with respect to turnaround time (less than one hour), and family commonality (greater than 65 %) are checked. The turnaround time is highly dependent on the amount of mission fuel, passenger operations, and cargo operations. Many assumptions are made with respect to airport hydrogen infrastructure in 2045. The turnaround time is assessed by putting all ground operations into a timetable, with time estimations for each of the operations. The turnaround schedule for variant which takes longer is shown in Figure 3.

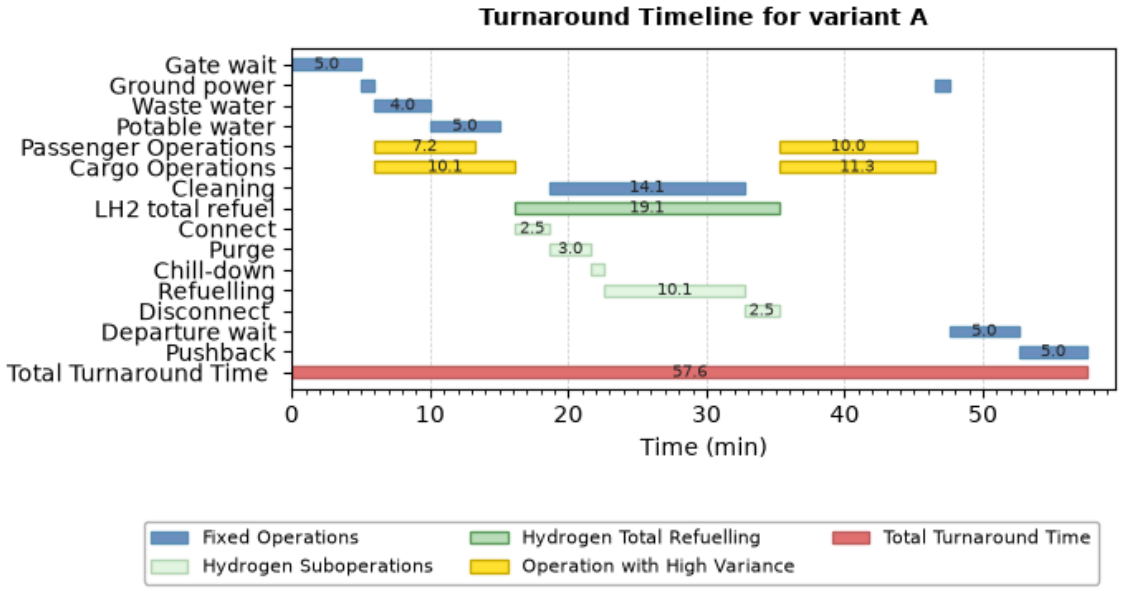

Figure 3: LEAF-A turnaround time

It can be seen that the turnaround time for LEAF-A is 58 minutes. It stands at 50 minutes for LEAF-B. The calculation includes a 10 minute margin on departure and arrival from and to the gate.

The aircraft commonality significantly decreases maintenance costs for customers. Commonality is assessed by part commonality. These parts are weighted over the total weight of the aircraft, after which a commonality of 75.6% is predicted. This comfortably meets stakeholder requirements.

The implementation strategies for the project are also looked at. Besides the two variants, an additional cargo variant can be made. This opens up the regional feeder freighter market, for which turboprops are often used. Particularly environmentally friendly options are expected to be of interest to airlines with global warming becoming more of a problem.

Cargo variant

A freighter aircraft can be made out of variant A by removing furnishings and reducing the crew number. The regional air cargo market commonly uses turboprop aircraft. Environmentally-conscious cargo airlines can be interested in this variant. The cargo variant can carry just over ten tons of payload, and has a range of 1500 km.

Sustainability

The major advantage of hydrogen combustion is the reduction of carbon emissions. Nonetheless, the 80-90% promised reduction in emissions depends on a world-wide effort to green hydrogen production. NO_x is also reduced by 70 and 60 percent for family members A and B during LTO cycles (up to 90 % during cruise), which meets the requirements. This is met due to a reduced fuel flow of hydrogen. Another important sustainability part is the recyclability. The fuselage, cabin interior, engine, and hydrogen tank are recyclable, which leads to a total of 32% by aircraft EOM. This does not yet include the wingbox or empennage, which are also expected to be able to be recycled.

Risk

With this novel design, risk has to be assessed, which is done using a RAMS study. The reliability of the aircraft is estimated using data from reference aircraft. This leads to a final dispatch reliability of 99.7%. The maintenance of the aircraft is also discussed, where the different maintenance checks are assessed. These include daily and weekly checks, and the occasional tank shop checks. The final aspect of a RAMS study is the safety of the aircraft family,

A RAMS study established the possible risks and their mitigations, such as hydrogen leakage. This particular risk was mitigated by having a vapour recovery adapter used during refuelling and defuelling

Figure 4: LEAF-A Assembly

Preface

This report was written by ten third-year students at the Faculty of Aerospace Engineering at TU Delft. The goal was to design a low-emission, high-commonality sustainable aircraft family of 2-3 regional aircraft with different range and payload capabilities. At the very beginning we were given an extensive list of stakeholder requirements, based on which derived our mission, system and subsystem requirements. Based on them three different aircraft concept were developed. Then a trade-off was conducted and it turned out that the strut-braced wing aircraft concept was performing the best.

This report is the continuation of the strut-braced wing design concept presented in the midterm report. Readers with a special interest in dry-wing design can study the contents of Chapter 4, while Chapters 5 and 6 deal with the structural considerations of the fuselage and the hydrogen tanks, respectively. Chapter 7 delves deeper into the propulsion system design. For those who want to investigate the viability of strut-braced aircraft family, they can check the cost analysis in Chapter 11. As sustainability is one of the vital aspects of this project special attention was given to Chapter 16.

We would like to thank our tutor P. Proesmans and our coaches D. Atmaca and F. Taruffi for their constant support during the Design Synthesis Exercise and for their immediate response to questions surrounding both the technical and logistical aspects of the project. We are also grateful to ir. J. Sinke, Dr. ir. R. Vos, Dr. A. G. Rao, Dr. ir. T. Sinnige, and Dr. F. De Domenico for answering technical related questions and for providing us with advice on how to advance further in the project. Finally, we would would like to thank GasTurb for providing us with a 30 day license to validate parts of our propulsion system.

Delft, 18 June 2026
Carlos Orce López, Marius Michaud, Viktor Nikolov, Lisa van den Berg, Toine van Wassenaar, Lindsay Landman, Seán McCarthy, Kacper Montewka, Nathan Overvelde, Daan Vlasblom

Contents

Nomenclature

Abbreviations

Symbol	Definition
AoA	Angle of Attack
AC	Air Conditioning
AC	Alternating Current
ACL	Altitude Clearance
ACM	Air Traffic Control Communications Management
AEP	Aircraft Estimated Price
AGB	Accessory Gearbox
AIR	Airlines
APT	Airports
APU	Auxiliary Power Unit
ASK	Available Seat Kilometre
BEMT	Blade Element Momentum Theory
BET	Blade Element Theory
BUD	Budget
B[#]	Block [Number]
CAD	Canadian Dollar
CASK	Cost per Available Seat Kilometre
CFD	Computational Fluid Dynamics
CFRP	Carbon Fibre Reinforced Polymer
CI	Commonality Index
CO_2	Carbon Dioxide
CST	Cost
ctrl	Controllability
CX	Customer
C[#]	Consequence [Degree]
D-ATIS	Digital Automatic Terminal Information Service
DC	Direct Current
DCL	Departure Clearance
DOC	Direct Operating Cost
DR	Dispatch Reliability
EOL	End of Lifetime
EOM	Empty Operative Mass
FBS	Functional Breakdown Structure
FC	Flight Cycles
FEM	Finite Element Method
FFM	Functional Flow Diagram
FH	Flight Hours
FL	Flight Level
GH_2	Gaseous Hydrogen
GPU	Graphics Processing Unit
HLD	High-Lift Device
HPC	High Pressure Compressor
HPT	High Pressure Turbine
HT	Horizontal Tail
ICAO	International Civil Aviation Organization
IOC	Indirect Operating Cost
ISA	International Standard Atmosphere
LCA	Life Cycle Assessment
L, LN	Landing
LE	Leading Edge
LEAF	Low-Emission Aircraft Family

Symbol	Definition
LH_2	Liquid Hydrogen
LPC	Low Pressure Compressor
LPC	Low Pressure Turbine
L[#]	Likelihood [Degree]
MAC	Mean Aerodynamic chord
MEL	Minimum Equipment List
MIS	Mission
MLG	Main Landing Gear
MRO	Maintenance, Repair and Overhaul
MTOM	Maximum Take-Off Mass
MTOW	Maximum Take-Off Weight
MTTR	Mean Time to Repair
NACA	National Advisory Committee for Aeronautics
NEO	New Engine Option
NLG	Nose Landing Gear
NOTAM	Notices to Air Missions
NOTOC	Notification to Captain
NO_x	Nitrous Oxides
nvPM	Non-Volatile Particulate Matter
OEM	Operational Empty Mass
OEM	Original Equipment Manufacturers
OOOI	Out, Off, On, In
OPR	Overall Pressure Ratio
OTH	Other
PAX	Passenger
PER	Performance
PPE	Personal Protective Equipment
RAMS	Reliability, Availability, Maintainability and Safety
RoI	Return on Investment
R&D	Research and Development
R-[#]	Risk [Number]
SAF	Safety
SAF	Sustainable Aviation Fuel
SAM	Serviceable Addressable Market
SBW	Strut-Braced Wing
SM	Safety Margin
SOM	Serviceable Obtainable Market
stab	Stability
STKCX	Stakeholder Customer Requirement
STOL	Short Take-Off and Landing
SURV	Surveillance
SUS	Sustainability
SV	Stretch Variant
SYS	System
TAM	Total Addressable Market
TAT	Turnaround Time
TE	Trailing Edge
TET	Turbine Entry Temperature
TMA	Terminal Manoeuvring Area
ULD	Unit Load Devices
USD	United States Dollar
U[#]	Unit Test [Number]

LEMAC	Leading Edge Mean Aerodynamic Chord
LG	Landing Gear
VLM	Vortex Lattice Method
VT	Vertical Tail
V&V	Verification and Validation

Greek Symbols

Symbol	Definition	Unit
α	Angle of Attack	[deg]
2α	Wing-Strut Attachment Angle	[deg]
β	Mass Fraction	[–]
β	Compressibility factor	[–]
β	Sideslip angle	[°], [rad]
β	Tip-back angle	[°], [rad]
γ	Specific Heat Ratio	[–]
γ	Heat efficiency	[–]
Γ	Lift distribution	[N/m]
δ	Angle of deflection	[deg]
Δ	Difference	[–]
ε	Downwash Angle	[deg]
ε	Exchanger Efficiency	[–]

Symbol	Definition	Unit
ϵ	Twist	[–]
η	Efficiency	[–], [%]
θ	Strut angle	[rad]
θ	Scrape angle	[°], [rad]
λ	Taper Ratio	[–]
Λ	Sweep Angle	[°], [rad]
ν	Poisson Ratio	[–]
ρ	Density	[kg/m^3]
σ	Tensile Stress	[Pa]
τ	Aileron Effectiveness	[-]
τ	Shear Stress	[Pa]
ϕ	Propeller-Tail Angle	[°], [rad]
Ψ	Turnover Angle	[°], [rad]
φ	Effective sweep angle	[rad]

Roman Symbols

Symbol	Definition	Unit
a	Induction factor	[-]
A	Area	[m^2]
A, AR	Aspect Ratio	[-]
b	Wingspan	[m]
B	number of blades	[-]
c	Chord	[-]
C	Coefficient	[-]
C	Cost	[USD]
C	Flow Capacity	[J/K/s]
C_d	Cost of Depreciation	
C_f	Skin Friction Coefficient	
C_l	2D Airfoil Lift Coefficient	[-]
C_L	3D Wing Lift Coefficient	[-]
C_m	Moment Coefficient	[-]
C_{pd}	Pressure Drag Coefficient	[-]
$\bar{c}$	Mean Aerodynamic Chord	[m]
d	Diametre	[m]
E	Elastic Modulus	[Pa]
f	Slenderness Ratio	[-]
F	Force	[N]
g	Gravitational constant	[m/s^2]
G	Shear Modulus	[Pa]
h	Height	[m]
i	Half-dome height	[m]
I	Area Moment of Inertia	[m^4]
J	Polar Moment of Inertia	[m^4]

Symbol	Definition	Unit
l	Length	[m]
m	Mass	[kg]
M	Pitching Moment	[Nm]
$\dot{m}$	Mass Flow	[kg/s]
M	Bending Moment	[Nm]
n	Load Factor	[-]
N	Normal Force	[N]
N	Number	[-]
p	Probability	[-]
p	Roll Rate	[rad/s]
q	Pitch Rate	[rad/s]
Q	First Moment of Inertia	[m^3]
r	Yaw Rate	[rad/s]
R	Radius	[m]
Re	Reynolds Number	[-]
S	Surface Area	[m^2]
S_{wet}	Wetted Area	[m^2]
t	Thickness	[m]
V	Shear Force	[N]
V	Velocity	[m/s]
V	Volume	[m^3]
w	Width	[m], [inch]
W	Weight	[N]
W/S	Wing Loading	[N/m^2]
W/P	Weight-to-Power	[–]
x	Longitudinal Axis	[m]

K_{fc}	Flight Control Factor	[-]
K_{lav}	Lavatory Factor	[-]
K_{fc}	Catering Factor	[-]

y	Lateral Axis	[m]
z	Vertical Axis	[m]

Subscripts and Superscripts

Symbol	Definition
a	Aileron
abs	Absolute
ac	Aerodynamic Centre
amb	Applied Maintenance Burden per Nautical Mile
ap	Airplane (Cost of Depreciation)
apc	Average Production Cost
app	Approach
aux	Auxiliary
av	Avionics
av	Average
avg	Average
c	cold
cg	Centre of Gravity
cr	Critical
CR	Cruise
D	Drag Force
dap	Airframe Depreciation
dapsp	Airplane Spare Parts Depreciation
dav	Avionics Depreciation
deng	Engine Depreciation
dengsp	Engine Spare Parts Depreciation
depr	Depreciation
dprp	Propeller Depreciation
emp	Empennage
eq	Equivalent
f	Flap
f	Friction
fin	Financing
fus	Fuselage
h	Horizontal Stabiliser
h	hot
ind	induced
inj	Injection
ins	Insurance
int	Interior
l	Rolling Moment
L	Lift Force
L,LN	Landing

Symbol	Definition
lab/ap	Labour (Cost) of Airframe and System Maintenance
lab/eng	Maintenance Labour (Cost) for the Engines
lat	Lateral
lf	Landing Fees
LH_2	Liquid Hydrogen
lnr	Landing, Navigaton, Registry
long	longitudinal
m	Pitching Moment
main	Maintenance
man	Manufacturing
mat	Material
mat/eng	Maintenance materials for Engine Parts
mw	Main Gear Wheel
n	Yawing Moment
N	Normal Force
nac	Nacelle
nf	Navigation Fees
nw	Nose Gear Wheel
pol	Fuel and Oil
prop	Propulsion
qc	Quality Control
rel	Relative
Q	Torque
req	Required
rt	Registration Taxes
sp	Spoiler
str	Stringer
T	Tangential Force
TO	Take-Off
T	Thrust
ts	Tensile Stress
v	Vertical Stabiliser
w	Wing
w	weld
wet	wetted
y	Yield

Trade-off weights

Excellent (2 pt): expected to exceed Green	**Good (1 pt):** expected to meet Cyan	**Neutral (0 pt):** Correctable Yellow	**Poor (-2 pt):** not expected to meet Red

1

Introduction

Author: Daan *Contributors: Viktor, Kacper*

Commercial aviation is a rapidly growing industry responsible for over 2% of worldwide annual carbon dioxide emissions [1]. This share is only expected to increase in the coming years, with passenger traffic set to double by 2050 compared to 2026 levels [2]. To address that challenge, a team of ten Aerospace Engineering students was tasked with a mission of developing a regional airliner family, ready for service in 2045, capable of significantly cutting down on emissions, reducing well-to-wake carbon dioxide emissions by 80%, nitrous oxides and non-volatile particulate matter by 30% and limiting noise. Results of the design process are presented in this report, covering steps and reasoning that lead to the creation of the LEAF family.

Up until now, the project has gone through numerous stages covering subsequent development phases of the commercial airliner and reporting on the progress made by the research team. Firstly, a *Project Plan* was created to establish the workflow for family development. Next, a *Baseline Report* followed, focusing on conducting research about the existing aircraft configurations and mission requirements. Lastly, a *Midterm Report* was created, where a trade-off was performed between different design options, found to be a laminar wing, lifting fuselage, and truss-braced wing design. The outcome of all that analysis is summarised and further developed in this *Final Report*, covering the development of the chosen final design: *A strut-braced wing aircraft powered by liquid hydrogen combustion in open-fan engines*. Early on in the detailed design phase, however, difficulties of obtaining reliable validation data for the proposed propulsion system have emerged, leading to a switch to a more conventional turboprop engine design, which was agreed upon with the client. Liquid hydrogen is still used as a source of energy.

Sizing of the unconventional aircraft design required developing special tools capable of running a convergence optimisation study for each of the aircraft family members. Python script was created covering Class I and Class II sizing methods, adjusted for novel technologies. Systems such as the wing, empennage, landing gear position, and fuel tank size were all taken into account in that algorithm, leading to a robust and versatile tool that can be used in the unconventional aircraft family design. Other systems such as the electrical and software systems are outlined. Extra emphasis is placed on propulsion design, as this unlocks a significant reduction in greenhouse emissions. Furthermore, attention is given to the structural design of the fuselage skin and frames, the strut and its attachment to the fuselage, and the floor beam structures. Finally, a detailed look is taken at the implementation of hydrogen fuel. With the aircraft family sized, the market is more closely analysed, airliner and manufacturing costs are defined, and a sustainability analysis is performed. This culminated in the design of the sustainable family.

The report is outlined as follows. The work performed previously on the strut-braced wing concept is summarised and updated, as shown in Chapter 2. Chapter 3 defines a methodology for more detailed aircraft design, which is iterated with the preliminary simulation. Chapter 4, 5, 6 and 7 focus on detailed subsystem design of the wing, fuselage, tank and propulsion system. The interfacing convergence script is explained in Chapter 8, where design values are also shown. The simulation and model are verified and validated in Chapter 9. The method of assembly is defined in Chapter 10, and costs, as well as technical budgets, are computed in Chapter 11 and Chapter 12, respectively. As a next step, the operational capabilities of the strut-braced aircraft are carefully assessed in Chapter 13 as a new freighter variant is considered. Chapter 14 discusses the hardware and software systems. Chapter 15 reveals the the future timeline of the project, while Chapter 16 explains the sustainability strategy behind the project. As a next step, in Chapter 17 a RAMS study is performed. Lastly, it is shown that the final family design complies with all stakeholder requirements in Chapter 18. The design of a sustainable aircraft family is then concluded in Chapter 19, and recommendations are given for future design processes.

2

Final design

Author: Lindsay *Contributors: Marius, Daan*

From a trade-off done in the midterm report [3], the final design is revised. Furthermore, it has been determined that the aircraft family consists of two members; LEAF-A able to carry 84 pax over a 1500 km range, and LEAF-B able to carry 58 over a 1300 km range. The chosen design for these aircraft is chosen such that this is the optimal design. Therefore, a closer look into the propulsion system is done. First, the fuel type is looked at in Section 2.1. After this, another trade-off is done in Section 2.2, to find the right engine fit for the design.

2.1. Updated fuel system

Author: Lindsay

The final fuel is now looked at again. Previously, it was decided to use 67% of liquid hydrogen as fuel, with the remaining fuel consisting of SAF. However, it was assessed that a full hydrogen solution might have a better environmental impact than the hybrid fuel option. However, this comes with a longer turnaround time due to the longer refuelling required [4]. The changes in commonality will be minimal, as the first-level structural design will not change drastically. The risk will stay about the same, if not less, as adding a hybrid system would make it more complicated and could increase the risk. The direct operating cost is expected to reduce slightly, as less fuel is needed, and the reduction in SAF is larger than the increase in hydrogen and tank mass. The final trade-off values when implementing the data from the class I estimations for the full hydrogen can be seen in Table 2.1.

Table 2.1: Final Values Trade-Off Full Hydrogen

Concept / Metric	Hybrid	Full Hydrogen
Environmental Impact (30%) [% compared to baseline]	4.8 CO_2, 61 NO_x Cyan	4.1 CO_2, 47.6 NO_x Cyan
Direct Operating Cost (25%) [USD/flight]	3150 Cyan	2750 Green
Commonality (20%) [%]	80 Green	80 Green
Turnaround time (15%) [minutes]	32 Cyan	33 Cyan
Risk (10%) [-]	Moderate Cyan	Moderate Cyan
Total Points	1.2	1.45

It can be seen here that full hydrogen outperforms the hybrid version. It is much better at reducing the NO_x emissions than the full hydrogen, as was expected. Besides the better environmental performance, it can also be seen that the direct operating cost of the full hydrogen concept is much less than the hybrid. This is because the full hydrogen needs less fuel, as mentioned before. The full hydrogen configuration has more mass for the tank and hydrogen, both being 100 kilograms. However, the mass of SAF is 300 kilograms, so the full hydrogen configuration weighs 100 kilograms less than the hybrid configuration. As the cost per kilogram for hydrogen and SAF is about the same, 2.23 $\$/kg$ [5], this leads to a big reduction in operating cost for the full hydrogen aircraft. With these values, a sensitivity study also had to be performed, to analyse the validity of these results, where full hydrogen version outperformed the hybrid throughout all of these. This shows that the full hydrogen concept would be a better version of the concept than previously chosen. Therefore, pure hydrogen combustion

is chosen as the final energy source.

2.2. Engine trade-off

Author: Lindsay

With the final fuel type chosen, the only thing left to optimise for in this concept is the propulsion type. In the initial trade-off, three different engines were chosen, which now gives room to identify which engine is the overall best fit for the concept [3]. From previous performance measurements, it is expected that the turboprop would give the most optimal environmental impact, but it also means the aircraft should fly at a lower Mach number. This will then increase the block time, and also increasing the crew costs in the DOC. Therefore, the trade-off is done one more time, to identify the performance of the following three different engine types: open-fan (as initially chosen), turbofan, and turboprop.

Table 2.2: Final Values Engine Trade-Off

Concept / Metric	Openfan	Turbofan	Turboprop
Environmental Impact (30%) [% Baseline]	4.1 CO_2, 47.6 NO_x Cyan	5.4 CO_2, 60.5 NO_x Cyan	5.0 CO_2, 36.1 NO_x Green
Direct Operating Cost (25%) [USD/flight]	2750 Green	3250 Cyan	3450 Cyan
Commonality (20%) [%]	80 Green	80 Green	80 Green
Turnaround time (15%) [minutes]	33 Cyan	33 Cyan	33 Cyan
Risk (10%) [-]	Moderate Cyan	Moderate Cyan	Moderate Cyan
Total Points	1.45	1.2	1.5

From this trade-off, it can be seen that the best option is the turboprop. It shows that the turbofan engine is the worst performer, due to high DOC and average environmental performance. The open-fan and turboprop are both very close, and with a sensitivity study it also shows that these are very sensitive to a change in weights of the metric. However, as the open-fan has very little research into actual validation, this is still not a good choice. The lack of information and data means that even if the engine is fully designed, it cannot be validated properly, which means it is impossible to be certain of the performance of this engine. This then leads to the aircraft not being able to be designed properly, and would make it impossible to understand the performance of the aircraft during actual operation. Therefore it is chosen to go ahead with the turboprop engine. This engine is very reliable and used a lot already nowadays, which would mean there is plenty of references available for validating any of the choices that might be made.

With these trade-offs done, the final design is set to be a conventional fuselage with a strut braced wing. The engine will be set on the wing, and it will be a turboprop with full hydrogen fuel.

2.3. Functional systems

Author: Nathan

As the final design is chosen, some of the functions can be specified in greater depth, while other functions are added. For example: the operating of the energy source is more specific then previous reports. It is now known that hydrogen is the energy source and therefore the level 3 and 4 functions have become more specific. For example, the hydrogen fuel requires an additional function of the aircraft; if the tank pressure reaches a pressure above 300 kPa, then venting should happen. Due to boil-off, the tank has to be relieved of pressure in case a mission takes longer than anticipated. Thus, an additional function has been added under the diversion function. The Functional Flow Diagram has not changed from the previously made Diagram.

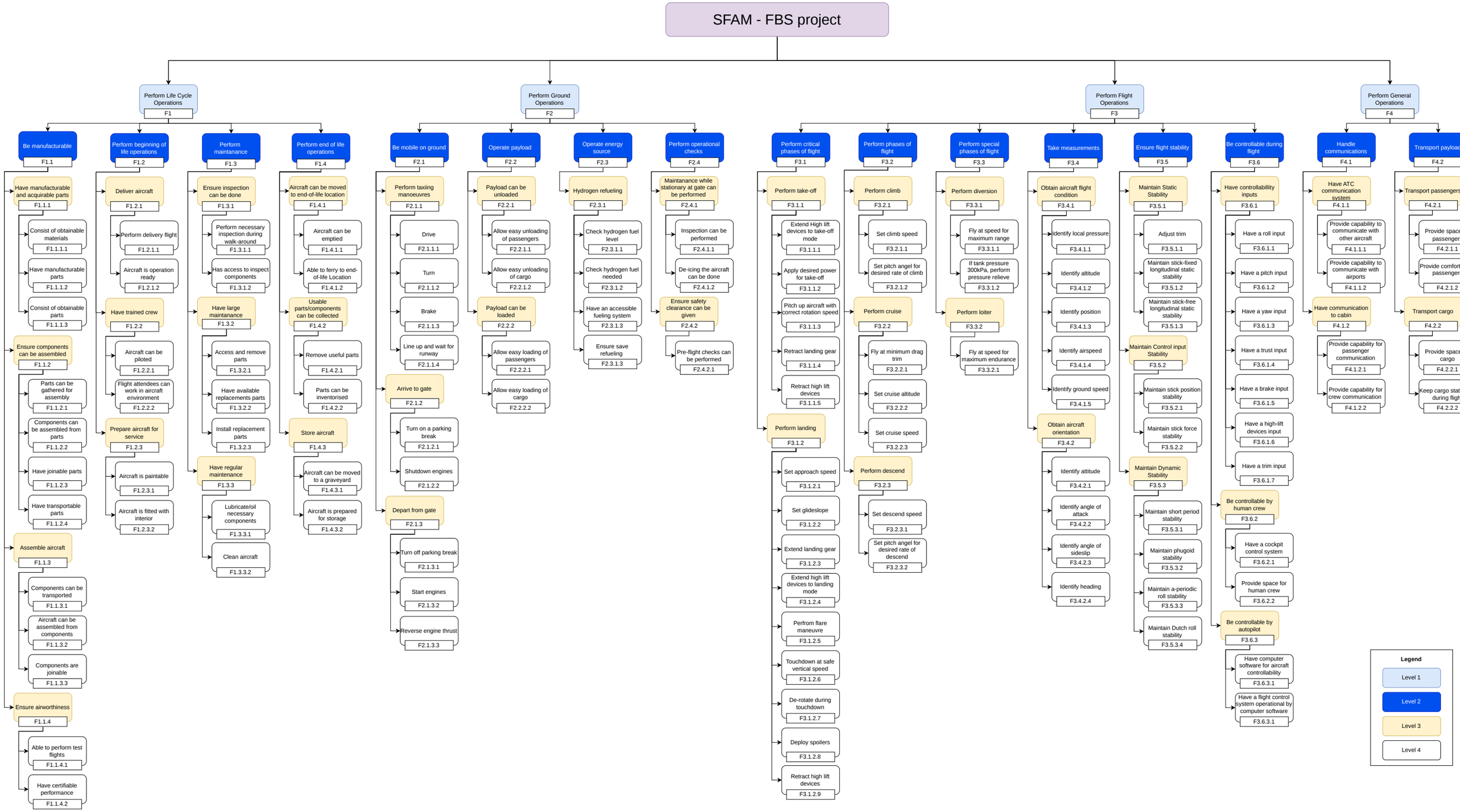

Figure 2.1: Functional Breakdown Diagram

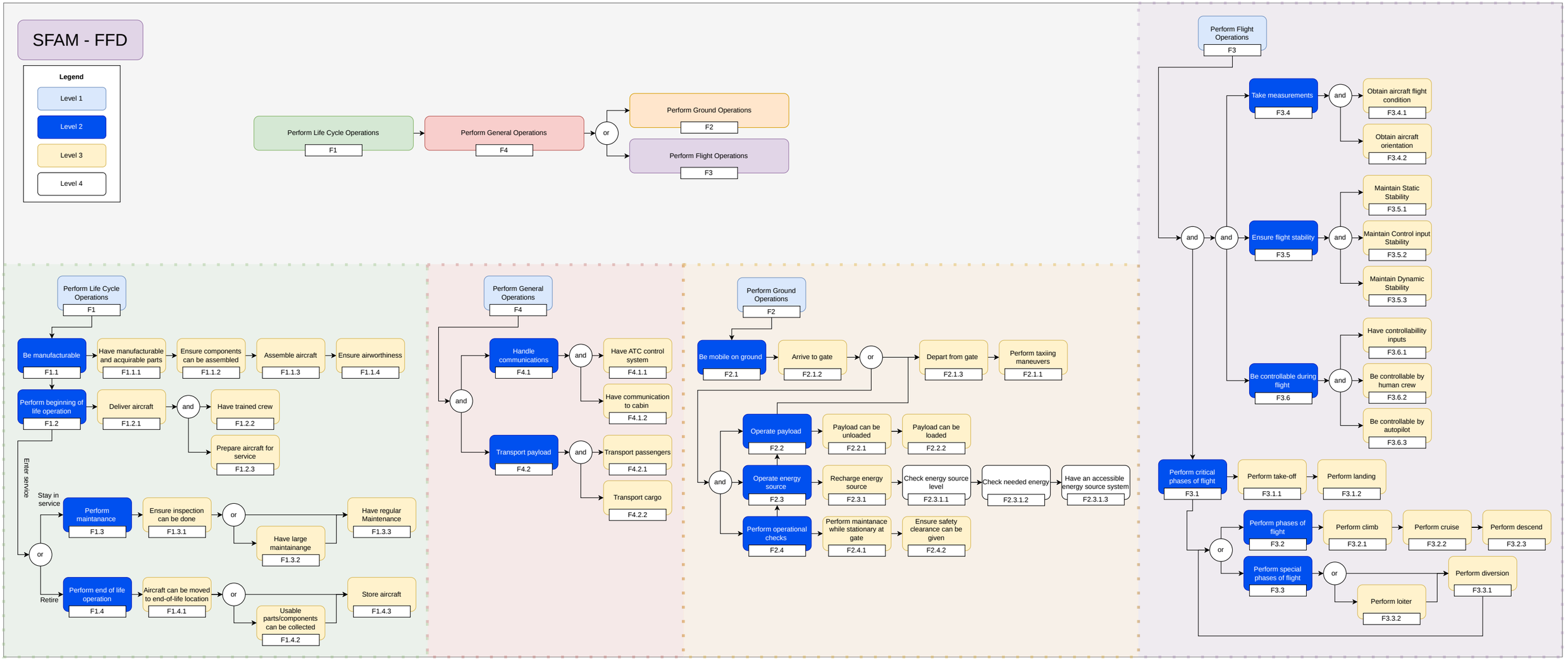

Figure 2.2: Functional Flow Diagram

3

Class II sizing

Author: Lisa, Lindsay, Daan, Toine, Nathan *Contributors: Marius*

After the final design is defined, the detailed sizing is performed. Class I sizing has been considered for multiple designs in the previous report. Upon this, the Class II sizing methods are continued. The aircraft's geometry, weight, and balance are calculated in further detail. The results are iterated through the Class I sizing method until the aircraft's MTOM, wing size, and empennage size converge.
For the wing, fuselage, and hydrogen tanks, more detailed sizing methods are used and included in the convergence loop. These are discussed in further chapters.

3.1. V-n diagram

Author: Lindsay

The first part of the design is to create a V-n diagram. These diagrams plot the load factors of the aircraft versus the velocity. The V-n diagram is made using the method proposed by Roskam [6].

Two different diagrams are obtained. The first one is the regular V-n diagram, which can be seen in Figure 3.1a. In this diagram, it can be seen that the aircraft will experience a maximum load factor of 2.5 and -1. This complies with regulations posed by CS 25 [7]. The stall speed is estimated with these calculations at 88 kts. The second diagram that is obtained is the gust diagram. This uses the data from the V-n diagram and adjusts it slightly to get the diagram shown in Figure 3.1b.

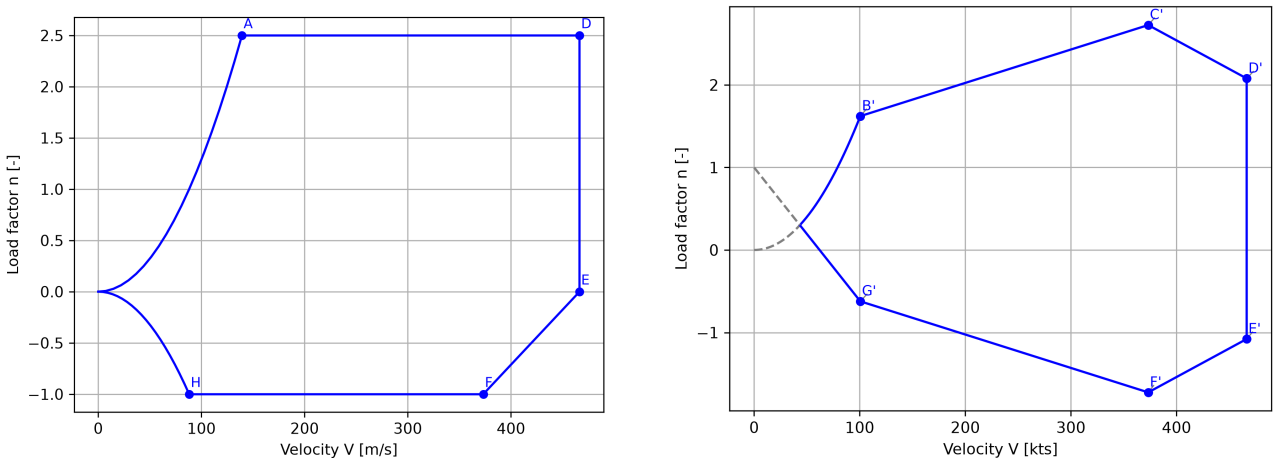

(a) V-n diagram

(b) Gust diagram

Figure 3.1: V-n and Gust load diagrams.

3.2. Component weights and centre of gravity

Author: Lisa

For the detailed design, the OEM is divided into individual components, which are sized and assigned a centre of gravity location. Summing the masses and their moments about the aircraft nose gives the OEM centre of gravity of the aircraft. This will feed into the loading diagram discussed in Section 3.3 and the empennage sizing discussed in Section 3.5. The estimation follows the Class II sizing method of Roskam Part V [8], with

each component group sized by the empirical relations found in Chapters 5-8 of the book. Three component groups are sized in more detail instead, discussed in more detail in further sections.

Component weight breakdown

The OEM is divided into structural, propulsion, and fixed equipment groups. Unless explicitly stated, the components are sized with the corresponding Roskam Part V relation [8]. The relations are stated with respect to imperial units. The inputs are therefore converted from SI and back.

The horizontal and vertical tail are driven by the their respective areas, the design dive speed taken from the V-n diagram of Section 3.1 and half-chord sweep [8]. The vertical tail weight is multiplied by an additional T-tail factor K_v that accounts for the horizontail tail mounted at the top. The nacelle mass is determined by the turboprop function of the the take-off shaft power [8]. The landing gear masses follow the retractable gear coefficients of other civil aircraft, with a high-wing correction factor $K_{g,r} = 1.08$ applied to both the main and nose landing gears [8]. Two structural groups are not sized according to Roskam since the strut-braced wing configuration for this size aircraft falls outside of the scope of Roskam's statistical relations. The strut-braced wing carries a different load path from a conventional wing, and its mass is therefore computed by a strut and wing-box structural model described in Chapter 4. The strut mass is contained within the single wing group mass. The fuselage group is sized using the structural calculations described in Chapter 5. The mass is built up from the skin, stringers, frames and floor beams sized against the CS-25 load cases [7].

The bare engine mass is taken as 820 kg per engine from a reference LH_2 aircraft study by Onorato et al. [9]. The propulsion installation group is sized with the Roskam relations for a turboprop, and doubled to be conservative on differences between kerosene (Roskam) and LH_2.

The flight control, electrical, instrumentation/avionics, oxygen, APU, furnishings, baggage-handling, and paint components are all sized with the standard Roskam relations for a transport aircraft [8]. The flight-control group uses the powered-controls factor $K_{fc} = 0.64$, the furnishings mass uses the short-range lavatory and catering factors $K_{lav} = 0.31$ and $K_{buf} = 1.02$. The passenger count is an input for air conditioning, oxygen and furnishing relations directly, so these groups differ between the two variants. The single aft tail-cone LH_2 tank is sized by the detailed tank design described in Chapter 6, where the tank is sized with the thermal/structural loading method of Onorato et al. [9].

Component positioning

Each component is assigned a location x_{cg} measured from the nose. The wing and tank stations are taken from their detailed design models so that the CG position is consistent with the method used to size the mass and geometry.

The empennage locations are placed from the most aft feasible position of the vertical tail root chord inside the fuselage, with the horizontal tail referenced from the vertical tail geometry so that both are consistent with the T-tail configuration. The nacelles and engines are placed at the spanwise engine location (30%) projected onto the fuselage axis, with the nacelle CG set at 40% of nacelle length aft of the nacelle nose per Roskam [8]. The components distributed over the fuselage (fuselage structure, flight control, electrical and paint) are placed at 43.5% of the fuselage length. The components distributed over the cabin (air conditioning, oxygen, furnishings and baggage equipment) are placed at the middle of the cabin. The avionics are placed in the nose and the APU at 95% of the fuselage length. The landing gear locations are taken from the landing gear sizing of Section 3.7 and the tank position from Chapter 6.

The OEM CG (Equation 3.1) comes from summing the moments of the masses of all components, expressed both as their absolute x-position and as a fraction of the MAC.

$$x_{cg,OEM} = \frac{\sum_i m_i x_{cg,i}}{\sum_i m_i}, \quad x_{cg,OEM} = \frac{x_{cg,OEM} - x_{LEMAC}}{\bar{c}} \times 100\%, \tag{3.1}$$

with x_{LEMAC} the leading edge MAC position and $\bar{c}$ the MAC. The x_{LEMAC} position is the design variable optimised in the upcoming sections to centre the loading distribution about the wing and minimise the horizontal tail area. The OEM CG is the anchor of the loading diagram, to which the payload and fuel loadings are added. Because the SBW has a short MAC relative to the long fuselage, an absolute shift in CG results in a relatively large excursion MAC%.

3.3. Loading diagram

Author: Lisa

The loading diagram follows the CG of the aircraft as it is loaded from the OEM up to the MTOM, across different loading sequences. The most aft and most forward CG limits are established that the aircraft must remain controllable and stable in. The CG excursion determined are input for the scissor plot and empennage sizing of Section 3.5 and to the landing gear placement of Section 3.7. The diagram is constructed separately for each variant since they differ in passenger count and cabin length. The method follows the standard loading procedure as taught by Systems Engineering & Aerospace Design (TU Delft, AE3211-I)[1].

Loading begins from the OEM CG and is loaded with cargo, passenger, and finally fuel. At each step a discrete mass Δm is added at its position Δx after which the mass and CG are updated as described in Equation 3.2.

$$m_{n+1} = m_n + \Delta m, \quad x_{n+1} = \frac{m_n x_n + \Delta m \Delta x}{m_{n+1}} \tag{3.2}$$

The CG is expressed as % of MAC. To find the CG limits, each loaded component is loaded in both forward-aft and aft-forward orders. The envelope of all sequences then gives the most forward and most aft CG positions.

Cargo is divided in a forward and aft cargo bay, placed at 25% and 75% of the cabin length. Each passenger is attributed 20 kg of cargo, which is distributed equally among the two cargo holds. The cabin has a 2+2 seats abreast configuration and is divided into the needed amount of seat rows for each variant with uniform seat pitch. Each passenger is taken to weigh 80 kg. Window and aisle seats are loaded as separate groups and are loaded both front-to-back and back-to-front, creating two potato shapes in the loading diagram. Finally, the LH_2 is loaded into the single aft tailcone tank, at the tank centroid x_{tank} from Chapter 6. Because the tank sits quite aft of the wing, fuel loading shifts the CG aft and ends at the MTOM.

The forward and aft CG positions are taken as the minimum and maximum positions reached across all loading sequences, after which a 2% MAC loading margin is applied to each side to obtain the operational CG limits. These are also the limits against which the empennage and landing gear are sized against. The resulting loading diagrams for both variants are shown in Figure 3.2a and Figure 3.2b. The final corresponding values can be found in Chapter 8.

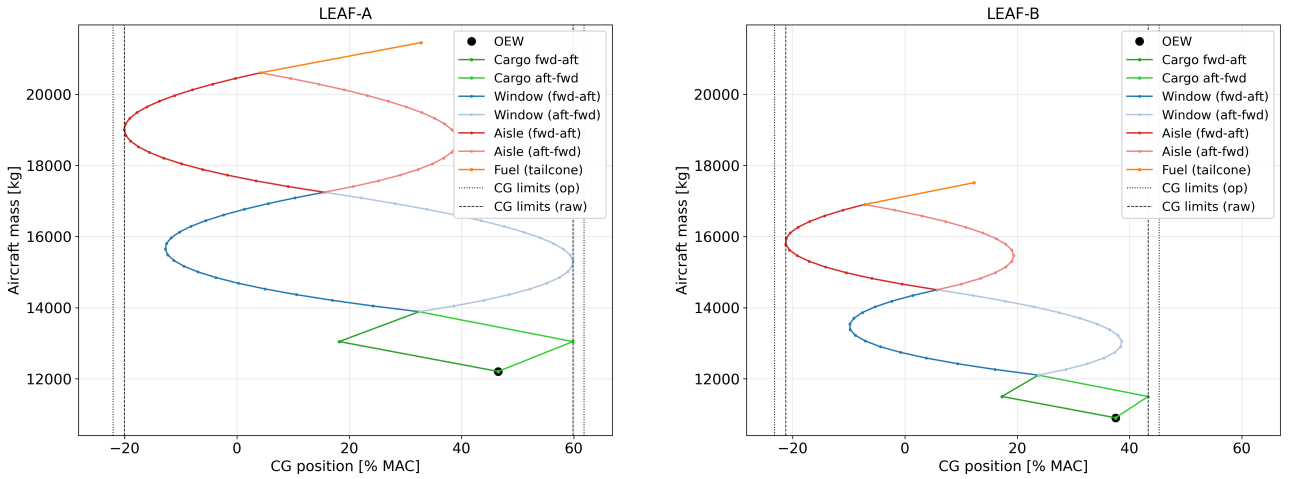

(a) Loading diagram for LEAF Variant A.

(b) Loading diagram for LEAF Variant B.

Figure 3.2: Loading diagrams for the LEAF variants. Following in the order cargo, window and aisle passengers and fuel. Each group is both loaded aft to forward and forward to aft. The raw and operational cg limits are shown as the black dotted lines. Both plots are on the same scale.

3.4. Aerodynamic parameters

Author: Lisa

The empennage sizing of Section 3.5 is done through combining the CG range calculation of Section 3.3 and a scissor plot. Generating the scissor plot requires aerodynamic parameters describing the lift, balance, and downwash of the wing, fuselage and tail combination. This section describes how these parameters are determined. They cover the lift-curve slopes of the wing and tail, the aerodynamic centre of the aircraft-less-tail, the downwash gradient at the tail, and the zero-lift pitching moment. They are evaluated at both the cruise

[1] `https://brightspace.tudelft.nl/d2l/le/content/782547/viewContent/4495962/View` *(Accessed: 10/06/2026)*

and approach conditions since stability is critical in cruise and controllability is critical at low speeds with flaps deployed. The methods follow Torenbeek [10].

Lift-curve slopes

The wing and horizontal tail lift-curve slopes are determined by the DATCOM relation [11].

$$C_{L_\alpha} = \frac{2\pi A}{2 + \sqrt{4 + \dfrac{A^2\beta^2}{\eta^2}\left(1 + \dfrac{\tan^2 \Lambda_{c/2}}{\beta^2}\right)}}, \quad \beta = \sqrt{1 - M^2}. \tag{3.3}$$

Where A is the aspect ratio, $\Lambda_{c/2}$ is the half-chord sweep, M the Mach number, and $\eta = 0.95$ the airfoil efficiency factor. Equation 3.3 is evaluated for both the wing and tail at the cruise and approach Mach numbers, giving $C_{L_{\alpha,h}}$ and $C_{L_{\alpha,w}}$ in each condition. Equation 3.4 subsequently computes the final lift-curve slope of the aircraft-less-tail, adding the fuselage lift carry-over and lift-loss terms [10].

$$C_{L_{\alpha,A\text{-}h}} = C_{L_{\alpha,w}} \left(1 + 2.15\frac{b_f}{b}\right)\frac{S_{net}}{S} + \frac{\pi}{2}\frac{b_f^2}{S}. \tag{3.4}$$

with b_f the fuselage width, b the wing span, S the reference wing area and S_{net} the wing area without the fuselage covered section.

Aerodynamic centre

The aerodynamic centre of the aircraft-less-tail x_{ac} starts at the wing quarter chord after which four corrections for the fuselage and propulsion are added as shown in Equation 3.5 [10]. All are expressed as a fraction of the MAC.

$$x_{ac} = x_{ac,w} + \Delta x_{ac,fus,1} + \Delta x_{ac,fus,2} + \Delta x_{ac,nac} + \Delta x_{ac,prop}. \tag{3.5}$$

Where the $x_{ac,w} = 0.25$. The two fuselage terms are the destabilising term due to the nose creating lift in front of the wing, and the stabilising term due to the upwash of the wing over the aft fuselage [10]. The nacelle term uses the wing-mounted nacelle factor $k_n = -4.0$ applied to the frontal area of the nacelle and its moment arm [10]. The propeller term is a contribution due to the turboprop propellers ahead of the wing generating a destabilising force in the propeller plane, which shifts the aerodynamic centre forward. This depends on the number of blades, the propeller diameter, and the moment arm.

Downwash gradient

The downwash gradient $d\varepsilon/d\alpha$ is calculated by the lift-curve slope of the wing, the aspect ratio, and the tail position relative to the wing [12]. With the position defined as the vertical offest $r = l_h/(b/2)$ and $m = z_h/(b/2)$ [12]. Here l_h is the tail moment arm, measured from the wing quarter chord MAC to the horizontal tail position, and z_h is the vertical offset of the horizontal tail defined as the span of the vertical tail (since it is a T-tail).

A second term due to the turboprop is added to the downwash. The propeller slipstream on the tail increases the dynamic pressure and downwash at the tail, and depends on the angle between the wing and horizontal tail vertical position $\phi = z_h/l_h$, the shaft power, cruise lift coefficient and tail arm. It is valid only for tail positions $0 < \phi < 30°$. Outside this range, the contribution is set to zero [12].

Zero-lift pitching moment

The zero-lift pitching moment about the aerodynamic centre $C_{m_{ac}}$ consists of the clean wing contribution and the flap and fuselage terms as shown in Equation 3.6 [10].

$$C_{m_{ac}} = C_{m_{ac,w}} + \Delta C_{m,flaps} + \Delta C_{m,fus}. \tag{3.6}$$

The clean wing term is calculated by applying the C_{m_0} of the airfoil over the wing planform. The flap addition is the contribution to the landing configuration for the single slotted Fowler flaps, the sizing of which is done in Chapter 4. The coefficients needed from Torenbeek are μ_1, μ_2, and μ_3. These are read from graphs, where $\mu_1 = 0.21$ was determined from $c_f/c' = 0.2521$ (with $c_f/c = 0.30$ and $c'/c = 1.190$), and $\mu_2 = 0.94$ and $\mu_3 = 0.047$ from the flap span ratio $b_f/b = 0.6861$ and taper ratio $\lambda = 0.460$. Then, the final flap contribution is calculated with $\Delta C_{l,max} = 1.9680$ for LEAF-A and $\Delta C_{l,max} = 1.4958$ for LEAF-B, and $S_{wf}/S = 0.8506$ with the equation taken from Torenbeek [10]. The flap moment is referenced to the aerodynamic centre through $\Delta C_{L,flap}(x_{ac} - 0.25)$. Lastly, the fuselage contribution $\Delta C_{m,fus}$ accounts for the pressure carry over of the wing lift onto the fuselage, calculated by a Torenbeek relation [10].

3.5. Empennage sizing

Author: Lisa *Contributor: Marius*

The horizontal tail is sized by combining the CG range of the loading diagram of Section 3.3 with the aerodynamic parameters of Section 3.4 in a scissor plot. The scissor plot shows the required tail ratio S_h/S as a function of the CG position. The requirements that have to be met is controllability at the most forward CG and stability at the most aft CG [10]. The intersection of the CG range with these requirements determines the minimum S_h/S that satisfies both.

The controllability requirement makes sure the aircraft can be trimmed and controlled at the most forward CG in the landing configuration, where the flaps are deployed and the moment about the CG is the largest. The stability requirement makes sure the aircraft remains stable at the most aft CG, with a static margin applied to the neutral point.

$$\left(\frac{S_h}{S}\right)_{ctrl} = \frac{x_{cg} + \dfrac{C_{m_{ac}}}{C_{L_{\alpha,A-h,app}}} - x_{ac}}{\dfrac{C_{L_h}}{C_{L_{A-h,app}}} \dfrac{l_h}{\bar{c}} \left(\frac{V_h}{V}\right)^2}, \tag{3.7}$$

$$\left(\frac{S_h}{S}\right)_{stab} = \frac{x_{cg} - (x_{ac} - SM)}{\dfrac{C_{L_{\alpha,h,cr}}}{C_{L_{\alpha,A-h,cr}}} \left(1 - \dfrac{d\varepsilon}{d\alpha}\right) \dfrac{l_h}{\bar{c}} \left(\frac{V_h}{V}\right)^2}. \tag{3.8}$$

with all CG positions defined as a fraction of the MAC. The controllability uses the approach condition, with $C_{L_h} = -0.8$ the maximum tail coefficient for an adjustable tail [2], $V_h/V = 1$ for a T-tail [3] and $C_{L_{A-h,app}}$ the aircraft-less-tail lift coefficient at approach. Equation 3.8 uses the cruise condition, with the lift-curve slopes and downwash gradient $d\varepsilon/d\alpha$ from Section 3.4. A static margin of $SM = 5\%$ MAC is applied to the stability line such that there is a margin between the most aft operational CG and the neutral point [10]. A T-tail configuration is vulnerable to deep stall since at high angle of attack the horizontal stabiliser is in the wake of the stalled wing, collapsing its local dynamic pressure. Due to this, both Equation 3.7 and Equation 3.8 are multiplied by a factor of 1.15 to provide some pitch ability near stall [4].

The horizontal tail area is minimised varying the wing position through x_{LEMAC}. Moving the wing shifts the OEM CG and the entire range, which trades the controllability and stability requirements against each other. The wing position is swept between 0.20 and 0.55 of the fuselage length, and at each position the aerodynamic coefficients, OEM CG, and loading diagram are recomputed so that both the CG range and the required S_h/S can be plotted for all wing positions. The optimum is the position that minimises the required S_h/S. This is ran for both Variants A and B, and the la absolute tail size determines the family tail size. It was found that LEAF-A is constraining. In Figure 3.3 it can be seen the minimal S_h/S is taken, where in Figure 3.3b it can be seen that controllability is constraining.

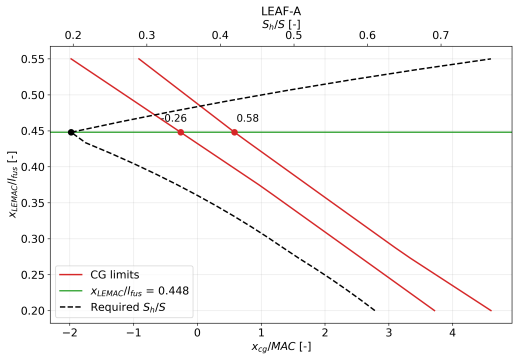

(a) Wing position/S_h/S versus the CG range. The green line indicates the final S_h/S and wing position for the converged result of LEAF-A, including its CG limits.

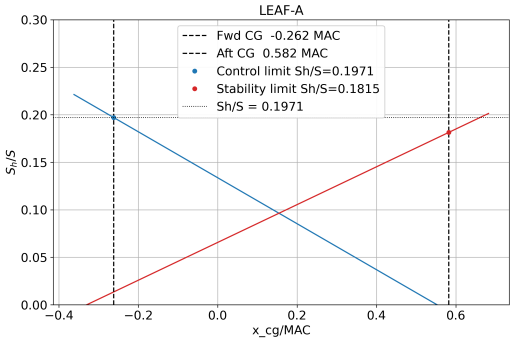

(b) Scissor plot for the resulting S_h/S for variant A. The blue line is controllability, and the red line is stability including a 5% stability margin.

Figure 3.3: Wing position and tail size plots for LEAF-A.

[2] `https://brightspace.tudelft.nl/d2l/le/content/782547/viewContent/4495955/View` *(Accessed: 10/06/2026)*
[3] `https://brightspace.tudelft.nl/d2l/le/content/782547/viewContent/4495954/View` *(Accessed: 10/06/2026)*
[4] `https://brightspace.tudelft.nl/d2l/le/content/782547/viewContent/4495996/View` *(Accessed: 10/06/2026)*

For LEAF-B, it means that the tail size is slightly oversized. Therefore the minimum S_h/S in Figure 3.4 is not hit, and neither the controllability nor stability limits are hit in Figure 3.4b.

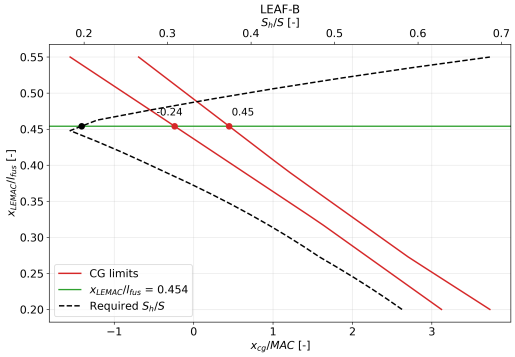

(a) Wing position/S_h/S versus the CG range. The green line indicates the final S_h/S and wing position for the converged result of LEAF-B, including its CG limits.

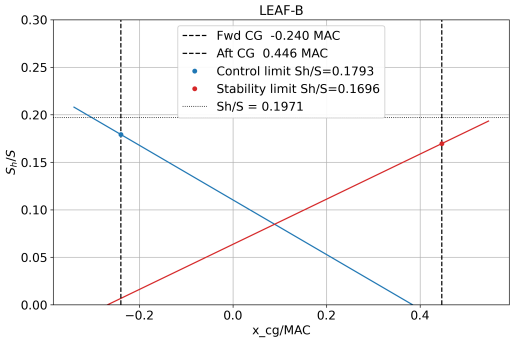

(b) Scissor plot for the resulting S_h/S for variant B. The blue line is controllability, and red stability including a 5% stability margin.

Figure 3.4: Wing position and tail size plots for LEAF-B.

The control surfaces on the empennage are not going to be sized in this section. However, as they are needed for the OpenVSP software analysis in Section 4.4, an assumption of their respective size is going to be made. For the rudder it is assumed to be 25% of the chord size, and running from 10 to 70% of the span. The elevators are also assumed to be 25% of the chord length and running from 50 to 100% of the half span.

3.6. Parasitic drag estimation

Author: Daan, Toine

In the preliminary sizing of the aircraft, the parasitic drag coefficient was estimated using both statistical data and estimates of the wetted area of individual aircraft structures. For more detailed design, the parasitic drag of each exposed structure is defined. This is seen in Equation 3.9 [11, 13]. C_{D_0} of each component consists of the skin friction coefficient C_f, the pressure drag coefficient C_{pd}, the interference factor between components R, and the component wetted area S_{wet}. Several exposed structures are accounted for in the drag estimation. These are the wing, fuselage, empennage, engines, flaps, landing gear, wave drag, pylons, wind shield, and strut. The wetted area of each component has been defined in the midterm report [3].

$$C_{D_0} = \frac{1}{S_{ref}} \sum_i C_{f_i} C_{pd_i} R_i S_{wet_i}. \tag{3.9}$$

Skin friction drag is caused by a fluid moving tangentially over a surface. Roskam found statistical relationships of the skin friction coefficient as a function of Mach and Reynolds number, which were derived from Datcom [11, 13]. The Reynolds number defined is local; for example, the empennage velocity is lower than the wing velocity. The skin friction coefficient, as a function of the Reynolds number, is shown in Figure 3.5.

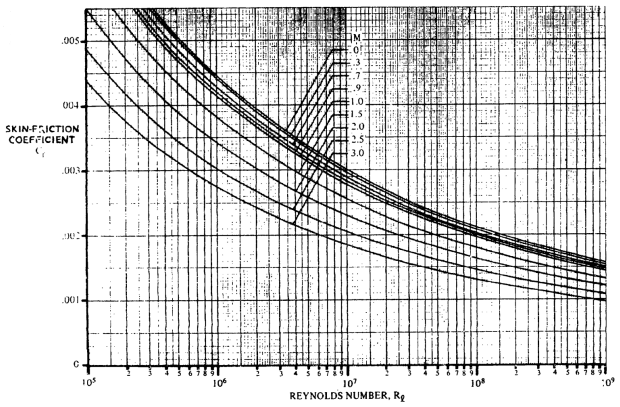

Figure 3.5: Skin friction coefficient as a function of Reynolds number and Mach number [11]

The pressure drag, also called the form factor, is dependent on the shape of a component. For example, the form factor of both the wing and empennage is computed identically, whereas the fuselage and canopy have the same pressure drag. The form factor of the wing, empennage, and strut is defined in Equation 3.10 [13]. It depends on the maximum thickness-to-chord ratio and its location.

$$C_{pd} = \left[1 + \frac{0.6}{(x/c)_m}\left(\frac{t}{c}\right) + 100\left(\frac{t}{c}\right)^4\right]. \tag{3.10}$$

The equation above is only relevant for lifting surfaces. For circular structures, such as the fuselage, as seen in Equation 3.11[13]. It is a function of the slenderness ratio f, seen in Equation 3.12. The slenderness is defined as the length of the circular component over the diameter.

$$C_{pd} = 1 + \frac{60}{f^3} + \frac{f}{400}, \tag{3.11}$$

$$f = \frac{l}{d}. \tag{3.12}$$

The interference drag is caused by multiple components being attached and impacting the airflow. So, for instance, the fuselage impacts the airflow over the wing and vice versa. This has been estimated using statistical data from Roskam, which depends on the Reynolds number of the fuselage. The interference factor found for the wing and fuselage is 1.018.

After the wetted area of each component has been estimated, the drag of each component can be computed. These drag components have been tabulated in Table 3.1. After computing the wave drag, a final zero lift drag of 0.028 has been found in cruise conditions. A limitation in the drag sizing is that the landing gear fairing's effect to a larger wetted-area is not taken into consideration.

Table 3.1: Drag for each component

Component	Drag counts: variant A	Drag counts: variant B
Wing	59	59
Fuselage	110	93
Empennage	97	97
Wave	4.6	4.4
Wind-shield	7.8	7.8
Strut	4.8	4.8
Total	**284**	**267**

3.7. Landing gear sizing

Author: Nathan

The chosen landing gear for both LEAF aircraft is the commonly used tricycle configuration. This consists of a single Nose Landing Gear (NLG), and 2 Main Landing Gear (MLG). The NLG is sized and positioned based on the weight load it can carry. This is computed by the arm of the NLG to the MLG. Then to size and position the main landing gear, the geometry of the aircraft and the most aft CG location are going to be restricting as they are based on the scrape angle, the tip over angle and the overturn angle. The scrape and tip over angle are used to position the main landing longitudinally. And the overturn angle is used to position them laterally. The MLG is sized laterally based on the position of the NLG, therefore, the NLG sizing has to be defined first. Since the aircraft cruise operating speed equals $M = 0.62$ retractable landing gear is a necessity and renders showcasing the recraction mechanism proposed will be presented.

Nose landing gear sizing

The NLG has to be positioned such that it does not carry loads up to 15% of the MTOM when the CG is in the most forward position, and no less than 8% of the MTOM when the CG is in the most aft position [14]. The load fraction of the NLG can then be expressed based on the MTOM and the arm of the NLG to the MLG:

$$\frac{F_{NLG}}{MTOM} = \frac{\Delta x}{l_{LG}}. \tag{3.13}$$

The term Δx is the arm between the CG and the MLG and l_{LG} is the arm between the NLG and MLG.

Main landing gear sizing

The positioning of the MLG begins with determining the scrape angle and positioning it tangent to a section of the tail. The point where this line is tangent has to be determined by equalising the slope of the underside tail curve to the scrape angle. The function of the underside tail curve with respect to the start of the underside of the tail is define as follows:

$$f_{u,tail}(x) = \left(\frac{z_{aft} + R_{fuselage}}{x_{aft}^2} \right) \cdot x^2. \tag{3.14}$$

z_{aft} is the height difference between the middle of the fuselage and the tip of the tail, and x_{aft} is the length of the tail. Then the derivative of this function needs to be put equal to $\tan \alpha_{scrape}$ and solve for x to find x_{scrape}. Then by putting this value into Equation 3.14 the value of h_{scrape} is found. The geometry of these values are shown in Figure 3.6a. With these values parametrised the actual position of the MLG can be parametrised. Figure 3.6b shows the reference system used to compute these parameters.

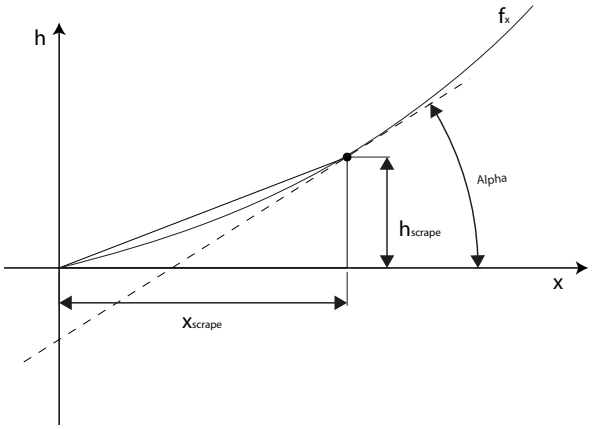

(a) Reference system used for parametrisation of the tangent point of the underside to the scrape line.

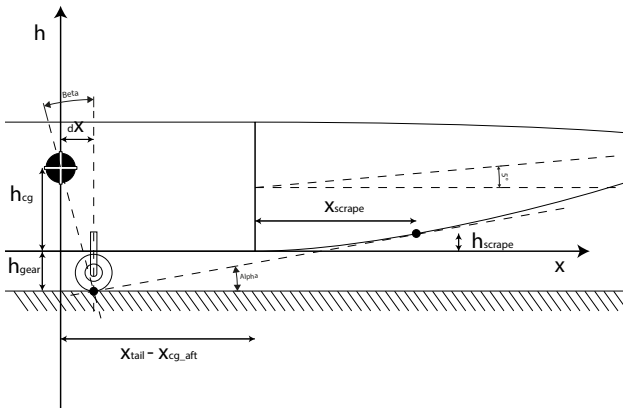

(b) Reference system used for parametrisation of MLG placement.

Figure 3.6: Reference systems used for MLG placement.

This reference system places the x-axis in the bottom of the fuselage, and the h-axis on the most aft CG position. Then the function scrape and the tip over line can be determined based on the geometry of the reference system. The following equations below are these functions:

$$f_{tipover}(x) = h_{CG} - \tan\left(90^\circ - \beta\right) \cdot x, \tag{3.15}$$

$$f_{scrape}(x) = h_{scrape} - \left(x_{scrape} + \left(x_{tail} - x_{CGaft}\right)\right) \cdot \tan \alpha_{scrape} + \tan \alpha_{scrape} \cdot x. \tag{3.16}$$

The x_{tail} and $x_{cg,aft}$ values in Equation 3.16 are taken with respect to the nose of the aircraft and are the start of the tail and aft most CG position. The intersection of these functions and solving for x results in the value Δx_{aft}, which is the value of the difference between the most aft CG position and the MLG position longitudinally. Then the height of the MLG is found by taking the absolute value of $f_{tipover}(\Delta x_{aft})$.

The determination of the scrape and tip-back angles is performed according to Gudmundsson [15]. He says the scrape angle should be chosen as the stall AOA of the clean configuration with 15° being the maximum . The tip-back angle is then taken to be higher then the scrape angle. The tip-back angle has to be chosen such that the load on the nose is within 8% (sufficient nose-wheel ground control) to 15% (main gear holds most weight near CG). The turnover angle is taken from Roskam [14] at 55° to position for lateral stability. The method of Roskam involves taking the arm between the NLG and MLG, drawing a triangle with a perpendicular line to the most foreward CG, that has the length of the height of the CG from the ground divided by tangent turnover angle. Figure 3.7 shows the geometry and the equations for calculating the lateral position based on this are shown below:

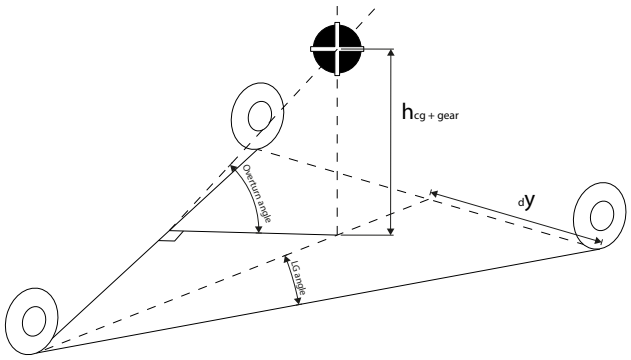

Figure 3.7: Lateral positioning of the MLG.

$$\sin\left(\phi_{LG}\right) = \frac{h_{cg+gear}}{\left(x_{CGaft} - x_{NLG}\right) \cdot \tan\left(\Psi_{over}\right)}, \tag{3.17}$$

$$\Delta y = \tan\left(\phi_{LG}\right) \cdot l_{LG}. \tag{3.18}$$

Δy is the lateral position w.r.t. the middle of the fuselage.

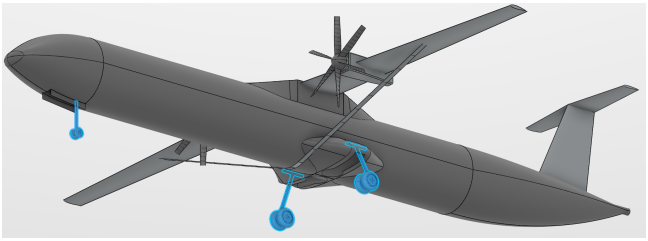

Figure 3.8: Tricicle Landing Gear configuration demonstrated on the of LEAF-A variant. Front and rear landing gear bays are clearly visible. Main landing gear is housed in a sponson attached to the lower section of the fuselage

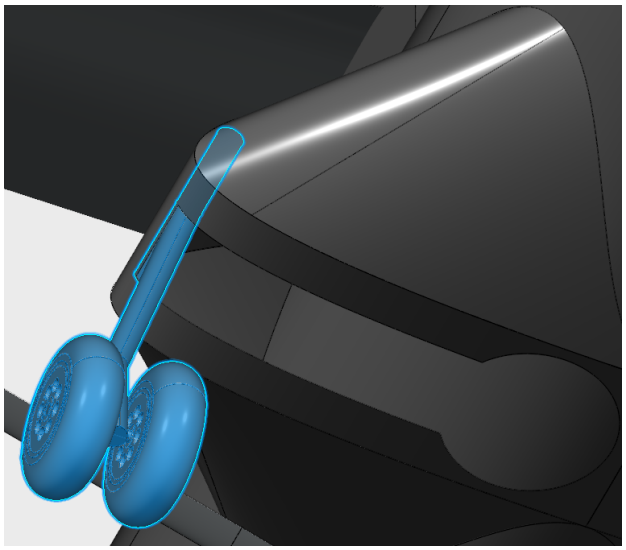

(a) Extended MLG. Landing gear mechanism revolutes around two fuselage frames extended into the sponson for additional structural support.

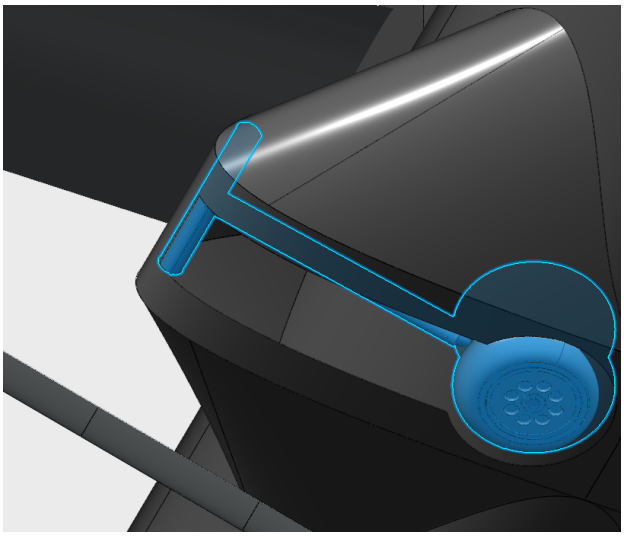

(b) Folded MLG. Sponson of sizable dimentions is required to house the MLG strut. Bending at the base of the MLG strut reduces its already sizable dimentions.

Figure 3.9: Main landing gear retraction mechanism.

4

Detailed wing design

Author: Kacper, Lindsay, Nathan

This chapter will dive into the design of the wing subsystem, one of the most important aircraft subsystems. First, in Section 4.1, a trade-off will be done for the airfoil of the aircraft. Then the wing geometry and the strut are defined. After that, the control surfaces, spoilers, and high-lift devices are designed. Lastly, the control and stability of the aircraft are looked at in Section 4.10.

4.1. Airfoil trade-off

Author: Lindsay *Contributor: Nathan*

In order to size the wing, an airfoil has to be chosen that complies with all the requirements and has optimal performance for the mission required. Therefore, a trade-off will be done, consisting of three airfoils. The chosen airfoils are the following: NACA 63-215, NACA 63(2)-215, and NACA 63-415, they can be seen in Figure 4.1.

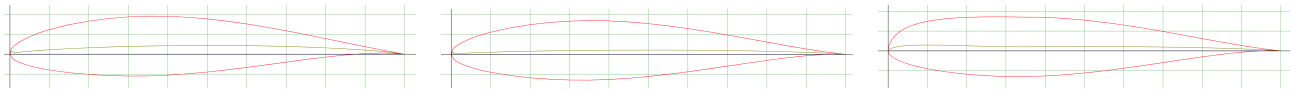

(a) NACA 63-415 **(b)** NACA 63-215 **(c)** NACA 63(2)-215 Mod B

Figure 4.1: Airfoil geometries considered for the wing design

These airfoils are chosen as there is no need for a supercritical airfoil. Furthermore, the NACA 6-series experiences lower friction drag during cruise as it sustains the boundary layer of up to 70% of the chord. The airfoils presented above showed great lift over drag characteristic due to them having a low drag bucket[1]. The thickness is also important as the high aspect ratio wing benefits from a thicker cross-sectional area, increasing the bending resistance of the structure exposed to vertical forces with a large moment arm. Therefore, an airfoil with a maximum thickness of $0.15c$ is chosen. Lift over drag ratio, so called ”finesse”, is an important parameter throughout the entirety of the flight but especially in cruise, where aircraft spends the most time. For this reason, and importance of 35% is put to this trade-off parameter. This value is obtained by using JAVAfoil and finding not only the final maximum lift over drag, but also looking at the plot and seeing how it performs over different angles of attack.

After this, the stall angle is also included as a metric, as it is important that the aircraft will be able to transport the payload safely. Therefore, the higher the stall angle is, the lower the chance of stalling the aircraft, making the aircraft safer. The stall angle is one of the most important parameters of the wing and airfoil, therefore this gets a weight of 30%. This value is also taken from JAVAfoil, where each of the values can be found after plotting the three airfoil’s lift slope.

Third of all, the thickness is also important. Thicker airfoils usually have a better resistance to bending, which would be preferable for the wings, with the long wingspan of the aircraft. This thickness is also important for putting a wing box into the wing. As a very rounded airfoil will be harder to have an consistent and most optimal wing box in the wing. This will be set to a score of 20% weight, as it is not the most important part of the airfoil, and it will be able to be reinforced or worked around, if necessary. This will get ranked based on analysis of the airfoil and seeing whether it can lead to good implementation.

[1] `https://ntrs.nasa.gov/api/citations/20050092351/downloads/20050092351.pdf`, (Accessed: (17-06-2026))

Lastly, the $c_{l_{max}}$ is chosen, as the more lift the airfoil is able to generate before stalling is a highly important part of the airfoil. However, this value can be increased by using high lift devices, which means the values just from the airfoil itself is not as relevant, so a score of 15% is given to this metric. This is another value that can be taken from lift curves obtained via JAVAfoil.

With all the metrics decided, the values per airfoil for these metrics are calculated. This data estimated with JAVAfoil is visualised in Figure 4.2.

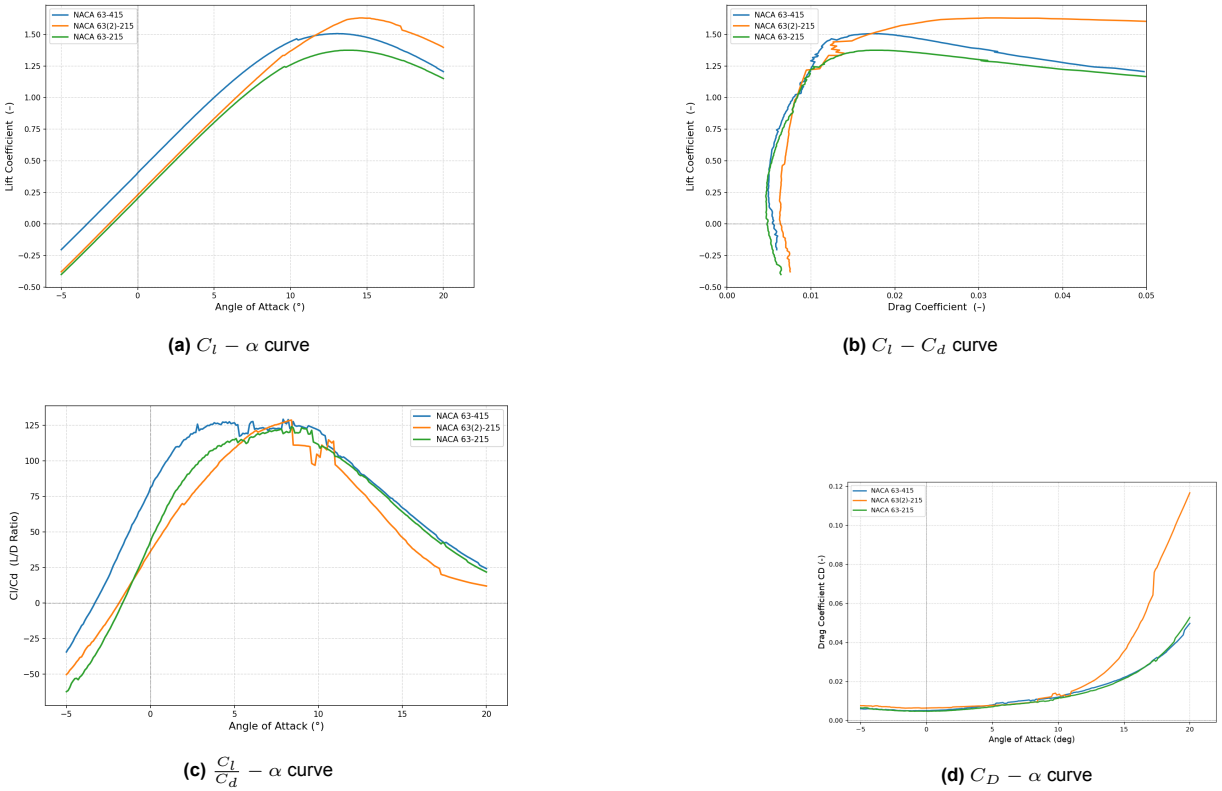

(a) $C_l - \alpha$ curve

(b) $C_l - C_d$ curve

(c) $\frac{C_l}{C_d} - \alpha$ curve

(d) $C_D - \alpha$ curve

Figure 4.2: JAVAfoil estimations for all airfoils

When first focusing on the stall angle of attack in Figure 4.2a, it can be seen that the NACA 63(2)-215 performs the best and gets a final stall angle, and maximum lift coefficient of 14.5° and 1.63 respectively. Therefore, for these two metrics this airfoil will get an excellent score. The other two airfoils both have a good performance when looking at the stall angle, but are not as excellent as the first one. The NACA 63-415 has a stall angle of 13°, and the NACA 63-215 of 13.5°. For the maximum lift coefficient, the NACA 63-415 has it of 1.51, so receiving an excellent score for this. The NACA 63-215 is at 1.38, which is much lower than the other two, so it gets a good score.

Then for the most important parameter, the C_l/C_d, from Figure 4.2b and Figure 4.2c, it can be seen that the NACA 63-415 has a good performance, as the lift over drag gets a very broad graph over the angle of attack, which means overall the lift is much higher than drag over many angles of attack. It can be seen that it is mostly higher for smaller angles of attack as well, which is preferable, since a regional jet usually does not fly with very high angles of attack. For this reason, the NACA 63-416 gets an excellent score in this metric. The other two have a similar curve seen in Figure 4.2c for small angles of attack. For larger angles of attack, the modified version has less good performance, as it gets less lift over drag than the normal version. However, the modified version has gets more lift when having more drag, making it outperform the other two airfoils there. For these reasons, both of these final two airfoils get a good score in this parameter, as they both have good and worse qualities over this metric.

Then the final metric to assess is the thickness, which accounts for wing box implementation as well as bending of the wing. By looking at the airfoils in Figure 4.1, it can be seen that the NACA63-415 has a thick middle part of the airfoil, which could lead to good input of a wing box. It is also thicker overall than the other two airfoils, making leading to an excellent score for this airfoil. The modified version has a very thick front of the airfoil, but is thinner that the former airfoil, so there can be enough space for a wing box to be implemented, and is

likely to resist bending well enough, but not as good as the 415. Therefore, this one also gets an good score. The normal NACA 63-215 is very skinny, and has a very rounded front, also making it a good score, as it is expected to meet the requirements, but not outperform them.

With these values values calculated, the final trade-off table is put together, and the final points are calculated. This can be seen in the Table 4.1.

Table 4.1: Final Values Airfoil Trade-Off

Concept / Metric	NACA 63-415	NACA 63(2)-215	NACA 63-215
C_l/C_d(35%)	129.36 Green	128.75 Cyan	124.19 Cyan
α_{stall} (25%)	13° Cyan	14.5° Green	13.5° Cyan
Thickness (20%)	High Green	Moderate Cyan	Moderate Cyan
$C_{l_{max}}$ (15%)	1.51 Green	1.63 Green	1.38 Cyan
Total Points	1.7	1.45	1

This shows that the final outcome of the trade-off is that the NACA 63-415, even after a sensitivity study, where all metrics were changes by plus and minus 10 percent, and this airfoil still won in each of these trade-off calculations. Therefore, this airfoil is chosen for the wings with parameters C_l/C_d = 129.39, $\alpha_{stall} = 13°$ and $C_{l_{max}} = 1.51$, even though the maximum lift coefficient is not the best. By adding high lift devices, it is expected to perform well enough still.

Limitations

As mentioned, JAVAfoil is used in order to obtain most values, but this program has quite some limitations and assumptions that have to be addressed. One of the limitations is that it does not model flow separation, which means it gets inaccurate after this occurs. However, the stall of the airfoil for the given flight conditions was needed, and therefore this was determined as a good option to estimate it. As mentioned by the JAVAfoil user manual, at stall the flow field is more three dimensional with vortices and spanwise flow [16]. Furthermore, JAVAfoil assumes inviscid, attached flow, and it does not account for compressibility effects. Therefore, it is recommended that further research can do a more accurate estimation, by means of using a more reliable program than JAVAfoil.

Drag divergence number

For the selected NACA 63-415 it is necessary to check whether sonic flow will be reached at any point along the airfoil in cruise speed condition of $M = 0.62$. If $M_A = 1$ occurs at the point of the lowest pressure (point A) aircraft may be exposed to sudden increase in drag due to transonic aerodynamic effects and as such it should be avoided. rerCondition for that is cruise speed lower than the critical Mach number $M_{critical} > M_{cruise}$, speed at which first point along the airfoil (point A) reaches Mach one.

To confirm transonic drag effects are not applicable for the selected NACA63-415 airfoil at cruise conditions XFOIL plotting software was used to obtain airfoil pressure distribution at the angle of attack of $\alpha = 3°$. Point A with the lowest pressure coefficient $C_{p_{min}}$ is of interest here, as seen in Figure 4.3. Minimum $C_{p_{min}}$ becomes more negative as angle of attack increases and $\alpha = 3°$ is an overestimated conservative value. Following [17] pressure coefficient plots were created for low speed conditions and are applicable for use in forthcoming Equation 4.1.

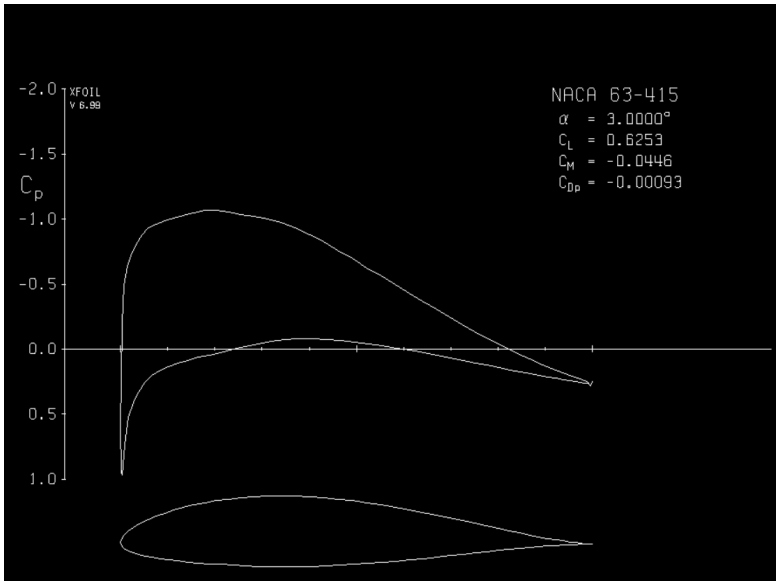

Figure 4.3: Low-speed Pressure Coefficient NACA 63-415 at $\alpha = 3°$

Critical Mach number follows from numerical evaluation of Equation 4.1 and was identified to be $M_{critical} = 0.75$, far above chosen cruise speed conditions.

$$\frac{C_{p_{min}}}{\sqrt{1 - M_{cr}^2}} = \frac{2}{\gamma M_{cr}^2} \left[\left(\frac{1 + [(\gamma - 1)/2] M_{cr}^2}{1 + (\gamma - 1)/2} \right)^{\frac{\gamma}{\gamma - 1}} - 1 \right]. \tag{4.1}$$

4.2. Wing 2D planform

Author: Kacper

Following a selection of NACA 63-415 airfoil for the cross-sectional profile of the wing, design of the 2D wing planform could commence. It was decided to size the wing for the heaviest of the family members to comply with the high 65% commonality requirement imposed on the program [18]. Truss-braced wing design leverages benefits of the reduced bending moment at the root provided by the supporting strut and additional lift that this structure may provide. The strut's presence, however, has to be considered when designing the main wing, not only due to a mutual joint, but also aerodynamic coupling between two lifting surfaces.

If the truss-braced wing concept is applied correctly, the total induced drag of the aircraft should not change compared to the same-size and geometry unsupported wing aircraft, with the remaining benefit of extra lift. The condition for that is a combined lift distribution closely resembling an elliptical lift distribution [19]. Steps towards achieving that goal will be mentioned in a different section.

Design of a 2D wing planform remains constrained by mission requirements. Firstly, as stated in [18] the aircraft has to comply with ICAO code C parking stands, limiting its possible wingspan to below 36 meters. Secondly, the requirement for a minimum cruise speed of $M = 0.6$ allowed for choosing a slower turboprop design, since up until $M = 0.663$ turboprop engines preserve their competitive efficiency advantage over the turbofan [20]. Subsequently, at a cruise speed of $M = 0.62$, wing sweep as a mechanism for reducing large drag increase encountered at supersonic speeds is not necessary [17] and no sonic flow occurs over the wings as described in Section 4.1.

Based on similar aircraft, a goal aspect ratio of $AR = 20$ was selected for the Class II optimisation software, same as for the SUGAR Volt project developed by Boeing [21]. The last remaining variable necessary for wing planform plotting is the taper ratio, determined in Chapter 3 chapter. Table 4.2 summarizes 2D wing geometry parameters and is followed by a graphical representation of one of the aircraft's wings Figure 4.4.

Table 4.2: Wing 2D Planform Parameters

Parameter	Value	Unit
Span (b)	29.9	[m]
Aspect Ratio (AR)	20	[-]
Taper Ratio (TR)	0.46	[-]
Sweep Angle $\Lambda_{c/4}$	0	[°]

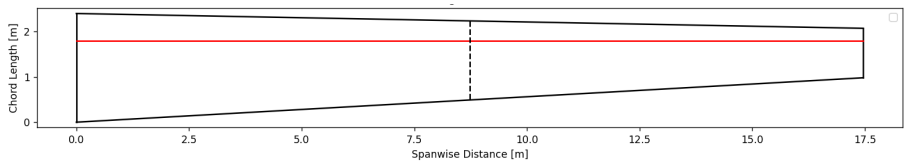

Figure 4.4: 2D Wing Planform as seen from above (XY plane). Effect of a $-2°$ anhedral is visible in projected half-span lower than half wing span.

4.3. Wing 3D geometry

Author: Kacper

Design of the 3D wing geometry was conducted based on the derived spanwise lift distribution as well as the resulting internal loading diagrams of the supported truss-braced wing. The problem was simplified to account solely for forces and moments acting in the vertical plane, neglecting effects of torsion and drag, as in terms of magnitude these are of a much smaller magnitude than the wing bending moment and lift force. The 3D geometry can also be used to predict the CG position and the wing mass by assigning a material density.

Wing lift distribution

For the purpose of obtaining the lift distribution along the span, a Dietrich Method was used for the normalised wing span coordinate, η [22]. This semi-empirical method splits the lift distribution into basic and additional lift distribution components.

The additional lift distribution is calculated for an untwisted wing with a lift coefficient $C_L = 1$. Firstly, the lift distribution function has to be calculated before converting it to the lift distribution. C's with a subscript are constant values specified by Torenbeek, and the sweep angle correction function is noted by f. More definitions can be found in [22].

$$L_a(\eta) = C_1 \cdot \frac{c(\eta)}{c_g} + C_2 \cdot \frac{4}{\pi}\sqrt{1-\eta^2} + C_3 \cdot f(\eta)$$

The basic lift distribution is for a twisted wing with a lift coefficient $C_L = 0$. Again, first lift distribution function is necessary.

$$L_b(\eta) = L_a(\eta) \cdot C_4 \cdot cos(\varphi_b) \cdot \left(\frac{\epsilon(\eta)}{\epsilon_t} + \alpha_{0_1}\right) \cdot \beta \cdot E$$

To obtain the total lift distribution, a sum of the lift distributions is needed:

$$\Gamma(\eta) = L_a(\eta) \cdot C_L + \frac{L_b(\eta) \cdot \epsilon_t \cdot c_{l_\alpha}}{E}$$

Following the integration of the total lift distribution, the total lift was obtained and scaled by a constant factor to preserve the overall distribution and guarantee lift-weight equilibrium for cruise conditions. The area integral over the half-wing was used by splitting the half-wing into 100 sections. For each section, the average is taken of the lift distribution of the section boundaries. When this is done, each lift distribution of each section is added to get the total lift distribution.

Internal force diagrams

The discussed truss-braced wing design can be described at best by the free body diagram showing forces and moments acting in the vertical plane Figure 4.5. To solve, an additional compatibility equation is necessary

to determine all four unknowns, $A_x, A_y, M_a, F_{strut\_y}$. It is presented as Equation 4.2. Vertical elongation of the strut at the joint has to equal the vertical deformation of the wing due to the lift distribution and additional force introduced by the strut, decreasing the wing's deformation.

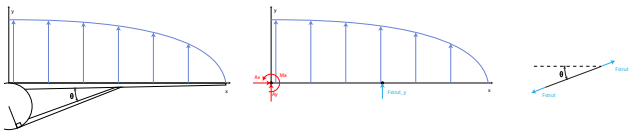

Figure 4.5: Free Body Diagram of a Truss-Braced Wing Concept.

$$y_{original} - \frac{F_{strut}\sin(\theta)x^3}{E_{wing}I(x)} = \frac{F_{strut}\sin(\theta)l_{strut}}{E_{strut}A(x)} \tag{4.2}$$

Geometrical properties, such as the area, $A(x)$, and second moment of area, $I(x)$, are changing along the wingspan, as the wing is tapered. Integration of the shear force exerted on the wing by the lift, strut force F_{strut_y} and wing-podded engine yields the bending moment. A summary of the internal wing forces can be seen in Chapter 4, showing the impact of the strut support on the overall wing loading. A reduction in bending moment from X% to Y% is achieved as a result.

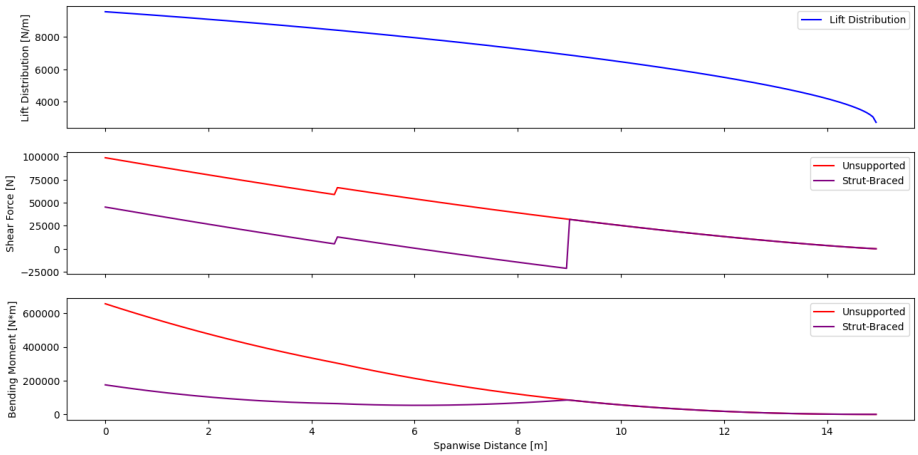

Figure 4.6: Internal Force Diagram showing Lift Distribution, Shear Force and Bending Moment along the wingspan. Impact of the Strut Load Relief can be seen.

Internal structure of the wing

In this subsection, the detailed design of the wing internal structure will be presented. This includes the number, location and thicknesses of internal wing components such as ribs and spars. Wing stringers were not considered in the vertical deformation calculations, however their presence would have been of great importance if torsion was considered. In that case zero thickness skin would carry the shear flow and stringers modelled with extra skin area all the wing normal forces acting in the spanwise direction.

Wing Skin

Skin is modelled as a constant-thickness plate covering an area of twice the projected wing area. A thickness of $t_{skin} = 2mm$ was chosen as twice the minimum skin thickness of the Boeing 727[2].

[2] `https://howthingsfly.si.edu/ask-an-explainer/how-thick-aluminum-covering-wings-commercial-airliner` *(Accessed: 14/06/2026)*

Wing Spars

Spars as the internal structure of the wing are primarily responsible for carrying the bending moment loads along the wingspan. They also form a part of a closed box together with the upper and lower surfaces of the wing skin, resisting torsional loads.

In case of the A320 two wing spars are used along the entire length of the wing[3]. For larger widebodies, such as the A330/A340, a third spar is often present running from the root towards the first inboard engine attachment point, providing additional flexural rigidity in an area where bending loads are the largest. Since in the discussed truss-braced wing design, the strut provides a bending moment relief in the wing root area, two spars are deemed sufficient, complying with industry norm for narrowbodies and creating a closed cross-sectional section within the wing, improving its torsional resistance.

In a conventional passenger airliner their chord-wise positioning represents a trade-off between providing enough volume in the center of the wing for fuel and allocating sufficient area for the high lift devices (HLD's). In the case of the developed sustainable family of aircraft, a decision has been made to not store fuel within the wing structure and instead position a pressurized hydrogen tank in the rear section of the aircraft, as will be further elaborated on in Chapter 6. Thus, all the priority has been given to the HLD's, placing both spars at $c_1 = 0.2$ and $c_2 = 0.55$ of the chord.

The cross-section of a spar was designed as an I-beam with a web thickness of $t_{web} = 20mm$ and spar caps of thickness of $t_{cap} = 10mm$ and width of $w_{cap} = 100mm$. The height of the spar varies along the wing-span as the wing is tapered.

Wing Ribs

Ribs are elements of the wing responsible for maintaining its aerodynamic cross-sectional shape. Their spacing was kept constant along the wingspan with span-wise separation equal to six times the thickness of the wing at the mean aerodynamic chord (MAC), as suggested in [23]. This resulted in spacing of $s_{ribs} = 1.35$ meters. In addition, one rib was added at the point of wing-strut connection to carry the loads between wing spars and the single force member strut. The total number of ribs including root and tip chord ribs for both wings reached $n_{ribs} = 25$.

Ribs are modelled as flat plates with a thickness of $t_{rib} = 20\ mm$. An additional rib connecting the strut and the wing has a thickness of $t_{rib_{extra}} = 80mm$. Cutouts are made for the fuel feeding system for wing-mounted engines, mechanisation of HLD's and EWIS (wiring and electrical connections), but were not considered in the model estimating weight and center of gravity position of the wing group. This is a conservative assumption.

Internal structure of the strut

The support strut is designed not only to relieve the bending loads at the root of the wing but also to generate additional lift while in flight. As such, its cross-section is an airfoil, with sources suggesting a use of symmetrical profiles with a thickness to chord ratio of no more than 20% [24]. NACA 0012 was used satisfying these conditions. To determine the overall dimensions of the strut, its length, chord and thickness, literature references and previously calculated internal loads will be used.

The strut connects the lower section of the wing with the fuselage, where it attaches tangentially to the circular fuselage cross section. At the wing, the span-wise attachment point is determined to be $\eta_{strut} = 0.6$, providing a large moment arm for the bending moment relief [19]. Both attachment points lie on the same x-coordinate meaning that the total length of the connecting strut can be determined from the 2D geometry, yielding $l_{strut} = 8.97\ m$. By choosing an aspect ratio $AR_{strut} = 38.6$, the same as for Sugar Volt [21], the chord of the straight, untapered strut can be determined as $c_{strut} = 0.23\ m$. The cross-section is assumed solid for mass calculations and stresses.

In the following section, the importance of the wing strut twist on the overall performance of the aircraft will be discussed using a simplified aircraft model created in the OpenVSP software, with the goal of obtaining a total lift distribution closely resembling the elliptical lift distribution for induced drag minimization [19].

4.4. Support strut twist

Author: Kacper

[3] https://www.abbottaerospace.com/aa-sb-001/22-aircraft-specific-design-features-and-design-methods/22-16-57-wings/22-16-9-some-transport-wing-layouts/ *(Accessed: 14/06/2026)*

Truss-braced wing design promises significant efficiency improvements over conventional aircraft configurations through the means of reduced induced drag, however, exploitation of this effect requires sophisticated optimization. The concept of a supported wing is well-known in general aviation, with Cessna 172[4] and Piper Cup[5] planes being good examples but lacking refinements reducing additional strut and interference drag. Strong coupling between the lifting surfaces and mutual dependence of aerodynamics and structures presents a significant design challenge that has to be considered.
While performing a literature study for the truss-braced configuration several sources studied possible aircraft performance improvements with strut twist variation along the span. In [25], a RANS-based (Reynolds-averaged Navier-Stokes) aerodynamic shape optimization of TBW was performed, keeping shape and geometric twist of the strut as variables in optimization. Another study is cited by Pranav Zinjarde [19], performed by NASA and Boeing during the SUGAR project [26]. For SUGAR planes with truss-braced structure, the main strut accounted for approximately 10% of the total aircraft drag, with interference effects between the main wing and strut accounting for 1%. Optimization of strut aerodynamic twist (varying the cross-section) was performed, reducing strut flow separation and total drag.
In this section, a short study of the effects of varying the geometric twist along the strut on the total drag will be performed. Results will be obtained with the OpenVSP software utilizing a vortex lattice method (VLM). It was necessary to separate the vertical tail (VT) and horizontal tail (HT) with a small gap to prevent ill-conditioned results stemming from crossing vortices in VLM method, visible as a small indent at the empennage intersection on Figure 4.7.

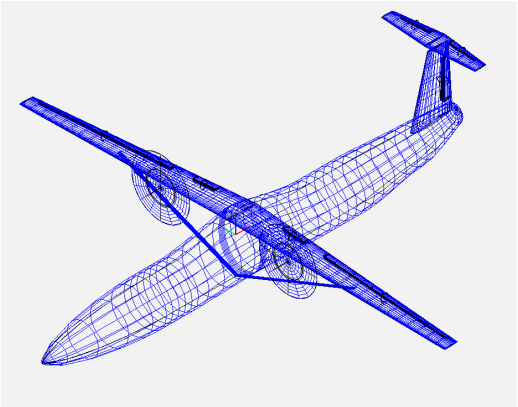

Figure 4.7: Simplified Model of the Aircraft with Initial Geometry

Initially, aircraft 3D geometry with a straight NACA0012 cross-section strut is used for the VSPAERO analysis to obtain aerodynamic properties as a function of the angle of attack alpha. These include induced drag, total drag and lift coefficients, as well as L/D ratio.

Lift Distribution along the span is plotted for each of the lifting surfaces separately, as sets of horizontal point sets shown in Figure 4.8a. Both propellers are rotating in a clockwise direction, exerting an impact on the wing lift distribution. The propeller on the port side contributes to up-wash of the wing close to the fuselage and down-wash closer to the tip. The opposite is true for the starboard side.

[4] `https://www.planespotters.net/photo/1078692/d-egbw-private-reims-aviation-f172m-skyhawk-c172` *(Accessed: 16/06/2026)*

[5] `https://www.planespotters.net/photo/1815074/d-eaer-private-piper-pa-18-95-super-cup` *(Accessed: 16/06/2026)*

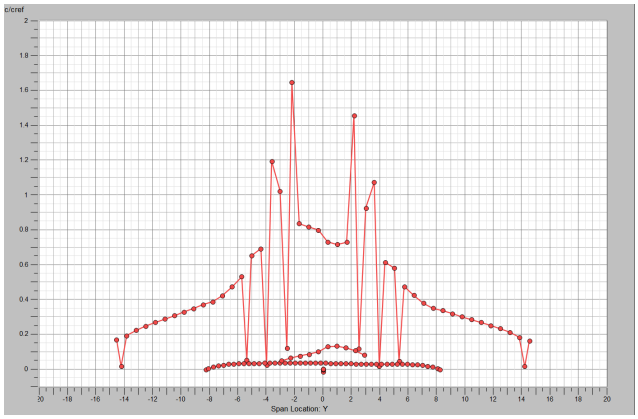

(a) Normalized Lift Coefficient Along the Wingspan. $\alpha = 2.5°$, $Re = 6 \times 10^6$, $M = 0.62$.

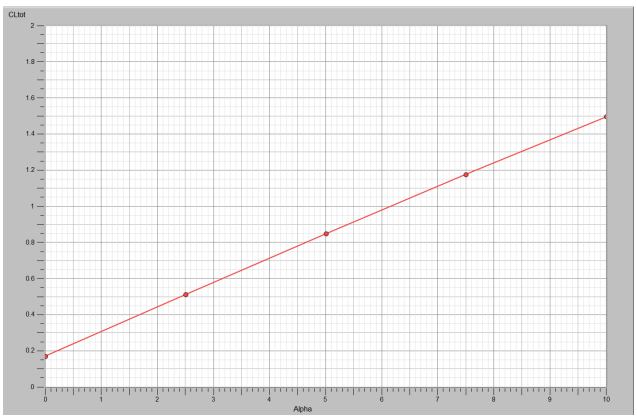

(b) Lift coefficient of the whole aircraft for a straight wing support strut. At angle of attack of 10 degrees C_L of 1.5

Figure 4.8: OpenVSP Initial Aerodynamic Analysis.

A few takeaway points for further strut twist analysis can be made based on initial geometry. Firstly, the contribution of the strut to the total lift is an order of magnitude smaller than that of the main wing. Thus, when varying its twist later in the analysis, the impact on the whole aircraft might be rather small. Secondly, the lift distribution of the main wing is far from resembling the elliptical shape, due to the presence of propeller wake and lift drop in the region where intersection with the fuselage takes place. A strut should be used to compensate for these distortions, smoothing peaks and sealing off valleys.

Second analysis was run for the geometrically twisted strut. Strut was divided into four sections, each assigned a different twist angle. Negative twist angles were assigned for sections closest to the fuselage, generating negative lift. This contribution should smoothen the overall lift distribution, decreasing the height of the peaks on both sides of the fuselage. Twist angles are chosen to resemble the twist distribution presented for SUGAR Volt aircraft proposed by Boeing and NASA [26].

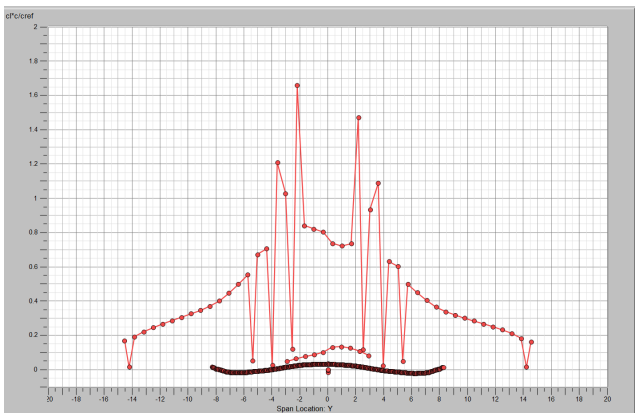

(a) Normalized Lift Coefficient Along the Wingspan. $\alpha = 2.5°$, $Re = 6 \times 10^6$, $M = 0.62$.

(b) Lift coefficient of the whole aircraft for a twisted wing support strut. Negative strut twist is applied along most of the strut. At angle of attack of 10 degrees C_L of 1.45

Figure 4.9: OpenVSP Modified Aerodynamic Analysis. Impact of strut twisting is noticeable in the aerodynamic results.

Based on the presented aerodynamic analysis it can be concluded that variation in the strut twist angle has little effect on the overall aircraft lift distribution. The chord-normalized lift coefficient of the strut is an order of magnitude smaller than the one of the main wing, as can be seen when comparing figures Figure 4.8a and Figure 4.9a. The sheer size of the strut may be the culprit here. For the known total length of the strut, an aspect ratio from [21] was assumed to calculate the chord of the untapered strut, resulting in a chord of $c = 0.23m$. This decision is thus not fully justified, since the initial studies of the strut-braced wing concept were relying on the efficiency gains that strut twist could promise. If the wing support strut would have a larger contribution to the total lift of the aircraft, effects of changing the strut twist angle would likely be more appealing.

4.5. Complete 3D wing model

Author: Kacper

With all the available geometrical information and calculated forces acting within the wing, it was possible to extend the Python plotting tool to 3D and present the wing's vertical deformation. Again, the impact of dihedral, twist, and tangential forces is neglected. Values used in the model are for the larger aircraft, variant A, with a $MTOM = 21810\ kg$. The model considers solely forces acting in the vertical direction, such as lift, engine weight, and vertical strut force. A section of the fuselage is included as a frame of reference. For aircraft variant A, with the presented MTOM mass displacement of the wing tip was reduced from 2.01 m to 0.54 m by adding the strut, preventing efficiency losses while in flight due to the reduced effective aspect ratio of the wing. Comparison including an exaggerated wing deformation is visible in Figure 4.10a and Figure 4.10b.

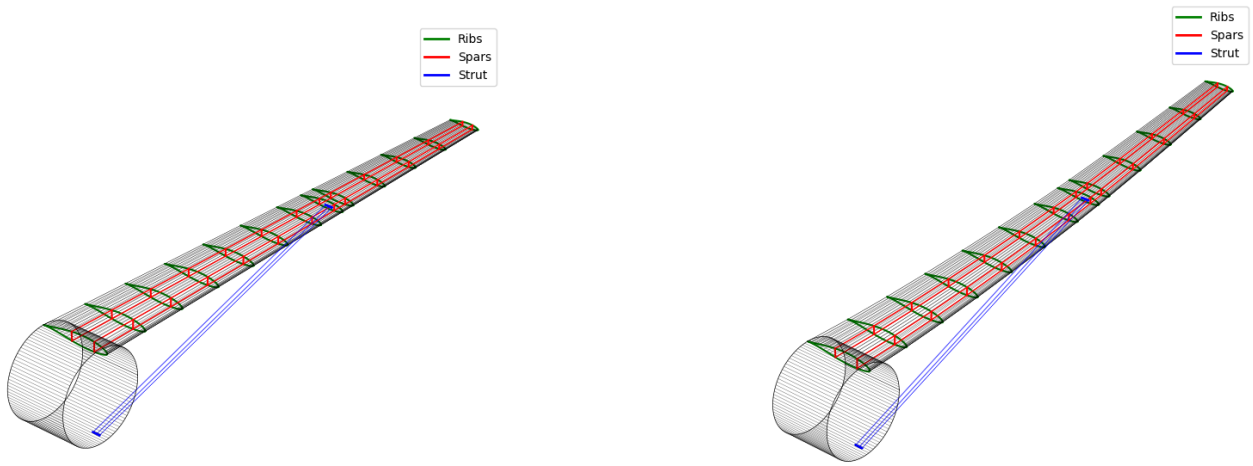

(a) Undeformed Truss-Braced Wing Model

(b) Deformed Truss-Braced Wing Model with exaggerated deformation for clarity

Figure 4.10: Comparison between Undeformed and Deformed Wing Geometries showcasing capabilities of the developed 3D plotting tool in Python

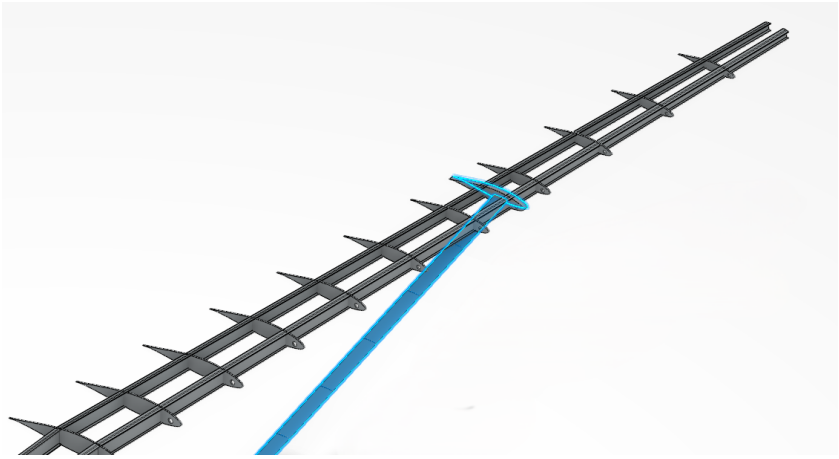

Figure 4.11: Internal structure of the wing features 2 spars and 25 ribs incorporated in the whole wing, for 12 ribs per wing. Center Rib, shown on the left lower corner is shared by both wings. Tip rib (right top) is removed to showcase I-Beam spar shape.

4.6. High-lift devices

Author: Nathan

The preliminary sizing of the High Lift Devices (HLD) is done by the method of Dieter Scholz [27], who based this method on DATCOM 1978 [11]. HLD's are used during take-off and landing procedures to increase the maximum lift coefficient of the wing. The working principles are, increasing the airfoil camber, energising the airflow and controlling the boundary layer, and increasing the wing area. These principles all have a different effect of the lift curve. By increasing the camber, the lift coefficient increases by a ΔC_l value, without affecting the slope. However, the angle of attack (AoA) at $C_{l_{max}}$ does decrease, as an increase in camber causes earlier flow separation. Boundary layer control uses high energy flow underneath the wing to re-energise the flow above the wing and delaying separation by removing the old boundary layer. This increases the stall AoA and therefore increases $C_{l_{max}}$. Finally, increasing the wing area increases the slope of the lift curve. This is because an increase in area, increases the lift. The C_{l_a} of the slope is based on the reference area and the lift equation: $\frac{L}{qSV^2}$. Therefore, if L increases while qSV^2 stays constant, C_l has to increase as well as C_{l_a}. In Figure 4.12 the effect in the lift curve is shown.

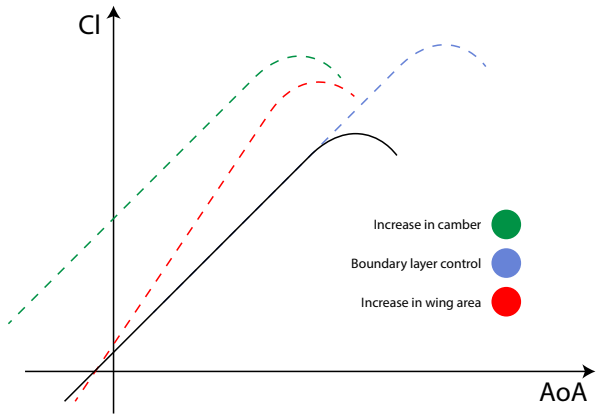

Figure 4.12: Effect on $C_l - \alpha$ curve because of the HLD principles.

Based on these principles the HLD's are chosen and sized.

HLD's can be divided into two groups, the Leading Edge (LE) group and the Trailing Edge (TE) group. The four most commonly used LE HLD's are: The LE Slot, the LE Flap, the Krüger Flap and the LE Slat. For the TE, the HLD's can be divided into Nonextending and Extending Flaps. The most commonly used nonextending are: Plain Flap, Split Flap and Single-Slotted Flap. The most commonly used extending are: Double-Slotted Flap, Triple-Slotted Flap and Fowler Flap. In Figure 4.13 the effect of these flaps on the lift curve is shown.

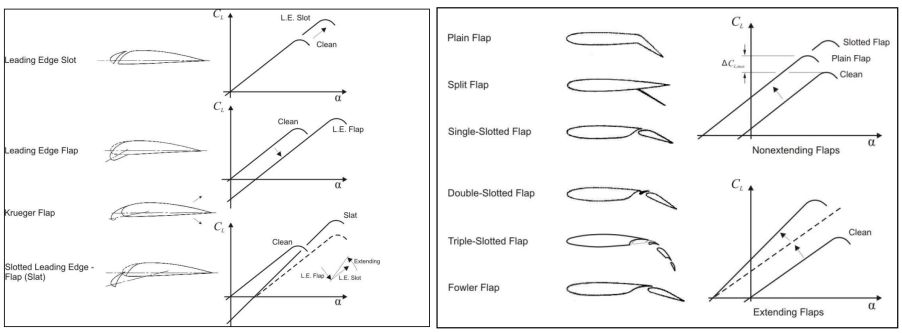

Figure 4.13: LE and TE HLD's and their effect on the lift curve slope.[27]

From Torenbeek [10], Split Flaps produce large amounts of drag due to flap deflection, particularly in case of small deflections. Therefore, making it less suitable for take-off. This type of flap must now be considered as obsolete. Plain Flaps also have a big flaw, as when deflection exceeds 10 to 15 degrees, flow separates immediately after the knuckle. Furthermore, lift effectiveness decreases and the drag increases to similar values

of those of the Split Flap [10]. Because of these flaws, during the sizing of the TE lifting devices, these flaps will not be considered. Triple-Slotted Flaps are used on several transport aircraft that have very high wing loadings. They also bring complicated flap supports and controls. They also bring a weight penalty due to their multi-track supports. Therefore, these will also not be considered for the HLD sizing as our aircraft family as it is redundant to achieve such a high $C_{l_{max}}$ for the size of the aircraft. For LE HLD's Torenbeek explains that Leaging Edge Flaps are less effective versions of slats [10]. Furthermore, Fixed Slots have a drag profile penalty prohibiting effective cruise. They are sometimes used on Short Take-off and Landing (STOL) aircraft [10]. These LE HLD's will therefore also not be considered. Krüger flaps perform in the same way as slats, but are thinner and more suitable on thin wings [10]. However, from Gudmundsson [15], the aerodynamic parameters of slats are better, as Figure 4.14 shows. Slats approximately have a higher $\Delta C_{l_{max}}$ and $\Delta\alpha_{stall}$. Therefore, only slats will be used for the sizing of the LE HLD's.

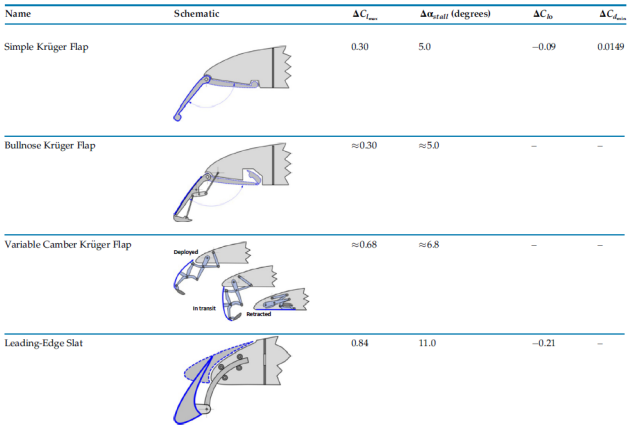

Figure 4.14: LE Krüger Flaps and Slat aerodynamic parameters.[15]

Leading-edge high-lift device sizing

For the sizing of the LE HLD's, a Take-off and Landing configuration needs to be considered. To determine the increase in the lift coefficient of the airfoil through slats, Equation 4.3 can be used [27, 11]:

$$\Delta C_{l,max,s} = c_{l,\delta,max} \cdot \eta_{max} \cdot \eta_{\delta} \cdot \delta_f \cdot \left(\frac{c'}{c}\right). \tag{4.3}$$

Here, $c_{l,\delta,max}$ is the theoretically maximum flap efficiency, η_{max} is an empirical factor taking the leading edge radius over relative thickness of the airfoil into account. Then, η_{δ} is an empirical factor taking the optimal deflection and actual deflection of the slat into account, δ_f is the actual deflection angle of the slat. Finally, $\frac{c'}{c}$ is the ratio of the extended and retracted chord length of the airfoil. These parameters were computed using the graphs provided by Scholz [27], taken from DATCOM 1978 [11]. The maximum deflection will be set at 20° as above that the deflection and excessively high lift coefficient is calculated. For take-off configuration the reference angle of 15° is used. This results in a Three-Position Slat for the LE [15]. The first position is the retracted one, the second one the Take-off configuration. The Third on is the Landing configuration. From Gudmundsson [15], the chord of the Slat is taken at $0.15c$, and the extended chord: $1c + 0.04c = 1.04c$. This gives the following parameters presented in Table 4.3 with the increase of the lift coefficient of the airfoil for both Take-off and Landing.

Table 4.3: Increase in lift coefficient of the airfoil for LE HLD.

Parameter	$c_{l,\delta,max}$	η_{max}	η_{δ}	δ_f	$\frac{c'}{c}$	$\Delta C_{l,max,s}$
Take-off	1.42	1.52	1	15	1.04	0.588
Landing	1.42	1.52	0.9	20	1.04	0.705

Trailing edge high lift device sizing

The HLD's considered for the TE are the Single-Slotted Flap, the Fowler Flap and the Double-Slotted Flap. The same configurations as for the LE HLD sizing will be considered, one for Take-off and one for Landing. To increase the lift coefficient of the airfoil through TE HLD's, Equation 4.4 can be used [27, 11]:

$$\Delta C_{l,max,f} = k_1 \cdot k_2 \cdot k_3 \cdot \Delta c_{L,max,base}. \tag{4.4}$$

$\Delta c_{L,max,base}$ is the maximum increase in the lift coefficient for a flap with a 25% flap chord at a reference flap angle. k_1 is which takes into account a relative flap chord that has a value other than 25%. k_2 is a factor which takes into account a flap deflection that differs from the reference value. k_3 is a factor which takes into account the flap kinematics. The values for these parameters are again taken from the graphs provided by Scholz [27], taken from DATCOM 1978 [11]. And for the flap chord $0.3c$ is taken for the 3 chosen TE flap types as this is typical for Slotted and Fowler Flaps [15]. Furthermore, with this flap chord $0.15c$, of space is left for the hinge and mechanism of the HLD, ensuring enough space between the TE Flap and Aft Spar. The flap deflection is different between the 3 types. From Torenbeek [10], typical flap angles for these TE flap types are presented in Table 4.4.

Table 4.4: Typical TE flap deflection angles.[10]

TE Flap type	Take-off	Landing
	Flap deflection	
Single Slotted	20°	40°
Fowler	15°	40°
Double Slotted	20°	50°

With these deflection angles and the chord of the flap determined, the parameters can be decided and the increase in lift coefficient can be calculated. Furthermore, the chord extension for Single Slotted, Fowler, and Double Slotted Flaps it is taken from Torenbeek [10]. The results are presented in Table 4.3.

Table 4.5: Increase in lift coefficient of the airfoil for TE HLD.

TE High Lift Device	Configuration	δ_{ref}	$\frac{c'}{c}$	$\Delta c_{L,max,base}$	k_1	k_2	k_3	$\Delta C_{l,max,f}$
Single Slotted	Take-off	45	1.05	1.58	1.05	0.7	0.55	0.639
	Landing	45	1.09	1.58	1.05	0.98	0.92	1.496
Fowler	Take-off	40	1.15	1.64	1.2	0.7	0.47	0.648
	Landing	40	1.20	1.64	1.2	1	1	1.968
Double Slotted	Take-off	50	1.18	1.74	1.2	0.67	0.40	0.560
	Landing	50	1.26	1.74	1.2	1	1	2.088

High-lift devices positioning

The positioning of the high-lift devices is done by taking into account that other subsystems are fitted on the wing as well like the engines and the ailerons. Torenbeek states that a typical arrangement of TE on a wing is divided into an inner and outer section [10]. It is also important to maximise the area the HLD's can take up to maximise the increase of the lift coefficient with deployed flaps. The inner section starts after the fuselage and ends where the engine starts. Then the outer part starts where the engine ends and ends where the aileron starts. For the LE arrangement that it runs from the fuselage until the end of the wing with and intersection where the engine is located. In Figure 4.15 the position of the LE and TE HLD's are shown and Table 4.6 shows the position of percentage of the half-span.

Table 4.6: Position of the HLD's as percentage of the half-span.

Parameter	b_{11}	b_{12}	b_{21}	b_{22} TE	b_{22} LE
Value (as % of half-span)	10.7	27.5	32.5	86.0	90.0

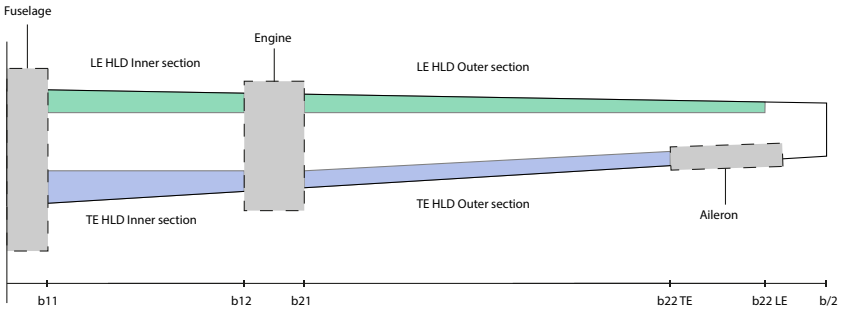

Figure 4.15: Positioning of the HLD's.

After positioning the HLD's the increase in lift coefficient of the wing can be computed. This is done with the following equations for the TE and LE [11, 27]:

$$\Delta C_{L,max,f} = \Delta C_{l,max,f} \cdot \frac{S_{w,f}}{S} \cdot K_\Lambda, \tag{4.5}$$

$$\Delta C_{L,max,s} = \Delta C_{l,max,s} \cdot \frac{S_{w,s}}{S} \cdot \cos\phi_{hinge}. \tag{4.6}$$

Equation 4.5 is for the TE, where $\frac{S_{w,f}}{S}$ is the area ratio of the wing area with TE HLD's over the wing area, K_Λ is an empirical correction factor taking into account the wing sweep. Equation 4.6 is for the LE, where $\frac{S_{w,s}}{S}$ is the area ratio for the LE, ϕ_{hinge} is the sweep angle at the LE hinge location. The HLD wing area for the TE and LE is based on the wing area that has a HLD in front or behind it. This value also differs between the LE and TE as the LE HLD covers more of the span than the TE does. Then to obtain K_Λ it is taken from a graph provided by Scholz and DATCOM [27, 11]. Table 4.7 shows the computed increase in lift coefficient.

Table 4.7: Lift coefficient increase of the wing due to HLD's.

Trailing Edge	$S_{w,f}$	K_Λ	$\Delta C_{L,max,f',TO}$	$\Delta C_{L,max,f,LN}$
Single Slotted	31.8	0.92	0.415	0.971
Fowler	31.8	0.92	0.420	1.277
Double Slotted	31.8	0.92	0.363	1.355
Leading Edge	$S_{w,s}$	ϕ_{hinge}	$\Delta C_{L,max,s,TO}$	$\Delta C_{L,max,s,LN}$
Slat	33.1	1.07	0.431	0.518

Then to compute the new value for the maximum lift coefficient, the following equation is used:

$$C_{L,max} = \frac{C_{l,max,clean} + \Delta C_{L,max,f} + \Delta C_{L,max,s}}{1.1}. \tag{4.7}$$

The 1.1 term it is divided by is a factor that ensures the aircraft can still stay in the air if the empennage creates negative lift to trim the aircraft [27]. $C_{l,max,clean}$ is the maximum lift coefficient of the clean wing. This value can be taken from a relation from DATCOM [11] with the following equation:

$$C_{l,max,clean} = \left(\frac{C_{L,max}}{c_{L,max}}\right) \cdot c_{L,max} + \Delta C_{L,max}. \tag{4.8}$$

Here $c_{L,max}$ is the maximum lift coefficient of the airfoil. The fraction is taken from a graph that related the maximum lift coefficient of the airfoil with a tapered, swept wing. In the case of an unswept wing at quarter chord, this value is 0.88. Finally, $\Delta C_{L,max}$ is a correction term for mach number, however, below mach 0.2 this value is 0. As during take-off and landing the aircraft flies below mach 0.2, and therefore the term is zero in this case. This gave the following value for the maximum lift coefficient of the clean wing: $C_{l,max,clean} = 1.324$.

Then by using Equation 4.7 the maximum lift coefficients can be computed for take-off and landing for three combinations of LE and TE HLD's. In Table 4.8 the results are shown.

Table 4.8: Maximum lift coefficients for take-off and landing configuration.

High Lift Device		$C_{L,max,TO}$	$C_{L,max,LN}$
LE	**TE**		
Slat	Single Slotted	1.97	2.56
Slat	Fowler	1.98	2.84
Slat	Double Slotted	1.93	2.91

From typical values for the maximum lift coefficient for Regional Turboprop aircraft provided by Scholz [27], these are within those ranges for both take-off: 1.7-2.1, and landing: 1.9-3.3. Furthermore, Scholz also provides values for combinations of slats and single slotted, single fowler, and double slotted flaps.

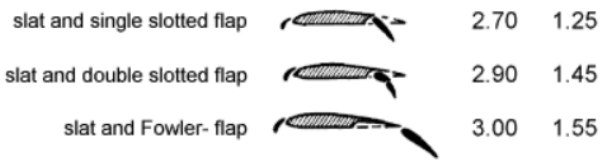

Figure 4.16: Combinations of Slats and TE HLD's. [27]

The first value in Figure 4.16 is the maximum lift coefficient of the entire wing in landing configuration, the second value is the added lift coefficient value of the HLD configuration to the plain wing. The double slotted flap differs from Table 4.8, however, this can be explained by the fact that the calculated value is of the of a double fowler flap, and from Scholz the value is of a double slotted flap. Therefore, the calculated value increases lift more.

4.7. Spoilers

Author: Nathan

The spoilers are going to be placed in front of the TE HLD's. They are going to be sized based on an equation from Gudmundsson [15] that calculates the added drag from a deployed spoiler. This equation is presented below:

$$\Delta C_{D_{sp}} \approx 1.17 \frac{b_{sp} h_{sp}}{S} \frac{\delta_{sp}}{90}. \tag{4.9}$$

Here b_{sp} and h_{sp} are equal to the length and height of the spoiler, δ_{sp} is the deflection of the spoiler. The factor of 1.17, the equation multiplies with, is based on the drag coefficient of a circular disk tangent to the airflow. The length of the spoilers are decided based on the positions of the TE HLD. There are 2 spoilers in front of the inner section, and 4 in front of the outer section. The height of the spoilers are computed based on a fraction of $b_{sp}/4$ and the deflection is taken at $70°$. In Table 4.9 the spoiler sizing is shown, as well as the aerodynamic properties during deployment for the wing.

Table 4.9: Spoiler sizing and aerodynamic properties.

Parameter	b_{sp}	h_{sp}	$\Delta C_{D_{sp}}$
Spoiler 1	1.675	0.42	0.0095
Spoiler 2	1.675	0.42	0.0095
Spoiler 3	1.926	0.48	0.0126
Spoiler 4	1.926	0.48	0.0126
Spoiler 5	1.926	0.48	0.0126
Spoiler 6	1.926	0.48	0.0126
Total	-	-	0.069

4.8. Ailerons

Author: Nathan

For the sizing of the aileron, '14 CFR 23.157 roll rate for take-off' states that an aircraft over 6000 pounds needs to perform a roll of 60 degrees from 30 degree angle in less than 10 seconds, for landing the same angle requirement within 7 seconds. With this the roll rate requirement can be calculated for both landing and take-off. For landing it is: $p_{req} = 8.57\ deg/s$, for take-off it is: $p_{req} = 6.00\ deg/s$. Ailerons are typically chosen only as big as required, to have an as large of flap span as possible[10]. For high-speed aircraft, there typically is an inner and outer aileron. However, this applies to transonic aircraft or faster and the LEAF family does not classify as transonic because the mach number is below 0.75. Therefore, only an outer aileron is sized for the family. The method for sizing the ailerons is based on one by Gudmundsson [15]. It uses the following expression with relation to the roll rate:

$$p = -\frac{C_{L_{\delta_a}}}{C_{L_p}} \cdot \delta_a \left(\frac{2 \cdot V}{b} \right). \tag{4.10}$$

$C_{L_{\delta_a}}$ is the roll authority coefficient and C_{L_p} is the roll damping coefficient.V is the free-stream velocity, and b is the wing span. Finally, δ_a is the aileron deflection angle which is the difference in angle between the left aileron and right aileron. To calculate the roll authority and roll damping coefficients the following expressions are used. For roll authority, Equation 4.11 from Sadraey [28], for roll authority:

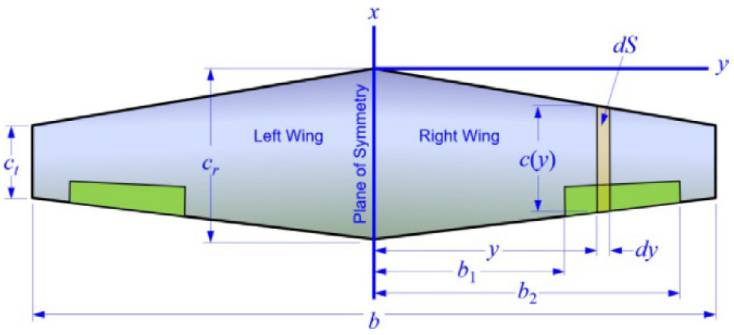

Figure 4.17: Definitions of the wing for aileron sizing calculations.

$$C_{L_{\delta_a}} = \frac{2 c_{l_a} \tau}{S b} \int_{b_1}^{b_2} c(y) \cdot y dy, \tag{4.11}$$

where c_{l_a} is the lift slope of the airfoil per radian, τ is the aileron effectiveness parameter taken from a graph relating it to the chord of the aileron [28]. $c(y)$ is the chord as function of the span, b_1 is the start of the aileron and b_2 is the end of the aileron as defined by Figure 4.17. Equation 4.12 for roll damping from Gudmundsson [15] for straight tapered wings:

$$C_{L_p} = -\frac{(c_{l_a} + c_{d_0}) \cdot c_r b}{24 S} (1 + 3\lambda), \tag{4.12}$$

where c_{d_0} is the minimum drag of the airfoil and c_r is the root chord. Then these coefficients are calculated, but first some parameters need to be defined and later iterated up on if the roll rate requirements are met or not. For example, the value for b_1 cannot be taken smaller then the value of b_{22} TE, as the aileron and TE HLD cannot overlap. Therefore, b_1 is taken to be at 87% of the half span. The typical chord of the aileron is taken at 0.25 of the chord length [28]. The corresponding τ value for this ratio is 0.48. For the deflection of the aileron, Sadraey defines a maximum upward and downward angle of 30 degrees [28]. Gudmundsson explained that typically for aileron deflections a ratio of 1:0.75 should be taken between upward and downward deflection [15]. By taking a maximum upward deflection of 30°, the downward deflection is then equal to 22.5°. This gives a δ_a of 52.5°. To compute the roll rate from these values, the free stream velocity at landing and take-off has to be determined. For landing the approach speed V_{app} is taken, and for take-off, the take-off safety speed V_2. These speeds differ between the preliminarily sized HLD's in Section 4.6 as their maximum lift coefficients are

different. Then the aileron can be sized, based on the landing and take-off configuration. In Table 4.10 the results of the computation of the roll rate due to the sizing of the aileron is shown.

Table 4.10: Roll rate due to aileron sizing calculations for the LEAF-A and B aircraft in landing and take-off configuration.

Parameter	Configuration	Roll rate requirement for maneuvre [deg/s]	b_1 [%]	b_2 [%]	Roll rate [deg/s]
LEAF-A	Take-off	6.0	87	92	13.5
	Landing	8.6	87	92	12.6
LEAF-B	Take-off	6.0	87	92	12.2
	Landing	8.6	87	92	11.4

4.9. Trade-off high-lift devices

Author: Nathan

In this section the HLD configuration is chosen for the LEAF family aircraft. For this, a trade-off is conducted based on the results from Section 4.6 and also form Section 4.8. As the family members differ in weight, the lift coefficient required for landing and take-off is also different. Therefore, a separate trade-off is conducted per family member. First, the criteria and weights need to be decided. The first criteria is the complexity of the system, then the component weight is considered. The performance is a big criteria to consider, and finally the compatibility with the ailerons is an important criteria. For the criteria only the TE is going to be evaluated as all three configurations have a slat as LE HLD.

Complexity (20%)

The Single Slotted flap has a slot entry that needs to be taken into account. This increases cruise drag and needs to be sealed. The flap requires at least two hinges, however, to minimise flap flex three or more should be considered [15]. For Single Slotted Fowler flaps, the complexity increases. The Fowler flap is a Single Slotted flap travelling aft on tracks [10]. This means besides guide slots and hinges, it needs an actuator. Translation requires the upper skin that covers the flap to be much stiffer to prevent the trailing edge skin to start deflecting upward. This creates a structural challenge [15]. The Double Slotted flap is taken to be a Double Slotted Fowler flap. These flaps have considerable extension due to basic flap motion, furthermore, the flap sections move relative to each other [10]. The shape of the slots must be very carefully optimised to obtain good performance. They require complicated and heavy systems and need substantial structural support due to high aerodynamic loads [15].

Weight (20%)

The weight of the components can be assumed to increase along with the complexity. As said, the Fowler flap system is a more complex Single Slotted flap system, therefore, it can be assumed that the weight of the Single Slotted Fowler flap is more. The Double Slotted Fowler flap is a significant increase of system complexity compared to the Single Slotted Fowler flap and therefore it is going to weigh more than the Single Slotted Fowler flap.

Performance (40%)

The performance criteria is based on the stall speed that can be achieved based on the maximum lift coefficient obtained from the HLD configuration. First, to define the criteria, the optimal stall speed has to be defined. For landing this is based on the minimum approach requirement *STKCX04* of 56.6 m/s, and the 14 CFR 25.125 requirement for approach speed, where $V_{app} < 1.23V_{stall}$. The aim is to get as close to the minimum approach speed as possible in the case $1.23V_{stall} > 56.6$. In the case where $1.23V_{stall} < 56.6$, the aim is to get V_{app}/V_{stall} as close to 1.23 as possible.

Compatibility (20%)

The compatibility criteria is based on fitting the ailerons on the wing planform. The current position of the aileron is set at 87% to 93% of the half wing span. In case this has to shift due to the HLD needing to increase in area, this would be seen as unfeasible, but still excepted to meet. Furthermore, it is also based on the design roll rate requirement and whether or not, with the speed during landing and take off, the HLD configuration can achieve this roll rate without changing the ailerons size. This is determined by a 'True' of 'False' statement, where True stands for requirement reached with current size, and False requirement not met. If the ailerons do have to

increase in size do to a 'False' statement, it is seen as correctable as there is space left on the wing to increase the size, but it is seen as very unfeasible.

Table 4.11: HLD trade-off for the LEAF-A

Concept / Metric	Single Slotted with Slat	Single Fowler with Slat	Double Slotted with Slat
Complexity (20%)	Medium Green	High Cyan	Very High Yellow
Weight (20%)	Light Green	Medium Cyan	Heavy yellow
Performance (40%)	$V_{stall,TO}$: 63.0 m/s Yellow $V_{stall,LN}$: 55.3 m/s	$V_{stall,TO}$: 62.9 m/s Cyan $V_{stall,LN}$: 52.5 m/s	$V_{stall,TO}$: 63.7 m/s Cyan $V_{stall,LN}$: 51.9 m/s
Compatibility (20%)	True Cyan	True Green	True Green
Total Points	1.0	1.2	0.8

Table 4.12: HLD trade-off for the LEAF-B

Concept / Metric	Single Slotted with Slat	Single Fowler with Slat	Double Slotted with Slat
Complexity (20%)	Medium Green	High Cyan	Very High Yellow
Weight (20%)	Light Green	Medium Cyan	Heavy yellow
Performance (40%)	$V_{stall,TO}$: 56.7 m/s Cyan $V_{stall,LN}$: 49.8 m/s	$V_{stall,TO}$: 56.6 m/s Green $V_{stall,LN}$: 47.3 m/s	$V_{stall,TO}$: 57.4 m/s Green $V_{stall,LN}$: 46.7 m/s
Compatibility (20%)	True Green	True Green	True Green
Total Points	1.6	1.6	1.2

The results of the trade off fit the LEAF-A aircraft with the Single Fowler with Slat, and the LEAF-B with either Single Slotted or Single Fowler with Slat, as they draw. The LEAF-B has a very close trade off between the HLD configurations, therefore, a sensitivity study has to be performed. By decreasing Performance to 30% and increasing Complexity and Weight to 25%, the Single Slotted won with 1.7 and the Single Fowler, being more complex and heavy, got 1.5. Furthermore, the Single Fowler and Double Slotted flaps are found to be on point with the criteria as the approach speed over the stall speed would be basically 1.23. Still, the Single Slotted performs sufficient enough as the stall speed for landing is excellent. Therefore, the LEAF-B variant is fitted with the Single Slotted with Slat configuration.

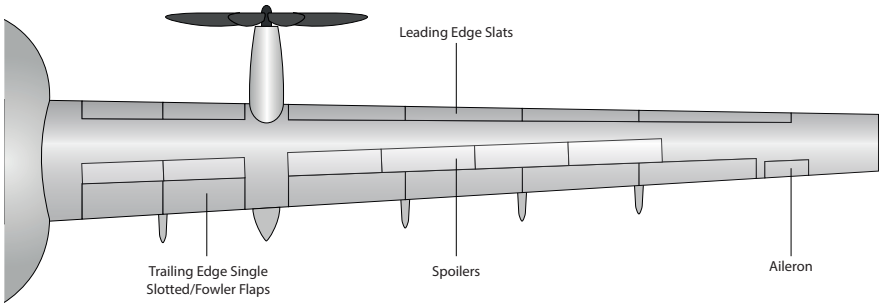

Figure 4.18: Final Wing Planform Design with LE and TE HLD's shown.

4.10. Stability & Control

Author: Carlos

Following the analysis of Section 4.4, the stability and control derivatives are used to derive a Linear 6-DOF state-space model [29]. Certain assumptions where used to simplify the equations of motions and are as follows:

- Steady-state
- Straight
- Symmetric flight condition

Aircraft Dynamics

These equations were used to simulate the response to several initial conditions detailed in Table 4.13, Figure 4.19a, Figure 4.19b and Figure 4.20 show the response for both symmetric and asymmetric equations.

Table 4.13: Initial Conditions

Type of motion	$[u, \alpha, \theta, q]$
Phugoid	[0.01, 0.0, 0, 0.0]
Short Period	[0.0, 3.0, 3.0, 0.0]
	$[\beta, \phi, p, r]$
Dutch Roll	[8.0, 0.0, 0.0, 0.0]

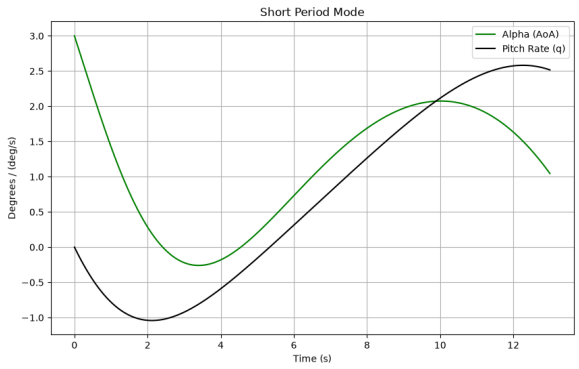

(a) Short Period - Open Loop

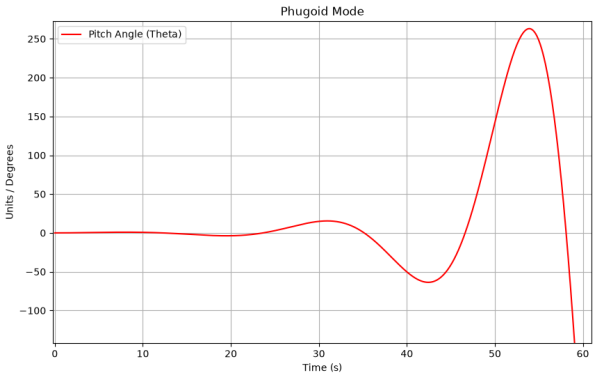

(b) Phugoid - Open Loop

Figure 4.19: Longitudinal Forced Response

As it can be seen the Phugoid and Dutch roll response are not naturally stable, this is further reinforced by their poles which were found to be $-0.39 \pm 0.56j, 0.12 \pm 0.27j$ for the longitudinal and $0.13 \pm 0.50j, -0.44, -0.00079$ for the lateral open poles. It is also important to note that the data extracted from OpenVSP has come into question because of what can be seen in Figure 4.20; the rapidly increasing amplitude of the side-slip could be attributed to a lack of inertia around the yaw axis in addition to the lack of dampening due to the vertical stabilizer. One of the main recommendations for further research outside of the scope of this project is to validate this OpenVSP data with either CFD or wind tunnel testing.

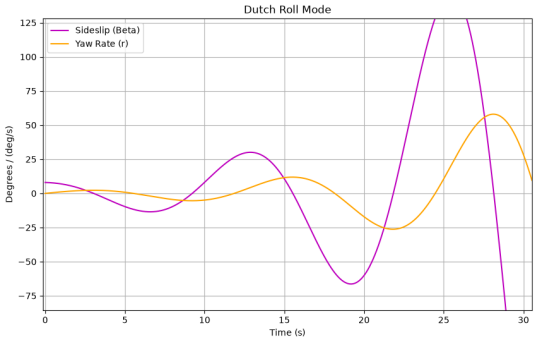

Figure 4.20: Dutch roll response

Control Logic

To ensure that the aircraft does not remain unstable, a closed loop algorithm has been implemented. There are many different controllers available but the main ones are as follows:

- P.I.D. (Proportional, Integral, Derivative)
- L.Q.R. (Linear Quadratic Regulator)
- Full State Feedback [Pole Placement]

PID is the most widely used controller in the industry, it is used both in aircraft and everyday use systems. The main benefit is that it does not require full awareness of the system, but its main drawback is it struggles with highly coupled systems such as the full aircraft dynamics. Methods like Full State Feedback assume a sensor suite capable of measuring every single parameter. It allows for a very specific closed loop dynamics selection via pole placement. The main limitation is that if the pole placement differs significantly from that of the open loop it might lead to unrealistic actuator control inputs. L.Q.R. is the most advanced option. It is an optimal form of Full State Feedback. Two penalty matrices can be defined: Q (state errors) and R (actuator effort), in order to achieve the desired dynamics. For this aircraft, pole placement full state feedback was chosen for its relative simplicity, while providing the necessary control.

The standard linear state-space system equations follow Equation 4.13

$$\dot{\mathbf{x}} = \mathbf{A}\mathbf{x} + \mathbf{B}\mathbf{u}. \tag{4.13}$$

In full state feedback the input $\tilde{\mathbf{u}}$ is defined as :

$$\mathbf{u} = -\mathbf{K}\mathbf{x},$$

with $\mathbf{x}$ the state vector and $\mathbf{K}$ a gain, leading to:

$$\dot{\mathbf{x}} = (\mathbf{A} - \mathbf{B}\mathbf{K})\mathbf{x}.$$

Pole Placement

$\mathbf{K}$ has to be reverse engineered from a set of closed loop poles. To do this first a set of poles has to be selected, some guidelines have been set by the US military a specification MIL-F-8785C[30] summarised by Torres.[6] The LEAF aircraft stands in the Class II aircraft category and the design flight condition is Category B flight with stability requirement Levels 1 or 2. From the specification, it can be found that ζ_{SP} for the short period can have values in the range 0.3-2, with phugoid Level 1: ζ_{ph} > 0.04 and Level 2: ζ_{ph} > 0.
The chosen longitudinal pole was set at $-0.60 \pm 0.60j, -0.08 \pm 0.08j$ to confirm if this complies with the specification the eigenvalues must be computed using Equation 4.14.

$$\omega_n = \sqrt{\sigma^2 + \omega_d^2}, \qquad \zeta = -\frac{\sigma}{\omega_n}. \tag{4.14}$$

This would lead to $\zeta_{SP} \approx 0.707$, $\zeta_{ph} \approx 0.707$. A similar procedure can be followed for the Dutch roll with selected pole $-0.80 \pm 1.20j$ to find $\zeta_{DR} \approx 0.5547$. The same forced response is then be plotted in Figure 4.21a,Figure 4.21b and Figure 4.22.

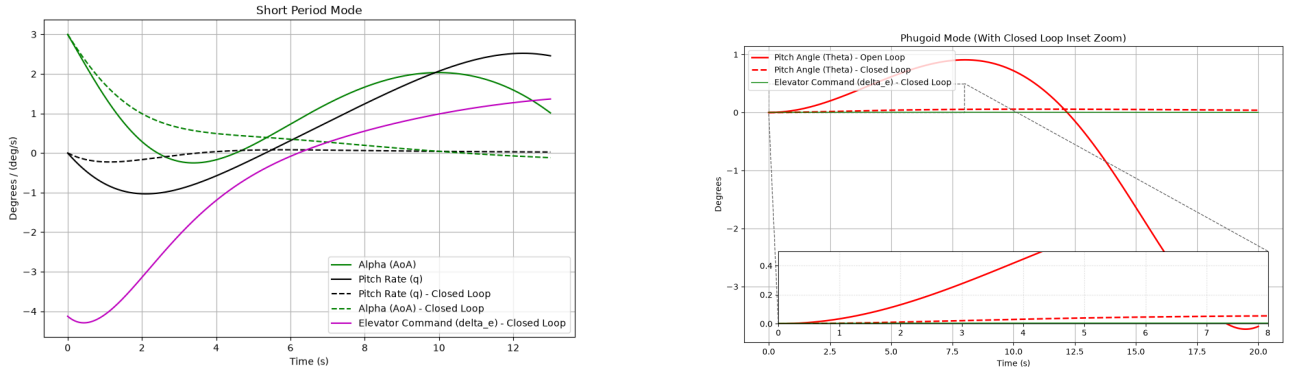

(a) Short Period - Closed Loop

(b) Phugoid - Closed Loop

Figure 4.21: Longitudinal Forced Response - Closed Loop

[6] https://www.cpdee.ufmg.br/~torres/wp-content/uploads/2018/02/flying_handling_qualities.pdf, *(Accessed 23/06/2026)*

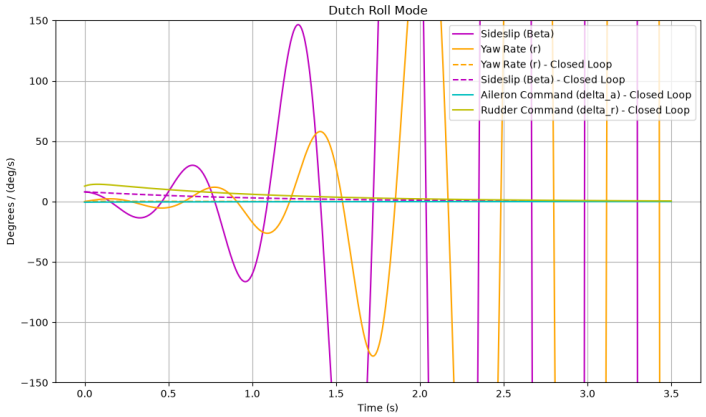

Figure 4.22: Dutch Roll response - Closed Loop

A final note is that although the poles comply with the requirement set out by MIL-F-8785C, if a more optimised pole placement is required at a later stage, L.Q.R. should be the next step. Furthermore, other lateral stability cases, such as roll, should be investigated.

5

Detailed fuselage design

Author: Daan, Toine, Viktor, Lindsay

In this chapter, the fuselage will be designed. Before anything is sized, the cabin layout will be designed. Then the fuselage-cross section will be examined: its skin, stringers and frames. In order to determine the fuselage skin thickness, the different load cases will be analysed and materials will be selected. Finally, a closer look is taken at the strut box and floor structures.

5.1. Cabin layout

Author: Lindsay

To finalise the fuselage design, the detailed cabin layout needs to be analysed. This includes positioning the doors, lavatory, fire extinguishers, and seats.

The seat pitch has been decided to be 31 inch, in order to give some comfort to the passengers. Increased seat pitch can also decrease the turnaround time, since there will be less seat interference from passengers putting their baggage in overhead bins [31]. This seat pitch will then also comply with the required minimum seat pitch of 29 inches, stated in STKPAX01-MIS01.

The emergency exits necessary are looked at first. From CS 25 requirements, it is mandatory that aircraft with 41 to 110 seats to have at least two exits on each side of the fuselage, mentioned in STKCX08-MIS01-SYS07. One exit on each side of the aircraft has to be at least a Type I exit or larger [7]. For all family members it is decided to use four oversized Type I exits, as these can be sized smaller than the bigger Type C doors if any space has to be saved. The Type I doors can be later resized if it is necessary to add for example a larger hydrogen tank into the cabin as well. Therefore, the doors have been sized to 30 inches wide and 73 inches high, with corner radii of 7 inches. These doors will be placed at the front and back of the aircraft, with all the seats of the passengers between them. The doors still comply with regulations, as the passengers furthest away from an emergency door are for the largest family member are about 8.5 metres away, for the smallest it is 7 metres. Both of these are much below the minimum as stated by AMC 25.807 [7].

The lavatory is placed at the back of the aircraft, so that it does not obstruct the passengers emergency path to the exits. This lavatory is sized as 48x42 inches, so that it fits perfectly in the space behind the exits and the tailcone[1]. The only thing left to place at this point are the fire extinguishers. For the smaller family member, at least two hand fire extinguishers are required, one of which in the pilot compartment. Besides this, each galley located above or below the passenger compartment must have one too. This means next to each of the exits, a hand fire extinguisher is placed, for fast function and easy access. The final cabin layout can be seen in Figure 5.1.

[1] https://www.seattletimes.com/nation-world/youre-not-imagining-things-the-lavatories-on-airplanes-are-getting-smaller/, *Accessed: 02-06-2026*

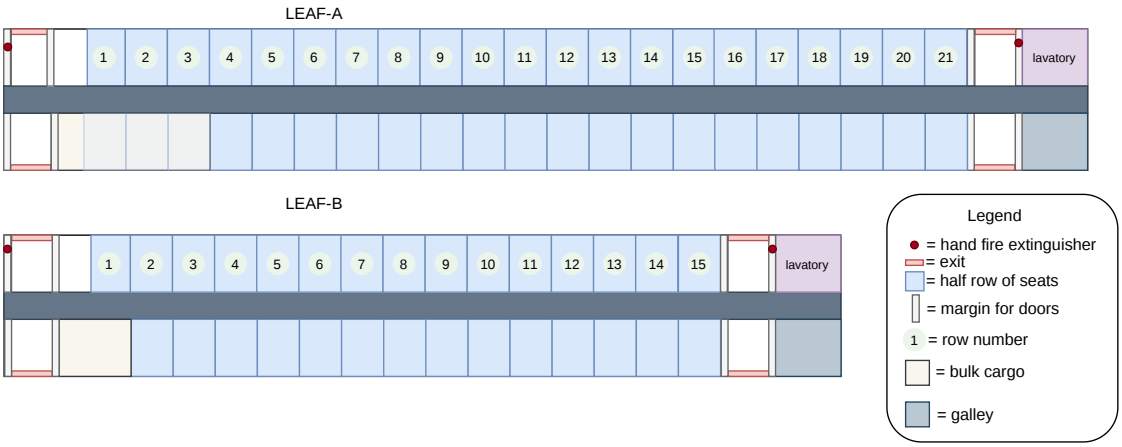

Figure 5.1: Cabin layouts for aircraft family

It can be seen here that the large family member has quite some excess space that is currently not used. This space can be used for extra cargo the stakeholders might be interested in transporting, or if necessary another hydrogen tank can be placed in this section, in order for the aircraft to either fly further, or not be required to have to under-belly hydrogen tanks as mentioned in previous reporting [3]. For LEAF-B, the first row is a half row of seats, in order to get to 58 passengers total. The other side of the half row is used for extra cabin luggage for the passengers or bulk cargo. LEAF-A can fly with either 84 or 76 passengers, which means three half rows in the beginning can either be seats to fly passengers, or also the bulk cargo or passenger cabin bag storage.

Customisation Strategies

The way as mentioned above is not the only cabin interior that can be applied to the aircraft. For example, the seat pitch can be changed to the minimum of 28 inches. For variant A, this will increase the number of rows from 15 to 17, and for variant B from 21 to 26, when also changing the excess cargo space to seats. It is also an option to add half a row next to the lavatory, in order to increase the available seats even more. These changes will lead to a slower turnaround time, as mentioned, that the (de)boarding will take longer, but these extra seats might be able to increase the profit of the flight. Besides having more passengers, it is also possible to take out all the seating arrangements, and change the aircraft from a passenger aircraft to a cargo aeroplane. This would then mean that even the floor could be changed, in order for unit load devices to be able to be put in the aircraft. It is recommended that in later work, these changes are inspected and worked out to find all possible implementations of this aircraft.

Additionally, the cabin can be changed to also include a business class. As the cabin has some space used for cargo or carry on luggage, this space can also be transformed to get business class seats. The first three rows can turn into business class seats with a seat pitch of 38 inches.[2] The other economy seats can still stay the same seat pitch. This does lead to an aircraft with 60 seats instead of 58. So any half row can be taken out to get the desired 58 passenger aircraft. Additionally, the seat pitch can be shortened, which means more business class seats can be put in.

5.2. Fuselage cross-section

Author: Daan *Contributors: Toine*

The fuselage structure consists of three main components: skin, panels, and stringers. This section will explore the structural design of these three elements. First, several assumptions are made, as seen below:

1. The fuselage skin will carry all torsion and shear flow caused by wing-induced lift and the empennage;
2. Stringers and the skin will carry the stress caused by the bending moment;
3. The frames and stringers will stiffen the skin to prevent plate buckling.

With these assumptions in place, the fuselage cross-section can be defined, as seen in Figure 5.3. For design purposes, the skin will be sized first, then the number of stringers will be determined, and finally the frame spacing will be computed.

[2] `https://www.qantas.com/en-au/onboard/fleet/e190`, *Accessed: 23/06/2026*

Skin thickness

Three loading modes determine the skin thickness. These are derived from the pressure difference between the cabin and the local atmosphere, the shear flow induced by the wing lift, and empennage-induced torsion. The pressure difference induced both hoop and longitudinal stress in the fuselage skin. Since hoop stress is most constraining, only this mode will be taken into account here. The hoop stress is given in Equation 5.1, where $\bar{p}$ is the pressure difference, and R and t are the fuselage radius and skin thickness, respectively. Using yield stress and rewriting the equation, the minimum required thickness can be found. The second mode looked at is lift-induced shear flow. The shear flow on the skin, caused by lift L is computed in Equation 5.2. Again, this equation can be rewritten and solved for the minimum thickness when using the yield shear stress. It is assumed that this stress is half of the normal shear stress, as per the Tresca yield criterion. Finally, torsion caused by the empennage is considered, as seen in Equation 5.3.

$$\sigma_{hoop} = \frac{\bar{p}R}{t}, \quad (5.1) \qquad \tau = \frac{2L}{2\pi Rt}, \quad (5.2) \qquad \tau_{yield} = \frac{T}{\pi R^2 t}. \quad (5.3)$$

The three thicknesses computed in Equation 5.1, 5.2, and 5.3 are compared, after which the maximum required thickness is taken. Four materials are considered, Aluminium-2024-T3, Ti-6Al-4V, T300/PEEK, a carbon-fibre composite with PEEK resin, and a novel aluminium-lithium composite. To decide which material to use for the skin, a trade-off is performed later in this section in Table 5.2. The skin thicknesses are 2.1, 0.8, 1.1, and 1.6 mm for the respective materials. As mentioned, the skin material is chosen later in this section, after the stringers and frames have been analysed.

Stringer design

The stringers are sized next. The stringer will be a variant of a z-stringer, as seen in Figure 5.2. This stringer is often used in aerospace design due to its high moment of inertia and ease of inspection. The width, w, is set at 20 mm, and the height is 50 mm. The stringer has a constant thickness, t, of 2 mm.

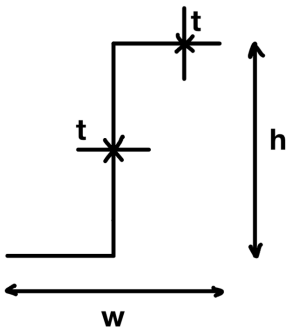

Figure 5.2: Z-stringer used as fuselage stiffener

With these dimensions, it is possible to determine the number of stringers needed. As mentioned in assumption 2, the stringers will mainly carry bending stresses, which are caused by aerodynamic moments. The resulting bending stress is determined in Equation 5.4.

$$\sigma_z = \frac{(M_y I_{xx} - M_x I_{xy})x + (M_x I_{yy} - M_y I_{xy})y}{I_{xx} I_{yy} - I_{xy}^2}. \quad (5.4)$$

Since the fuselage is symmetric, I_{xy} is 0. Additionally, I_{xx} and I_{yy} of the fuselage are identical. To determine the area moment of inertia of the entire cross-section, first the geometric properties of an individual stringer are looked at. These properties are tabulated in Table 5.1. Next, the moment of inertia is determined for the fuselage cross-section. This is defined as the skin contribution plus the addition of all the stringers.

Table 5.1: Geometric properties of the z-stringer

Parameter	Value	Unit
w	50	mm
h	20	mm
t	2.0	mm
A	140	mm^2
I_{xx}	4.6×10^4	mm^4
I_{yy}	4.4×10^3	mm^4
J_r	5.0×10^4	mm^4

The moment of inertia of the fuselage is defined by Equation 5.5. The first term defines the moment of inertia of a thin-walled circular section, that being the fuselage [32]. As mentioned, the cross-section I_{xx} is defined by the contributions from the skin and the stringers. Due to the distance of the stringer to the neutral axis, an additional Steiner term is needed. This is defined as the stringer area multiplied by the distance squared.

$$I_{xx} = \frac{\pi t d^3}{8} + \sum_{i=1}^{n} \left(I_{xx,str} + A_{str} y^2 \right) \tag{5.5}$$

The bending moment experienced by the fuselage is determined next. It is known that the internal moment is largest at the wing, and thus, the value is analysed here. It is assumed that the mass of the aircraft is a distributed load over the entire fuselage. While this is not entirely accurate, it will overestimate the bending moment, introducing a margin of safety. The bending moment caused by the wing is defined in Equation 5.6. Additionally, inertial loading caused by manoeuvres also induces a bending moment. From the loading diagram, the inertial force was found to be 2.5 MTOM. Combining the two contributions to the bending moment, the local internal moment was approximately 3.9 MNm. With the yield stress of the aluminium alloy used for the stringers being 345 MPa, 62 stringers are needed for structural integrity, following from Equation 5.4.

$$M_{wing} = C_m \frac{1}{2} \rho V^2 S \bar{c} \tag{5.6}$$

Plate buckling

The final loading mode considered on a general fuselage cross-section is plate buckling. It is assumed that the fuselage is a cylindrical shell, where normal and axial stresses on the skin can induce local plate buckling. As mentioned already, stringers and panels are used to stiffen the plate. The fuselage is thus divided into smaller panels, as seen in Figure 5.3. The critical buckling load of a thin plate is given by Equation 5.7 [32]. ν is the Poisson ratio of a material, and k is the plate buckling coefficient. For now, it is assumed that the plate is simply supported, with k having a value of 4.

$$\sigma_{cr} = \frac{k \pi^2 E}{12(1-\nu^2)} \left(\frac{t}{b} \right)^2 . \tag{5.7}$$

It should be mentioned that Equation 5.7 is valid for pure loading cases, meaning that in combined loading cases, superposition must be used. Additionally, because the fuselage is circular and stiffened, the problem becomes non-linear, meaning that the equation above cannot be used anymore. The method to analyse this problem has been described by Monteiro et al. [33]. First, the equation of motion must be set up, as well as the kinematic equations of displacement. Then, the buckling equations are linearised. It is assumed that the material is isotropic, and the boundary conditions are elastically restrained. Furthermore, no plate torsion is taken into account. This means that an upper bound is found for the critical plate buckling load.

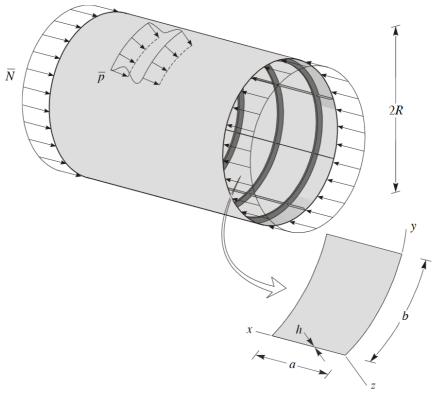

Figure 5.3: Cross-section of a stiffened fuselage [33]

The loading on a local plate has been non-dimensionalised, and is given by Equation 5.8. The normal loading $\bar{N}$ is given by both the longitudinal stress by pressure difference and bending stress. $\bar{p}R$ constitutes the axial loading caused by the pressurised cabin. Additionally, as torsion of an individual plate is not taken into account, plate rotation is ignored.

$$\eta = \frac{\bar{p}R}{\bar{N}}. \tag{5.8}$$

Next, the torsional rigidity of the designed stringers is defined and altered. The final equation for torsional rigidity is seen in Equation 5.9 Equation 5.9 [32, 33]. J_r is the stringer polar moment of inertia, K is a constant that relates to the boundary conditions, and is assumed to be 2. b has been defined in Figure 5.3, and λ_a is the eigenvalue corresponding to a buckling wave pattern in the a-direction. D_{22} is a matrix entry corresponding to the Galerkin method, as defined by Monteiro et al. [33].

$$\vartheta = \frac{G_r J_r}{2D_{22}K} \frac{b}{\pi} \lambda_a^2. \tag{5.9}$$

Finally, the critical buckling load is defined in Equation 5.10. As seen before, the method uses eigenvalue λ_a for the a-direction, and since buckling waves can also form in the b-direction, λ_b is defined. These are dependent on the wave-number pair (m, n). This is always an integer pair, corresponding to the number of whole waves. For each pair, the buckling load is computed, after which a minimum is given. G is a symmetric 3x3 matrix, with entries G_{ij}. Lastly, the critical buckling load is compared to the loading on the panel. Consequently, the panel amount is analysed, and if the panel loading is greater than the critical buckling load, more panels are added.

$$\lambda_{cr} = \min_{m,n} \frac{\|[G]\|}{\left(G_{12}^2 - G_{11}G_{22}\right) G_{00}}. \tag{5.10}$$

Now, a comparison must be made between skin materials. The materials that will be compared are Aluminium-2024-T3, Ti-6Al-4V, T300/PEEK, a carbon-fibre composite with PEEK resin, and a novel aluminium-lithium composite. Material properties have been obtained from either GrantaEduXP or various sources. The materials are traded based on three criteria. First, mass is considered, as it is desired to have an aircraft which is as light as possible. Next, recyclability is taken into account. STKCX16 requires that at least 30% of a single aircraft must be recycled, with respect to the OEM. The fuselage will have a considerable mass, meaning that it would be preferable if most, if not all, of the fuselage materials can be recycled. Finally, cost is taken into account, as it will reduce the purchasing cost, making it more attractive to stakeholders. The trade-off can be seen in Table 5.2.

Table 5.2: Fuselage material trade-off

Concept / Metric	Aluminium-2024-T3	Ti-6Al-4V	T300/Peek[34]	Aluminium-2050 2198-T851[3]
Mass (40%)	3050 kg Yellow	4746 kg Red	1648 kg Green	2676kg Cyan
Recyclability (35%)	Excellent Green	Excellent Green	Poor Red	Excellent Green
Total Skin Cost[$] (25%)	6200 Green	26500 Cyan	57400 Red	27800 Cyan
Total Points	1.2	0.15	-0.4	1.35

It can be seen that the aluminium-2050 alloy performs best in this trade-off. It has a low mass and great recyclability. The price per kilogram is higher than the 2024 alloy; however, this price is likely to reduce in 2045, meaning it will perform even better in a future trade-off. Using this material as skin led to a skin thickness of 1.6 mm. Lastly, a brief overview is given of the overall fuselage cross-section, as seen in Table 5.3. The bending analysis with this skin material found 56 stringers to be sufficient to prevent critical bending at the mentioned 3.9 MNm. The buckling analysis showed that 64 frames are needed, in addition to 72 stringers. Since 72 stringers is the critical value, this number is used. In Figure 5.4, a cross-section with 72 stringers is shown, at a position without a frame. This does not conclude detailed structural design, however. Across the length of the fuselage, some frames have to be altered to accommodate the wing and the landing gear. Additionally, a strut box has to be designed. This is performed in the following sections.

Component	Value	Unit
Skin thickness	1.6	mm
No. stringers	72	[-]
No. frames	64	[-]
Total fuselage mass	2676	kg

Table 5.3: Final generalised fuselage cross-section for family member A

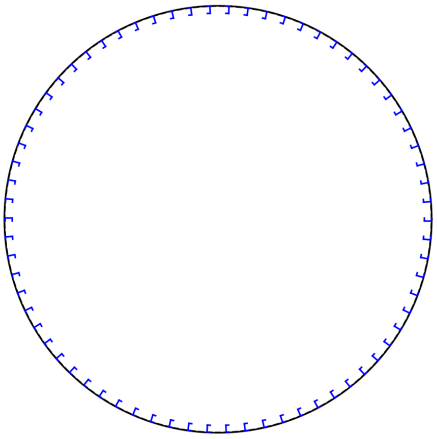

Figure 5.4: Final fuselage cross-section without frames

5.3. Fuselage frames

Author: Viktor *Contributors: Toine, Kacper*

The airframes are the backbone of the fuselage as they support wing-induced lift and bending moments. They also prevent plate buckling, which explained in the previous section. The 64 frames, shown in Figure 5.6, look identical at first glance, however, as the wing, landing gears, and empennage interfere with the fuselage, the frames along the fuselage close to the wing and empennage will differ.

As it has been explained in the previous section, the fuselage will have 72 z-stringers for stiffeners that will go through the frames, and the majority of them will have a spacing of 52 cm as shown in dark blue. The skin thickness in these members is only driven by the hoop stress.

Under the wing, the frames in green, the z-stringers carry the bending moment again, but this time the fuselage skin must also carry the shear flow due to the wing-induced lift, apart from the hoop and longitudinal stresses.

[3] `https://www.aubertduval.com/en/products/`, *Accessed: 10-6-2026*

The shear flow is the highest around the neutral axis, however, the fuselage skin thickness is again driven by the hoop stress. Looking at the cross section of these frames, one can also spot the wingbox fairing in light green on top of the fuselage. The frames have spacing of 47 cm and 51 cm in front of and behind the landing ger respectively.

Focusing on the frame where the strut is attached to the fuselage, this frame supports all previous loads with the addition of the normal and shear forces induced by the struts attachments. As the strut forces are quite huge, a curved I-beam beneath the floor is designed to take these loads. The winbox fairing is again present.

Another important pair of frames are the two shown in purple surrounding the landing gear, which have a spacing of 104 cm. In the cross-section there are three fearings shown: one on top for the wingbox, and two at the bottom for the landing gear in its retracted state.

Finally, there is a region of the fuselage skin thickness coloured in dark red, which marks the region in which no critical system should be located as per STKCX08-MIS01-SYS01-PROP04.

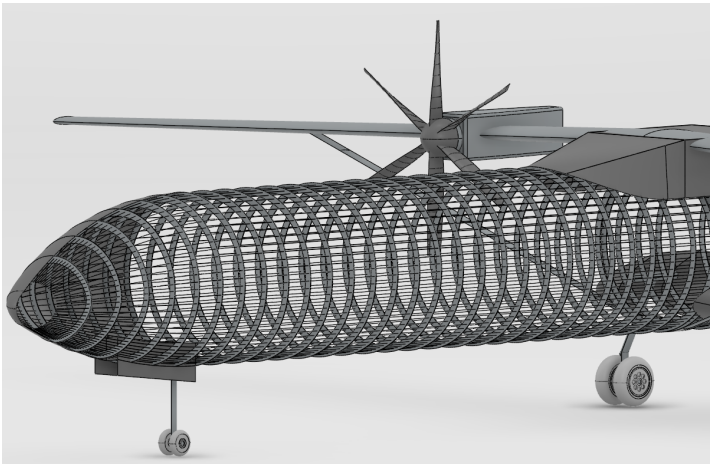

Figure 5.5: CATIA model showing a part of the fuselage featuring 64 fuselage frames and 72 stringers. Nose tip frames leave space for a radome integration.

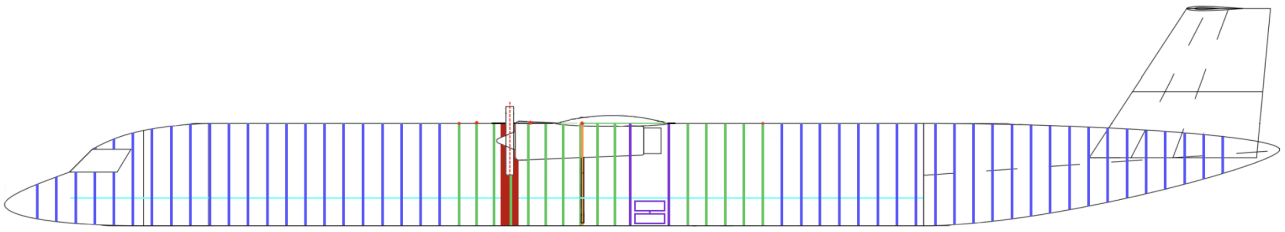

Figure 5.6: Schematics of the 64 airframes along the fuselage length

5.4. Strut support

Author: Toine, Viktor *Contributor: Daan*

In this section, the structure that carries the load from the struts will be designed. This structure will be called a strut beam for the rest of this section and report. With such a structure, the struts will not only be attached to the skin but also to the beam.

As seen in Section 5.2, the frames that help carry the loads in the fuselage are circular. By combining the frame and the strut beam into a single structure, the structural mass can be minimised. For the strut beam, four different cross-sections are considered. The first one is the I-beam, shown in Figure 5.7a. It is good in bending due to the flanges located far from the cg. Furthermore, the shear centre is located in the web, so when there is a vertical force on the web, there is no additional torsion. The second cross-section is the C-Beam, shown in Figure 5.7b, and similar to the I-beam, it is good in bending due to the flanges being far away from the cg. However, the shear centre is located to the right of the web, which means that when there is a vertical force on the web, the structure experiences torsion. This torsion would require a higher thickness, thus increasing the

structural mass. The third cross-section is a rectangle, shown in Figure 5.7c, which is good in torsion because it is a closed section. Furthermore, it is good in multiple load cases, and can take both horizontal and vertical forces well. However, due to it being a closed section, it is difficult to inspect. The last cross-section that is looked at is the circular section, shown in Figure 5.7d, and similar to the rectangle, it is a closed section and thus good in torsion, with a downside of difficult inspection.

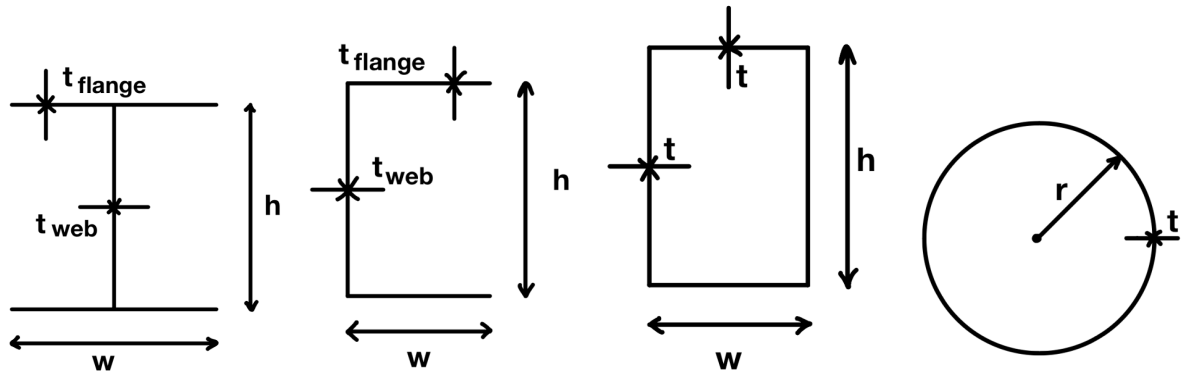

(a) I-Beam **(b)** C-Beam **(c)** Rectangle **(d)** Circle

Figure 5.7: Beam cross-sections

To find the dimension of the strut beam, a couple of assumptions need to be made:

1. The shear force acts at the shear centre of the beam, and thus does not induce an additional torsion;
2. The shear flow is only taken by the skin and the flange directly attached to the skin;
3. The strut is a two-force member, and thus only carries a force in the direction of the strut;
4. The strut beam can be modelled as a straight beam to solve for dimensions.

After making these assumptions, it is important to see the effects it has on the structure. Assumption 1 underestimates the loads of the strut beam, since it does not look at the potential torsion of the beam. Assumption 2 overestimates the shear flow taken by the flange. Assumption 3 slightly underestimates the load in the strut beam as well as the strut itself, because it does not take into account the bending in the strut. Assumption 4 gives smaller deflections than they would truly be and that is why a safety factor of 1.25 will be introduced. The FBD of the strut beam can be seen in Figure 5.8. The angle of 2α is the angle between the strut and the wing. Using this FBD, internal normal and shear force, and the moment (NVM) diagrams can be made to determine the maximum normal force, shear force, and moment. From this, the maximum internal moment is used in Equation 5.4. For this equation, M_y is zero, and I_{xy} is zero due to symmetry of the cross-sections. For the y-value, half of the height is used to get the maximum normal stress. Furthermore, the maximum shear force can be found, and is used for the shear flow calculation using Equation 5.12, where V_x is zero. The third equation that is used is Equation 5.11, where F refers to the normal force applied to the surface, A. After all the stresses are computed, the normal stresses are added together. With the use of Mohr's circle, the shear stress is converted to normal stress, such that 1 normal stress is found. This total normal stress is then checked to be lower than the yield stress divided by the safety factor of 1.25 to ensure that the structure will not yield.

$$\sigma = \frac{F}{A} \qquad (5.11)$$

$$q_b = -\frac{V_y I_{yy} - V_x I_{xy}}{I_{xx} I_{yy} - I_{xy}^2} \int_0^s ty \, ds + \frac{V_x I_{xx} - V_y I_{xy}}{I_{xx} I_{yy} - I_{xy}^2} \int_0^s tx \, ds \qquad (5.12)$$

For the four beam cross-sections, 3 materials are chosen that are commonly used in the aerospace industry, Aluminium- 2024-T3, Ti-6Al-4V, and T300/PEEK, a carbon-fibre composite with PEEK resin. This differs from the fuselage materials, namely, Aluminium-2050 2198-T851 is not looked at here. This is because the material is very expensive compared to the relatively low density reduction it provides. The dimensions and masses of these beams are calculated for all 3 materials, and then a trade-off is made between the materials and beams. For the iterations, the dimensions have a minimum and a maximum value. The first one worth mentioning is the thickness, which has a minimum of 1 mm to keep the structure manufacturable. The second one is the height, which has a maximum value of a quarter of the radius of the fuselage. This is done to prevent the optimisation using all of the space. The masses of each beam with each material are tabulated in Table 5.4. As shown, the I-beam and C-beam have the lowest mass. But due to the shear centre of the I-beam located in the section, it can better withstand a shear force not at the shear centre. So, an I-beam is selected for the strut beam, and a trade-off is made for the materials in Table 5.5. The trade-off results in the Aluminium-2024-T3 material.

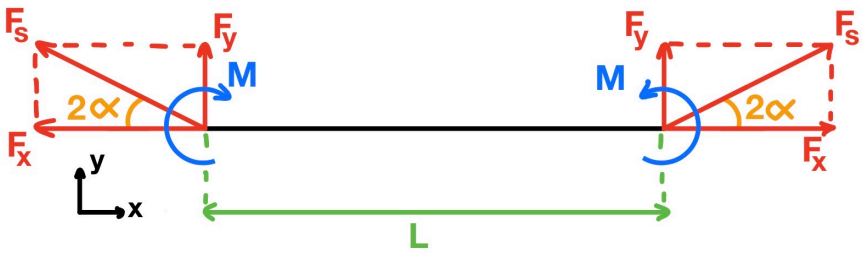

Figure 5.8: FBD of the strut beam

This material will also be used for the other frames in the fuselage. The final dimensions of the strut beam are tabulated in Table 5.6.

Type of beam	Aluminium-2024-T3	Ti-6Al-4V	T300/PEEK
I-Beam	18	12	6
C-Beam	18	12	6
Rectangle	24	17	7
Circle	34	21	10

Table 5.4: Masses of different materials and different cross-sections of the strut beam in kilograms

Table 5.5: Strut I-beam material trade-off

Concept / Metric	Aluminium-2024-T3	Ti-6Al-4V	T300/Peek[34]
Mass (40%)	18 kg Cyan	12 kg Cyan	6 kg Green
Recyclability (35%)	Excellent Green	Excellent Green	Poor Red
Total Beam Cost[$] (25%)	71.4 Green	325.50 Red	723.45 Red
Total Points	1.6	0.6	-0.4

Component	Value [m]
h	0.400
w	0.280
t_{flange}	0.006
t_{web}	0.001

Table 5.6: Final dimensions strut beam

5.5. Floor structure

Author: Toine, Viktor

In this section, the support structure of the floor will be designed. It will consist of both longitudinal and lateral beams, and supporting rods. The terminology that is used in this section and the rest of the report can be seen in Figure 5.9.

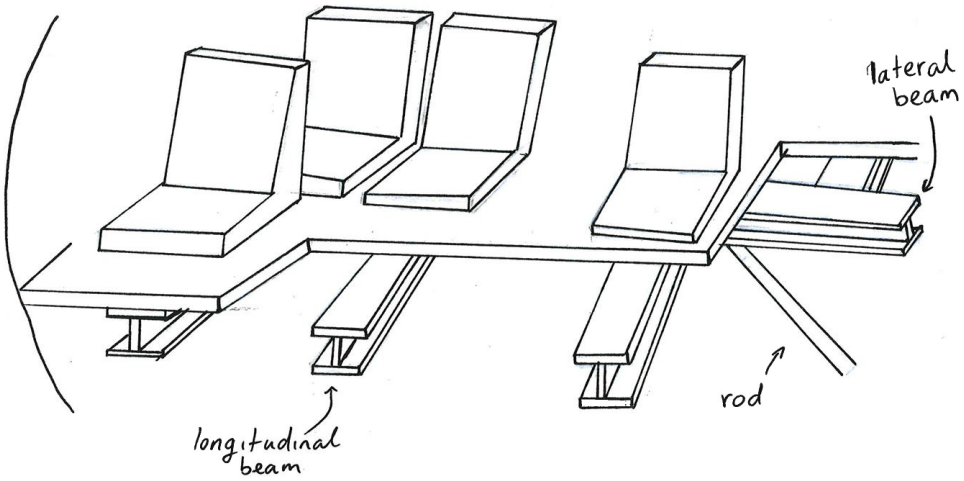

Figure 5.9: 3D-view floor structure with terminology

Due to the same reasoning as in Section 5.4, I-beams will be used for this. The longitudinal beams will be supported by the lateral beams. And rods will be attached from the frame to the lateral beams to support them. Furthermore, the same three materials are looked at as with the strut beam. The FBD of the longitudinal and lateral beam can be seen in Figure 5.10a and Figure 5.10b, respectively. It needs to be noted that the lateral beams are located at every frame, and the longitudinal beams are located under every seat and in between the frames. This means that the lateral beam will carry the longitudinal beam and thus needs to take the reaction forces from the lateral beam. Symmetry can be used to solve the reaction forces of the longitudinal beam. This results in $A_y = B_y$ and $M_a = M_b$. Then the reaction force A_y can be applied to the lateral beam at the point of attachment with the longitudinal beams.

For the calculations, a couple of assumptions need to be made:

1. The weight of the seats is distributed only over the lateral beams;
2. The lateral beams do not have a distributed load on them;
3. The lateral beams are only supported by the rods and not the frames;
4. The rods are a 2-force member, and thus only take a force in the direction of the rod.

After making these assumptions, it is important to look at the effects it has on the structure. Assumption 1 overestimates the loads on the longitudinal beams. Assumption 2 does not affect the total reaction loads on the lateral beam, as the longitudinal beam creates reaction forces that are equal to the distributed load. Assumption 3 overestimates the loads in the rod. Assumption 4 slightly underestimates the load in the rod, since it ignores the internal bending moment. To prevent the material from yielding, a safety factor of 1.25 is added. With these assumptions, the normal and shear stresses can be calculated. This is done with the same procedure as described in Section 5.4. The masses of the floor structure parts are tabulated in Table 5.7. For the rod, it can be seen that a circular cross-section has a lower mass. With all the masses computed, a material trade-off is done for every component similar to the one done in Section 5.4. The trade-off for all 3 components results in a material of Aluminium-2024-T3. The final dimensions for the longitudinal and lateral beam are tabulated in Table 5.8. The final diameter of the circular rod is **10 mm** with a thickness of **1 mm**.

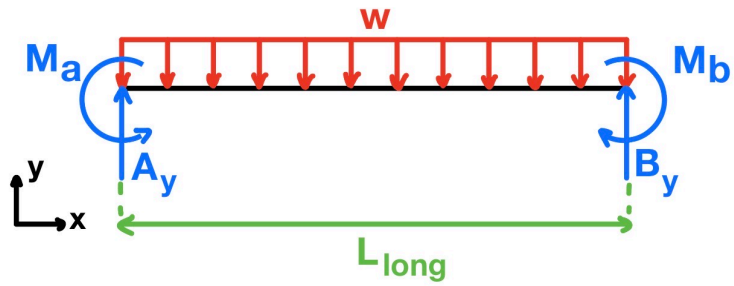

(a) Longitudinal

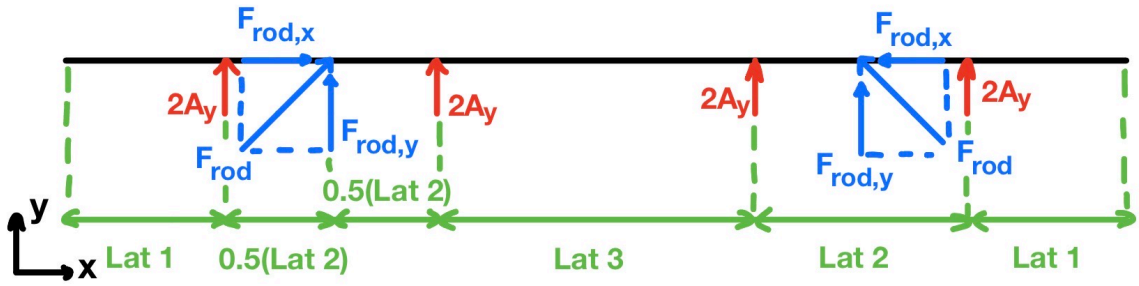

(b) Lateral

Figure 5.10: FBDs of floor beams

Table 5.7: Masses of different materials and different cross-sections of the floor structure in kilograms

Type of beam	Aluminium-2024-T3	Ti-6Al-4V	T300/PEEK
Longitudinal	24	26	10
Lateral	35	34	15
Rectangle Rod	8	13	5
Circular Rod	7	10	4

Table 5.8: Final dimensions longitudinal and lateral beams

Parameters	Longitudinal Beam	Lateral Beam
h [mm]	45	60
w [mm]	10	10
t_{flange} [mm]	1	1
t_{web} [mm]	1	1

6

Detailed tank design

Author: Lisa

The preliminary tank sizing for the midterm design used fixed insulation thickness and geometry estimates with sizing correction factors. In this detailed design phase, the single aft tailcone liquid hydrogen tank is sized with the thermal and structural loads procedure of Onorato et al. [9].

A single non-integral tank is placed in the unpressurised tailcone, aft of the rear pressure bulkhead. For sizing it is assumed that the fuselage frames are sized at half the width of the cabin frames. This is justified because the cabin frames have to additionally withstand pressurisation loads with respect to what the tailcone frames have to carry.

The tailcone geometry is common across the variants with an identical cabin diameter and tailcone length. Since both variants share the same tailcone, they also share the same tank. The volume is sized by the Variant A mission (84 PAX/1500 km), while the insulation thickness is sized by the most constraining variant's mission.

6.1. Tank geometry

Author: Lisa

The tank is shaped as a frustum shell following the tailcone taper, with ellipsoid caps at both ends. The forward cap major half length is set by the cabin diameter, and the aft cap major half length is set by the taper at the start of the APU/empennage region. For the APU/empennage, the last 4.32 m of the tailcone is reserved.

The outline of the tailcone is modelled as a quadratic taper from the cabin radius of $R1 = 1.377$ m down to the tail tip. The tail tip is defined as the point (x_{aft}, z_{aft}), 9.66 m along a 5 degree tilt from the origin (0,0), which is defined at the center of the start of the tailcone. The quadratic tapers are subsequently defined as below:

$$z_{top} = R1 + \frac{z_{aft} - R1}{x_{aft}^2}x^2, \quad z_{bottom} = -R1 + \frac{z_{aft} + R1}{x_{aft}^2}x^2. \tag{6.1}$$

Within this envelope, the outer tank geometry is found by a grid search over four variables. The first 2 variables are the frustum/ellipsoidal caps major axis forward and aft radii. The third variable is the vertical starting position z_0 from $z = 0$. And lastly, the fourth variable is the inclination α of the tank axis. The combination that maximises the outer tank volume while staying inside the tailcone is selected. The search converges to a forward outer radius of $R1_o = 1.3168$ m, an aft outer radius of $R2_o = 0.9612$ m, no vertical offset, and a positive inclination of $\alpha = 3.33°$. The outer radii are with respect to the outer layering of the tank. These are ordered as polyurethane insulation, aluminium structural shell, and inner part of the tank as can be seen in Figure 6.1. The resulting layout of the tank within the tailcone is shown in Figure 6.2.

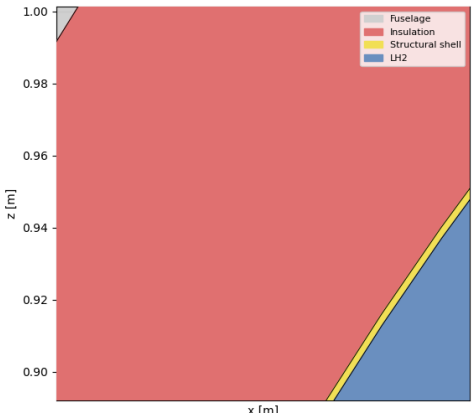

Figure 6.1: Layering of the tank structure.

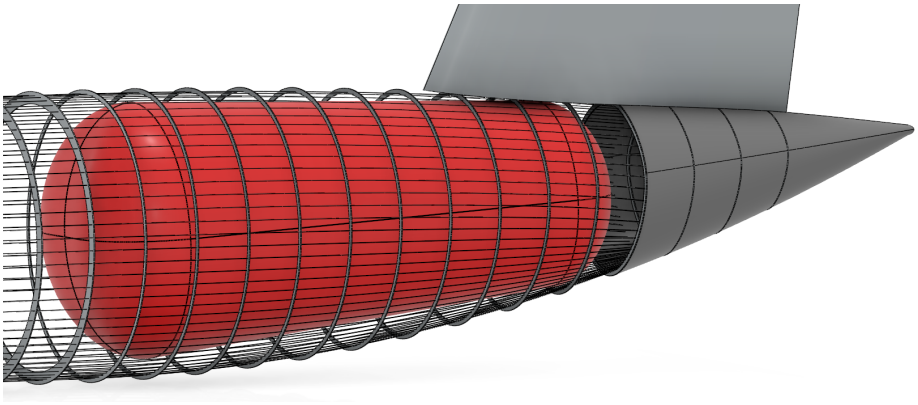

Figure 6.2: Placement of the aft tank in the tailcone of the aircraft. Identical for both LEAF variants.

6.2. Structural shell sizing

Author: Lisa

The material of the shell is aluminium 2219-T851 with a density $\rho_{Al} = 2840$ kg/m^3, and the tank is insulated with polyurethane foam, which has a density $\rho_{ins} = 32$ kg/m^3 [9, 35]. The tank is assumed to only carry the pressure load and is not part of the fuselage's primary structure. The shell can therefore be sized using the hoop stress, without stringer or frame analysis. Furthermore, the bay is unpressurised, so the external pressure on the shell is assumed to be the minimum ambient pressure rather than the cabin pressure.

The shell thickness is sized for the pressure load by Barlow's formula:

$$t_s = \frac{(P_{vent} - P_{out})r_s}{\sigma e_w}, \tag{6.2}$$

Where r_s is the structural shell radius, $P_{out} = P_{amb,min}$ is the minimum ambient pressure since the bay is unpressurised, and e_w is an efficiency factor. Using the same method of Onorato et al., with a venting pressure of $P_{vent} = 300$ kPa and $P_{amb,min} = 22.8$ kPa (36 000ft, conservative maximum altitude), and applying the Goodman relation twice, a $\sigma = 172.8$ MPa operating stress of Al-2219 was determined. The shell radius is taken at the larger forward radius, which slightly oversizes the shell. The choice of venting pressure varies considerably in literature. Gomez and Smith use 172 kPa [36], Onorato et al. use between 250 and 300 kPa [9], and Di Summa uses 400 kPa [37]. A low venting pressure requires thick insulation or results in large amounts of venting, while a high venting pressure requires a thick, heavy shell. The value of 300 kPa chosen for this design is taken from the regional hydrogen aircraft sizing Onorato et al. found, where shell thickness drives the tank mass, and insulation thickness limits the geometric volume available for LH_2 storage [9].

The ellipsoidal caps have a major-to-minor axis ratio of $a/b = 1.6$, as this ratio is shown to have the lowest DOC according to Brewer [35]. The cap shell thickness is reduced by a factor of $(a/b)/2 = 0.8$ relative to the frustum shell thickness. A higher a/b reduces the tank length and the outside area contributing to heat leak, but reiases the stress in the cap and therefore needs a thicker shell. A more hemispherical cap (lower a/b) lowers the shell thickness at the cost of greater length. The $a/b = 1.6$ has been found to balance the heavier shell against the larger length, area, and boil-off, which all feed into fuel burn and structural cost [35]. With the insulation thickness from the next Section, the shell thickness is $t_{shell} = 2.318$ mm for the frustum and 1.854 mm for the caps

6.3. Insulation sizing

Author: Lisa

Insulation thickness trades tank mass and available volume against the amount of hydrogen that must be vented. It is sized here from the in-flight pressure buildup over the full mission.

The tank pressure changes due to boil-off of the liquid hydrogen, fuel draw, and (optionally) venting. The homogeneous model of Onorato et al., originally from Lin et al., is integrated over time [9, 38].

$$\frac{dP}{dt} = \frac{\phi}{V} \cdot \left[\dot{Q}_w + \dot{W}_{mix} - \dot{m}_g \cdot h_{lg} \cdot \left(1 + \frac{\rho_g}{\rho_l - \rho_g}\right) - \dot{m}_l \cdot h_{lg} \cdot \left(\frac{\rho_g}{\rho_l - \rho_g}\right) \right], \tag{6.3}$$

where ϕ is the energy derivative (pressure rise per energy input per volume) evaluated at each step:

$$\phi = 1/\left(\rho_{mean}\left(\frac{\partial u}{\partial P}\right)_{\rho_{mean}}\right). \tag{6.4}$$

ρ_{mean} is calculated determining the quality $x_\rho = [1+(\rho_f/\rho_g)(\beta/(1-\beta))]^{-1}$, with the fill fraction $\beta = (m/\rho_{lh2})/V_{tank}$ at the current liquid hydrogen mass m. Subsequently, the mean density is calculated as $\rho_{mean} = [x_\rho/\rho_g + (1 - x_\rho)/\rho_f]^{-1}$. The partial derivative is calculated using the separate partial derivatives of the liquid and gaseous hydrogen internal energies with respect to pressure. The qualities at these states must again be calculated, with now quality defined as $x_u = (1/\rho_{mean} - 1/\rho_f)/(1/\rho_g - 1/\rho_f)$. The respective internal energies u are divided as $u = x_u u_g + (1 - x_u)u_f$, and deriving these with respect to pressure gives the partial derivative $(\partial u/\partial P)_{\rho_{mean}}$ such that Equation 6.4 can be used to calculate the energy derivative [38]. All properties (ρ_f, ρ_g, h_{lg} and the two $\partial u/\partial P$ derivatives) are tabulated with the CoolProp library for parahydrogen between P_{min} and P_{vent}. The partial derivatives are determined by calculating the change in internal energy over a ± 50 Pa central difference. The table is linearly interpolated and integrated over the mission time with a 10 s timestep.

The insulation layer is an order of magnitude thinner than the tank radius, so conduction is modelled as one-dimensional flat-plate conduction [9].

$$\dot{Q}_w = \frac{(T_{out} - T_{fuel})k_{ins}A}{t_{ins}}, \tag{6.5}$$

with A the outer insulation surface area. T_{out} is taken as the ISA static temperature at the aircraft's altitude plus 24.5 K to take into account a hot day, and T_{fuel} is 20 K. A constant effective conductivity $k_{ins} = 0.022$ W/(mK) is used and the entire result is multiplied by 1.30 to account for additional leakage through the supports and piping [9, 35]. The fluid mixer is not modelled, so the rate of work done on the fluid is set to $\dot{W}_{mix} = 0$. When venting is active, $\dot{m}_g$ is set to hold the pressure at the vent limit P_{vent}. The minimum operating pressure is $P_{min} = 125$ kPa, keeping it above ambient pressure at all times to prevent air from coming into the tank. The tank is assumed to be at P_{min} at gate release.

Besides the pressure rise from boil-off, the tank also experiences hydrostatic pressure increase from accelerations of the aircraft. These are estimated at the critical state defined by CS-25.

$$\Delta P_{hydrost} = \rho_{mean} \cdot K \cdot g \cdot l, \tag{6.6}$$

with ρ_{mean} evaluated at every integration step, $K = 9$ is the critical CS-25 forward linear acceleration, and l the characteristic tank length in the direction of the acceleration, taken here as the frustum length along the tank axis. For sizing purposes, the total pressure $P + \Delta P_{hydrost}$ is held to P_{vent}, so the tank never sees more than P_{vent} even under the critical forward acceleration.

The pressure integration is done over the extended mission of each variant, consisting of the nominal flight plus diversion and loiter. Both variants consist of the same segment durations, with only the cruise segment scaling with the design range. After a 30 min ground hold, the aircraft climbs for 10 min to 25 000 ft cruise altitude, cruises for the time dependent on variant and descends for 15 min to end the nominal mission. The reserve segment is the same for both variants and is driven by the 1 hour diversion requirement: a 5 min go-around, 7 min diversion climb to 15 000 ft, 43 min diversion cruise, and a 10 min descent (1h of diversion flight in total). Finally, there is a 30 min loiter at 15 000 ft and ending with 10 min of final approach and landing, with an additional 5 min arrival-gate hold. Venting is permitted from the end of diversion cruise onward.

The fuel draw $\dot{m}_l$ in Equation 6.3 is modelled per flight phase from the power [39].

$$\dot{m}_l = \frac{P}{H \cdot \eta_{tot}}, \quad P = W\left(\frac{V}{(L/D)} + \frac{dh}{dt}\right). \tag{6.7}$$

Where H is the specific energy, η_{tot} is the total engine efficiency. The power is calculated by the power required $P_r = W(V/(L/D))$ plus the power used for climb $W(dh/dt)$, which equals zero for level flight and is negative for descent. The landing phase is approximated by 30% of the cruise flow. No LH_2 is drawn during the taxi and ground phases, because the engines are off and the draw by the APU is neglected. This is conservative for insulation sizing, since not drawing any fuel increases pressure build up. The resulting fuel burn profile over the previously defined mission profiles is scaled such that the time integral of the burn profile exactly matches the mission fuel mass from the Class I sizing. The scale is 1.046 for Variant A and 1.060 for Variant B, both close to one. This confirms that the raw power fuel calculation already reproduces the Class I fuel mass to within $5 - 6\%$, so the scaling is only a minor and conservative adjustment. The scaling is done to guarantee

consistency between the tank sizing and Breguet range sizing, while letting the power demand govern the shape of the mass flow. The resulting fuel mass plots for both variants are shown in Figure 6.3.

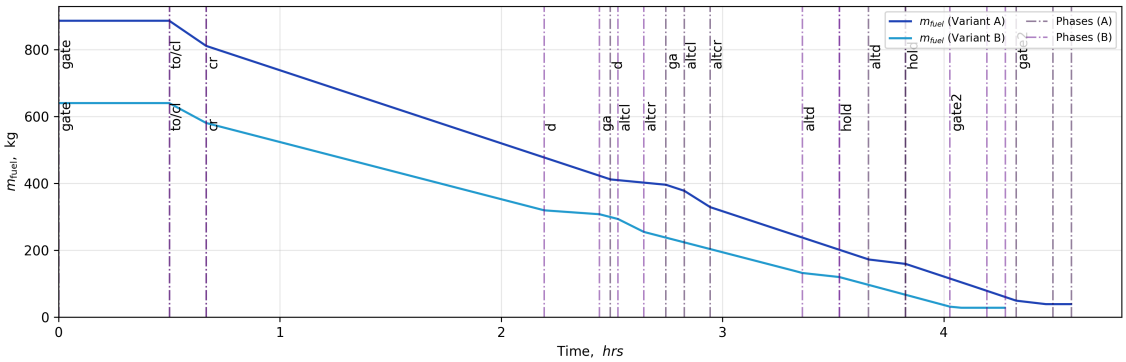

Figure 6.3: Fuel mass remaining over the extended mission of variants A and B.

The insulation is not sized to suppress venting entirely since this would demand an infeasibly thick insulation layer. It is designed to delay it until further into reserve phases of the extended mission [9]. For a nominal mission, the tank then never vents, and the extra hydrogen carried in case of a needed extension can be recovered on the ground. Venting late in the mission is also thermodynamically the most effective, as ϕ is largest when the tank is nearly empty.

The insulation thickness is found by bisection as the minimum thickness for which the unvented total pressure $P + \Delta P_{hydrost}$ first reaches P_{vent} no earlier than the end of diversion cruise. From that point, gas venting is allowed and holds the tank at the vent limit through the final approach and landing. This is calculated for both variants, where the most constraining determines the final insulation size. Variant A requires 14.97 cm of insulation, and Variant B needs 16.08 cm. Therefore, a final $t_{ins} = 16.08$ cm is taken. Running the nominal mission and diversion without venting confirms that Variant A first crosses the vent limit at 4.09 h (14740 s) some time after the end of diversion cruise, and Variant B at 3.30 h (11880s), near the end of diversion cruise The resulting pressure plots are shown in Figure 6.4. Because both variants share the same tank, the smaller Variant B fuel load means a lower fill fraction and therefore a lower ρ_{mean}, which results in a higher dP/dt as can be seen from Equation 6.4 and Equation 6.3. The shorter mission of Variant B would delay the vent limit because of the shorter integration time, however as Figure 6.4 shows, the high dP/dt dominates.

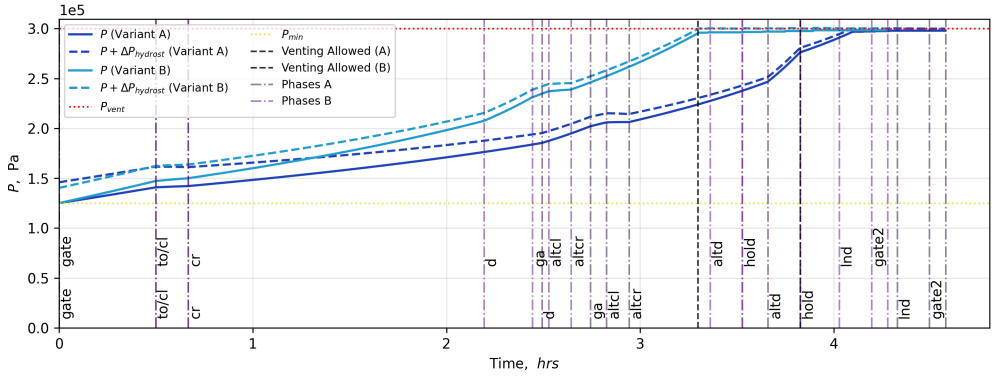

Figure 6.4: Tank pressure over the full mission for Variants A and B, showing the static pressure and the total pressure including the hydrostatic increment. Venting is allowed to start from the end of diversion cruise, and holds the pressure at P_{vent}

The available LH_2 volume is smaller than the internal tank volume because of ullage, thermal contraction, and internal equipment. The allowances given by Onorato et al., originally from Brewer, are 2%, 0.9% and 0.6%, respectively, reducing the fillable volume to 96.5% [9, 35]. Furthermore, the fuel mass loaded needs to be 4.6% higher than the required fuel mass due to a 0.3% trapped fuel allowance and 4.3% residual fuel needed for pressurisation [9, 35]. The fuel is therefore never drawn below that 4.6% fraction to prevent a pressure spike from an emptying tank at the end of the extended mission.

With the governing insulation thickness, the tank provides 14.01 m^3 of usable volume, which allows for a max-

imum of 994.9 kg of LH_2 loaded, and a maximum mission fuel of 951.1 kg LH_2. Variant A required 847.5 kg, so the tank has a 12.2% fuel margin. The total tank structural mass adds up to 389.7 kg, consisting of 208.9 kg structural and 180.7 kg insulation mass. This gives a gravimetric index of $\eta_{grav} = 0.39$ (m_{tank}/m_{fuel}). This value is consistent with the study done by Onorato et al., giving gravimetric indices between 0.361 and 0.415 for regional aircraft [9].

6.4. Sensitivity

Author: Lisa

For this sizing, a venting pressure of $P_{vent} = 300$ kPa is taken, following the method from Onorato et al. [9]. However, the vent pressure is a design variable that balances the insulation size with shell mass, and it is interesting to analyse the result of the sizing for a range of values for P_{vent}. From literature, we can define a range of $P_{vent} = 172$ kPa [36] to $P_{vent} = 400$ kPa [37].

Table 6.1: Sensitivity Analysis for P_{vent}

P_{vent} **[kPa]**	t_{shell} [mm]	t_{ins} [cm]	m_{shell} [kg]	m_{ins} [kg]	$m_{LH2,max}$ [kg]	η_{grav}
172	1.042	35.14	72.4	352.2	631.1	0.673
200	1.339	27.19	104.3	286.1	771.8	0.506
225	1.591	22.91	131.3	247.3	854.2	0.443
250	1.836	19,94	157.6	219.1	914.0	0.412
275	2.078	17.78	183.3	197.8	958.9	0.398
300	2.318	16.08	208.9	180.7	994.9	0.392
325	2.557	14.73	234.3	166.9	1024.0	0.392
350	2.794	13.62	259.7	155.2	1048.4	0.396
375	3.031	12.73	284.7	145.8	1067.8	0.403
400	3.268	11.92	310.0	137.2	1085.7	0.412

The sensitivity analysis shows the optimum vent pressure is around 300-325 kPa, where η_{grav} is at its minimum of 0.392. This confirms that the 300 kPa used in the design is a good choice in this case. It is also well visible that the structural mass rises when the vent pressure rises, while the insulation mass rises when the vent pressure decreases. Below 250 kPa, the insulation becomes so thick that the tank is not able to load the required fuel anymore (847.5 for Variant A, for which 886.5 loadable volume is needed for pressure residual). The thick insulation in combination with the lower available volume, increases the gravimetric index. On the other hand, above 325 kPa, the structural mass dominates again and η_{grav} rises again.

There are some limitations to the model. The most significant one is that the outer geometry of the tank is found by maximising the enclosed volume that fits within the tailcone, independent of the fuel mass the aircraft requires. A tank sizing closer to Variant A's fuel requirement would get a higher fill fraction, and especially important for Variant B, a higher ρ_{mean}, lower ϕ and lower dP/dt. This can delay the vent time and/or lower the insulation thickness and therefore tank mass. The current result is thus a feasible and conservative design rather than a proven optimal solution. Ít is therefore recommended that the tank geometry should be sized against Variant A's fuel requirement with a target fill fraction, rather than just maximising the space available.

7

Detailed propulsion design

Author: Seán, Carlos

The propulsion system is one of the most critical systems in any aircraft; it is a critical driver of both the aircraft performance and efficiency. This section will describe the methodology and results of the propulsion design are explained. This is made up of two main components. First, the engine core. This is a gas turbine engine of which the methodology and results are described in Section 7.1. The second main component to be designed is the propeller. The methodology and design of this component are described in Section 7.2.

7.1. Core

Author: Seán *Contributors: Carlos*

First, the design of the engine core is looked at. This is a hydrogen gas turbine which will drive the propeller through a gas turbine. A two spool engine configuration is chosen where the propeller is connected to the low pressure compressor and turbine through a gearbox. Two compressor stages are necessary to achieve the required overall pressure ratio, which is why a single spool engine does not comply [40]. This leaves two viable options: first a three spool engine with a free power turbine, or a two spool engine where the power turbine drives the propeller and LPC. The latter option is chosen as it offers reduced complexity and weight through the reduction of the number of spools and turbine stages [40]. Additionally, this configuration has desirable characteristics for open-fan architectures [41]. Given the high cruise Mach number, this aircraft family resembles the operating conditions of open-fans, meaning these desirable characteristics should extend to this application.

Core methodology

In order to design the gas turbine core of the turboprop propulsion system, a simplified model is created. A visualisation of the components and the link between each is shown in Figure 7.1. Here the flow of the air between components is indicated with blue arrows, the flow of fuel with red arrows, and white links indicate mechanical links between components. To perform the analysis, each component within the system is independently modelled using simplified equations for flow throughout. Here there are five components which are modelled: the inlet, compressors, combustion chamber, turbines and heat exchanger. Importantly, the exhaust nozzle is not modelled, as almost no performance is extracted from the exhaust flow in turboprop engines. As explained by N. Grech [42], hydrogen fuel has to be heated up before injection into the combustion chamber in order to avoid icing issues. It is found that using a recuperator to exchange heat with the exhaust flow offers the best improvement in efficiency. Hence, this concept is also chosen for our design. This concept has both positive and negative effects on engine efficiency. Pressure is lost through the heat exchanger, which means less pressure can be extracted through the turbine stages as the LPT can not expand the airflow all the way to ambient conditions. This leads to slightly reduced efficiency, however, the heat exchanger also improves efficiency by heating up the fuel. Additionally, the heat exchanger introduces additional weight.

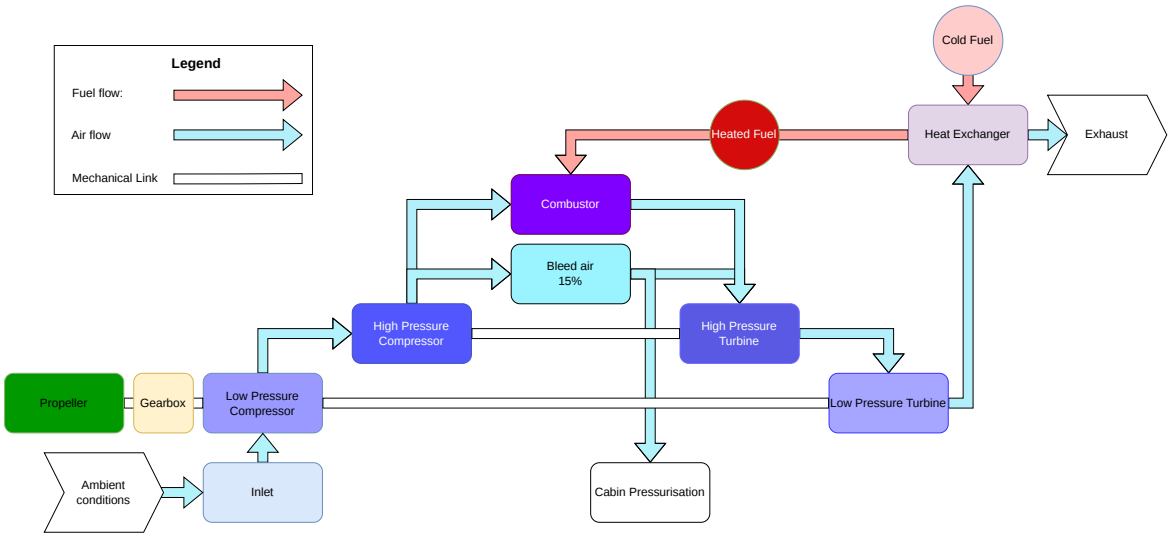

Figure 7.1: Turboprop cycle visualisation

The model for the inlet is based on the diffuser efficiency, r_d. Here, Equation 7.1 and 7.2 describe the rise in temperature and pressure as the flow decelerates through the inlet.

$$\frac{T_{\text{out}}}{T_{\text{amb}}} = \left(1 + \frac{\gamma - 1}{2} M^2\right), \tag{7.1}$$

$$P_{\text{out}} = P_{\text{amb}} \left(1 + \frac{\gamma - 1}{2} \text{M}^2\right)^{\frac{\gamma}{\gamma - 1}} r_d. \tag{7.2}$$

The operation of the compressor can be modelled based on the polytropic efficiency, η_p, as described by E.S. Richardson[43]. The pressure rises through the compressor stages and is based on the defined pressure ratio. Following this, the temperature rise through the compressor can be determined with Equation 7.3. From here, the power required to drive the compressor can be determined with Equation 7.4 based on the temperature rise.

$$\frac{T_2}{T_1} = \left(\frac{p_2}{p_1}\right)^{(\gamma-1)/(\gamma\eta_p)}, \tag{7.3}$$

$$P_{required} = \dot{m} C_p (T_{out} - T_{in}). \tag{7.4}$$

The turbine is modelled similarly, however, here the required power output is determined based on the power balance on each shaft first. The LPT power, with Equation 7.5, based on the low speed shaft balance. The HPT power, with Equation 7.6, based on the high speed shaft power balance. Following this, the temperature drop across each turbine stage can be determined with Equation 7.7 given the required power output. Finally, the pressure drop, with Equation 7.8.

$$P_{LPT} = P_{LPC} + P_{\text{shaft}}, \tag{7.5}$$

$$P_{HPT} = P_{HPC}, \tag{7.6}$$

$$P_{produced} = \dot{m} C_p (T_{in} - T_{out}), \tag{7.7}$$

$$\frac{T_2}{T_1} = \left(\frac{p_2}{p_1}\right)^{\eta_p(\gamma-1)/\gamma}. \tag{7.8}$$

For the combustion chamber model, a goal for the turbine entry temperature is determined later in the report when the core operating conditions are defined. With this value, the required fuel flow is given by Equation 7.9. Here, the fuel flow follows from the required energy input to raise the flow out of the combustor to the required temperature. The pressure drop across the combustion chamber is determined based on the methodology described by E.S. Richardson [43]. The pressure drop is then computed with Equation 7.10.

$$\dot{m}_a c_{p,a} (T_{\text{ref}} - T_{\text{in}}) - \dot{m}_f LCV + \dot{m}_p c_{p,p} (T_{\text{out}} - T_{\text{ref}}) = 0, \tag{7.9}$$

$$\Delta P = \frac{1}{2} \rho V^2 \left(\frac{T_{\text{out}}}{T_{\text{in}}} - 1\right). \tag{7.10}$$

Some additional considerations have to be made for the airflow. First of all, a part of the flow from the HPC is extracted as bleed flow. This value was determined to be 15%, as found by B. Liu[44]. A small part of this flow has to be extracted. As specified by CS 25 [7], 0.25 kg per minute of airflow into the cabin is required per passenger. The remaining bleed flow is reintroduced into the core as cooling flow at the HPT in order to keep the turbine blades at the correct temperature. This flow is modelled by separately expanding to the HPT exit pressure, after which it mixes with the hot flow before entering the LPT.

In order to model the heat exchanger, a simplified model is used, as described by N. Grech [42]. Here the fuel exit temperature can be determined with Equation 7.11, where C is the flow capacity as of Equation 7.12. Here, C_{min} is the minimum value of the hot and cold flow. Finally, the exit temperature of the exhaust flow can be determined with Equation 7.13. In this process, a heat exchanger efficiency, ε, of 0.35 is chosen as a conservative estimation for the range given.

$$\varepsilon = \frac{C_c(T_{c,\text{out}} - T_{c,\text{in}})}{C_{\min}(T_{h,\text{in}} - T_{c,\text{in}})}, \tag{7.11}$$

$$C = C_p \dot{m}, \tag{7.12}$$

$$C_{p_{H_2}} \dot{m}_{H_2} \cdot \Delta T_{H_2} + C_{p_{air}} \dot{m}_{air} \cdot \Delta T_{H_2} = 0. \tag{7.13}$$

Throughout this process, the specific heat capacity, C_p and the specific heat ratio, γ, have to be known. However, these values vary with temperature. The values are determined with Equation 7.14 and 7.15, based on the methodology described by NASA[1]. Here, Θ is a reference value, which is equal to 3056 K. Here it is assumed the the mix of combustion products and air flow can be modelled the same as air since hydrogen only makes up a very small proportion of the flow. However, in the future, the accuracy of this assumption should be checked to ensure the increases air humidity caused by the hydrogen combustion does not affect this assumption.

$$c_p = (c_p)_{\text{perf}} \left\{ 1 + \frac{\gamma_{\text{perf}} - 1}{\gamma_{\text{perf}}} \left[\left(\frac{\Theta}{T} \right)^2 \frac{e^{\Theta/T}}{\left(e^{\Theta/T} - 1 \right)^2} \right] \right\}, \tag{7.14}$$

$$\gamma = 1 + \frac{\gamma_{\text{perf}} - 1}{1 + (\gamma_{\text{perf}} - 1) \left[\left(\frac{\Theta}{T} \right)^2 \frac{e^{\Theta/T}}{\left(e^{\Theta/T} - 1 \right)^2} \right]}. \tag{7.15}$$

Finally, it is assumed that the pressure at the exit of the heat exchanger is equal to ambient conditions, meaning the flow is fully expanded. This allows for an iteration loop to be set up to determine the required air mass into the engine. The iteration goes as follows:

Algorithm 1: Engine design iteration procedure

Result: Perform propulsion iteration
Assume initial air mass flow and injection temperature;
while *Air mass flow and fuel injection temperature are not converged* **do**
    Perform inlet calculations;
    Perform compressor calculations;
    Perform combustion chamber calculations;
    Perform turbine calculations;
    Perform heat exchanger calculations;
    Update fuel injection temperature;
    Update air mass flow based on the difference between exhaust pressure and ambient pressure;
end
Compute final parameters;

Core operating conditions

The model is now established and the parameters within it have to be determined. To determine the overall pressure ratio (OPR) and turbine entry temperature (TET) some historical trends were analysed. Based on H. Acar et al.[45], OPR and TET were estimated to be roughly 27 and 1800 K respectively. For this, however, aircraft cruise is the most constraining flight condition. This means that the TET has to be considered to be lower for these continual operations. Based on the gas turbine described by F. Tiemstra [46], the TET at cruise is estimated to be roughly 13% lower than take-off. This allows the determination of a corrected cruise TET of 1560 K. Additionally, the limits in pressure ratio created by the size of this engine have to be considered. After a discussion with an expert[2], it is found that the size of the compressor blades limits the overall pressure ratio as tip losses make a high pressure ratio impractical. Therefore, a decision to choose a slightly lower OPR of 22.0. The pressure ratio for the LPC and HPC is determined for the given overall pressure ratio through an analysis in GasTurb[3], which gave an LPC pressure ratio of 2.66 and an HPC pressure ratio of 8.26. Finally,

[1] `https://www.grc.nasa.gov/www/BGH/realspec.html`, *Accessed: 01/06/2026*
[2] Discussion with Prof.dr. Arvind Gangoli Rao, dd. 04-06-2026
[3] Gasturb is an industry software package used to analyse and optimise gas turbine pereformance

the compressor and turbine polytropic efficiencies are determined based on a reference [46], from which the compressor polytropic efficiencies are found to be 0.91 and the turbine polytropic efficiencies 0.93. These values are assumed to be constant across the different operating conditions.

In order to correctly scale the aircraft power with the operating altitude and cruise mach number, GasTurb is once again used as reference. The air mass flow is determined for the design cruise condition, in addition to Take-off and Climb. This allows for a comparison of the air mass flow results and allows the implementation of the design conditions within iteration without the need for GasTurb. This is done by scaling the air mass flow based on the necessary flight condition.

Table 7.1: Main core parameters

Configuration:	**Unit**	**Cruise**	**Take-Off**	**Climb**
Overall pressure ratio	[-]	22.0	19.8	21.1
LPC Pressure ratio	[-]	2.66	2.65	2.66
HPC pressure ratio	[-]	8.26	7.48	7.94
Compressor polytropic efficiency	[-]	0.91	0.91	0.91
Turbine polytropic efficiency	[-]	0.93	0.93	0.93
Turbine entry temperature, TET	[K]	1560	1600	1572
Air mass flow	[kg/s]	8.00	14.80	10.76

Core staging

To finalise the design of the core , a preliminary estimation is made of the stages per core section. This is done by estimating the work coefficient, ψ, for each core section. These values can be found in Table 7.2. The enthalpy change per stage is calculated with Equation 7.16, where the blade speed is estimated based on the limit on the tip Mach number and the stage air temperature. Following this, the number of stages can be estimated based on the total enthalpy change over the section [43].

$$\Delta h_{0_{stage}} = \psi \cdot U^2, \tag{7.16}$$

$$\Delta h_{0_{section}} = C_p(T_{out} - T_{in}). \tag{7.17}$$

Table 7.2: Engine stage results

Section:	**work coefficient**, ψ	**number of stages**
LPC	0.43	3
HPC	0.43	6
HPT	1.4	1
LPT	1.6	2

7.2. Propeller design

Author: Carlos Contributors: Seán

Following on the final design detailed in Chapter 2, a propeller design is needed to complete the propulsion system design. Propeller design is notorious for its complexity, it requires additional considerations such as the differences in airflow velocity at different points in the blade. Blade element theory (BET) forms the basis for a modern analysis of turboprop rotors, because it provides estimates of the radial distributions of blade aerodynamic load over the rotor disk. BET slices the blade into smaller sections radially, then these act as a quasi-2D airfoil to produce aerodynamic force. Corrections can also be applied to take into account tip losses and three dimensional effects. One of the main limitations of BET is that it has no physical mechanism to calculate the induced velocity due to the effect of the other rotating blades. First envisioned in the 1940s by Gustafson and & Gessow, a new methodology was proposed by which momentum theory could be used to complement BET. Momentum theory describes the rotor as an infinitely thin disc, inducing a constant velocity along the axis of rotation [4]. From there an induced velocity can be calculated, so as to obtain the net thrust and

[4] `https://en.wikipedia.org/wiki/Momentum_theory`, *Accessed: 01/06/2026*

power from BET, forming the (Blade Element Momentum Theory) BEMT method.

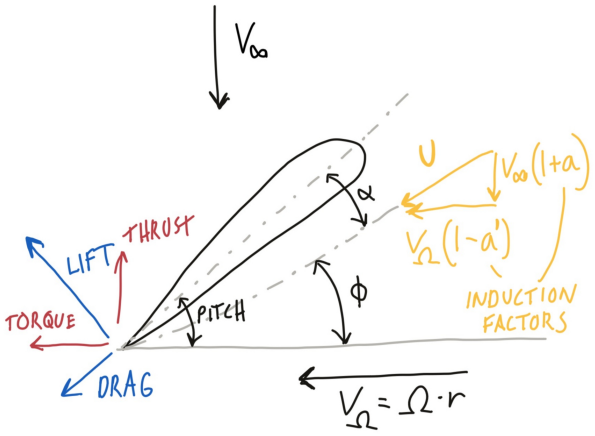

Figure 7.2: Rotor force diagram

Consider a propeller blade element at a distance r with thickness dr. Starting from the actuator disk concept, far upstream there is V_∞, at the rotor disk the flow is disturbed, defining $V_x = V_\infty + v_i$ as the axial induced velocity, where v_i is negative in the sign convention used in propeller theory [47]. A key concept in BEMT is the induction factors, these allow us to modify the incoming velocity to something that resembles the flow affected by downwash.

$$a = \frac{-v_i}{V_\infty}, \tag{7.18}$$

so the *Axial velocity through disk* is defined by Equation 7.19.

$$V_x = V_\infty(1 - a). \tag{7.19}$$

As for the tangential velocity it is composed by the radial velocity and the induced swirl as shown in Equation 7.20

$$\begin{aligned} V_\theta &= \Omega R + {v_\theta}^{ind}, \\ a^{'} &= \frac{{v_\theta}^{ind}}{\Omega R}. \end{aligned} \tag{7.20}$$

The tangential velocity (in rotor plane) is given by Equation 7.21

$$V_\theta = \Omega R(1 + a^{'}). \tag{7.21}$$

The resultant relative velocity is given by Equation 7.22

$$U = \sqrt{V_x^2 + {V_\theta}^2}. \tag{7.22}$$

From Figure 7.2, it can be seen that the local inflow angle can be expressed from the local velocities as:

$$\tan(\phi) = \frac{(1-a)\Omega R}{(1+a')V_\infty}.$$

Forces acting on the rotor section can be written as given in Equation 7.23:

$$\begin{aligned} \Delta T &= \sigma\pi\rho U^2 C_T r \Delta r, \\ \Delta Q &= \sigma\pi\rho U^2 C_Q r^2 \Delta r, \end{aligned} \tag{7.23}$$

Here $\sigma = Bc/(2\pi R)$ is the rotor solidity. Thrust and torque coefficients can be calculated from the following expressions using tabulated values for the 2D airfoil's C_l and C_d using the local angle of attack for the section:

$$\alpha = pitch - \phi, \tag{7.24}$$

$$C_T = C_l \cos\phi - CC_d \sin\phi, \tag{7.25}$$

$$C_Q = C_l \sin\phi + CC_d \cos\phi. \tag{7.26}$$

Combining the equations leads to the induction factors:

$$a = \frac{1}{\kappa - C}, \qquad a' = \frac{1}{\kappa' + C},$$

$$\kappa = \frac{4\sin^2\phi}{\sigma C_T}, \qquad \kappa' = \frac{4\sin\phi\cos\phi}{\sigma C_Q}.$$

To find a solution at each stage, a root finding method can be used to find ϕ, leading to a calculation of the induction factors allowing for the calculation of the forces at each section, which can be integrated along the rotor length. Additional corrections are needed to complete the BEM method. BEMT assumes an infinite number of blades to create the actuator disk being modelled by Momentum theory. In reality a finite number of blades leads to tip vortices where high pressure air leaks:

$$f = \frac{B \cdot \Delta r}{2 \cdot r \cdot \sin\phi}, \qquad F = \frac{2\arccos(e^{-f})}{\pi}. \tag{7.27}$$

Finally, a 3D stall delay correction is applied, C_l, C_d data is typically measured in 2D wind tunnels where the flow is purely chord-wise, on a rotating blade centrifugal forces move the boundary layer air radially outward [48]. The corresponding delay in flow separation allows the inner blade section to experience higher lift ant high angles of attack before stalling than 2D predictions.

$$C_{l_{inv}} = \sqrt{{C_{l_{2d}}}^2 + C_d^2}, \tag{7.28}$$

$$C_{l_{3D}} = C_{l_{2D}} + a\left(\frac{c}{r}\right)^h \cos\theta^n (C_{l_{inv}} - C_{l_{2d}}). \tag{7.29}$$

where a=2.2, h=1.3, n=4 are empirical constants given by Chaviaropoulos [48].

Planform shaping

Once the methodology has been chosen, the shape of the propeller can start to be defined. There are three main variables that define the shape of a blade,

- Twist
- Chord size
- Sweep

Because BEMT is being used, these variables have to be defined for each cut performed along the blade radius.

Twist

Twist is applied to try to match the ideal AoA of the airfoil to that of the blade section. To achieve this the a new relative velocity must be computed for the incident air flow onto the blade section.

$$\phi = rpm \cdot \frac{(2\pi)}{60},$$

$$\alpha = \arctan\left(\frac{V_\infty}{\omega \cdot r}\right),$$

$$Twist = \alpha_\infty + \alpha_{opt}. \tag{7.30}$$

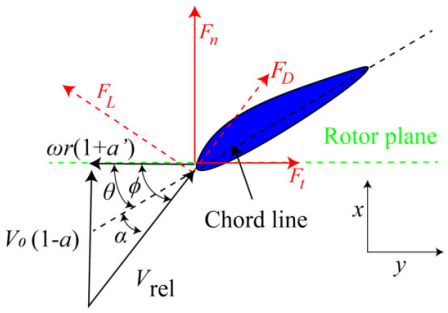

Figure 7.3: Twist angle

Twist is therefore independent of chord geometry and just dependent on airfoil selection and rpm.

Chord Size

Chord size is the most complicated of all of the geometric variables, its value at each stage can vary the performance and there is no direct recipe for what works best. Therefore, an optimization algorithm is implemented to reduce the design search space. Furthermore, a spline is defined by means of a 3rd order polynomial, the coefficients where then fed as the design variables of the optimization. As for the algorithm itself, a differential evolution was chosen. It is a population-based optimization algorithm primarily used to find the global minimum or maximum. The algorithm works as follows:

1. **Initialization**
   An initial number of candidate solutions (a population) is chosen which covers the entire design space.
2. **Mutation**
   To create a new direction to explore, the algorithm picks three random vectors from the population X_1, X_2, X_3 and it calculates the difference between them and applies a factor F. It then adds the difference to the third vector X_1 to create a mutant vector.

   $$\text{Mutant} = X_1 + F \cdot (X_2 - X_3)$$

   One of the main benefits of this algorithm is that if the population is initially very far apart it will take big steps to converge, but once it has converged it will automatically refine the search.
3. **Crossover**
   It then mixes these new coefficients with an existing spline to create a brand new candidate spline shape. This is controlled by the Crossover Probability which decides whether to keep the original value or the mutated one.
4. **Selection**
   Finally, the algorithm evaluates a specific objective function (in this case the efficiency of the propeller) for both the original target vector and the new trial vector, should the trial vector yield a better result, it replaces the old one in the next generation.[5]

The main benefit of this algorithm is that it does not care about gradients or derivatives and therefore has a lesser chance of landing on a local minima or maxima. Additional constraints have been set to the coefficients of our 3rd order polynomial to ensure that the populations being generated followed some structural and power constraints based on the mission. The following input data is fed into the algorithm to be used to compute the efficiency for each population.

```
[case]
rpm = 1000
v_inf = 205.36

[rotor]
nblades = 6
diameter = 4.05
radius_hub = 0.2
section = NACA_63815 NACA_63815 NACA_63815 NACA_63815 NACA_63815 NACA_63815 NACA_63815 NACA_63815 NACA
    _63815 NACA_63815
```

[5] https://medium.com/@reshma_shaji/differential-evolution-what-it-is-and-how-does-it-work-81d3415c2367

```
radius = 0.2 0.3825 0.565 0.7475 0.93 1.1125 1.295 1.4775 1.66 1.8425
pitch = 88.1767967341275 82.96318568133903 77.92783604884629 73.13462059042304 68.62817603588574
    64.43401166578806 60.56098762918913 57.004986117055914 53.75277481861629 50.7854321242995

[fluid]
mu = 1.802e-5

[additionaldata]
machnumber = 0.62
altitude = 25000
numberofstations = 10
%
```

Resulting in the following chord lengths at each stations shown in Figure 7.4:

```
    chord = 0.321 0.321 0.316 0.305 0.291 0.275 0.259 0.244 0.230 0.221
```

One final correction has to be applied to ensure that all of the sections are subsonic. The current implementation of BEMT assumes that the flow is not only subsonic but outside of the transonic regime, therefore a correction is applied to ensure compliance. The main issue with the analysis that is performed is the assumption that the sweep being applied does not affect the performance of the blade. Further research should focus on applying a correction factor for this effect.

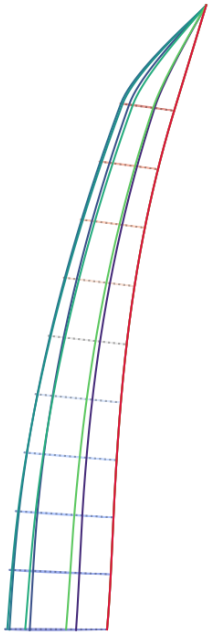

Figure 7.4: Blade geometry

Pitch correction

One of the main assumptions of turboprops is keeping constant rpm, this allows for a constant speed propeller. Constant speed propellers provide improved efficiency and performance while reducing the engine's wear[6]. This leads to some issues though it means that the propeller, if not modified, would perform the same at all flight conditions. To mitigate this, the pitch of the propeller blades can be varied to ensure optimal performance at all stages of the flight. Figure 7.5 represents the adjusted pitch of the entire bled to ensure enough power at all flight phases and altitudes, while also maximising efficiency.

[6] https://hartzellprop.com/3-key-benefits-constant-speed-propellers/

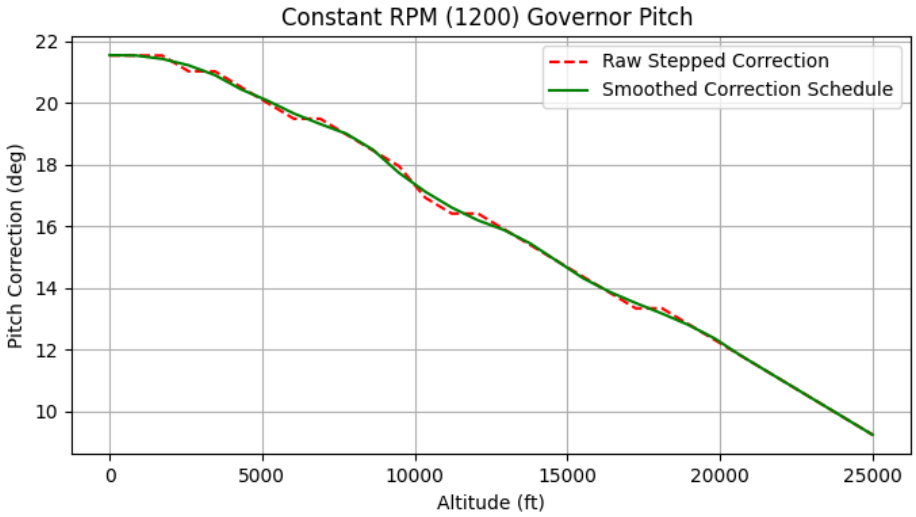

Figure 7.5: Pitch Governor

Detailed engine render

Based on the presented propulsion system results a model of the turboprop engine could be created. Integration into the wing is made through a nacelle housed inside the wing. Propeller is attached to the shaft driven by a low pressure spool via a gearbox.

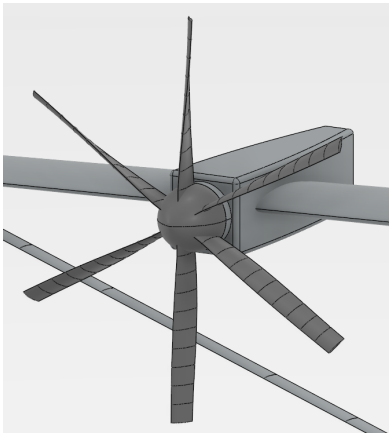

Figure 7.6: CATIA model of a 6 Blade Turboprop Engine integrated into the wing structure. NACA 63815 cross-section is used. Pitch angle and chord are varied along 10 propeller blade sections.

Noise analysis

In order to ensure the aircraft is allowed to operate at airports, it has to be ensured it meets noise requirements. These requirements are described by ICAO annex 16, volume I, chapter 14[49]. Here it can be seen that three different requirements must be met: lateral/full power, approach and flyover. As described by Equation 7.31[7], propeller noise can be scaled by the tip Mach number. Hence, the propeller noise of the LEAF family can be estimated relative to a reference. For this reference, the ATR 72 was selected, for which the noise specifications can be found in Table 7.3, 7.3.[8] The rpm and blade diameter of the ATR-72 are 1200 and 3.93 m respectively, as specified by Y. Teeuwen [50]. For the LEAF family, the rpm and diameter are 1000 and 4.05 m respectively. This allows the tip mach number to be estimated for each, after which the ATR 72 noise can be scaled to the LEAF family to estimate the noise. The results from this analysis can be found in Table 7.4, where the requirements and margins are also specified. For the purpose of this calculation, it is assumed that the forward velocity is relatively small at the specific flight conditions compared to the rotational velocity.

[7] `https://eaglepubs.erau.edu/introductiontoaerospaceflightvehicles/chapter/propellers/`, *Accessed: 19/06/2026*
[8] `https://eco-profi.info/download_dBA/samolet/013_icao_atr72.pdf`, *Accessed: 19/06/2026*

$$\mathrm{SPL} \propto 10\log_{10}(W) \propto 60\log_{10}(M_{\text{tip}}). \tag{7.31}$$

Table 7.3: ATR 72 reference noise

	Lateral/Full-Power	Approach	Flyover
Noise Level (EPNdB)	86.3	94.4	85.7
Noise Limit (EPNdB)	94	98	89
Noise margin (EPNdB)	7.7	3.6	3.3

When comparing the ATR and the LEAF family, it can be concluded that there is a large margin between both. Hence, the assumptions should not affect the conclusion that the requirements will be met.

Table 7.4: LEAF family noise

	Lateral/Full-Power	Approach	Flyover
Estimated noise Level (EPNdB)	82.4	90.5	81.8
Noise Limit (EPNdB)	94	98	89
Estimated margin (EPNdB)	11.6	7.5	7.2

8

Final design solution

Author: Marius, Seán

In this chapter, the convergence script is provided, followed by the final data, from which requirement compliances can be verified. The convergence script is shown in Section 8.1 and the (sub-)system sizing algorithms are shown in Section 8.2. Then, a sensitivity study is performed on the effect of cruise altitude on fuel consumption. This serves to validate the altitude requirement in the context of the Mission Need Statement. This is done in Section 8.3. At the end of the chapter, in Section 8.4, several tables display all the values resulting from the script.

8.1. Overall convergence script

Author: Marius, Seán

In order to synthesise all the new methodologies and designs from the previous chapters, a convergence script is written in Python. A pseudo-algorithm is shown in algorithm 2. A family design is considered to be converged when the 'Cost' is below the 'Target'. Cost is evaluated for the values of variant A, according to Equation 8.1. It is worth noting, that according to the family design philosophy, wing area and horizontal tail area are the same. To complement the cost function, a maximum iteration number (100) is also added, and a tracking function is returned at the end of the iteration to track other key parameters (such as LEMAC location) over time. The design hence is considered 'converged'. The data provided in Table 8.2 is based on Target $= 0.005$. It typically converges in 10 minutes and takes 10-15 iterations for the current target value. Given the approximative nature of the methods, a sum of 0.5% relative difference between the key values in Equation 8.1, along with the tracker plot is considered sufficient. Verification and validation for the code is provided later in Chapter 9.

$$\text{Cost} = \left|\frac{\text{MTOM}_{i-1} - \text{MTOM}_i}{\text{MTOM}_i}\right| + \left|\frac{S_{i-1} - S_i}{S_{i-1}}\right| + \left|\frac{S_{H_{i-1}} - S_{H_i}}{S_{H_{i-1}}}\right| \tag{8.1}$$

Algorithm 2: Final Design Sizing

Result: Final aircraft data
Initialise aircraft *A* and *B* ; ▷Output Midterm report
Initialise high lift devices for *A* and *B*; ▷Consult algorithm 3
Initialise matching data for *A* and *B* ; ▷Consult algorithm 4
while *Cost* > *Target* **do**
  Update matching for *A* and *B* ; ▷Consult algorithm 4
  Update mass estimates for *A* and *B* ; ▷Consult algorithm 5
  Update empennage geometry for *A* and *B* ; ▷Consult algorithm 6
  Update wing geometry for *A* and *B* ; ▷Consult algorithm 7
  Update landing gear positioning for *A* and *B* ; ▷Consult algorithm 9
  Update profile drag estimates for *A* and *B* ; ▷Consult algorithm 10
  Update fuel estimates and MTOM for *A* and *B* ; ▷Consult algorithm 11, algorithm 8
  Determine cost ; ▷Consult Equation 8.1
end
Refine fuselage mass for *A* and *B* ; ▷Consult Chapter 5
Size control surfaces for *A* and *B* ; ▷Consult Section 4.8

Before the 'while loop', the aircraft are initialised and a preliminary sizing of the high lift devices is performed in order for inputs for the matching diagram iteration. Indeed, HLD configurations for various flight segments are necessary to compute the necessary wing loading and specific power. There is no explicit method to resize engine mass; a power estimate is refined during algorithm 4.

It is noted that a 'Refine fuselage mass' module is implemented after the loop. This is a minor part (< 5%) of the fuselage mass which costs a very significant computation time. It refers to Section 5.4. A conservative initial assumption from previously run trials is used during the 'while loop'. Given the minor fraction and conservative value, this simplification is considered acceptable.

8.2. Family updates

Author: Marius, Seán

The design philosophy used was to size for the 'critical' aircraft which constrained a particular value, and apply it to the other aircraft. This was applied for wing design, empennage design, engine design, fuselage section design and landing gear design.

Algorithm 3: Update high-lift devices

Result: HLD compliance and sizing with requirements
Assign single fowler flaps and slats to variant *A*;
Assign single slotted flaps and slats to variant *B*;
for *All variants* **do**
  for *Landing, Take-Off, Cruise conditions* **do**
    Compute S_{HLD}/S ; ▷Consult Section 4.6
    Compute $C_{L_{max}}$; ▷Consult Section 4.6
    Compute V_{s1g} ; ▷Consult Section 4.6
  end
end

It is noted that the high lift device (HLD) systems on board differ between the two variants. There is precedent for this choice in the industry with the A320 family being an example. The stretched A321 variant has double fowler flaps, whereas the other members have single fowler flaps. This was the only case where the aircraft variants differed. The corresponding wing sizing from the matching diagram would account for the variant's respective resultant lift coefficients[1].

Algorithm 4 uses the exact same strategy from the *Midterm report* for finding the power and wing loading which satisfied climb gradient, rate, and LTO requirements. The EOM buildup, as described by algorithm 5, synthesises several chapter conclusions and stores them in the general aircraft objects.

[1]This applies to the A321 CEO version,https://www.airbus.com/en/products-services/commercial-aircraft/passenger-aircraft/a320-family, (Accessed: 17/06/2026)

Algorithm 4: Update matching diagram

Result: S_{ref} and P_{req}
for *All variants* **do**
  Find W/P, W/S, P_{req};
  if *Variant* $S_{ref} > S_{crit}$ **then**
    $S_{crit} = S_{ref}$;
  end
  if *Variant* $P_{req} > P_{crit}$ **then**
    $P_{crit} = P_{ref}$;
  end
end
for *All variants* **do**
  Assign S_{crit} and P_{crit};
  Check compliance with variant matching diagram;
end
for *All variants* **do**
  Compute engine parameters for cruise power requirement ; ▷Consult algorithm 1
  for *All power requirements* **do**
    Compute off design performance;
    if $P_{av} < P_{req}$ **then**
      Print 'error'. Re-start design cycle with different engine specifications or cruise altitude requirement;
    end
  end
end

Algorithm 5: Update masses

Result: EOM build-up
for *All variants* **do**
  Compute EOM position and value;
  Compute empennage mass;
  Compute wing mass ; ▷Consult Chapter 4
  Compute airframe mass ; ▷Consult Chapter 5
  Assume engine mass [9] and compute propulsion system mass;
  Compute landing gear mass;
  Compute internal systems (AC, oxygen, flight control, avionics) mass;
  Add hydrogen tank mass ; ▷Consult algorithm 11
  Compute miscellaneous masses (APU, furnishings, cargo equipment, paint);
end

Algorithm 6 is the most complicated algorithm for family design. The aircraft is sized for the largest horizontal tail area required to achieve control and stability margins between the two variants. This is achieved by assuming the quarter chord tail location, relative to the back of the tail cone. The wing position is hence constrained for both aircraft, in order to achieve a suitable 'tail length'. The surfaces of the empennage and their dimensions are then adjusted. A sizing of lateral stability for the vertical tail is beyond the scope of the study. Hence, the vertical tail is sized based on the tail volume of the ATR72. Finally, a constraint is added that the horizontal tail's root chord cannot exceed the tip chord of the vertical tail. Should the root chord exceed, it will be made equal to the vertical stabiliser's tip chord. This constraint is common for T-tail empennages.

Algorithm 6: Update empennage

Result: S_H, S_V, wing position, x_{cg} (front and aft)
for *All variants* **do**
  Find $x_{wingLEMAC}$ for lowest S_H/S ; ▷Consult Section 3.5
  Assign all positions;
  Find S_H;
  if S_H > $S_{H_{crit}}$ **then**
    $S_{H_{crit}}$ = S_H;
  end
end
for *All variants* **do**
  Assign $S_{H_{crit}}$;
  Update planform parameters for vertical and horizontal tails;
  Update vertical area (based on assumed V_V);
  if S_H > $S_{H_{crit}}$ **then**
    $S_{H_{crit}}$ = S_H;
  end
  if S_V > $S_{V_{crit}}$ **then**
    $S_{V_{crit}}$ = S_V;
  end
end
for *All variants* **do**
  Assign $S_{H_{crit}}$;
  Assign $S_{V_{crit}}$;
  Update planform parameters for vertical and horizontal tails;
end
if c_{r_H} > c_{t_V} **then**
  for *All variants* **do**
    c_{r_H} = c_{t_V} ;
    Update horizontal tail geometry;
  end
end

Given STKCX25 requires the aircraft's wingspan to not exceed 36 [m]. This is checked in this function and applied to all variants, allowing the aspect ratio to decrease from the target value of 20. In practice, this check was never necessary. A value of 35.998 [m] was selected to offer 1 [mm] on both sides of the aircraft.

Algorithm 7: Update wing

Result: Update wing geometry
for *All variants* **do**
  Compute wing geometry;
  if b > *36 m* **then**
    b = 35.998;
    Update wing geometry;
  else
    Ensure AR = 20 and update wing geometry;
  end
end

Algorithm 8 is very simple and merely adds all main values as a conclusion to an iteration.

Algorithm 8: Update MTOM

Result: MTOM
for *All variants* **do**
  $MTOM$ = sum(m_{fuel}, m_{crew}, m_{tank}, m_{pl}, EOM) ; ▷Consult Chapter 6 for fuel and tank mass
end

Algorithm 9: Update landing gear position

Result: Landing gear positioning (x, y, height)
Find longest aircraft: 'Critical aircraft';
for *All variants* **do**
  x_{NLG} = Nose length;
end
$\theta = 10°$;
$\beta = 20°$;
Find scrape point (x,z) of 'Critical aircraft' ; ▷Consult Section 3.7
Find Δx and h_{gear} of 'Critical aircraft'; ▷Consult Section 3.7
Find $\Delta x_{wing} = x_{MLG} - x_{wing}$ of 'Critical aircraft'; ▷Consult Section 3.7
for *All variants* **do**
  Assign h_{gear} for main and nose gear;
  Find and assign x_{MLG} using Δx_{wing};
  if $0.08 <$ *Nose load* < 0.15 **then**
    Print 'Error'. Re-start design cycle with different β angle;
  end
end
for *All variants* **do**
  Find y_{MLG} from $\Psi = 54.9°$; ▷Consult Section 3.7
  if $y_{MLG} > y_{MLG_{crit}}$ **then**
    $y_{MLG_{crit}} = y_{MLG}$;
  end
end
for *All variants* **do**
  Assign $y_{MLG_{crit}}$;
  if $\Phi > 54.9°$ **then**
    Print 'Error'. Re-start design cycle with different β angle;
  end
end

Algorithm 9 is very complicated given that commonality of the landing gear sizing should be implemented. Landing gear represents just under 10 % of the EOM and is hence not negligible.

The nose landing gear position is fixed at the end of the nose for both aircraft, which means the nose fuselage section is common between the variants. The main landing gear is positioned relative to the wing location for both aircraft. This is to say, the wheel track is common between the variants, and the longitudinal distance between the main gear and the wing's LEMAC is constant. This allows for a common wing-fuselage connection section between the variants. The actual compliance to angles as established in Section 3.7 is checked but no particular measures are implemented automatically by the script.

Algorithm 10 is a simple algorithm to update profile drag and Oswald efficiency values for the newly iterated geometry. The aircraft are treated separately.

Algorithm 10: Update profile drag estimates

Result: C_{D_0}, e
for *All variants* **do**
  for *Cruise, Take-off, Landing flight condition* **do**
    Compute C_{D_0} ; ▷Consult Chapter 3
    Compute e;
  end
end

Fuel estimates are based on the methodology introduced in Chapter 6 which uses Breguet range for various flight segments, based on the mission profile. In order to achieve commonality, a single tank is sized for the two variants, even though on variant B, it is not filled to the same level.

Algorithm 11: Update fuel estimates

Result: m_{fuel}, m_{tank}, x_{tank}
for *All variants* **do**
  Run tank sizing ; ▷Consult Chapter 6
  if $m_{fuel} > m_{fuel_{crit}}$ **then**
    $m_{tank_{crit}} = m_{tank}$
  end
  Assign m_{fuel};
  Assign $m_{tank_{crit}}$;
end

8.3. Sensitivity study

Author: Marius *Contributor: Seán*

A sensitivity study on the effect of cruise altitude on fuel mass was performed. The cruise altitude was changed during the initialisation of the aircraft variant. The altitude mainly affects cruise drag, which in turn affects fuel and power required. On the counterpoint, the regional range of the aircraft (climbing time is larger fraction of higher altitude flights), as well as available power from thinner air limits fuel efficiency benefits and aircraft performance, respectively. Running the code for an evolving cruise altitude reflects this. For slightly different converged dimensions (S_{ref} changes by 2 m^2 between FL180 and FL300 designs, for example), the conclusions are demonstrated in Table 8.1.

Table 8.1: Altitude Sensitivity Study. M = 0.62

Design cruise altitude [ft]	Block fuel variant A [kg]	Block fuel variant B [kg]
16,000	876	639
19,000	863	627
22,000	850	615
23,000	847	612
25,000	840	605
27,000	833	599
28,000	830	596
29,000	827	593
30,000	824	590
31,000	821	587
32,000	P not met	P not met
33,000	P not met	P not met

It can be observed, that it is recommended for the aircraft to fly higher to deliver some fuel consumption benefits. Nonetheless, according to the script, the actual benefits are very marginal, especially with respect to STKCX02 (FL250 cruise is achievable). Flying at FL310 compared to FL250 reduces block fuel by 2.3 % for variant A and up to 3.0 % for variant B. The exact altitude where power requirements are no longer met across all flight conditions is not computed, and can be subject to further study. Sensitivity to higher cruise speeds can also be an interesting subject of study, though it is likely to increase block fuel as transonic flow regimes are reached beyond Mach 0.62.

8.4. Data

Author: Marius, Lisa, Daan, Seán *Contributor: Nathan*

All dimensions and performance data is presented in Table 8.2. Aerodynamic coefficients and specific structural dimensions were already specified in previous chapters.

Table 8.2: Converged Results

Parameter	Unit	A (84 PAX, 1,500 km)	B (58 PAX, 1,300 km)
Masses			
Maximum Take-Off	kg	21,810	17,670
Operational Empty	kg	12,080	10,780
Payload	kg	8,400	5,800
LH_2 fuel	kg	840	605
Tank	kg	390	390
Fuselage airframe	kg	2,650	2,120
Wing	kg	1,500	1,500
Horizontal tail	kg	100	100
Vertical tail	kg	170	170
Landing gear (nose and main)	kg	980	980
Propulsion system	kg	350	340
Flight control system	kg	380	330
Electrical system	kg	510	470
Avionics	kg	200	200
Air conditioning	kg	640	460
Oxygen system	kg	60	45
APU	kg	185	185
Furnishings	kg	1,570	1,120
Cargo equipment	kg	19	11
Airframe paint	kg	98	80.
Crew (2 pilots, 2 attendants)	kg	400	400
Major Aerodynamic coefficients			
Zero-lift drag coefficient	-	0.0435	0.0417
Oswald efficiency factor	-	0.67	0.67
Lift-to-drag ratio	-	15.6	15.9
Wetted area	m^2	397	353
Fuselage parameters			
Fuselage length	m	33.65	29.05
Cabin length	m	20.28	15.66
Nose length	m	3.75	3.75
Nose cone length	m	5.50	5.50
Tail length	m	2.06	2.06
Tail cone length	m	9.62	9.62
Landing gear parameters			
Gear height (Nose and main)	m	1.56	1.56
MLG longitudinal position	m	16.9	15.0
MLG lateral position	m	2.9	2.9
NLG longitudinal position	m	3.75	3.75
Engine specifications			
Engine Mass	kg	820	820
Available shaft power at cruise	kW	4,690	4,690
Available shaft power at take-off	kW	7,380	7,330
Average available shaft power at climb	kW	5,060	5,050
Thermal efficiency at cruise	-	0.423	0.430

Table 8.2 – *Continued from previous page*

Parameter	**Unit**	**A** (84 PAX, 1,500 km)	**B** (58 PAX, 1,300 km)
Thermal efficiency at take-off	-	0.366	0.370
Thermal efficiency at climb	-	0.363	0.369
Wing parameters			
Wing loading	N/m^2	4,800	3,890
Wing area	m^2	44.7	44.7
Wing span	m	29.7	29.7
Aspect ratio	-	20	20
Root chord	m	2.05	2.05
Tip chord	m	0.94	0.94
Taper ratio	-	0.46	0.46
LEMAC position	m	14.7	12.8
MAC	m	1.56	1.56
Horizontal tail parameters			
Horizontal tail area	m^2	8.22	8.22
Horizontal tail span	m	6.41	6.41
Aspect ratio	-	5	5
Root chord	m	1.60	1.60
Tip chord	m	0.80	0.80
Taper ratio	-	0.46	0.46
Quarter chord position	m	32.7	28.1
MAC	m	1.34	1.34
Quarter chord sweep	degrees	4.0	4.0
Spanwise MAC position	m	2.94	2.94
Vertical tail parameters			
Vertical tail area	m^2	11.6	11.6
Vertical tail height	m	4.81	4.81
Aspect ratio	-	2	2
Root chord	m	3.2	3.2
Tip chord	m	1.6	1.6
Taper ratio	-	0.5	0.5
Quarter chord position	m	31.9	27.2
MAC	m	2.49	2.49
Quarter chord sweep	degrees	15.0	15.0
Spanwise MAC position	m	2.4	2.4

9

Verification and Validation Campaign

Author: Viktor, Toine, Daan *Contributors: Marius*

In this chapter, the verification and validation (V&V) procedures will be described. First, the mission will be verified and validated. Only then will the design procedures behind the Strut-Braced Wing (SBW) final concept be presented as blocks in a Code Flow Block Diagram. The separate blocks of this diagram will be tested in a structured way via a number of unit tests, after which all verification procedures on the Sustainable Aircraft Family design tool will be described. Finally, the method behind the validation of several blocks will be explained, results will be provided, and recommendations will be provided on how the validation can be further expanded.

9.1. Mission V&V

Author: Daan *Contributors: Viktor*

Before the model can be verified and validated, a V&V procedure for the mission is outlined. Starting with the verification, there are four methods to verify the mission, those being: analysis, demonstration, inspection, and tests. In the baseline report, the verification of all requirements has already been given [51]. Then in the midterm report [3], the most relevant mission requirements were encapsulated in the trade-off criteria: environmental impact, commonality, direct operating cost (DOC), turnaround time (TAT) and risk.

A killer stakeholder requirement was STKCX12: ”The aircraft shall reduce well-to-wake CO_2 emissions by 80% versus an Embraer 175 (or similar) on nominal missions, for equal payload/range combinations.” This is verified by either testing or analysis. To perform an analysis, the Sustainable Aircraft Family design tool was created and updated to determine carbon dioxide (CO_2), nitrogen oxides (NO_x), non-volatile particulate matter (nvPM) and noise emissions, based on mass flow, and the emissions coming from the engines per kilogram of fuel burned. In the future, these requirements can also be tested by operating the engine for an hour and measuring the emissions afterwards.

Another critical stakeholder requirement was STKCX17-MIS01: ”The family shall achieve a commonality index of at least 65%.” This is verified through an analysis of comparing the weight of different components of variants A and B, which indicates if the parts are identical. A further inspection can also be conducted.

Moving to the validation of the mission, it must be shown that the product designed both fulfils the desires of the stakeholders and is safe. The first test done is stress-testing. This will involve introducing severe turbulence. According to STKCX08-MIS01-SYS14, the aircraft shall maintain dynamic stability. This will induce vibrations on the aircraft, and to be validated, this must dampen without requiring too much input from a pilot. This test can be performed in already existing wind tunnels, where the usually laminar flow will be made turbulent.

To test operation readiness of the refuelling system, the aircraft is placed in an airport. It is assumed that around 2045, airports will have sufficient infrastructure to refuel hydrogen aircraft. During this test, it must be shown that the aircraft can land, taxi to the terminal, refuel, perform other necessary operations such as loading/unloading of cargo, and then taxi back to the runway within an hour.

Finally, mission scenario tests are performed, such as wing deflection tests, in test facilities of other aircraft manufacturers, such as Boeing. Here, loading tests, such as an ultimate wing loading test, are performed on the wing structure to determine and validate tip deflection. If proved the wing performs safely, passengers will be transported safely during nominal flight conditions.

9.2. Code flow block diagram

Author: Viktor *Contributors: Marius*

The strut-braced wing (SBW) design concept has a variety of objectives, namely: to reduce emissions, to achieve a high commonality index (CI), to maximise dispatch availability (DA), and to minimise turnaround time (TAT) and direct operating cost (DOC). To do so in addition to the already developed Module 1 ”Initial Design Concepts” of the sustainable aircraft family design tool, Module 2 ”Final Design Concept”, consisting of 21 blocks (B1-B21), was developed mainly on Python. However, as it can be seen in Figure 9.1, a variety of tools have been used: The DOC is performed in Excel, the control surfaces are designed both in Excel and on Python, and the Control Derivatives are extracted via XFLR5 and OpenVSP.

The tool gets inputs from mass, fuselage dimensions, wing dimensions and position, empennage and undercarriage dimensions and engine parameters. Based on this input, a number of classes are initialised: AircraftData, FuselageData, WingData, MassData, HorTail, VerTail, EngineData, AeroData, MaterialData, FlightCondition, StrutData, FloorData, DragTest and TESTData. The latter two are for verification. Similar as in Module 1, elements such as the wing, engines, empennage and landing gear will be further designed, but this time a Class II weight and drag estimations will be performed as seen in Figure 9.1. After all components are sized a cost (error) analysis is performed and if the error is lower than the target, the objectives of the strut-braced wing design concept are verified if they are met. As a final step, the controls surfaces of the aircraft are designed and the control derivatives are estimated. The result of all components designed and the objectives' completion verified is the Low-Emission Aircraft Family (LEAF).

9.3. Verification methods and results

Author: Viktor *Contributors: Marius*

Controlled verification is ensured by executing a standard list of verification tests which are to be performed only on Module 2 of the Sustainable Aircraft Family design tool as Module 1 was verified in the midterm report [3]. For that purpose, unit tests (U1-U6) are defined, applicable to the code blocks defined in Figure 9.1.

The catalogues of standardised unit test types, shown in Table 9.1, are to be applied to each software block as defined in Figure 9.1. The catalogue defines the intent, typical execution, and pass criteria of each unit test type, paired with unique identifiers for traceability. Note that not all test types apply to all blocks, where correct application ensures that irrelevant tests are not forced onto units where the underlying test principles are not applicable. In Table 9.2, it is tabulated which unit test is applied to which block of code. Furthermore, it can be found what the input, expected output, actual output, and pass condition are for each unit and integrated test. Lastly, it can be seen whether the test passed or failed.

The process detected several mistakes ranging from minor to major impacts, and some are shown. An error with a surprisingly large impact was the computation of the downwash gradient which contained a unit conversion error when accounting for propeller slipstream effects. Another caught mistake was an incorrect estimation of nacelle mass, because of the definition of engine mass, from which it was estimated. A clear error also came when the strut wetted area was not included within the total profile drag estimation and that landing gear drag was added in the cruise condition. Upon iteration subsystem tests, it was discovered that Oswald efficiency factor or vertical tail area never changed between 2 consecutive iterations, a clearly non-physical consequence from coding errors. These are examples of caught mistakes that allowed for an ultimate pass of all the unit and system tests shown in Table 9.2. It should be noted that values may not always match final results as different trial data may have been used. Pass/Fail results are for the last attempt of a particular test.

Table 9.1: Unit test type catalogue used for the Sustainable Aircraft Family design tool verification campaign.

ID	Name	Purpose / failure mode caught	Typical execution	Pass criterion
		Numerical Robustness Tests		
U1	**Determinism Test**	Catch unintended non-determinism (hidden state, random seeds, order dependence).	Repeat identical inputs at least twice and compare results.	Exact match or within stated tolerance (`atol`/`rtol`) for float outputs.
		Interface Tests		
U2	**Class Initialisation Test**	Ensures class objects are initialised correctly.	Create an object and check if all its attributes are initialised.	All attributes are initialised.

Continued on next page

ID	Name	Purpose / failure mode caught	Typical execution	Pass criterion
U3	**Input Shape Test**	Ensure upstream inputs are interpreted correctly.	Provide valid inputs including boundary cases.	Correct interpretation and handling.
U4	**Input Validation Test**	Reject malformed or inconsistent inputs.	Feed deliberately valid/invalid inputs.	Controlled error without invalid outputs.
		Logic Tests		
U5	**Analytical Reference Test**	Validate against hand-solvable cases.	Compare with analytical solutions.	Agreement within tolerance.
U6	**Sanity Test**	Catch physically impossible inputs.	Provide invalid properties and assertions.	No NaN/Inf and controlled failure.

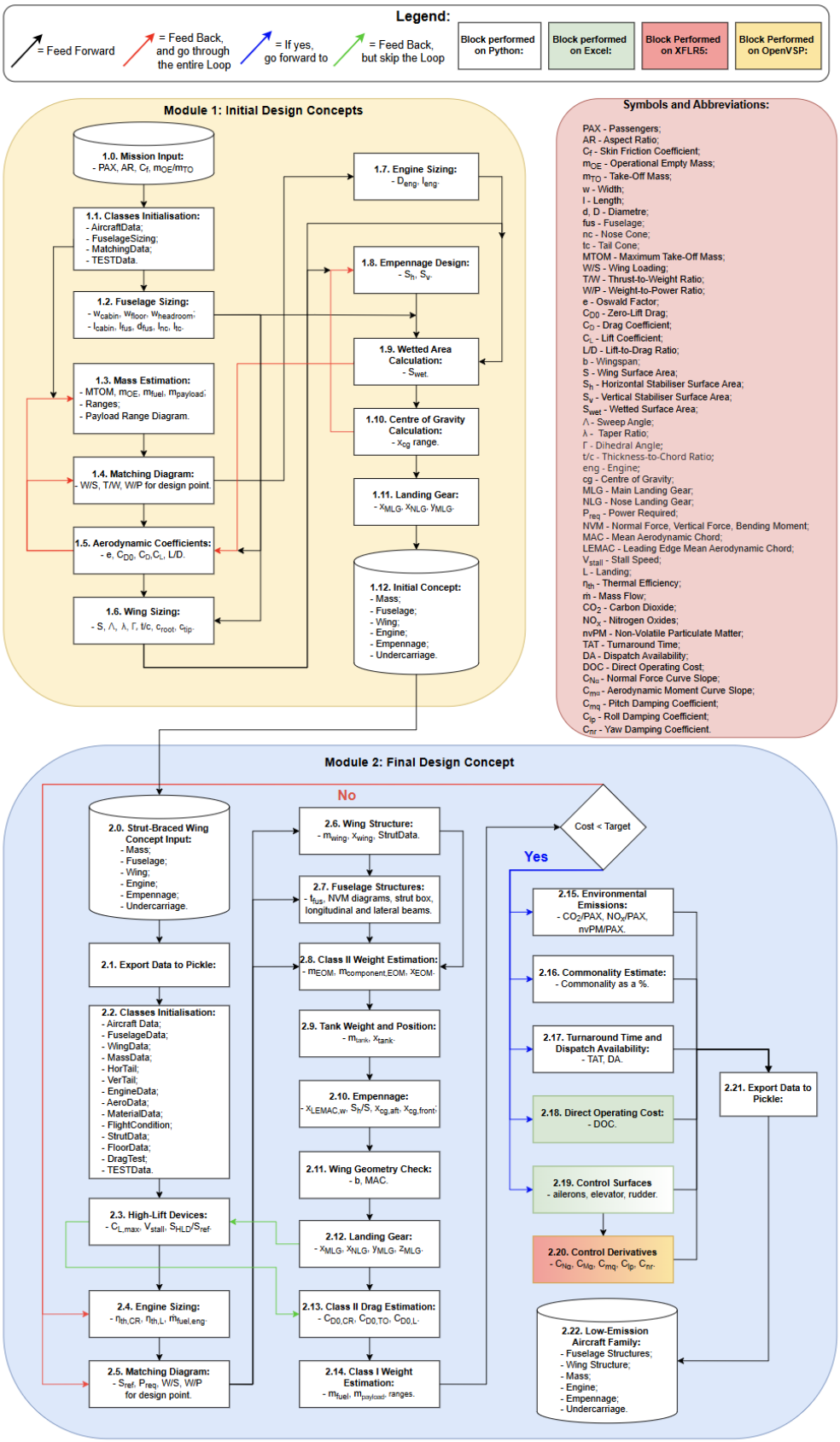

Figure 9.1: Code Flow Block Diagram

Table 9.2: Verification tests result table. It shows test-ID, inputs, expected outputs, actual outputs, pass conditions and the final pass/fail verdict.

Test ID	Input	Expected Output	Actual Output	Pass Condition	Pass/Fail
Block 1 'Export Data to Pickle' Unit Tests					
B1-U1	2x same parameters for: mass, fuselage, wing, engine, empennage, undercarriage.	2x same pickle file contents	2x same pickle file contents	2x same pickle file contents	Pass
B1-U2	AircraftData, FuselageSizing, MatchingData, TESTData objects.	All class attributes are initialised	All class attributes are initialised	All class attributes are initialised	Pass
B1-U3	Parameters for: mass, fuselage, wing, engine, empennage, undercarriage.	All variables have input values	All variables have input values	All variables have input values	Pass
B1-U4	Parameters for: mass, fuselage, wing, engine, empennage, undercarriage.	All variables have valid input values	All variables have valid input values	All variables have valid input values	Pass
Block 2 'Classes Initialisation' Unit Tests					
B2-U1	2x same Aircraft Data, FuselageData, WingData, MassData, HorTail, VerTail, EngineData, AeroData, MaterialData, FlightCondition, StrutData, FloorData, TESTData objects.	2x same attribute values.	2x same attribute values.	2x same attribute values.	Pass
B2-U2	Aircraft Data, FuselageData, WingData, MassData, HorTail, VerTail, EngineData, AeroData, MaterialData, FlightCondition, StrutData, FloorData, TESTData objects.	All class attributes are initialised	All class attributes are initialised	All class attributes are initialised	Pass
B2-U3	Aircraft Data, FuselageData, WingData, MassData, HorTail, VerTail, EngineData, AeroData, MaterialData, FlightCondition, StrutData, FloorData, TESTData objects.	All class attributes have input values	All class attributes have input values	All class attributes have input values	Pass
B2-U4	Aircraft Data, FuselageData, WingData, MassData, HorTail, VerTail, EngineData, AeroData, MaterialData, FlightCondition, StrutData, FloorData, TESTData objects.	All class attributes have valid input values	All class attributes have valid input values	All class attributes have valid input values	Pass
Block 3 'High-Lift Devices' Unit Tests					
B3-U1	2x same $MTOM$, S_{ref}, $\Lambda_{0.15c}$, $C_{L_{max,clean}}$, $C_{L_{\alpha,clean}}$, ρ, b, c_r, λ, AR.	2x same $C_{L,max,TO}$, $C_{L,max,L}$, $V_{stall,TO}$, $V_{stall,L}$, $(S_{HLD}/S_{ref})_{TO}$, $(S_{HLD}/S_{ref})_L$	2x same $C_{L,max,TO}$, $C_{L,max,L}$, $V_{stall,TO}$, $V_{stall,L}$, $(S_{HLD}/S_{ref})_{TO}$, $(S_{HLD}/S_{ref})_L$	2x same $C_{L,max,TO}$, $C_{L,max,L}$, $V_{stall,TO}$, $V_{stall,L}$, $(S_{HLD}/S_{ref})_{TO}$, $(S_{HLD}/S_{ref})_L$	Pass
B3-U6	$MTOM$, S_{ref}, $\Lambda_{0.15c}$, $C_{L_{max,clean}}$, $C_{L_{\alpha,clean}}$, ρ, b, c_r, λ, AR.	$0 < C_{L,max,TO} < C_{L,max,L}$, $0 < V_{stall,TO} < V_{stall,L}$, $0 < (S_{HLD}/S_{ref})_{TO} < (S_{HLD}/S_{ref})_L$	$0 < C_{L,max,TO} < C_{L,max,L}$, $0 < V_{stall,TO} < V_{stall,L}$, $0 < (S_{HLD}/S_{ref})_{TO} < (S_{HLD}/S_{ref})_L$	$0 < C_{L,max,TO} < C_{L,max,L}$, $0 < V_{stall,TO} < V_{stall,L}$, $0 < (S_{HLD}/S_{ref})_{TO} < (S_{HLD}/S_{ref})_L$	Pass
Block 4 'Engine Sizing' Unit Tests					
B4-U1	2x same $P_{req,AC}$, M, h, $\eta_{polytropic}$, pressure ratios, N_{blades}, RPM	2x same $P_{req,prop}$, η_{prop}, $\dot{m}_{fuel}$, $\dot{m}_{air}$, T_{inj}	2x same $P_{req,prop}$, η_{prop}, $\dot{m}fuel$, $\dot{m}_air$, T_{inj}	2x same $P_{req,prop}$, η_{prop}, $\dot{m}fuel$, $\dot{m}_air$, T_{inj}	Pass
B4-U4	$P_{req,AC}$, M, h, $\eta_{polytropic}$, pressure ratios, N_{blades}, RPM	$P_{req,AC} > 0, 0 < M < 1, h > 0, 0 < \eta_{polytropic} < 1$, pressure ratios>0, $N_{blades} > 0$, $RPM > 0$	$P_{req,AC} > 0, 0 < M < 1, h > 0, 0 < \eta_{polytropic} < 1$, pressure ratios>0, $N_{blades} > 0$, $RPM > 0$	$P_{req,AC} > 0, 0 < M < 1, h > 0, 0 < \eta_{polytropic} < 1$, pressure ratios>0, $N_{blades} > 0$, $RPM > 0$	Pass
B4-U6	$P_{req,AC}$, M, h, $\eta_{polytropic}$, pressure ratios, N_{blades}, RPM	$P_{req,prop} > 0, 0 < \eta_{prop} < 1, \dot{m}_{fuel} > 0$, $\dot{m}_{air} > 0, T_{inj} > 273.15\ [K]$	$P_{req,prop} > 0, 0 < \eta_{prop} < 1, \dot{m}_{fuel} > 0$, $\dot{m}_{air} > 0, T_{inj} > 273.15\ [K]$	$P_{req,prop} > 0, 0 < \eta_{prop} < 1, \dot{m}_{fuel} > 0$, $\dot{m}_{air} > 0, T_{inj} > 273.15\ [K]$	Pass
Block 5 'Matching Diagram' Unit Tests					
B5-U1	2x same MatchingData object.	2x same W/S, T/W, W/P, graphs.	2x same W/S, T/W, W/P, graphs.	2x same W/S, T/W, W/P, graphs.	Pass
Block 6 'Wing Structure' Unit Tests					
B6-U1	2x same S_{ref}, M, h, Γ, d_{fus}, AR, λ, S_{ref}/S_{wet}, $C_{L_{CR}}$, C_{D_0}, m_{eng}, d_{eng}, d_{prop}	2x same x_{cg}/MAC, m_{wing}, $S_{wet,strut}$, F_{strut}, strut-wing attachment angle α	2x same $P_{req,prop}$, η_{prop}, $\dot{m}fuel$, $\dot{m}_air$, T_{inj}	2x same $P_{req,prop}$, η_{prop}, $\dot{m}fuel$, $\dot{m}_air$, T_{inj}	Pass

Continued on next page

Test ID	Input	Expected Output	Actual Output	Pass Condition	Pass/Fail
B6-U4	S_{ref}, M, h [ft], Γ, d_{fus}, AR, λ, S_{ref}/S_{wet}, $C_{L_{CR}}$, C_{D_0}, m_{eng}, d_{eng}, d_{prop}	$S_{ref} > 0, 0 < M < 1, h > 0, \Gamma < 0$, $d_{fus} > 0$, $AR > 0, 0 < \lambda < 1, S_{ref}/S_{wet} > 0$, $C_{L_{CR}} > 0, 0 < C_{D_0} < 1, m_{eng} > 0$, $d_{eng} > 0, d_{prop} > 0$	$S_{ref} > 0, 0 < M < 1, h > 0, \Gamma < 0$, $d_{fus} > 0$, $AR > 0, 0 < \lambda < 1, S_{ref}/S_{wet} > 0$, $C_{L_{CR}} > 0, 0 < C_{D_0} < 1, m_{eng} > 0$, $d_{eng} > 0, d_{prop} > 0$	$S_{ref} > 0, 0 < M < 1, h > 0, \Gamma < 0$, $d_{fus} > 0$, $AR > 0, 0 < \lambda < 1, S_{ref}/S_{wet} > 0$, $C_{L_{CR}} > 0, 0 < C_{D_0} < 1, m_{eng} > 0$, $d_{eng} > 0, d_{prop} > 0$	Pass
B6-U6	S_{ref}, M, h [ft], Γ, d_{fus}, AR, λ, S_{ref}/S_{wet}, $C_{L_{CR}}$, C_{D_0}, m_{eng}, d_{eng}, d_{prop}	$0 < x_{cg}/MAC < 1, m_{wing} > 0$, $S_{wet,strut} > 0, F_{strut} > 0$, strut-wing attachment angle $\alpha > 0$	$0 < x_{cg}/MAC < 1, m_{wing} > 0$, $S_{wet,strut} > 0, F_{strut} > 0$, strut-wing attachment angle $\alpha > 0$	$0 < x_{cg}/MAC < 1, m_{wing} > 0$, $S_{wet,strut} > 0, F_{strut} > 0$, strut-wing attachment angle $\alpha > 0$	Pass
		Block 7 'Fuselage Structures' Unit Tests			
B7-U1	2x same TESTData, Fuselage, Wing, aero, Material, Alu2024T3, Ti6Al4V, Glare, AluLi objects.	2x same attribute values.	2x same attribute values.	2x same attribute values.	Pass
B7-U2	TESTData, Fuselage, Wing, aero, Material, Alu2024T3, Ti6Al4V, Glare, AluLi objects.	Initialised $d_{fus,outer}$, $d_{fus,inner}$, t_{fus}, Δp, N_{str}, N_{frames}, l_{fus}, MAC, S_{ref}, $C_{m_{ac_w}}$, $MTOM$, V_{CR}, x_{LEMAC}, w_{seat}, l_{seat}, $l_{long\ beam}$, z_{floor}, $w_{armrest}$, w_{aisle}, Alu2024T3 and AluLi: ρ, $\sigma_{ts,y}$, E, ν, τ.	Initialised $d_{fus,outer}$, $d_{fus,inner}$, t_{fus}, Δp, N_{str}, N_{frames}, l_{fus}, MAC, S_{ref}, $C_{m_{ac_w}}$, $MTOM$, V_{CR}, x_{LEMAC}, w_{seat}, l_{seat}, $l_{long\ beam}$, z_{floor}, $w_{armrest}$, w_{aisle}, Alu2024T3 and AluLi: ρ, $\sigma_{ts,y}$, E, ν, τ.	Initialised $d_{fus,outer}$, $d_{fus,inner}$, t_{fus}, Δp, N_{str}, N_{frames}, l_{fus}, MAC, S_{ref}, $C_{m_{ac_w}}$, $MTOM$, V_{CR}, x_{LEMAC}, w_{seat}, l_{seat}, $l_{long\ beam}$, z_{floor}, $w_{armrest}$, w_{aisle}, Alu2024T3 and AluLi: ρ, $\sigma_{ts,y}$, E, ν, τ.	Pass
B7-U3	TESTData, Fuselage, Wing, aero, Material, Alu2024T3, Ti6Al4V, Glare, AluLi objects.	Inputs of $d_{fus,outer} = 3$ $[m]$, $d_{fus,inner} = 2.75$ $[m]$, $t_{fus} = 0.001$ $[m]$, $\Delta p = 75000$ $[Pa]$, $N_{str} = 70$, $N_{frames} = 64$, $l_{fus} = 33.65$ $[m]$, $MAC = 2.12$ $[m]$, $S_{ref} = 65.64$ $[m^2]$, $C_{m_{ac_w}} = -0.045$, $MTOM = 26000$ $[kg]$, $V_{CR} = 191.977$ $[m/s]$, $x_{LEMAC} = 18.5$ $[m]$, $w_{seat} = 0.43$ $[m]$, $l_{seat} = 0.7874$ $[m]$, $l_{long\ beam} = 0.516$ $[m]$, $z_{floor} = 0.75$ $[m]$, $w_{armrest} = 0.05$ $[m]$, $w_{aisle} = 0.51$ $[m]$; **Alu2024T3:** $\rho = 2780$ $[kg/m^3]$, $\sigma_{ts,y} = 345$ $[MPa]$, $E = 73$ $[GPa]$, $\nu = 0.33$, $G = 28$ $[GPa]$, $\tau = 172.5$ $[MPa]$; **AluLi:** $\rho = 2710$ $[kg/m^3]$, $\sigma_{ts,y} = 441$ $[MPa]$, $E = 76$ $[GPa]$, $\nu = 0.33$ $[GPa]$, $G = 30$ $[GPa]$, $\tau = 220.5$ $[MPa]$.	Inputs of $d_{fus,outer} = 3$ $[m]$, $d_{fus,inner} = 2.75$ $[m]$, $t_{fus} = 0.001$ $[m]$, $\Delta p = 75000$ $[Pa]$, $N_{str} = 70$, $N_{frames} = 64$, $l_{fus} = 33.65$ $[m]$, $MAC = 2.12$ $[m]$, $S_{ref} = 65.64$ $[m^2]$, $C_{m_{ac_w}} = -0.045$, $MTOM = 26000$ $[kg]$, $V_{CR} = 191.977$ $[m/s]$, $x_{LEMAC} = 18.5$ $[m]$, $w_{seat} = 0.43$ $[m]$, $l_{seat} = 0.7874$ $[m]$, $l_{long\ beam} = 0.516$ $[m]$, $z_{floor} = 0.75$ $[m]$, $w_{armrest} = 0.05$ $[m]$, $w_{aisle} = 0.51$ $[m]$; **Alu2024T3:** $\rho = 2780$ $[kg/m^3]$, $\sigma_{ts,y} = 345$ $[MPa]$, $E = 73$ $[GPa]$, $\nu = 0.33$, $G = 28$ $[GPa]$, $\tau = 172.5$ $[MPa]$; **AluLi:** $\rho = 2710$ $[kg/m^3]$, $\sigma_{ts,y} = 441$ $[MPa]$, $E = 76$ $[GPa]$, $\nu = 0.33$ $[GPa]$, $G = 30$ $[GPa]$, $\tau = 220.5$ $[MPa]$.	Inputs of $d_{fus,outer} = 3$ $[m]$, $d_{fus,inner} = 2.75$ $[m]$, $t_{fus} = 0.001$ $[m]$, $\Delta p = 75000$ $[Pa]$, $N_{str} = 70$, $N_{frames} = 64$, $l_{fus} = 33.65$ $[m]$, $MAC = 2.12$ $[m]$, $S_{ref} = 65.64$ $[m^2]$, $C_{m_{ac_w}} = -0.045$, $MTOM = 26000$ $[kg]$, $V_{CR} = 191.977$ $[m/s]$, $x_{LEMAC} = 18.5$ $[m]$, $w_{seat} = 0.43$ $[m]$, $l_{seat} = 0.7874$ $[m]$, $l_{long\ beam} = 0.516$ $[m]$, $z_{floor} = 0.75$ $[m]$, $w_{armrest} = 0.05$ $[m]$, $w_{aisle} = 0.51$ $[m]$; **Alu2024T3:** $\rho = 2780$ $[kg/m^3]$, $\sigma_{ts,y} = 345$ $[MPa]$, $E = 73$ $[GPa]$, $\nu = 0.33$, $G = 28$ $[GPa]$, $\tau = 172.5$ $[MPa]$; **AluLi:** $\rho = 2710$ $[kg/m^3]$, $\sigma_{ts,y} = 441$ $[MPa]$, $E = 76$ $[GPa]$, $\nu = 0.33$ $[GPa]$, $G = 30$ $[GPa]$, $\tau = 220.5$ $[MPa]$.	Pass
B7-U4	TESTData, Fuselage, Wing, aero, Material, Alu2024T3, Ti6Al4V, Glare, AluLi objects.	All inputs should be above 0, apart from $C_{m_{ac_w}} < 0$.	All inputs should be above 0, apart from $C_{m_{ac_w}} < 0$.	All inputs should be above 0, apart from $C_{m_{ac_w}} < 0$.	Pass
B7-U5	TESTData, Fuselage, Wing, aero, Material, Alu2024T3, Ti6Al4V, Glare, AluLi objects.	$A_{beam} = 0.052$ $[m^2]$, $I_{xx,\ I,C-beam} = 0.0387$ $[m^4]$, $I_{xx,\ rect\ beam} = 0.0587$ $[m^4]$, $I_{xx,\ circ\ beam} = 0.0314$ $[m^4]$, $F_{s,hor} = 0$ $[N]$, $F_{s,ver} = 10$ $[N]$, $l_{rod} = 0.583$ $[m]$, $t_{fus} = 0.00165$ $[m]$, $I_{yy,str} = 0.0112$ $[m^4]$, $I_{zz,str} = 0.0109$ $[m^4]$, $I_{yy,fus} = 0.0106$ $[m^4]$, $m_{empty\ fus} = 2515$ $[kg]$, $\sigma_{y,N_y,strut} = 6.108$ $[MN]$, $\sigma_{y,M_x,strut} = 9.095$ $[MN]$, $\sigma_{x,M_y,long\ floor\ beam} = 248.9$ $[MN]$, $\sigma_{y,N_y,lat\ floor\ beam} = 39.52$ $[MN]$, $\sigma_{y,M_x,lat\ floor\ beam} = 228.3$ $[MN]$ $\tau_{z,strut} = 76979$ $[N]$, $\tau_{z,long\ floor\ beam} = 21724$ $[N]$, $\tau_{z,lat\ floor\ beam} = 69309$ $[N]$ $\sigma_{y,max,strut} \approx 15.2$ $[MPa]$, $\sigma_{y,max,long\ floor\ beam} \approx 248.9$ $[MPa]$, $\sigma_{y,max,lat\ floor\ beam} \approx 267.8$ $[MPa]$	$A_{beam} = 0.052$ $[m^2]$, $I_{xx,\ I,C-beam} = 0.0387$ $[m^4]$, $I_{xx,\ rect\ beam} = 0.0587$ $[m^4]$, $I_{xx,\ circ\ beam} = 0.0314$ $[m^4]$, $F_{s,hor} = 0$ $[N]$, $F_{s,ver} = 10$ $[N]$, $l_{rod} = 0.583$ $[m]$, $t_{fus} = 0.00165$ $[m]$, $I_{yy,str} = 0.0112$ $[m^4]$, $I_{zz,str} = 0.0109$ $[m^4]$, $I_{yy,fus} = 0.0106$ $[m^4]$, $m_{empty\ fus} = 2515$ $[kg]$, $\sigma_{y,N_y,strut} = 6.108$ $[MN]$, $\sigma_{y,M_x,strut} = 9.095$ $[MN]$, $\sigma_{x,M_y,long\ floor\ beam} = 248.9$ $[MN]$, $\sigma_{y,N_y,lat\ floor\ beam} = 39.52$ $[MN]$, $\sigma_{y,M_x,lat\ floor\ beam} = 228.3$ $[MN]$ $\tau_{z,strut} = 76979$ $[N]$, $\tau_{z,long\ floor\ beam} = 21724$ $[N]$, $\tau_{z,lat\ floor\ beam} = 69309$ $[N]$ $\sigma_{y,max,strut} \approx 15.2$ $[MPa]$, $\sigma_{y,max,long\ floor\ beam} \approx 248.9$ $[MPa]$, $\sigma_{y,max,lat\ floor\ beam} \approx 267.8$ $[MPa]$	Values for A_{beam}, $I_{xx,\ I,C-beam}$, $I_{xx,\ rect\ beam}$, $I_{xx,\ circ\ beam}$, $F_{s,hor}$, $F_{s,ver}$, l_{rod}, t_{fus}, $I_{yy,str}$, $I_{zz,str}$, $I_{yy,fus}$, $m_{empty\ fus}$, $\sigma_{y,N_y,strut}$, $\sigma_{y,M_x,strut}$, $\sigma_{x,M_y,long\ floor\ beam}$, $\sigma_{y,N_y,lat\ floor\ beam}$, $\sigma_{y,M_x,lat\ floor\ beam}$ $\tau_{z,strut}$, $\tau_{z,long\ floor\ beam}$, $\tau_{z,lat\ floor\ beam}$, $\sigma_{y,max,long\ floor\ beam}$, $\sigma_{y,max,lat\ floor\ beam}$ within 0.01 relative tolerances.	Pass

Continued on next page

Test ID	Input	Expected Output	Actual Output	Pass Condition	Pass/Fail
B7-U6	TESTData, Fuselage, Wing, aero, Material, Alu2024T3, Ti6Al4V, Glare, AluLi objects.	$A_{beam} > 0, I_{xx,beam} > 0, F_{s,hor} > 0, F_{s,ver} > 0, l_{rod} > 0, t_{fus} > 0, I_{xx,stringer} > 0, I_{zz,stringer} > 0, I_{xx,fus} > 0, m_{empty\ fus} > 0$,, $V_{z,strut} > 0, V_{z,longitudinal\ floor\ beam} > 0, V_{z,lateral\ floor\ beam} > 0$	$A_{beam} > 0, I_{xx,beam} > 0, F_{s,hor} > 0, F_{s,ver} > 0, l_{rod} > 0, t_{fus} > 0, I_{xx,stringer} > 0, I_{zz,stringer} > 0, I_{xx,fus} > 0, m_{empty\ fus} > 0$,, $V_{z,strut} > 0, V_{z,longitudinal\ floor\ beam} > 0, V_{z,lateral\ floor\ beam} > 0$	$A_{beam} > 0, I_{xx,beam} > 0, F_{s,hor} > 0, F_{s,ver} > 0, l_{rod} > 0, t_{fus} > 0, I_{xx,stringer} > 0, I_{zz,stringer} > 0, I_{xx,fus} > 0, m_{empty\ fus} > 0$,, $V_{z,strut} > 0, V_{z,longitudinal\ floor\ beam} > 0, V_{z,lateral\ floor\ beam} > 0$	Pass
		Block 8 'Class II Weight Estimation' Unit Tests			
B8-U1	2x same Wing, Fuselage, EngineData, MassData, HorTail and VerTail objects.	2x same mass and x-position of the: wing, horizontal tail, vertical tail, fuselage, wing frames, nacelles, landing gear, engines, tanks, propulsion system, flight controls, electrical system, avionics, AC, Oxygen, APU, furnishings and cargo.	2x same mass and x-position of the: wing, horizontal tail, vertical tail, fuselage, wing frames, nacelles, landing gear, engines, tanks, propulsion system, flight controls, electrical system, avionics, AC, Oxygen, APU, furnishings and cargo.	2x same mass and x-position of the: wing, horizontal tail, vertical tail, fuselage, wing frames, nacelles, landing gear, engines, tanks, propulsion system, flight controls, electrical system, avionics, AC, Oxygen, APU, furnishings and cargo.	Pass
B8-U5	Mass and x-position of the: wing, horizontal tail, vertical tail, fuselage, wing frames, nacelles, landing gear, engines, tanks, propulsion system, flight controls, electrical system, avionics, AC, Oxygen, APU, furnishings and cargo.	Commonality index between 65% and 100%.	Commonality index between 65% and 100%.	Commonality index between 65% and 100%.	Pass
B8-U6	Mass and x-position of the: wing, horizontal tail, vertical tail, fuselage, wing frames, nacelles, landing gear, engines, tanks, propulsion system, flight controls, electrical system, avionics, AC, Oxygen, APU, furnishings and cargo.	Commonality index of 71% (Trial data different than actual).	Commonality index of 71% .	Value for commonality index within 0.01 relative tolerance from expected.	Pass
		Block 9 'Tank Weight and Position' Unit Tests			
B9-U1	2x same AircraftData objects.	2x same m_{tank}, x_{tank}	2x same m_{tank}, x_{tank}	2x same m_{tank}, x_{tank}	Pass
B9-U6	AircraftData objects.	$m_{tank} > 0, x_{tank} > 0$	$m_{tank} > 0, x_{tank} > 0$	$m_{tank} > 0, x_{tank} > 0$	Pass
		Block 10 'Empennage' Unit Tests			
B10-U1	2x same x_{LEMAC}/l_{fus} array of 25 equidistant points within $[0.20, 0.55]$, SM=0.05	2x same S_h, S_v b_h, b_v, MAC_h, MAC_v, Λ_h, Λ_v, $x_{cg,aft}$, $x_{cg,front}$, $x_{cg,rel}$, $x_{cg,abs}$.	S_h, S_v b_h, b_v, MAC_h, MAC_v, Λ_h, Λ_v, $x_{cg,aft}$, $x_{cg,front}$, $x_{cg,rel}$, $x_{cg,abs}$.	S_h, S_v b_h, b_v, MAC_h, MAC_v, Λ_h, Λ_v, $x_{cg,aft}$, $x_{cg,front}$, $x_{cg,rel}$, $x_{cg,abs}$.	Pass
B10-U6	x_{LEMAC}/l_{fus} array of 25 equidistant points within $[0.20, 0.55]$, SM=0.05	$S_h > 0, S_v > 0\ b_h > 0, b_v > 0, MAC_h > 0, MAC_v > 0, \Lambda_h > 0, \Lambda_v > 0, 0 < x_{cg,front} < x_{cg,aft} < l_{fus}, 0 < x_{cg,rel} < 1, 0 < x_{cg,abs} < l_{fus}$	$S_h > 0, S_v > 0\ b_h > 0, b_v > 0, MAC_h > 0, MAC_v > 0, \Lambda_h > 0, \Lambda_v > 0, 0 < x_{cg,front} < x_{cg,aft} < l_{fus}, 0 < x_{cg,rel} < 1, 0 < x_{cg,abs} < l_{fus}$	$S_h > 0, S_v > 0\ b_h > 0, b_v > 0, MAC_h > 0, MAC_v > 0, \Lambda_h > 0, \Lambda_v > 0, 0 < x_{cg,front} < x_{cg,aft} < l_{fus}, 0 < x_{cg,rel} < 1, 0 < x_{cg,abs} < l_{fus}$	Pass
		Block 11 'Wing Geometry Check' Unit Tests			
B11-U1	2x same AircraftData object.	2x same S_{ref}, b, MAC, Λ, AR.	2x same S_{ref}, b, MAC, Λ, AR.	2x same S_{ref}, b, MAC, Λ, AR.	Pass
B11-U6	AircraftData object.	$S_{ref} > 0, 0 < b \leq 36, MAC > 0, \Lambda > 0, 0 < A \leq 20$.	$S_{ref} > 0, 0 < b \leq 36, MAC > 0, \Lambda > 0, 0 < A \leq 20$.	$S_{ref} > 0, 0 < b \leq 36, MAC > 0, \Lambda > 0, 0 < A \leq 20$.	Pass
		Block 12 'Landing Gear' Unit Tests			
B12-U1	2x same TESTData object.	2x same $x_{MLG}, x_{NLG}, y_{MLG}, h_{MLG}, h_{NLG}, P_{mw}, P_{nw}, \varphi$	2x same $x_{MLG}, x_{NLG}, y_{MLG}, h_{MLG}, h_{NLG}, P_{mw}, P_{nw}, \varphi$	2x same $x_{MLG}, x_{NLG}, y_{MLG}, h_{MLG}, h_{NLG}, P_{mw}, P_{nw}, \varphi$	Pass
B12-U6	TESTData object.	$x_{MLG} > 0, x_{NLG} > 0, y_{MLG} > 0, h_{MLG} > 0, h_{NLG} > 0, 0.85\ W/N_{mw} < P_{mw} < 0.92\ W/N_{mw}, 0.08\ W/N_{nw} < P_{nw} < 0.15\ W/N_{nw}, \varphi > 0$	$x_{MLG} > 0, x_{NLG} > 0, y_{MLG} > 0, h_{MLG} > 0, h_{NLG} > 0, 0.85\ W/N_{mw} < P_{mw} < 0.92\ W/N_{mw}, 0.08\ W/N_{nw} < P_{nw} < 0.15\ W/N_{nw}, \varphi > 0$	$x_{MLG} > 0, x_{NLG} > 0, y_{MLG} > 0, h_{MLG} > 0, h_{NLG} > 0, 0.85\ W/N_{mw} < P_{mw} < 0.92\ W/N_{mw}, 0.08\ W/N_{nw} < P_{nw} < 0.15\ W/N_{nw}, \varphi > 0$	Pass
		Block 13 'Class II Drag Estimation' Unit Tests			
B13-U1	2x same DragTest, Wing, Fuselage, HorTail, VerTail, Cruise, RoskamTest objects.	2x same C_{D_w}, $C_{D_{fus}}$, $C_{D_{emp}}$, $C_{D_{flap}}$, $C_{D_{wave}}$, $C_{D_{nac\ pylon}}$, $C_{D_{windshield}}$, $C_{D_{strut}}$, $C_{D_{0,TO}}$, $C_{D_{0,CR}}$, $C_{D_{0,L}}$.	2x same C_{D_w}, $C_{D_{fus}}$, $C_{D_{emp}}$, $C_{D_{flap}}$, $C_{D_{wave}}$, $C_{D_{nac\ pylon}}$, $C_{D_{windshield}}$, $C_{D_{strut}}$, $C_{D_{0,TO}}$, $C_{D_{0,CR}}$, $C_{D_{0,L}}$.	2x same C_{D_w}, $C_{D_{fus}}$, $C_{D_{emp}}$, $C_{D_{flap}}$, $C_{D_{wave}}$, $C_{D_{nac\ pylon}}$, $C_{D_{windshield}}$, $C_{D_{strut}}$, $C_{D_{0,TO}}$, $C_{D_{0,CR}}$, $C_{D_{0,L}}$.	Pass

Continued on next page

Test ID	Input	Expected Output	Actual Output	Pass Condition	Pass/Fail
B13-U5	TESTData object.	$C_{D_w} \approx 0.0066$, $C_{D_{fus}} \approx 0.0071$, $C_{D_{emp}} \approx 0.0012$, $C_{D_{flap}} = 0.0066$, $C_{D_{wave}} \approx 0.0010$, $C_{D_{nac\ pylon}} \approx 0.0001$, $C_{D_{windshield}} \approx 0.0004$, $C_{D_{strut}} \approx 0.0009$, $C_{D_0,TO} = 0.038$, $C_{D_0,CR} = 0.028$, $C_{D_0,L} = 0.038$.	$C_{D_w} \approx 0.0066$, $C_{D_{fus}} \approx 0.0071$, $C_{D_{emp}} \approx 0.0012$, $C_{D_{flap}} = 0.0066$, $C_{D_{wave}} \approx 0.0010$, $C_{D_{nac\ pylon}} \approx 0.0001$, $C_{D_{windshield}} \approx 0.0004$, $C_{D_{strut}} \approx 0.0009$, $C_{D_0,TO} = 0.038$, $C_{D_0,CR} = 0.028$, $C_{D_0,L} = 0.038$.	Values for C_{D_w}, $C_{D_{fus}}$, $C_{D_{emp}}$, $C_{D_{flap}}$, $C_{D_{wave}}$, $C_{D_{nac\ pylon}}$, $C_{D_{windshield}}$, $C_{D_{strut}}$, $C_{D_0,TO}$, $C_{D_0,CR}$, $C_{D_0,L}$ within 0.01 relative tolerance from expected.	Pass
B13-U6	DragTest, Wing, Fuselage, HorTail, VerTail, Cruise, RoskamTest objects.	$0 < C_{D_w} < 1, 0 < C_{D_{fus}} < 1$, $0 < C_{D_{emp}} < 1, 0 < C_{D_{flap}} < 1$, $0 < C_{D_{wave}} < 1, 0 < C_{D_{nac\ pylon}} < 1$, $0 < C_{D_{windshield}} < 1, 0 < C_{D_{strut}} < 1$, $0 < C_{D_0,TO} < 1, 0 < C_{D_0,CR} < 1$, $0 < C_{D_0,L} < 1$.	$0 < C_{D_w} < 1, 0 < C_{D_{fus}} < 1$, $0 < C_{D_{emp}} < 1, 0 < C_{D_{flap}} < 1$, $0 < C_{D_{wave}} < 1, 0 < C_{D_{nac\ pylon}} < 1$, $0 < C_{D_{windshield}} < 1, 0 < C_{D_{strut}} < 1$, $0 < C_{D_0,TO} < 1, 0 < C_{D_0,CR} < 1$, $0 < C_{D_0,L} < 1$.	$0 < C_{D_w} < 1, 0 < C_{D_{fus}} < 1$, $0 < C_{D_{emp}} < 1, 0 < C_{D_{flap}} < 1$, $0 < C_{D_{wave}} < 1, 0 < C_{D_{nac\ pylon}} < 1$, $0 < C_{D_{windshield}} < 1, 0 < C_{D_{strut}} < 1$, $0 < C_{D_0,TO} < 1, 0 < C_{D_0,CR} < 1$, $0 < C_{D_0,L} < 1$.	Pass
Block 14 'Class I Weight Estimation' Unit Tests					
B14-U1	2x same TESTData object.	2x same R_{lost}, R_{eq}, R_{aux}, R_{ferry}, $m_{payload}$, m_{fuel}/m_{TO}, m_{TO}, m_{crew}.	2x same R_{lost}, R_{eq}, R_{aux}, R_{ferry}, $m_{payload}$, m_{fuel}/m_{TO}, m_{TO}, m_{crew}.	2x same R_{lost}, R_{eq}, R_{aux}, R_{ferry}, $m_{payload}$, m_{fuel}/m_{TO}, m_{TO}, m_{crew}.	Pass
B14-U5	TESTData object	$R_{lost} \approx 290$ [km], $R_{eq} = 2985$ [km], $R_{aux} = 1485$ [km], $m_{payload} = 8400$ [kg], $m_{fuel}/m_{TO} = 0.035$, $m_{crew} = 400$ [kg]	$R_{lost} \approx 290$ [km], $R_{eq} = 2985$ [km], $R_{aux} = 1485$ [km], $m_{payload} = 8400$ [kg], $m_{fuel}/m_{TO} = 0.035$, $m_{crew} = 400$ [kg]	Values for R_{lost}, R_{eq}, R_{aux}, $m_{payload}$, m_{fuel}/m_{TO}, m_{crew} within 0.01 relative tolerance	Pass
B14-U6	TESTData object	$R_{lost} > 0$, $R_{eq} > 0$, $R_{aux} > 0$, $R_{ferry} > 0$, $m_{payload} > 0$, $m_{fuel}/m_{TO} > 0$, $m_{TO} > 0$, $m_{crew} > 0$	$R_{lost} > 0$, $R_{eq} > 0$, $R_{aux} > 0$, $R_{ferry} > 0$, $m_{payload} > 0$, $m_{fuel}/m_{TO} > 0$, $m_{TO} > 0$, $m_{crew} > 0$	$R_{lost} > 0$, $R_{eq} > 0$, $R_{aux} > 0$, $R_{ferry} > 0$, $m_{payload} > 0$, $m_{fuel}/m_{TO} > 0$, $m_{TO} > 0$, $m_{crew} > 0$	Pass
Block 15 'Environmental Emissions' Unit Tests					
B15-U1	2x same $\dot{m}_f$	2x same $gCO_2/(PAX \cdot km)$, $gNO_x/LTO\ cycle$, $nvPM/LTO\ cycle$ emissions.	2x same $gCO_2/(PAX \cdot km)$, $gNO_x/LTO\ cycle$, $nvPM/LTO\ cycle$ emissions.	2x same $gCO_2/(PAX \cdot km)$, $gNO_x/LTO\ cycle$, $nvPM/LTO\ cycle$ emissions.	Pass
B15-U5	$\dot{m}_f$	**Variant A:** $gCO_2/(PAX \cdot km) = 0.0588$ (for manufacturing), $gCO_2/(PAX \cdot km) = 3.78$ (for operations), $gCO_2/(PAX \cdot km) = 0.326$ (for maintenance), $gCO_2/(PAX \cdot km) = -0.01$ (for EOL), $gCO_2/(PAX \cdot km) = 4.16$ (in total); **Variant B:** $gCO_2/(PAX \cdot km) = 0.0358$ (for manufacturing), $gCO_2/(PAX \cdot km) = 3.60$ (for operations), $gCO_2/(PAX \cdot km) = 0.317$ (for maintenance), $gCO_2/(PAX \cdot km) = -0.007$ (for EOL), $gCO_2/(PAX \cdot km) = 3.945$ (in total).	**Variant A:** $gCO_2/(PAX \cdot km) = 0.0588$ (for manufacturing), $gCO_2/(PAX \cdot km) = 3.78$ (for operations), $gCO_2/(PAX \cdot km) = 0.326$ (for maintenance), $gCO_2/(PAX \cdot km) = -0.01$ (for EOL), $gCO_2/(PAX \cdot km) = 4.16$ (in total); **Variant B:** $gCO_2/(PAX \cdot km) = 0.0358$ (for manufacturing), $gCO_2/(PAX \cdot km) = 3.60$ (for operations), $gCO_2/(PAX \cdot km) = 0.317$ (for maintenance), $gCO_2/(PAX \cdot km) = -0.007$ (for EOL), $gCO_2/(PAX \cdot km) = 3.945$ (in total).	Values for variants A and B for $gCO_2/(PAX \cdot km) = 0.0588$ regarding manufacturing, operations, maintenance, EOL and emissions in total within 0.01 relative tolerance.	Pass
B15-U6	$\dot{m}_f$	$gCO_2/(PAX \cdot km) > 0$ (apart from EOL emissions which can also be negative), $gNO_x/LTO\ cycle > 0$, $nvPM/LTO\ cycle > 0$ emissions.	$gCO_2/(PAX \cdot km) > 0$ (apart from EOL emissions which can also be negative), $gNO_x/LTO\ cycle > 0$, $nvPM/LTO\ cycle > 0$ emissions.	$gCO_2/(PAX \cdot km) > 0$ (apart from EOL emissions which can also be negative), $gNO_x/LTO\ cycle > 0$, $nvPM/LTO\ cycle > 0$ emissions.	Pass
Block 16 'Commonality Estimate' Unit Tests					
B16-U1	2x same mass and x-position of the: wing, horizontal tail, vertical tail, fuselage, wing frames, nacelles, landing gear, engines, tanks, propulsion system, flight controls, electrical system, avionics, AC, Oxygen, APU, furnishings and cargo.	2x same commonality index.	2x same commonality index.	2x same commonality index.	Pass
B16-U5	Mass and x-position of the: wing, horizontal tail, vertical tail, fuselage, wing frames, nacelles, landing gear, engines, tanks, propulsion system, flight controls, electrical system, avionics, AC, Oxygen, APU, furnishings and cargo.	Commonality index between 65% and 100%.	Commonality index between 65% and 100%.	Commonality index between 65% and 100%.	Pass

Continued on next page

Test ID	Input	Expected Output	Actual Output	Pass Condition	Pass/Fail
B16-U6	Mass and x-position of the: wing, horizontal tail, vertical tail, fuselage, wing frames, nacelles, landing gear, engines, tanks, propulsion system, flight controls, electrical system, avionics, AC, Oxygen, APU, furnishings and cargo.	Commonality index of 71%.	Commonality index of 71%.	Value for commonality index within 0.01 relative tolerance from expected.	Pass
			Block 17 'Turnaround Time and Commonality' Unit Tests		
B17-U1	2x same times, passenger rates, liquid hydrogen mass rate, and cargo masses.	2x same $t_{LH_2}, t_{unloading\ cargo}, t_{board}, t_{deboard}, t_{loading\ cargo}, t_{unload\ end}, t_{refuel\ end}, t_{load\ end}$	2x same $t_{LH_2}, t_{unloading\ cargo}, t_{board}, t_{deboard}, t_{loading\ cargo}, t_{unload\ end}, t_{refuel\ end}, t_{load\ end}$	2x same $t_{LH_2}, t_{unloading\ cargo}, t_{board} > 0, t_{deboard}, t_{loading\ cargo}, t_{unload\ end}, t_{refuel\ end}, t_{load\ end}$	Pass
B17-U6	Times, passenger rates, liquid hydrogen mass rate, and cargo masses.	$t_{LH_2} > 0, t_{unloading\ cargo} > 0, t_{board} > 0, t_{deboard} > 0, t_{loading\ cargo} > 0, t_{unload\ end} > 0, t_{refuel\ end} > 0, t_{load\ end} > 0$	$t_{LH_2} > 0, t_{unloading\ cargo} > 0, t_{board} > 0, t_{deboard} > 0, t_{loading\ cargo} > 0, t_{unload\ end} > 0, t_{refuel\ end} > 0, t_{load\ end} > 0$	$t_{LH_2} > 0, t_{unloading\ cargo} > 0, t_{board} > 0, t_{deboard} > 0, t_{loading\ cargo} > 0, t_{unload\ end} > 0, t_{refuel\ end} > 0, t_{load\ end} > 0$	Pass
			Block 18 'Direct Operating Cost' Unit Tests		
B18-U1	2x same fuel used, engine and frame weights, MTOWs, salaries and N_{crew}, annual hours crew, $V_{CR}, R_{nom}, AEP, N_{prop}, N_{seats}$ C_{ins}, C_{fuel} [USD/gallon], $\rho_{fuel}, N_{eng}, SHP_{TO}, C_{pers}, C_{crew}, C_{fuel}, C_{main}, C_{depr}, C_{landing}, C_{eng}, DOC, ASK, CASK$.	2x same $t_{LH_2}, t_{unloading\ cargo}, t_{board}, t_{deboard}, t_{loading\ cargo}, t_{unload\ end}, t_{refuel\ end}, t_{load\ end}$	2x same $t_{LH_2}, t_{unloading\ cargo}, t_{board}, t_{deboard}, t_{loading\ cargo}, t_{unload\ end}, t_{refuel\ end}, t_{load\ end}$	2x same $t_{LH_2}, t_{unloading\ cargo}, t_{board} > 0, t_{deboard}, t_{loading\ cargo}, t_{unload\ end}, t_{refuel\ end}, t_{load\ end}$	Pass
B18-U6	Times, passenger rates, liquid hydrogen mass rate, and cargo masses.	$t_{LH_2} > 0, t_{unloading\ cargo} > 0, t_{board} > 0, t_{deboard} > 0, t_{loading\ cargo} > 0, t_{unload\ end} > 0, t_{refuel\ end} > 0, t_{load\ end} > 0$	$t_{LH_2} > 0, t_{unloading\ cargo} > 0, t_{board} > 0, t_{deboard} > 0, t_{loading\ cargo} > 0, t_{unload\ end} > 0, t_{refuel\ end} > 0, t_{load\ end} > 0$	$t_{LH_2} > 0, t_{unloading\ cargo} > 0, t_{board} > 0, t_{deboard} > 0, t_{loading\ cargo} > 0, t_{unload\ end} > 0, t_{refuel\ end} > 0, t_{load\ end} > 0$	Pass
			Block 19 'Control Surfaces' Unit Tests		
B19-U1	2x same $C_{l_\alpha}, C_{D_0}, S_{ref}, b, c_r, \lambda, AR, MTOM, \Lambda_{0.15c}, C_{L_\alpha,clean}, C_{L_{max,clean}}, \rho$	2x same $p_{TO}, p_{TO,des}, p_L, p_{L,des}$.	2x same $p_{TO}, p_{TO,des}, p_L, p_{L,des}$.	2x same $p_{TO}, p_{TO,des}, p_L, p_{L,des}$.	Pass
B19-U4	$C_{l_\alpha}, C_{D_0}, S_{ref}, b, c_r, \lambda, AR, MTOM, \Lambda_{0.15c}, C_{L_\alpha,clean}, C_{L_{max,clean}}, \rho$	$0 < C_{L_\alpha,clean} < C_{l_\alpha}, 0 < C_{D_0} < 1, S_{ref} > 0, b > 0, c_r > 0, 0 < \lambda < 1, 0 < AR \leq 20, MTOM > 0, \Lambda_{0.15c} > 0, 0 < \rho < 1.225\ [kg/m^3]$	$0 < C_{L_\alpha,clean} < C_{l_\alpha}, 0 < C_{D_0} < 1, S_{ref} > 0, b > 0, c_r > 0, 0 < \lambda < 1, 0 < AR \leq 20, MTOM > 0, \Lambda_{0.15c} > 0, 0 < \rho < 1.225\ [kg/m^3]$	$0 < C_{L_\alpha,clean} < C_{l_\alpha}, 0 < C_{D_0} < 1, S_{ref} > 0, b > 0, c_r > 0, 0 < \lambda < 1, 0 < AR \leq 20, MTOM > 0, \Lambda_{0.15c} > 0, 0 < \rho < 1.225\ [kg/m^3]$	Pass
B19-U6	$C_{l_\alpha}, C_{D_0}, S_{ref}, b, c_r, \lambda, AR, MTOM, \Lambda_{0.15c}, C_{L_\alpha,clean}, C_{L_{max,clean}}, \rho$	$p_{TO} > p_{TO,des} > 0, p_L > p_{L,des} > 0$	$p_{TO} > p_{TO,des} > 0, p_L > p_{L,des} > 0$	$p_{TO} > p_{TO,des} > 0, p_L > p_{L,des} > 0$	Pass
			Block 20 'Control Derivatives' Unit Tests		
B20-U1	2x same Strut, Fuselage, Empennage, Propeller, Wing geometries, α, Re, ρ	2x same $C_{F_x}, C_{F_y}, C_{F_z}, C_{M_x}, C_{M_y}, C_{M_z}, C_L, C_D, C_S, C_{M_l}, C_{M_m}, C_{M_n}$ all with respect to $\alpha, \beta, p, q, r, M, U$.	2x same $C_{F_x}, C_{F_y}, C_{F_z}, C_{M_x}, C_{M_y}, C_{M_z}, C_L, C_D, C_S, C_{M_l}, C_{M_m}, C_{M_n}$ all with respect to $\alpha, \beta, p, q, r, M, U$.	2x same $C_{F_x}, C_{F_y}, C_{F_z}, C_{M_x}, C_{M_y}, C_{M_z}, C_L, C_D, C_S, C_{M_l}, C_{M_m}, C_{M_n}$ all with respect to $\alpha, \beta, p, q, r, M, U$.	Pass
B20-U4	Strut, Fuselage, Empennage, Propeller, Wing geometries, α, Re, ρ	$0° \leq \alpha \leq 10°, Re > 0, 0 < \rho < 1.225\ [kg/m^3]$	$0° \leq \alpha \leq 10°, Re > 0, 0 < \rho < 1.225\ [kg/m^3]$	$0° \leq \alpha \leq 10°, Re > 0, 0 < \rho < 1.225\ [kg/m^3]$	Pass
			Block 21 'Export Data to Pickle' Unit Tests		
B21-U1	2x same Aircraft Data, FuselageData, WingData, MassData, HorTail, VerTail, EngineData, AeroData, MaterialData, FlightCondition, StrutData, FloorData, TESTData objects.	2x same attribute values.	2x same attribute values.	2x same attribute values.	Pass
B21-U3	Aircraft Data, FuselageData, WingData, MassData, HorTail, VerTail, EngineData, AeroData, MaterialData, FlightCondition, StrutData, FloorData, TESTData objects.	All variables have input variables.	All variables have input variables.	All variables have input variables.	Pass

Continued on next page

Test ID	Input	Expected Output	Actual Output	Pass Condition	Pass/Fail
B21-U4	Aircraft Data, FuselageData, WingData, MassData, HorTail, VerTail, EngineData, AeroData, MaterialData, FlightCondition, StrutData, FloorData, TESTData objects.	All variables have valid input variables.	All variables have valid input variables.	All variables have valid input variables.	Pass
B21-U6	Aircraft Data, FuselageData, WingData, MassData, HorTail, VerTail, EngineData, AeroData, MaterialData, FlightCondition, StrutData, FloorData, TESTData objects.	All variables have valid output variables.	All variables have valid output variables.	All variables have valid output variables.	Pass

9.4. Validation

Author: Toine, Daan Contributors: Seán

In this section, the validation of the models will be discussed. The final simulation will be validated where possible. For the scope of this model validation, subsystems and systems simulation are taken into account. The validation is based on both research and modelling. Additionally, recommendations are given for subsystems that could not be validated at this stage.

Methodology

As mentioned, this validation procedure analyses subsystems. In the midterm, the validation procedure was accepted for a discrepancy of 10%. This large margin was mainly taken because many assumptions had to be made to design a preliminary aircraft family. For the validation of the final design, a 3% difference is found acceptable. This is explained in part by the detailed subsystem design and the introduction of a more rigorous iteration. Many assumptions have been relaxed, and thus the discrepancy has been made significantly smaller.

Structures validation

The code analysing plate buckling is validated using the results from the paper that gave the equations [33]. Monteiro et al. analysed a stiffened fuselage in both pure normal loading and pure axial loading. This has also been used to validate the general fuselage design. The same parameters have been used in the paper to check if the results are similar. This includes the specific loading, as well as fuselage and stringer geometry.

Panel 1 has been analysed for the validation process. The results from the simulations are subsequently compared. The parameters analysed are both the critical normal force and axial force in their respective cases. The unit of these forces is N/mm. Additionally, the buckling wave pair is compared. The results of this test have been tabulated in Table 9.3. The critical normal force, N_{cr}, differs by 0.05%, and the critical axial pressure, p_{cr}, differs by 0.42%. Additionally, the wave number corresponds precisely. This makes this part of the code validated.

Table 9.3: Validation results of the general fuselage simulation

	Normal loading	**Wave number**	**Axial Loading**	**Wave number**
Simulation	21.95	(5,1)	4.79	(1,3)
Results by Monteiro et al. [33]	21.96	(5,1)	4.77	(1,3)

The strut beam can be validated using Finite Element Method (FEM). This can be used to analyse the curved beam in more detail and see what the effects are on the structure. Furthermore, the found dimensions can be validated by modelling the expected forces on the aircraft. The tank can also be validated using FEM. It can be checked that the designed structure will withstand the internal pressure of 300 kPa until venting happens. As FEM is considered outside the scope of this project, it is recommended for a more rigorous simulation in the future.

Aerodynamics

The drag and lift coefficients can be validated either by a wind tunnel test or with a test flight. Similarly, the high-lift devices can be validated by either of these tests as well. When the wind tunnel is used, a small model can be made to check whether the airflow will result in the expected lift and drag. In the case of a test flight, the drag and lift coefficients could be obtained by conducting a static test. This entails flying at approximately the same altitude and measuring the angle of attack. This results in finding the C_{L_α} and C_D.

Propulsion

For the design of the engine, the core has been modelled. This can be validated by using the software GasTurb. The sections of the engine can be seen in Figure 9.2. The model and GasTurb results have been tabulated in Table 9.4. First, important parameters are compared, after which the different stages are analysed. For the stages, the respective pressures and temperatures are shown, as these have a large impact on both engine performance and efficiency.

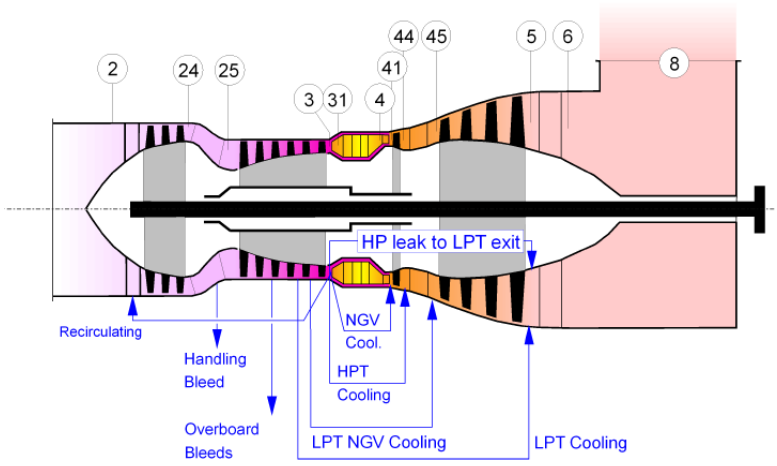

Figure 9.2: Engine sections

-

The overall propulsion values coincide nicely. The maximum error of these is the airflow, with a difference of 1.25%. This would suggest that most of the assumptions made when designing the engine still hold. 5 stage parameters differ by more than 3%. First, the low-pressure and high-pressure compressor exit temperatures have a deviation of 3.43% and 3.36%, respectively. Furthermore, the low-pressure turbine exit temperature has a 4% pressure discrepancy. Lastly, the pressures at the exit of the high- and low-pressure turbines have a 4.3% and 7.3% margin of error.

These differences can be explained by the assumptions made while modelling the core. The first one is that the model assumes that the interstage pressure losses are zero; however, this is not the case for GasTurb and real life. Furthermore, the fuel injection temperature differs between the model and GasTurb. Previous sections found that the injection temperature could not be too low to prevent freezing of fuel piping. GasTurb could not model this change. Lastly, the heat exchanger might cause different performance. However, GasTurb cannot model a heat exchanger, which caused inflated discrepancies. Taking these assumptions into account, the model is assumed to be validated at this stage. The outliers can be explained well by the assumptions and limitations of the validation model. If these limitations were removed, it is expected that the values would match more closely.

Table 9.4: Core validation data

	Model results		**GasTurb results**	
Power [kW]	3420		3400	
Thermal Efficiency [-]	0.432		0.437	
Fuel flow [kg/s]	0.066		0.066	
Air flow [kg/s]	8.10		8.00	
Stage results	**pressure [Pa]**	**temperature [K]**	**pressure [kPa]**	**temperature [K]**
ambient conditions	37.6	238.6	37.7	238.8
Inlet exit	47.5	257.0	48.9	257.1
LPC exit	126.35	359.3	130.2	347.4
HPC exit	1043.7	676.3	1075.2	654.3
Combustor exit	1041.5	1560.0	1042.9	1560.0
HPT exit	391.5	1258.3	409.1	1237.2
LPT exit	46.5	721.3	50.2	751.7
Heat Exchanger exit	37.6	693.9	n/a	n/a

The propeller of the engine can be validated by using either a wind tunnel or Computational Fluid Dynamics (CFD). These tests can check if the actual airflow is the same as the one that is expected for the model.

Aircraft system validation

Similar to the midterm report, the aircraft simulation will be compared to an existing aircraft. Since the final design is a regional turboprop aircraft, this baseline shall be taken again. The aeroplane chosen is the ATR72-600. This is a well-documented aircraft, making it a good point of reference. In Table 9.5, the input to the simulation is given.

The tabulated data differs slightly from the midterm report. First, the engine parameters are not assumed. This is because the engines are more accurately sized. This alteration will significantly improve model accuracy. Furthermore, mass fractions are not given, as the individual mass of components is computed. Lastly, interior design has been altered. As the seat pitch of the aircraft family is larger, this would give a longer fuselage, and thus results in a larger error.

Table 9.5: Reference values for validation aircraft

Variable	**ATR72-600**	**Unit**
Passengers	72	[-]
Aspect Ratio	12	[-]
Cruise Altitude	7,620	[m]
Cruise Mach	0.5	[-]
Range	1,615	[km]
Seat pitch	29	[in]
Take-off Length	1,300	[m]

As mentioned before, a discrepancy of 3% is deemed acceptable, since the simulation is much more refined compared to the midterm. Many assumptions have been relaxed compared to the preliminary sizing. The

masses are computed more accurately, as well as the take-off power. This means that a small error would be appropriate. The individual differences are then computed for the modelled ATR. As further validation is quite difficult, this is the furthest validation analysis performed for this report.

The final results are tabulated in Table 9.6. It can be seen that the model, in general, aligns closely to the baseline aircraft. One value stands out, however, being the horizontal tail area. This can be explained by a culmination of smaller model errors. Since the take-off mass is slightly lower, a larger counter moment from the wing is needed for static stability. This requires a larger tail area. Furthermore, when performing the OpenVSP simulation, it was noted that the value of pitching moment with respect to alpha, used in horizontal tail sizing, is very sensitive to the location of the centre of gravity. Additionally, the fuselage length is slightly underestimated, and thus the tail moment arm is reduced. Both require a larger horizontal tail area to achieve static stability.

In general, the normalised differences are not significant except for the horizontal tail area. The errors are not extremely large, and they can likely be explained by either incorrectly assumed statistical values or the model assumptions, many of which have been mentioned before. Since the errors are not too high, the assumptions are still determined to hold. Additionally, if the take-off mass or the cabin length were to increase, the simulated horizontal tail area would likely decrease. Thus, the model was deemed to properly predict the initial aircraft sizing, finishing the validation process.

Table 9.6: Simulation results of the baseline turboprop

Variable	Baseline Prop	Simulation	Unit	Difference	Normalised Difference [%]
MTOM	23,000	22,700	kg	-300	-1.3
Fuel mass	2,000	2,046	kg	46	2.30
Wing area	61.0	60.5	m^2	-0.5	-0.82
Wing span	27.06	26.95	m	-0.011	-0.41
Fuselage length	27.17	26.78	m	-0.39	-1.4
Take off power	498	492	MW	-6	-1.2
EOM/MTOM	0.565	0.566	-	0.001	0.18
Horizontal tail area	11.7	12.3	m^2	0.6	5.1
Vertical tail area	14.1	13.9	m^2	-0.2	-1.4

As mentioned in this chapter, additional validation methods can be employed. These include FEM, wind tunnel tests, and CFD. These are considered outside the scope of the current project. The implementation of these methods and tests, however, would add a desired level of robustness and create a more rigorous simulation. Hence, for future iterations of this design, it is recommended to use these tools.

10

Production plan

Author: Sean, Daan

This section will outline the production plan for the LEAF aircraft family. First, a description of the different sub-assemblies is provided in Section 10.1. Next, the final assembly process is described in Section 10.2 and a block diagram showing the production plan can be found below.

10.1. Subsystem assembly

Each critical sub-assembly is separately manufactured in parallel. The first of these are the fuselage sections. First, frames and stringers are manufactured and riveted to a skin section. These panels are bolted together until half shells are made. At the same time, the floor is made. This consists of the floor, floor beams, seat tracks, and the strut box that will carry most of the strut loads. The half shells are connected, and the floor is integrated. This will create individual barrels. These smaller barrels will be connected later during final assembly [52].

The wing sub-assembly is made up of a number of parts. This includes the spars, ribs, stringers, and skin panels, which make up the wing box. The leading edge and trailing edges are manufactured separately. Notably, the 2 different family members have different trailing edge devices, resulting in two different manufacturing processes for the different aircraft variants. Additionally, the ailerons and engine nacelles are manufactured, after which the final wing is assembled [52].

The empennage components are assembled in a similar way to the wing. Here the vertical and horizontal stabilisers are assembled from the spars, ribs, stringers, skin panels, leading edges, and elevators or rudders. The final sub-assembly is the engine. This starts by manufacturing the compressor and turbine blades. These are used to assemble the stages of the core. Finally, the engine is assembled from all its components, which includes the combustion chamber and bleed system, in addition to all other minor components.

10.2. Final assembly

After manufacturing all subsystems, these are integrated. Starting from the individual barrel structures, these are connected, after which the nose and tail are bolted onto the main panels. Bolting has to be used for the tail, as it is a composite structure, whereas the main fuselage is metallic. Next, installation of radial doublers and other critical components happens. At the same time, the hydrogen tank is added to the assembly. This already includes the insulation, but not yet piping. With these final components, the fuselage skeleton has been assembled.

With the skeleton defined, the wing and strut are integrated. Just like the empennage, the wing is made from a carbon fibre composite. Hence, bolting is performed. Most of the exterior has been assembled at this stage, and the next component integrated is the landing gear. The hydraulics or electrical systems have not been added, and with the interior and cockpit, these are connected [52]. The final stage is installing the propulsion system and piping to the aircraft structure. First, the engine core and propellers are installed, after which the engine is mounted. Final checks are performed to ensure that every component is assembled and integrated, concluding the manufacturing process.

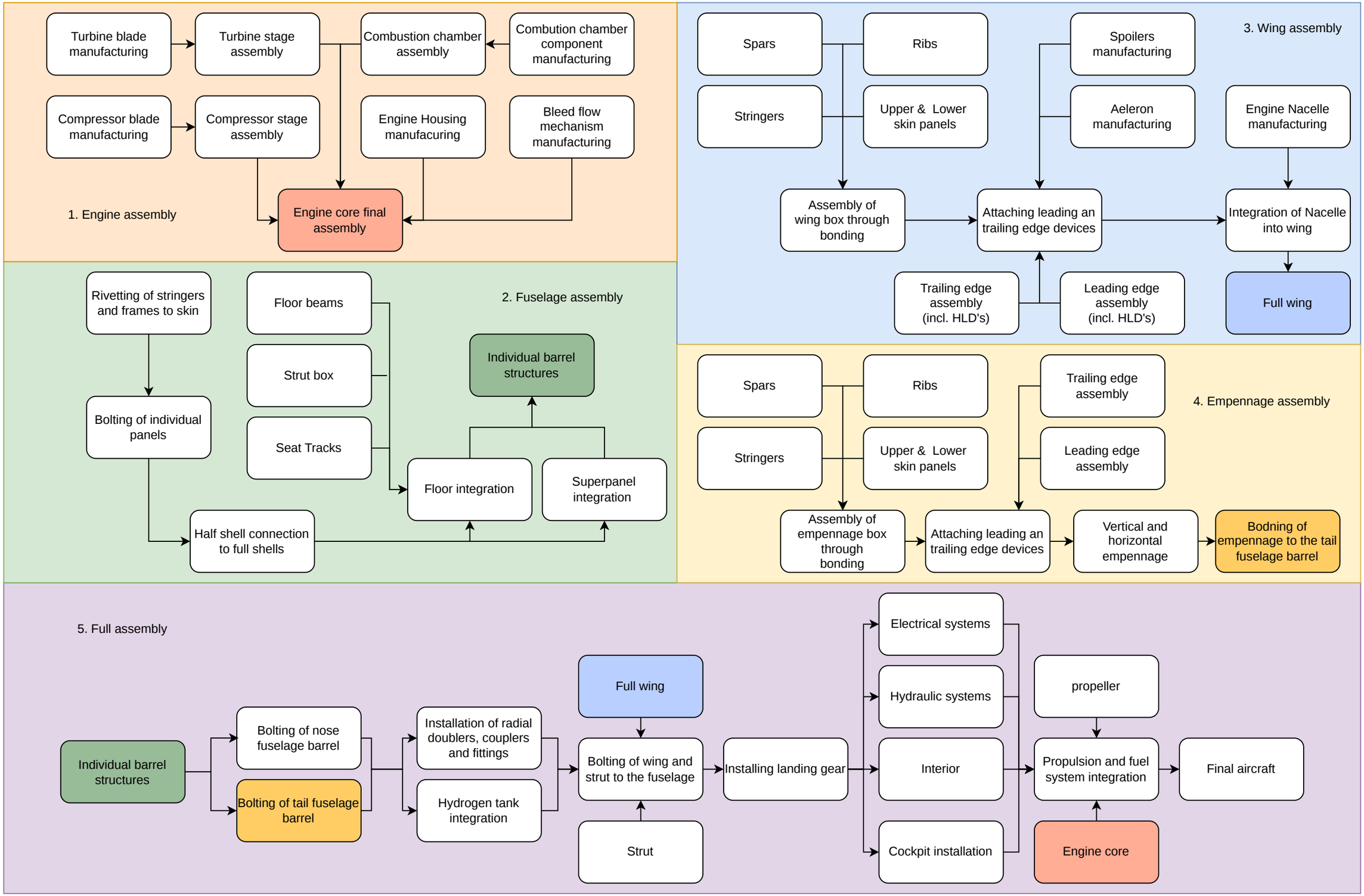
Turbine blade manufacturing
Turbine stage assembly
Combustion chamber assembly
Combution chamber component manufacturing
Compressor blade manufacturing
Compressor stage assembly
Engine Housing manufacuring
Bleed flow mechanism manufacturing
1. Engine assembly
Engine core final assembly
Spars
Ribs
Spoilers manufacturing
3. Wing assembly
Stringers
Upper & Lower skin panels
Aeleron manufacturing
Engine Nacelle manufacturing
Assembly of wing box through bonding
Attaching leading an trailing edge devices
Integration of Nacelle into wing
Trailing edge assembly (incl. HLD's)
Leading edge assembly (incl. HLD's)
Full wing
Rivetting of stringers and frames to skin
Floor beams
2. Fuselage assembly
Individual barrel structures
Strut box
Bolting of individual panels
Seat Tracks
Floor integration
Superpanel integration
Half shell connection to full shells
Spars
Ribs
Trailing edge assembly
4. Empennage assembly
Stringers
Upper & Lower skin panels
Leading edge assembly
Assembly of empennage box through bonding
Attaching leading an trailing edge devices
Vertical and horizontal empennage
Bodning of empennage to the tail fuselage barrel
5. Full assembly
Electrical systems
Full wing
propeller
Individual barrel structures
Bolting of nose fuselage barrel
Installation of radial doublers, couplers and fittings
Hydraulic systems
Bolting of wing and strut to the fuselage
Installing landing gear
Interior
Propulsion and fuel system integration
Final aircraft
Bolting of tail fuselage barrel
Hydrogen tank integration
Strut
Cockpit installation
Engine core

11

Cost

Author: Kacper, Lindsay, Daan

In this chapter, a detailed overview of the operational costs for the proposed aircraft family will be presented. In addition to these values, data for the Embraer 190 will be given to provide a point of reference and present the compliance with mission cost requirements. Finally, the return on investment and a cost breakdown structure are given

11.1. Direct operating cost

Author:Lindsay Contributor: Kacper

Direct Operating Cost (DOC) is the cost associated directly to the aircraft operations. These costs differ per aircraft performing a mission. This cost is the first thing necessary when calculating the cost per available seat kilometre. This cost is split up into multiple different parameters, which all combined make up the DOC. It is set up into cost of flying, maintenance, depreciation, fees, and financing.

Direct Operating Cost of Flying

First the direct operating cost of flying, $\mathrm{DOC}_{\mathrm{flt}}$, is assessed. This talks about all the different costs that are directly related to flying the aircraft. This includes the crew cost, fuel and oil cost, and insurance cost. Therefore the cost is calculated using Equation 11.1:

$$\mathrm{DOC}_{\mathrm{flt}} = C_{\mathrm{crew}} + C_{\mathrm{pol}} + C_{\mathrm{ins}}. \tag{11.1}$$

Explanation on the cost acronyms is followed below:

- C_{crew} - crew cost. This is estimated using the salaries of the flight attendants and pilots, while also taking into account the travel expense and vacation pay and training for the crew [53]. [1,2,3]
- C_{pol}- the fuel and oil cost. The fuel cost is assessed by finding the fuel price and density, as well as the total fuel needed for the flight. The oil is approximated as 5% of the entire C_{pol}, as a more accurate approximation at this stage is not yet possible [4, 54, 53, 5].[4,5]. For the E190 comparison, the used fuel for the same missions have been approximated in order to also get this value [55].[6,7]
- C_{ins} - the insurance cost. This is the total cost of the insurance for the airframe for passenger and third party liability as well as ground and flight risk of experiencing airframe damage. As this value depends mostly on the operator's choice of insurance, an approximation can be made using the annual block hour utilisation and block speed, as well as the annual hull insurance rate and aeroplane market price. The insurance cost is estimated by taking the insurance for the E190; a factor of 1.1 is applied for the designs, as these will be more novel technologies, and it is therefore expected that the insurance will be higher than for conventional aircraft [56].

[1] https://www.aspm.faa.gov/aspmhelp/index/ASPM__Analysis__Block_Time_Comparison.html, *Accessed: 03-06-2026*

[2] https://www.bls.gov/oes/2023/may/oes532031.htm, *(Accessed: 13/05/2026)*

[3] https://atpflightschool.com/become-a-pilot/airline-career/commercial-pilot-salary.html, *(Accessed: 13/05/2026)*

[4] https://arc-refuellers.be/products/dispensers/, *(Accessed: 19/05/2026)*

[5] https://aviationbenefits.org/other-environmental-challenges/climate-action/sustainable-aviation-fuel/conversions-for-saf/, *(Accessed: 19/05/2026)*

[6] https://www.iata.org/en/publications/economics/fuel-monitor/, *Accessed: 05-06-2026*

[7] https://www.klm.nl/en/information/travel-class-extra-options/aircraft-types/embraer-190, *Accessed:05-06-2026*

Direct Operating Cost of Maintenance

The total cost assumed to be parted into the maintenance cost is as follows:

$$\mathrm{DOC}_{\mathrm{maint}} = C_{\mathrm{lab/ap}} + C_{\mathrm{lab/eng}} + C_{\mathrm{mat/ap}} + C_{\mathrm{mat/eng}} + C_{\mathrm{amb}}. \tag{11.2}$$

- $C_{\mathrm{lab/ap}}$ - the labour cost of airframe and system maintenance, without the engines. This is implements the cost for the airframe mechanics [8], and the number of maintenance man hours needed per block hour. [53]
- $C_{\mathrm{lab/eng}}$ - maintenance labour cost for the engines. This is assumed taking into account the number of engines and maintenance hours needed per block hour per engine. [53]
- $C_{\mathrm{mat/ap}}$ - maintenance cost for materials of the airframe. Takes into account the maintenance cost per aircraft block hour. [53]
- $C_{\mathrm{mat/eng}}$ - maintenance materials for engine parts. This accounts for the material cost per engine per aircraft block hour, as well as the number of hours between engine overhauls.
- C_{amb} - the applied maintenance burden per nautical mile. This uses some statistics while including some previous parameters to find the overall applied burden.

Direct operating cost of depreciation

Total direct operating costs associated with depreciation, expressed in USD/nm (US Dollars per nautical mile) are a sum of individual depreciation costs. For this purpose aircraft is split into the airframe and major components representing a substantial fraction of the total aircraft cost.

$$DOC_{depr} = C_{dap} + C_{deng} + C_{dprp} + C_{dav} + C_{dapsp} + C_{dengsp}. \tag{11.3}$$

Explanation of the depreciation cost acronyms is provided below.

- C_{dap} - airframe depreciation cost without engines, propellers, avionics and spares. Airframe depreciation period is taken as 20 years, as used by the Lufthansa Group for newly acquired aircraft [57].
- C_{deng} - engine depreciation cost. Depreciation period same as for the airframe, as cited in [57].
- C_{dprp} - propeller depreciation cost. Depreciation period taken from Aeroplane Cost Estimation [53] as 7 years.
- C_{dav} - avionics depreciation cost. Depreciation period taken from Aeroplane Cost Estimation [53] as 5 years.
- C_{dapsp} - aeroplane spare parts depreciation. It includes a factor accounting for repair and maintenance, as well as residual resale value of aeroplane spare parts. Depreciation period same as for the airframe, cited in [57] as 20 years.
- C_{dengsp} - engine spare parts depreciation. It includes a factor equal to the ratio of costs between the cost of the engine spare parts and the cost of one engine, as well as perceived resale value of engine spare parts. Depreciation period equal to that of the engine, equal to 20 years [57].

Annual utilisation of the Embraer 190 aircraft in block hours oscillates around 2600 hrs/yr [58]. For the LEAF family yearly utilisation values are assumed to reach levels similar to the ATR42/72 aircraft, serving predominantly shorter flights with high frequency [59].

Direct operating cost of landing, navigation and registration fees

This component of direct operating cost accounts for Landing, Navigation and registration fees in USD/nm. All formulas were sourced from Aeroplane Design Part VIII [53].

$$DOC_{lnr} = C_{lf} + C_{nf} + C_{rt}. \tag{11.4}$$

- C_{lf} - landing fees. Directly proportional to the MTOM of the aircraft. After landing the aircraft has to take-off again.
- C_{nf} - navigation fees. Assumed to be $10USD$ per flight.

[8] `https://careers.klm.com/en/jobs/aircraft-maintenance-technician-b1-and-or-b2/21125/`, *Accessed:04-06-2026*

- C_{rt} - direct registration fees. Proportional to the aircraft MTOW and DOC (Direct Operating Cost).

Direct operating cost of financing

No matter if the aircraft is leased or purchased fully by its operator, additional costs of financing have to be accounted for. Roskam [53] proposes to scale the total DOC by a factor to account for lease or opportunity cost of capital when funds are used for an aircraft purchase.

$$DOC_{fin} = 1.07DOC. \tag{11.5}$$

Total direct operating cost

With all contributions calculated, the total cost can be calculated for the different aircraft. These are then compared to the E190 on the same mission as well. The depreciation and landing, navigation, registration fees are assumed to stay the same for the E190, regardless of the different missions applied.

Table 11.1: Direct Operating Cost (DOC) in USD/nm

Cost	LEAF A [USD/nm]	LEAF B [USD/nm]	Embraer 190 mission A [USD/nm]	Embraer 190 mission B [USD/nm]
C_{crew}	3.16	3.42	2.86	3.10
C_{pol}	2.45	2.04	8.33	6.09
C_{ins}	0.97	1.06	0.81	0.88
DOC Flying	**6.58**	**6.52**	**12.00**	**10.08**
$C_{lab/ap}$	0.49	0.52	0.52	0.56
$C_{lab/eng}$	0.10	0.11	0.27	0.29
$C_{mat/ap}$	1.40	1.52	1.14	1.23
$C_{mat/eng}$	1.67	1.81	3.04	3.30
C_{amb}	2.16	2.32	2.78	3.01
DOC Maintenance	**5.82**	**6.28**	**7.75**	**8.40**
C_{dap}	1.41	0.73	1.43	1.56
C_{deng}	0.32	0.35	0.60	0.65
C_{dprp}	0.09	0.10	0.00	0.00
C_{dav}	0.92	1.00	1.06	1.16
C_{dapsp}	0.16	0.10	0.17	0.18
C_{dengsp}	0.24	0.26	0.45	0.49
DOC Depreciation	**3.15**	**2.55**	**3.70**	**4.04**
C_{lf}	0.12	0.11	0.26	0.30
C_{nf}	0.01	0.01	0.01	0.01
C_{rt}	0.00	0.00	0.01	0.01
DOC Landing, Navigation, Registration Fees	**0.14**	**0.13**	**0.28**	**0.32**
DOC Financing	**1.07DOC**	**1.07DOC**	**1.07DOC**	**1.07DOC**
Total DOC	**15.74**	**15.44**	**24.53**	**23.49**

With all the variables calculated, and the total DOC, the cost per available seat kilometre can be calculated. This is done by transforming the DOC from USD per nm into just USD, so the costs are multiplied by each of their respective flight ranges. To get the final CASK, this cost is then divided by the available seat kilometres (ASK), which is the total seats available times the flight range in kilometres. For the E190, a total amount of 106 seats are assumed in the aircraft.[9]

Table 11.2: CASK for the aircraft

Parameter	LEAF-A	LEAF-B	E190 mission A	E190 mission B
Range [km]	1500	1300	1500	1300
DOC [USD/nm]	15.74	15.44	24.53	23.49
DOC [USD]	12751	19871	20150	16491
ASK	126000	75400	159000	137800
CASK[USD/ASK]	0.101	0.144	0.132	0.127

It can be seen here that the costs per available seat kilometre of the LEAF variant A is less than the Embraer on a respective mission. The LEAF variant here costs 76.5% of the CASK of an E190 on this mission. For mission B, LEAF is slightly more expensive. This makes sense, as there are less seats in the LEAF, and the ASK is just over half for the LEAF compared to the E190. This leads to the LEAF CASK being 113.4% of the E190 CASK, which shows that it still complies with the set requirement, as it is below 115% of the E190 CASK.

It is recommended for later research to perform a more detailed cost analysis. This calculation had some assumptions, mostly focused on the cost of the hydrogen in 2045. This is assumed from a paper by Johansen [5], however, the exact value will be unknown until the time arrives. The flight cost, including fuel cost, are 39% of the total direct operating cost, by far the biggest part of the DOC.

11.2. Indirect operating cost

Author: Kacper

Indirect operating costs (IOC) of aircraft are a broad category concerning all the costs incurred while operating commercial aeroplanes not linked to providing the basic air transportation service. Examples may include components such as meals, insurance premiums, freight handling costs, promotion, sales and onboard entertainment costs. As a result IOC differ significantly between various operators and cannot be drastically influenced by the aircraft designer, remaining the sole choice of the operator. Budget carriers, even when operating the same aircraft type as legacy carriers may keep almost identical DOC while having a strong tendency to minimise the IOC. For the above reasons further discussion of the IOC is omitted.

11.3. Return on investment

Author: Daan *Contributor: Lindsay*

To realise this project, investments are needed. To realise the profitability of these investments, the return on investment has to be determined. This metric is defined in Equation 11.6. R is the revenue, and E are the expenses. Since 2045 will be the entry year, it is assumed that this year will be profitable for the manufacturer. This means that the return on investment will also be determined in 2045.

$$\text{RoI} = \frac{R - E}{E}. \tag{11.6}$$

As a profit baseline, the Embraer E175 was chosen. The profit of the E175 is 46 million USD[10]. Next, the total revenue in the year of entry is determined. To facilitate this, the part of the market share has to be captured. The total addressable market is defined by the total aviation market. In 2026, this accounted for 125 billion USD of revenue, and assuming a growth of 4% a year, in 2045 this will be 263 billion total addressable market

[9] https://www.klm.nl/en/information/travel-class-extra-options/aircraft-types/embraer-190, *Accessed:16/06/2026*
[10] https://www.aeroflap.com.br/en/find-out-how-much-an-embraer-plane-and-jet-costs/, *Accessed: 23-6-2026*

(TAM) USD[11]. The total market of regional aircraft on Earth is approximately 14.5 billion USD, and this is also converted to 2045, assuming a yearly growth of 4%, resulting in a serviceable addressable market (SAM) of 30.4 billion USD[12]. Lastly, the serviceable obtainable market is considered. This is the realistic part of the market to enter. It is assumed that these are regional turboprop aircraft, where ATR has a 75% market share. This converts to a total serviceable obtainable market (SOM) of 3.37 billion USD in 2045[13]. The market shares can be seen in Figure 11.1.

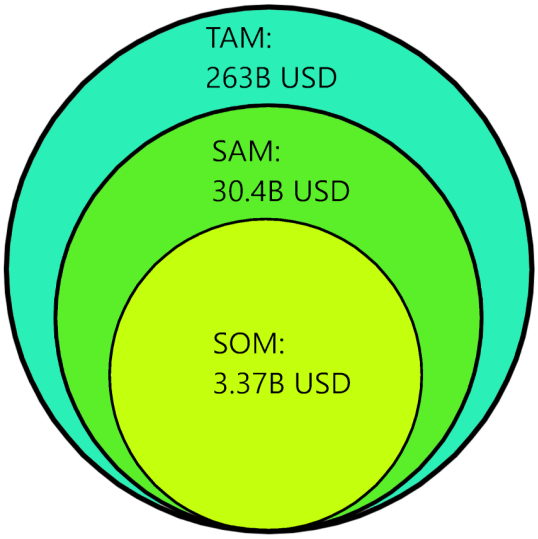

Figure 11.1: Market sizes for the LEAF aircraft family

With the SOM defined, an estimate can be made about revenue in 2045. It is assumed that a SOM market share of 20% can be reached that target year, as the demand for low-emissions aircraft is increasing. This means that a novel solution will enter a market gap, resulting in a significant available market share. This results in 690 million USD revenue, and using the profit on an E175, this corresponds to 15 aircraft sold.

Development cost

With the expected profits defined, a look is taken at all the expenses. These include the development, production, and direct operational cost. The maximum development cost is defined by STKCX24 and shall be no more than 150% of a similar single baseline variant. The actual development cost for this aircraft family is, however, quite difficult to define, as much of the required data is private. Hence, the methodology from the baseline report is used, with a slight alteration [51]. The baseline report assumed three aircraft, whereas the final design was iterated to two members. Combining this with the previously defined methodology, the following costs are computed in Equation 11.7:

$$\text{COST} = \left(3.70 \times 10^9 [\text{CAD}] \cdot 0.73 \frac{[\text{USD}]}{[\text{CAD}]}\right) \cdot \frac{\text{avg}(58, 84) \text{ pax}}{50 \text{ pax}} = 3.84 \times 10^9 \text{ [USD]}. \tag{11.7}$$

Again, this can be validated against the larger Bombardier C-series. Despite the aircraft carrying up to 160 passengers, the development costs can be scaled easily. The same methodology is used again, once more with the alteration of two family members. This cost is determined in Equation 11.8. Then, the average of the two costs is taken and multiplied by 1.5 per STKCX24. This yielded a total development cost of 5.45 $\cdot 10^9$ USD. It should be mentioned that this is an upper bound and the true development cost cannot exceed this value.

$$\text{COST} = 7.00 \text{ [USD]} \times 10^9 \frac{\text{avg}(58, 84) \text{ PAX}}{\text{avg}(130, 160) \text{ PAX}} = 3.43 \times 10^9 \text{ [USD]}. \tag{11.8}$$

[11] https://www.statista.com/outlook/mmo/aircraft/worldwide?, *Accessed: 08-06-2026*
[12] https://www.sphericalinsights.com/reports/regional-jet-market, *Accessed:08-06-2026*
[13] https://airinsight.com/atrs-turboprop-monopoly-in-slow-growth-market/,*Accessed: 08-06-2026*

Production cost

After the development cost, the production costs have to be calculated. These are estimated with the method proposed by Roskam [53]. This computes the total program production cost, which is altered to get the production cost of one aircraft. The calculation of these costs requires multiple inputs from the aircraft Class II estimation, such as the maximum take-off weight, the fuel weight, and the cruise velocity. The main function to calculate the production cost can be seen in Equation 11.9:

$$C_{apc} = C_{(e+a)} + C_{int} + C_{man} + C_{mat} + C_{tool} + C_{qc}. \tag{11.9}$$

- $C_{(e+a)}$ - engine and avionics costs. The engine cost has been calculated with the depreciation cost, and the avionics cost is estimated as 100,000 USD.[14]
- C_{int} - cost of aeroplane interior. This can differ greatly between aircraft, but is estimated per passenger interior cost.
- C_{man} - total cost of manufacturing phase. This includes the labour cost of manufacturing and the total man-hours required for the program [15].
- C_{mat} - the material cost while manufacturing. It uses the building cost for manufacturing and the flight cost of the aircraft.
- C_{tool} - tooling cost of the aircraft. Requires the man-hours and labour rate per man-hour for tooling.
- C_{qc} - quality control cost. Assumed to be $0.13C_{man}$ [53]

The different costs are all separately calculated, after which the final value for the production cost is assessed.

Operational cost

The final cost is the direct operational cost. This expense is different from the cost defined in Section 11.1. In that section, the operating cost for the use of the aircraft was defined. This section will dive into the operating cost of the manufacturing process for the aircraft family. To determine these expenses, a look is taken at the financial statements of Airbus, Boeing, and Bombardier. These values are analysed, and then normalised for the number of aircraft sold. In the year 2025, Airbus had an operating expense of 6500 million USD [16]. The operating expenses of Boeing accounted for 2456 million USD in 2025[17], and the expenses of Bombardier in the first quarter of 2026 were 116 million[18].

Airbus delivered 793 aircraft in 2025, which resulted in a direct operating cost per aircraft of 8.20 million USD per aircraft[19]. Boeing delivered 600 aircraft, resulting in a direct operating cost per aircraft of 4.09 million USD per aircraft[20]. Finally, Bombardier delivered 157 aircraft, making the direct operating cost per aircraft of 2.96 million USD per aircraft[21]. A trend can be seen that the operating cost per aircraft is proportional to the number of aircraft sold. The average of these costs is taken, being 5.08 million USD operating cost per aircraft.

All costs are now combined. Another assumption is introduced: The main development costs occur between 2026 and 2041, and after 2041 orders are placed for family members. This results in an R&D cost of 363 million USD during these years. Looking at the target year of 2045, the production expenses are estimated to be 218 million USD for 15 aircraft, and the operating costs are 76.2 million USD. This results in a total cost of 657 million USD. Using Equation 11.6, the return on investment is computed to be 5.0%. The final cost breakdown is shown in Table 11.3.

[14] https://www.gulfcoastavionics.com/blogs/blog/aircraft-instrument-panel-upgrade-cost-guide?srsltid=AfmBOop9RQ2iUK8CIKAp0zBOvZtciHzhRYF_b0T_qAqNaA7779gJ0Tcl, *Accessed:08-06-2026*

[15] https://www.salary.com/research/salary/hiring/aircraft-manufacturing-engineer-salary, *Accessed:09-06-2026*

[16] https://www.macrotrends.net/stocks/charts/EADSY/airbus-se--/operating-expenses, *Accessed: 9-6-2026*

[17] https://investors.boeing.com/investors/reports/, *Accessed: 9-6-2026*

[18] https://bombardier.com/en/investors/financial-reports, *Accessed: 9-6-2026*

[19] https://www.airbus.com/en/newsroom/press-releases/2026-01-airbus-reports-793-commercial-aircraft-deliveries-in-2025, *Accessed: 9-6-2026*

[20] https://investors.boeing.com/investors/news/press-release-details/2026/Boeing-Announces-Fourth-Quarter-Deliveries/default.aspx, *Accessed: 9-6-2026*

[21] https://bombardier.com/en/media/news/bombardier-exceeds-all-2025-guidance-metrics-successfully-completes-its-turnaround-pl *Accessed: 9-6-2026*

	Return
Revenue	675.0
Development cost	363.0
Production cost	218.0
Operation cost	76.2

Table 11.3: Revenue and losses projection for the fiscal year 2045 in million USD

It should be mentioned that throughout this section, many assumptions have been made, which impact the validity of the computed rate of return. First, the revenue may be slightly underestimated. The obtainable market size has been limited, and selling 15 aircraft in 2045 may underestimate the sales. Furthermore, the operating cost is overestimated. The methodology used looked at statistics and trends of larger aircraft manufacturers, and per aircraft, it was found that the operating cost increased if a manufacturer sold more aircraft. This can be explained by the increase in infrastructure that is needed for scaling, driving up these expenses. If this is taken into account, the return on investment moves to the more conventional value 7.5%[22].

Some assumptions may overestimate the return on investment, however. The expected market share may also be less sizeable. In the early stages of life as a manufacturer, scaling may prove to be difficult. Thus, the profit may actually be overestimated. Secondly, the development cost for larger aircraft is much lower per aircraft than for small families. This means that the development costs are likely underestimated, especially since this is a novel configuration. Furthermore, the production costs are based on statistics of existing aircraft. Material costs have increased since Roskam released his book, and quality control of the novel configurations will further drive up costs. That means that the return on investment is reduced, and may drop below zero. This means that the profitability of this project is largely based on the growing aviation market, as well as the ability to capture a sizeable market share.

For that reason, a sensitivity study of the return on investment is performed. This study is based on the three most important variables: market share, development costs, and production costs. The market share is expressed in aircraft sold, and as mentioned, this scaling may prove to be difficult, or the sales may be underestimated. Hence, for this analysis, a range of 10 to 20 aircraft sold is looked at. This is shown in Figure 11.2a. It can be seen that for 15 aircraft, the return on investment is 5%. The break-even lies slightly below 14 aircraft. This suggests that selling 13 aircraft or less, corresponding to a market share of about 17%, will result in a negative return on investment. It is thus vital for the profitability of this project to capture a sizeable market share during the start of operations.

Moving to the development costs, it was chosen to analyse the return on investment for a range of $\pm$ 10%. These results are shown in Figure 11.2b. Again, a deviation of 0 results in a return on investment of 5%. Moreover, the returns remain positive until an increase of 9.8% in the development costs. This suggests that only a significant increase in development costs may risk the profitability of the project. The last analysis is shown in Figure 11.2c for the production costs. It was found that even a 10% increase in these costs will result in profitable operations. The profit margin decreases, yet remains positive.

From this analysis, the market share was determined to be the driving parameter for profitability. If a market share of 17% cannot be captured, revenue may be lower than expenses. There are two ways to mitigate this risk. The first is an increasing demand in both low-emission aircraft and regional aircraft. Current trends show this may be happening, so this strategy would be a viable option. Secondly, a larger market share is achieved. This would require fast scaling, which is tremendously difficult in the aerospace industry. This would thus be the less likely option. To conclude, with the current assumptions in place, the project is profitable. However, there exist unknown parameters which may result in losses and a negative return on investment.

[22] https://www.iata.org/en/iata-repository/publications/economic-reports/aviation-value-chain/, *(Accessed: 09/06/2026)*

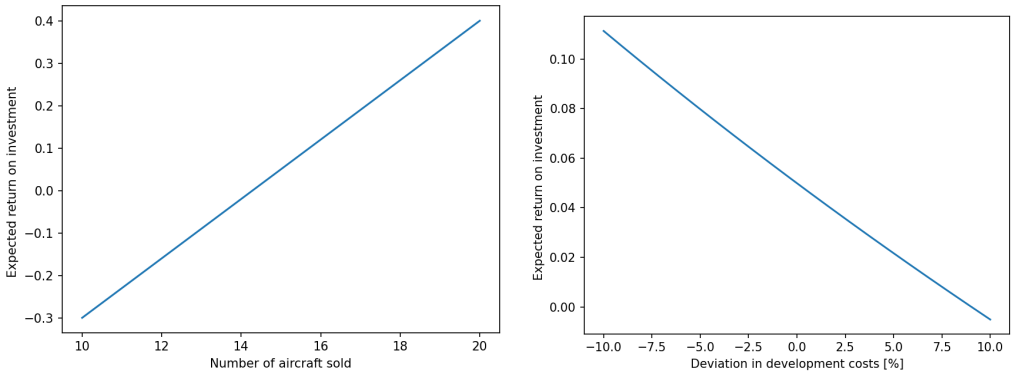

(a) Sensitivity analysis of the market share

(b) Sensitivity analysis of the development costs

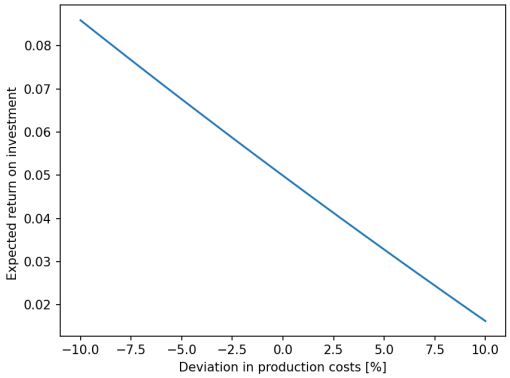

(c) Sensitivity analysis of the production costs

Figure 11.2: Sensitivity analysis of the return on investment

11.4. Cost breakdown structure

Author: Lindsay

With all the costs calculated, they are put into a cost breakdown structure, showing the different costs for both aircraft variants. These costs can be seen in Table 11.4:

Table 11.4: Cost breakdown structure

System	LEAF-A Value [2026$]	LEAF-B Value [2026$]
DOC	12816	10882
Operating Expenses	76200000	76200000
Production Cost	218000000	218000000
R&D Cost	363000000	363000000
EP	3000000	3000000
PP	102000	102000
Avionics	3640000	3640000

The final costs can be seen, these are all previously calculated. All these costs already have a safety margin in there, to account for the novel configuration and fuel type.

12

Technical resource allocation

Author: Toine

Since technical resources are limited during the design of the aircraft, the most important parameters are looked at in the technical resource budget. The table can be seen in Table 12.1. Each parameter has a specification value, which in most cases comes from the requirements of Chapter 18. In other cases, such as the MTOM, a source has been found to get a maximum MTOM. With the specification value defined, a contingency margin was defined in the baseline report [51], which results in a target value for the parameter. In the penultimate column, the actual value has been tabulated. This shows that all parameters except two, meet or exceed the specification value. The first parameter that must be noted is the actual value of the maintenance cost has been estimated to be higher than the specification value. This is due to the family aircraft being a novel aircraft and thus found to be acceptable. The second parameter that stands out is the field length. For this, the target value was 1700 meters, but the actual value is far below this, being 1300 meters. The first reason for this is the high available power the engine delivers at sea level. The second reason is that the high-lift devices increase the lift coefficient significantly.

Table 12.1: Budget allocation of technical resources and their respective contingency

Technical Resources [Unit]	Specification Value	Target Value	Actual Value	Derived from
Range and Endurance:				
Max nominal range A [km]	1500	1575	1575	STKCX05-MIS01
Max nominal range B [km]	1300	1365	1365	STKCX06-MIS01
Diversion time [min]	60	75	75	STKCX08-MIS01-SYS04, STKCX08-MIS01-SYS05
Weight:				
EOM A [kg]	–	–	12290	–
EOM B [kg]	–	–	10990	–
Max MTOM A [kg]	–	–	22030	–
Max MTOM B [kg]	39000	37050	17890	Delta Pilot Working Agreement [60]
Aircraft Availability:				
Dispatch reliability [%]	95	98	99.7	STKCX09-MIS01-SYS02
Turn-around-time [min]	60	45	54.5	STKCX27-MIS01
Performance:				
Power at cruise [kW]	–	–	4664	–

continued on next page

Technical Resources [Unit]	Specification Value	Target Value	Actual Value	Derived from
Cruise:				
Cruise mach number [-]	0.6	0.62	0.62	STKCX01-MIS01-SYS01
Cruise altitude (minimum) [ft]	25000	25500	25000	STKCX02-MIS01
Cruise altitude (maximum) [ft]	26000	26500	26000	STKCX02-MIS01-SYS01
Descent and Landing:				
Minimum Approach speed [m/s]	56.6	59.43	65	STKCX04-MIS01
Field length [m]	1800	1700	1300	STKCX03-MIS01
Flight Envelope:				
Stall speed [m/s]	46	45	45.3	STKCX04-MIS01-SYS02
Dive speed	0.75	0.775	0.775	STKCX08-MIS01-SYS12
Load factor (minimum)	-1	-1	-1	STKCX08-MIS01-SYS10
Load factor (maximum)	2.5	2.5	2.5	STKCX08-MIS01-SYS11
Cost:				
Maintenance cost [$\$/h_{\text{flying}}$]	1000	980	1400	Orixaviation [61]
Development cost [$10^9\$$]	5.625	5.5125	0.36	–
Series production cost [10^9\$]	TBD	TBD	0.218	–
Emissions:				
CO_2 emissions	2.14	2.033	0.336	STKCX12-MIS01-SYS01
NO_x emissions	0.028	0.0266	0.00022	STKCX13-MIS01
Ultra-fine matter emissions [pt/cm^3]	1000000	950000	0	STKCX14-MIS01
Lateral noise [EPNdB]	94	89.3	82.4	STKCX15-MIS01
Approach noise [EPNdB]	98	93.1	90.5	STKCX15-MIS01
Approach noise [EPNdB]	89	84.6	81.8	STKCX15-MIS01

13

Operational assessment

Author: Lindsay, Lisa

After finalising the aircraft family, it is necessary to look at how the product can be placed into the market. Therefore, first an updated market analysis is done in Section 13.3, focusing on what future usage of the aircraft depends on. After this, operational implementation strategies are assessed in Section 13.4, discussing potential ways of usage for airlines, and how the usage can be increased.

13.1. Turnaround time

Author: Lindsay

With the aircraft final parameters from the Class II estimations, the turnaround time of the aircraft can be calculated. Between the two family members, the only difference is in the passenger loading and the cargo loading. The passengers deboarding are assumed to be 20 PAX/min per door, and a boarding of 12 PAX/min per door [62]. For the cargo an unloading and loading of 110 kg/min and 95 kg/min, respectively [62]. The ground operations, such as the potable water services were taken from Sanchez [63]. These were implemented, where the cleaning of the aircraft can be performed if needed. The time taken for cleaning can be varied, depending on the use of the aircraft.

For the refuelling, a mass flow of 1.5 kg/s was assumed [4]. For the refuelling, operations such as purging, and chill down are also included in the liquid hydrogen ground operations.

The final turnaround time for both aircraft is calculated, adding all the separate times. Some are assumed to take place at the same time, such as cargo and passenger operations. However, these operations are expected to have to be separated from the refuelling[1]. With the order placed, the turnaround time can be seen in Figures 13.1 and 13.2:

[1] https://www.tudelft.nl/en/stories/articles/flying-on-liquid-hydrogen-outstanding-challenges-and-solutions/the-ground-truth-airport-operations-for-hydrogen-powered-aviation, *(Accessed:10/06/2026)*

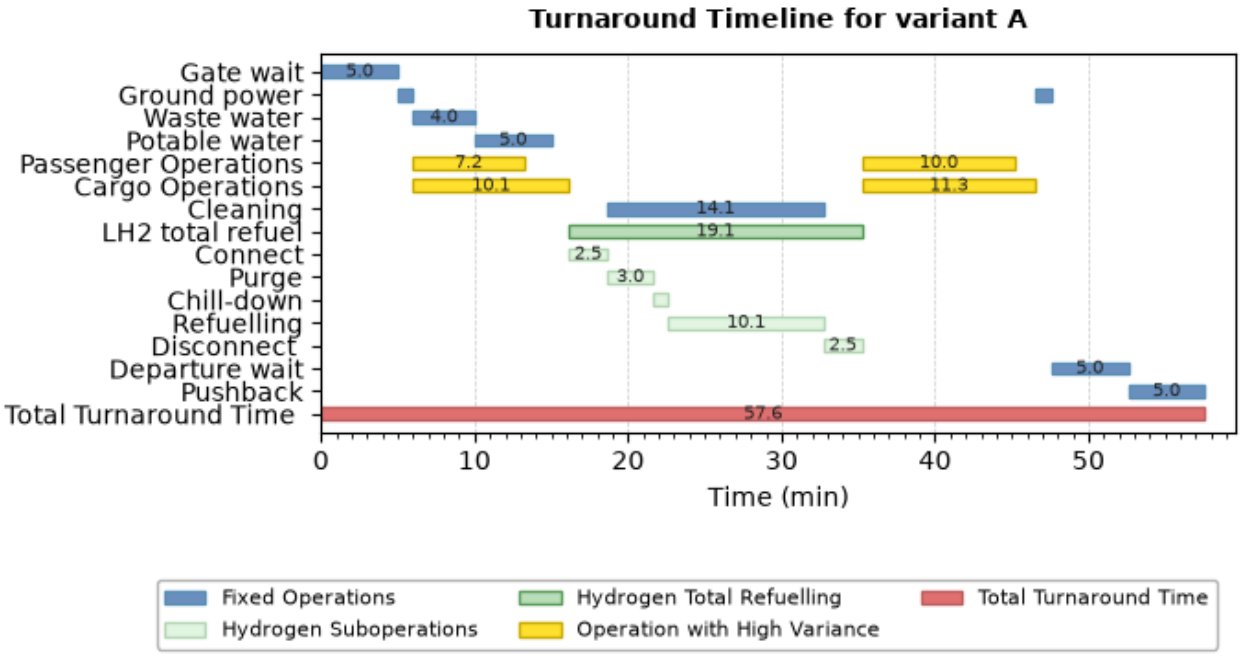

Figure 13.1: LEAF-A turnaround time

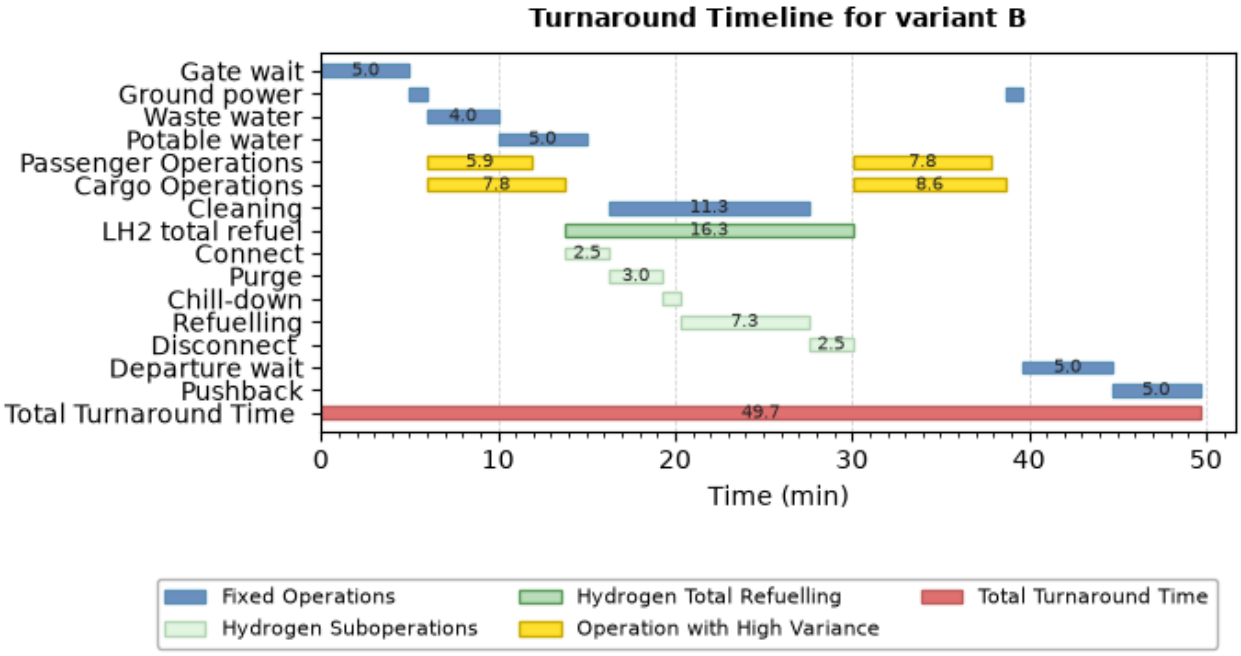

Figure 13.2: LEAF-B turnaround time

It can be seen that the turnaround times of both aircraft meet the requirement of the 60 minute full load turnaround time. LEAF-A achieves a final time of 57.6 minutes, and LEAF-B has a 49.7 minute turnaround time. For both aircraft variants, a gate and departure wait of 5 minutes is included. This is added as a buffer, and to ensure that the aircraft is placed in a safe zone, as it contains a hydrogen tank.

13.2. Commonality

Author: Lindsay

As mentioned before, the commonality is a key indicator of the mission. It has been set that the commonality index shall be at least 65% (STKCX17). Commonality can be defined in numerous ways. For this application, the aircraft component commonality index (CI) is used, as proposed by Zhang et al. [64]. This calculation is slightly modified, in order to derive the part commonality between the two aircraft. This part commonality is decided to be the most important type of commonality, as then the parts are assumed to be able to be manufactured and maintained with the same toolsets. When a certain part of the aircraft is the same for both the aircraft variants, they get set as common, otherwise as uncommon. Then the average is calculated over all the parts to find the percentage, the total calculation can be seen in Equation 13.1:

$$CI = \frac{\sum_{i=1}^{n} W_{B,i} f_i}{\sum_{i=1}^{n} W_{B,i}}. \tag{13.1}$$

Where the final commonality is CI, and $f_{1,i}$ is the commonality relationship between the target and baseline aircraft. For this, the baseline will be Aircraft A of the family, and the target would be aircraft B. $f_{1,i}$ is 1 when both aircraft subsystems are the same, and 0 when they differ. These are then multiplied by the weight of the system $W_{B,i}$, and to get the percentage divided by sum of the weights of all components.

This calculation led to the following result as seen in Table 13.1:

Table 13.1: Part commonality assessment between LEAF-A and LEAF-B

System	Com.
Wing	YES
Horizontal tail	YES
Vertical tail	YES
Nose cone	YES
Tail cone	YES
Cabin	NO
Wing frame	YES

System	Com.
Nacelle	YES
Landing gear	YES
Engines	YES
Tanks	YES
Propulsion system	NO
Flight controls	NO
Electrical	NO

System	Com.
Avionics	YES
AC	NO
Oxygen	NO
APU	YES
Furnishings	NO
Cargo	NO

A threshold of 1% is applied to the differences between the aircraft variants, to ensure that some minor calculation rounding does not reduce the accuracy of the result. This leads to a final part commonality of 75.6%, which means the requirement of 65% commonality is met. It is assumed that with this commonality being so large, the aircraft are able to be manufactured and maintained with the same toolsets. Full LEAF aircraft family is presented in Figure 13.3 showcasing the difference in capacities of both variants.

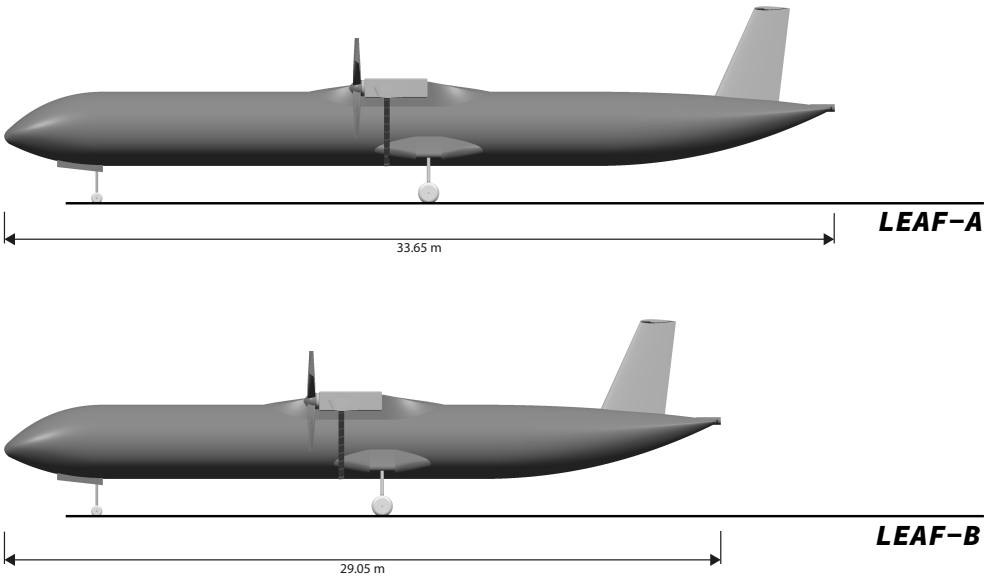

Figure 13.3: LEAF Family featuring LEAF-A and LEAF-B

13.3. Market analysis

Author: Lindsay

With the final design, the implementation into the market can be evaluated. During the first analysis done in a previous report, it became clear that there were some market opportunities for this aircraft, depending on the operational integration [51]. It is important to analyse what factor the future usage of the aircraft depends on.

A big necessity for this aircraft to fly in 2045 is airport infrastructure. It has been discovered that many airports around the world already have plans for adapting hydrogen into airport operations, and it is estimated that hydrogen storage and liquefaction will be possible from 2035 onwards [65]. A significant uncertainty results from the implementation progress of hydrogen production plants at airports, but this can be solved by transporting hydrogen to airports [65]. This assumes a significant growth in green hydrogen production worldwide.

Another factor aircraft implementation depends upon is short-haul flight market. This aircraft will require a network of flights that can be covered by regional aircraft. According to Boeing's market outlook, over 29,500 single-aisle aircraft is expected to be needed by airlines over the next 20 years [66]. Boeing also expects that over the next 20 years, nearly 80% of aeroplanes currently in service will be replaced [67].

With the continuation of global warming, markets can be further opened up if governments decide to increase the tax on kerosene aircraft. This would make it more financially beneficial to fly with sustainable aircraft, to reduce the overall emissions of an airline. The idea of a novel aircraft is not new, as there are a few novel designs that are currently assessed by the market. These aircraft include the ES-30 by Heart Aerospace and the Elysian E9X[2,3]. These examples show that this aircraft family aligns with the realistic possibilities in the near future.

13.4. Operational implementation strategies

Author: Lindsay

It is clear that the aircraft has a place in the market, when the implementation of the family is optimised. Potential implementation strategies for it can be assessed, such as the aircraft as a feeder to hub airports, a sustainable regional point-to-point airline, or by taking advantage of remote places with government subsidies, for example. These different types of integration of the family are assessed, as well as the type of customer that can want the aircraft.

[2] `https://heartaerospace.com/es-30/` *(Accessed: 06/05/2026)*
[3] `https://elysianaircraft.com/` *(Accessed: 06/05/2026)*

Passenger operations

As shown by an ATR turboprop market outlook, regional turbojets are of great use for opening new routes, and figuring out whether or not these routes are profitable, as these jets are the first to come, and so there will be less competition than in bigger cities [68]. ATR also shows that turboprop aircraft can be implemented for growing, stable, and decreasing demand [68]. They state that it can adopt a mixed-fleet strategy for growing demand, has regular regional services for stable demand, and smaller turboprops with less capacity can be applied to decreasing demand. For the changing demand over routes, it is more profitable to have the family aircraft there. If the demand for a certain route increases and a smaller aircraft cannot take all the passengers that would want to take the flight, this would lead to passenger spill. This family concept could reduce the spill, by recapturing the spilled passengers when changing the variant from the smaller to the bigger variant. As crew are qualified to fly both aircraft, the aircraft can be changed when demand is high without needing to change the crew assigned to the flights.

Cargo variant

As mentioned in Chapter 2, the aircraft can also be modified to function as a cargo aircraft. The regional freighter fleet currently consists of 92% turboprops [68], and 67% of turboprop freighters that have been implemented in freighter fleets were previously passenger aircraft of about 70-seats. This shows that LEAF-A can be converted into turboprop regional freighter fleets, as well. Besides this, the intra-Europe cargo is expected to grow with 2.1% [67], which shows that the increase of freighters is also needed.

As found by the European Commission, cargo has a catchment area of 800 km [69]. This means that the aircraft do not have to land in major hubs, but can instead go to smaller, more remote airports, as long as they are within a 12-hour truck range [70]. The cargo implementation can be done by a non-integrator airline, as many of the top cargo carriers around the world are non-integrators[4]. This means that the aircraft can be put into the market with a main focus on passenger transport, while also regionally transporting cargo with a small number of cargo aircraft.

There are multiple ways of transporting cargo in aircraft, the first one that can be implemented is using unit load devices (ULD). Using the exact same cross-section as the passenger variant means that the only ULD that can be implemented is the LD3-45[5]. This cross-section can be seen in Figure 13.4:

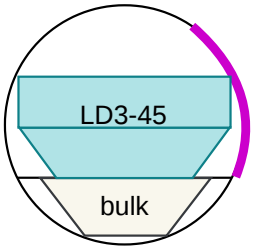

Figure 13.4: Cargo cross-section with ULDs

By only using the cylindrical part of the cabin from LEAF-A, a total of 11 ULDs fit in the aircraft. However, it can be seen that there is a lot of excess volume that is not used when using the unit load devices. Nevertheless, they are very simple to implement, as the ULDs can be completely filled before the aircraft arrives. Then they only have to be put into the aircraft, which will save time compared to bulk cargo. Loading and unloading a container takes 1.5 min, while bulk cargo unloads 150 kg/min, and loads 120 kg/min [62].

Due to the inefficiency of the space used, another option is to use personalised pallets. The pallets can be entirely filled up to the dimensions available in the aircraft when having personalised pallets. The pallets can then be put into the aircraft the same way ULD's would be implemented. This option can lead to a third family member, the LEAF-F. Specifications on the cabin and the cross-section can be seen in Figure 13.5:

[4] https://www.aircargonews.net/data-hub/top-airfreight-forwarders-airlines-airports/top-25-cargo-carriers/, *Accessed: 08-06-2026*

[5] https://www.mainfreight.com/belgium/en-nz/info-point/air-freight-containers, *Accessed:09/06/2026*

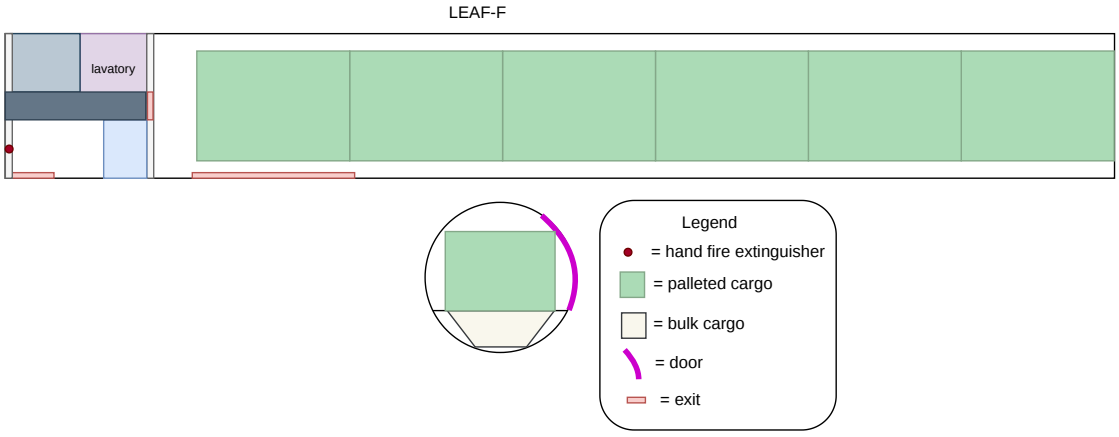

Figure 13.5: LEAF-F freighter cabin option

It can be seen that when keeping the floor at the same level as the passenger variants, there is quite some underfloor area still available after loading the pallets. This underfloor area, as well as some spots far back in the aircraft, can be used for regular bulk cargo. By using both pallets and bulk, the aircraft available volume can be optimised as best as possible.

For the doors of the aircraft, one type I door is used, and one bigger cargo door. The cargo door is assumed to be the same door as the ATR-72 freighter[6].

With this aircraft variant also initially designed, the sizing methods are performed, and the following payload-range comparison is made between the now three designs, and can be seen in Figure 13.6:

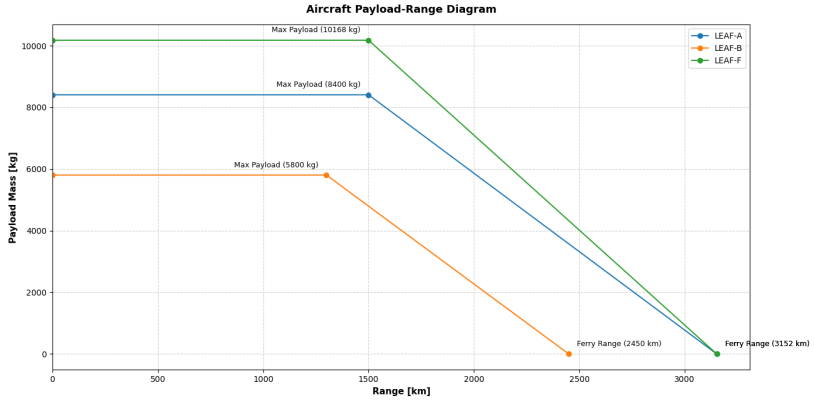

Figure 13.6: Payload range for all variants

It can be seen that LEAF-A and LEAF-F both have the same range, which makes sense as the freighter is a modified LEAF-A version. The freighter variant carries an additional 2 tonnes. This comes from the fact that the furnishings and two flight attendants from LEAF-A are exchanged to cargo. This leads to a final payload mass of over 10 tons.

It is recommended for further research to design the details of the freighter, such as the floor. The floor at this point is assumed to be the same as the passenger aircraft. The strength of the floor when putting more weight of the cargo on it will have to be analysed. Additionally, the floor of freighters is usually a special cargo floor over which the pallets or ULDs can slide from the door the their respective place in the aircraft.

13.5. Operational flow

Author: Lindsay, Lisa

[6] `https://www.atr-aircraft.com/aircraft-services/aircraft-family/atr-72-600f-freighter/`, *Accessed:10/06/2026*

The final part of the operational assessment is to show the operational flow diagram of the aircraft. The diagram can be seen on the next page. First, it focuses on the operations and communications of the aircraft during the flight mission. It describes the different components that interact with the aircraft during the mission, such as the air traffic control, airline operational centre, and the aircraft and flight crew. These components have different interactions for the different aircraft mission states.

Besides this, it also shows the turnaround operations. These are mainly focused around the high-risk, novel operations required for the hydrogen handling. There are two different types of hydrogen refuelling, truck based and with (underground) pipes. The truck-based refuelling is expected to be the first possible way of refuelling hydrogen [71]. Implementing pipes at airports, especially smaller, regional airports, will be very costly.

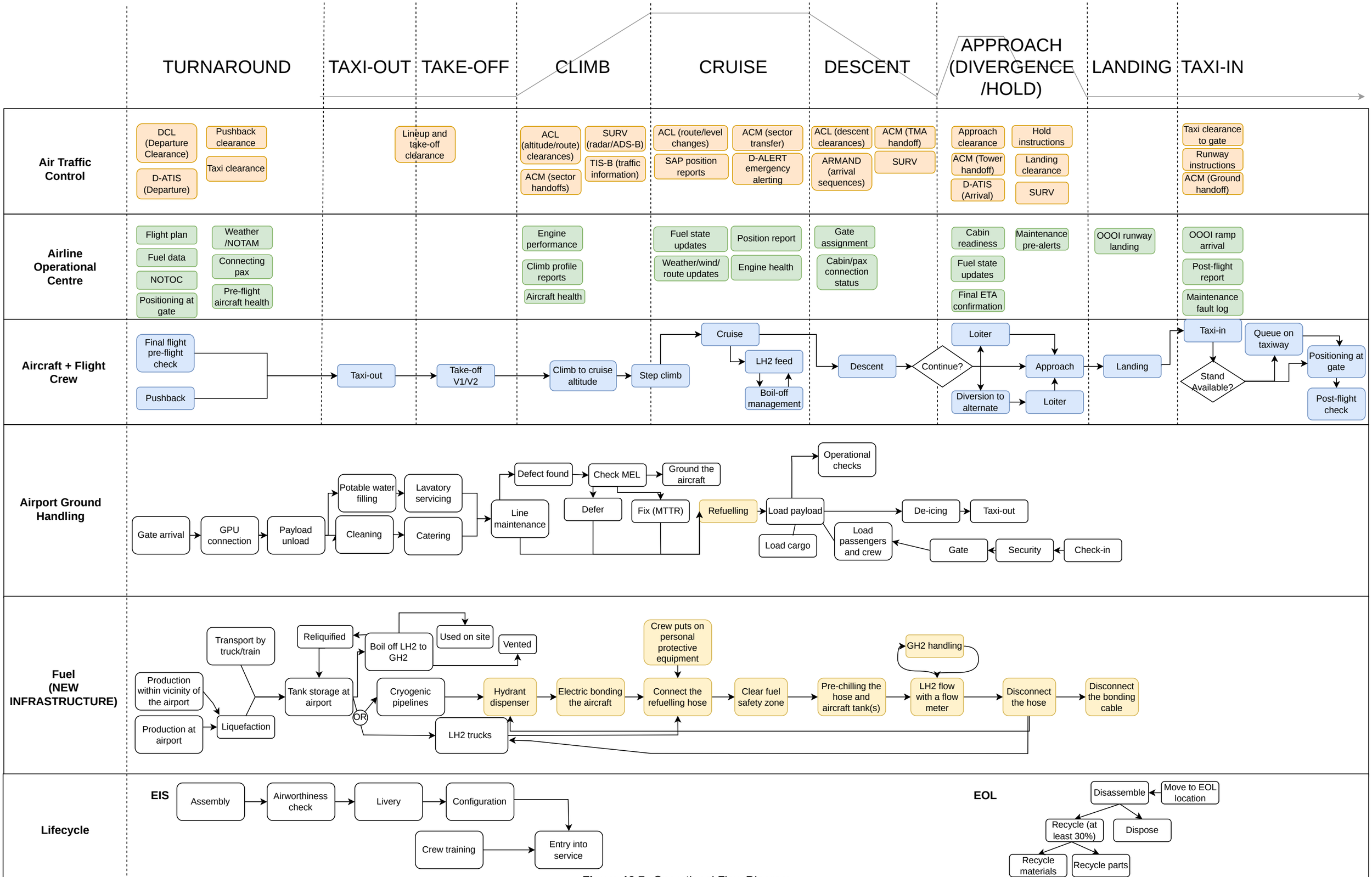

Figure 13.7: Operational Flow Diagram

14

System specifications

Author: Carlos, Daan, Lindsay, Lisa

In addition to the aircraft system, other systems are defined as well. These include the hardware and software, electrical, and data handling systems. In this chapter, these systems are shown and explained in more detail.

14.1. Hardware and software systems

Author: Carlos

The overall aircraft and system architecture is illustrated in Figure 14.1. The diagram displays the flow of energy, fluids, mechanical power and data between major subsystems of the aircraft. The turboprop engines act as the primary source of energy during flight, they provide mechanical power through the AGB which gets distributed to an alternator, hydraulic pump and fuel pumps. The hydraulic pressure accumulated can be used to move actuator in control surfaces and HLD's as well as retracting and deploying the landing gear.
The fuel system is similar to that that you would find in a SAF aircraft but with some mayor distinctions, mainly the need for emergency pressure relieve valves and a Fuel-Exhaust heat exchanger to evaporate the fuel before combustion. Finally a pneumatic system is needed to incorporate compressed bleed air into the cabin, this air must cross an air to air cooler to decrease its temperature using ram air.

The software suite onboard is shown in Figure 14.2, it displays the flow of data sensor inputs and mayor software blocks running on onboard hardware. At the core of the software stack is the kernel were a systems manager, sensor fusion engine and a computer redundancy controller, these utilities are necessary to maintain both connection with sensors but also to have an idea on how the onboard computers are behaving real time. Navigation, Control logic, actuator commands and engine controllers are connected; additional cabin systems such as onboard entertainment, PA systems and canbin atmosphere control have been added.

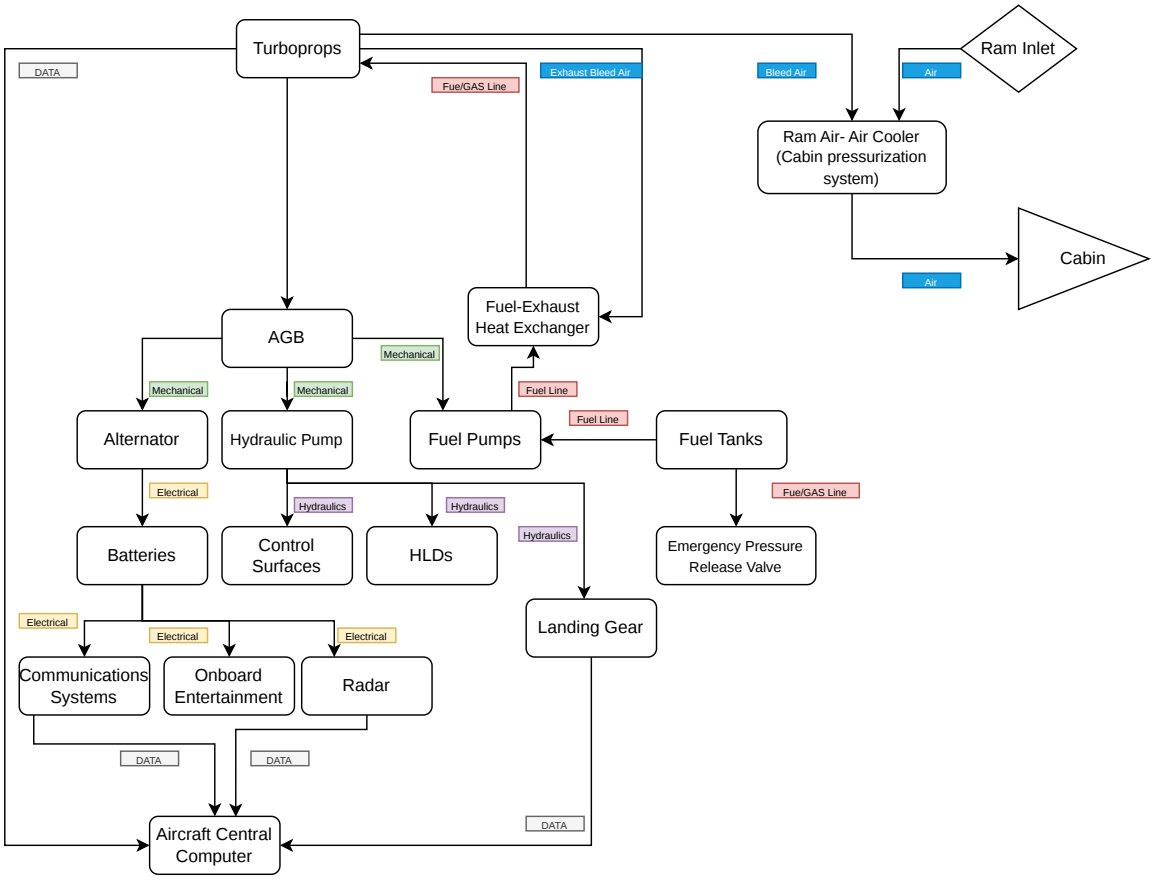

Figure 14.1: Hardware Block Diagram

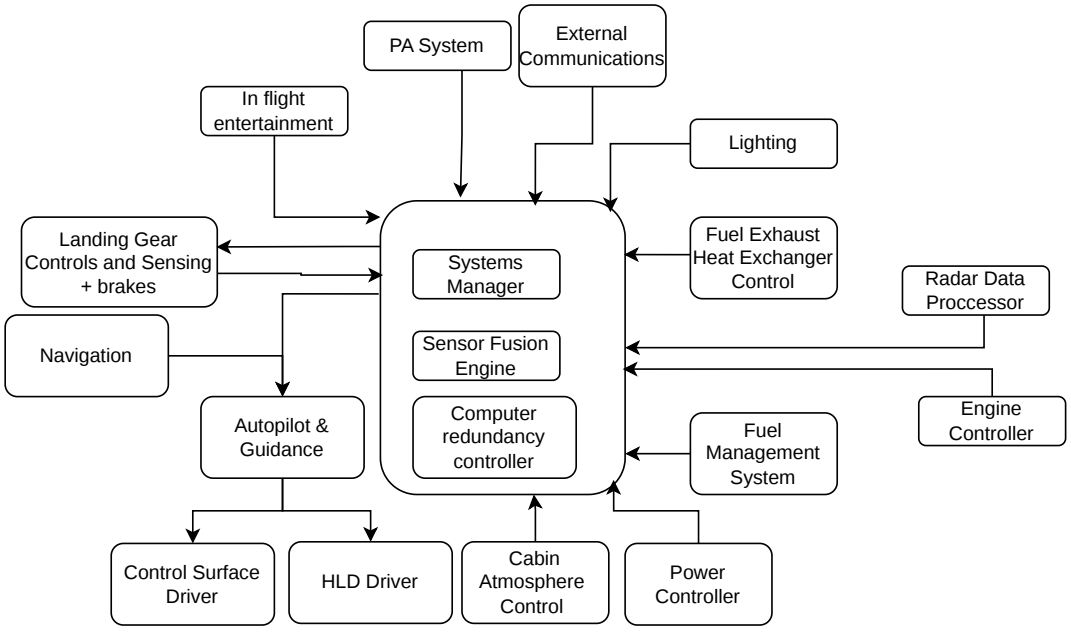

Figure 14.2: Software Block Diagram

14.2. Electrical system

Author: Daan

With the hardware and software system defined, a look is taken at the electrical system. The aircraft members have two ways of producing power. First, the engines will generate energy to be used in-flight. Second, the aircraft can be plugged into a ground generator for supply of electricity at airports. This electricity is then used throughout the entire aircraft to power other systems and subsystems. The general electrical system is shown as a block diagram in Figure 14.3.

Starting at the top, the power source is shown. These are the propeller cores. The accessory gearbox is a mechanical component that extracts rotational power from these cores. The AGB regulates the rotational power to other units, such as the fuel, oil, and hydraulic pumps. The mechanical power is then transferred to the alternator. This component converts the mechanical power into electric power. It relies on a rotating magnet inside a stator. The emerging current is alternating current (AC).

Here, a split happens. The aircraft needs a backup generator in case the engine fails: the battery. The battery can also serve as the main energy source. The alternating current of the alternator flows into the battery, which charges during flight. After the engines fail or are switched off, critical aircraft systems receive power from the batteries. In addition, it is used to kickstart the engines, as shown in the block diagram. The battery powers the clock and switches, such as the oil pressure switch. The power from the battery is converted to direct current (DC) and flows to the electrical bus, the main distributor of electricity throughout the aircraft. Alternatively, the alternator can supply the bus directly, where AC is converted to DC through another transformer.

From the electrical bus, most systems receive electrical power. These include the avionics, primary bus, and the hydrogen pressure system. As mentioned in Chapter 6, the excess pressure tank is vented to the atmosphere. Even though this valve operates on pressure, the pressure is indicated via an electrical system and shown to the pilot. Fuses and circuit breakers regulate the power each component receives. Circuit breakers are preferred, as the pilot can reset the system and they are reusable, improving sustainability.

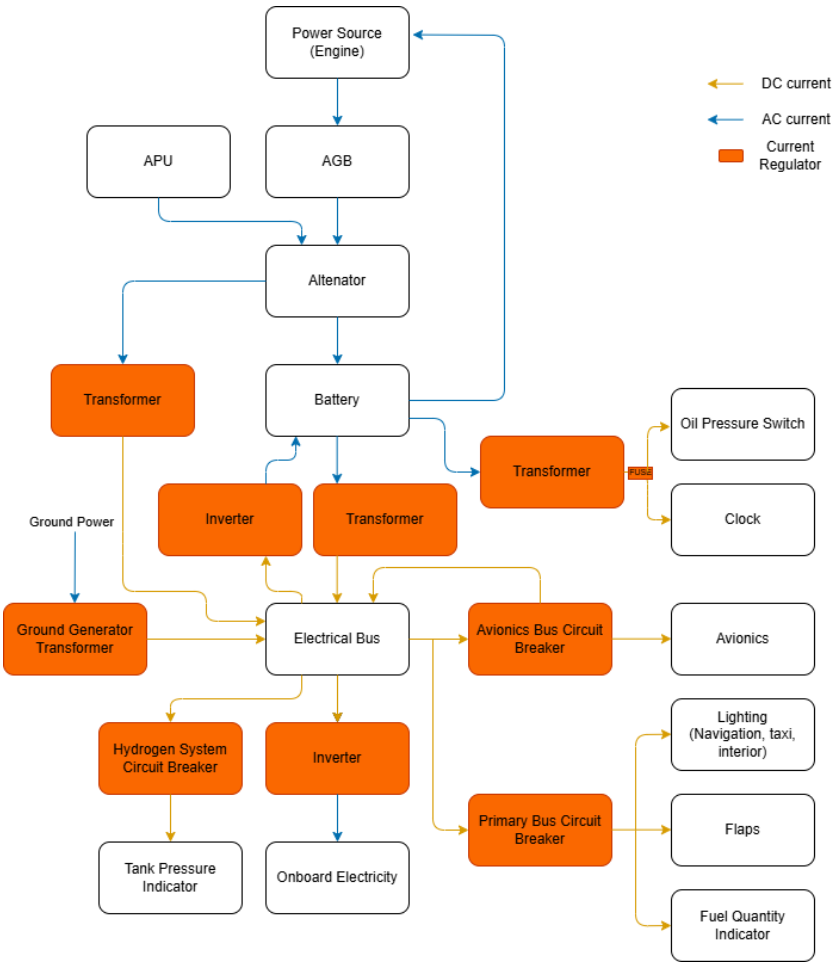

Figure 14.3: Electric system of the aircraft family

14.3. Data handling system

Author: Lindsay

After realising the electrical and hardware, software diagrams, the data flow of the aircraft can be visualised. The data is centralised in the flight computer, where all the data is stored and flows from and to. The systems after this are the multiple aircraft systems: cockpit control, autopilot, navigation system, engine control, fuel system, and structural data control. The figure can be seen in Figure 14.4.

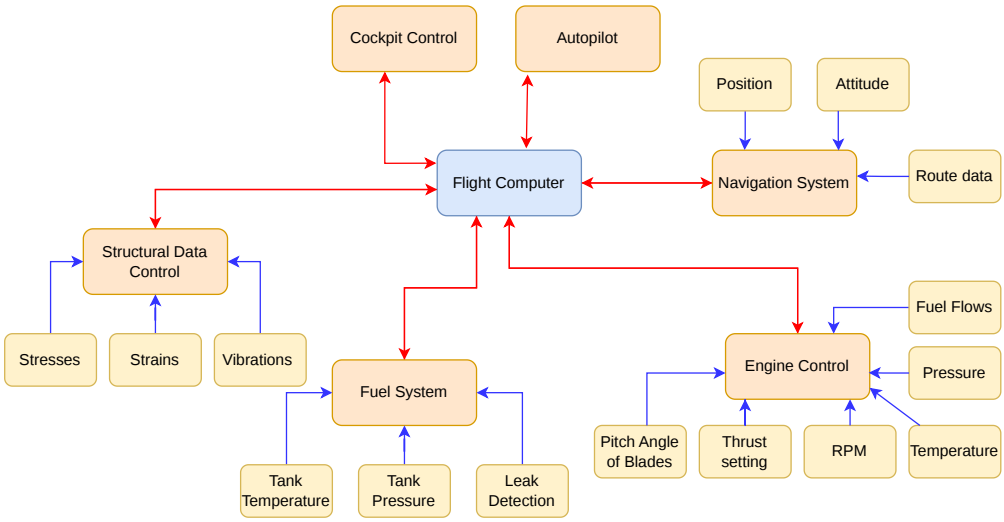

Figure 14.4: Data Handling Block Diagram

The most important subsystems are also shown in this diagram. The data from these subsystems flow into the main systems, which then flow back and forth between the flight computer. If the subsystems have a parameter that does not meet the requirements, or is close to failing, this data flows to the flight computer. The flight computer forwards it to the cockpit control, which means that the pilots are able to change their settings and make sure the requirements are met.

For example, an important parameter is the tank pressure. As previously mentioned, if the tank pressure is too high, venting will have to take place. The data of the tank pressure flows all the way to the flight computer, after which it is visible for the pilots. When the pressure is too high, and the pilots receive a warning, they can implement the venting to make the pressure lower.

14.4. Fuel system

Author: Lisa

The fuel system consists of all systems that carry hydrogen between the tailcone tank and the engines, including refuelling, defuelling, venting, pressurisation, and engine feed. The way the system works is quite different from a kerosene fuelling system since the fuel is a cryogenic liquid stored at 20 K with constant boil-off, must not allow air to enter, and vaporises in any line that loses pressure or warms up [35]. The system described here follows the reference liquid-hydrogen fuel system of Brewer [35], adapted from the four-engine, multiple-tank configuration of that study to LEAF's two-engine turboprop single-tank. The fuel goes from the tailcone tank, through a surge box and boost pumps, through a valve, foam-insulated lines, a high pressure pump and flow-control valve at each engine. Brewer achieves redundancy by feeding each engine from a different tank [35]. Since LEAF only has a single tank, redundancy is achieved by dividing the tank's fuel delivery into two feed groups, each with their own boost pumps and shutoff valve. Furthermore, by providing a crossfeed connection so that either engine and the APU can be fed from the tank if a group fails. The tank is held above ambient pressure at all altitudes so that air can never be drawn in with $P_{min} = 125$ kPa, and below the venting pressure $P_{vent} = 300$ kPa used to size the structural shell and insulation in Chapter 6. Therefore, the system must relieve pressure when it reaches P_{vent} and build pressure when it goes toward P_{min}. The way this is done is described in Section 14.4.

Engine feed and boost pumps

Liquid hydrogen cannot be drawn from the tank without pump assistance due to vaporisation in the line with loss of pressure. Each feed group therefore uses tank mounted boost pumps at the low point of the tank which raise the pressure enough to keep the hydrogen cool enough to reach the engine high-pressure pump [35]. As opposed to kerosene aircraft, an LH_2-powered aircraft is not able to take off with an inoperative boost pump. Therefore, each engine must have two pumps operating simultaneously during take-off and climb. Additionally, a third pump is added for redundancy such that the aircraft does not have to be grounded when a boost pump is inoperative. The boost pumps are housed in a surge box that traps nearby liquid to minimise unusable fuel and keeps the pumps fed in unusual situations such that it doesn't draw vapor. In the case of negative or zero g flight when fuel is pressed to the top of the surge box, there is a pressurised accumulator after the boost-pump check valves that prevents engine starvation. At cruise, a single feed group is able to feed both engines through teh crossfeef, such that electricity use is decreased. The feed lines themselves are insulated with foam. The same polyutherene foam as used for the tank in Chapter 6 is used as the outside layer of an inner stainless stell tube that carries the hydrogen. This is enclosed by an outer tube again to contain leakage, and acts as protection. Although vacuum-jacketed lines have lower heat leak, the foam is chosen because they are less likely to be damaged, cheaper to manufacture and maintain, and quicker to repair [35]. Due to cryogenic temperatures, the lines will contract which is taken into account by adding bends to the lines. At each engine, the hydrogen goes through the engine-mounted high-pressure pump. Here it is warmed and vaporised in the engine heat exchangers, where it is let into the combustor by a flow-control valve. Because the engine pump must be chilled before operation, a short idle period is needed before the engine is brought up to power [35].

Fuelling and defuelling

Fuelling and defuelling are done through a fuelling adapter and a vapour recovery adapter in the tailcone. The fuelling adapater delivers the LH_2 to the tank, and the cold GH2 accumulating in the tank due to the incoming LH_2 is returned through the vapour recovery adapter to the airport for re-liquefaction or direct use in airport operations as described in Chapter 13 [35, 72]. Both the ground and the aircraft side of the refuelline have an adapter with quick-disconnect valves that open only when both sides are connected. The flow itself enters via the bottom of the tank through an opening with perfoto maintain low flow velocity, low velocity so no turbulence forms [35]. Defuelling is done by the boost pumps also with both the fuelling adapter and vapour recovery adapter connected to ground. Some heat may be added through the tank pressure-generation system to hold the tank above the minimum pressure during defuelling.

Tank venting and pressurisation

The vent system relieves pressure to keep it below P_{vent} and the pressure-generation system builds pressure when it gets close to P_{min}. A vent box inside the tank ensures that the GH_2 can be vented without releasing LH_2. Its inlet is placed in the ullage above the LH_2 for the worst-case attitude situation. From the vent box the GH_2 passes through an absolute pressure relief and vent valve assembly. There are two regulators (one for redundancy) that hold the tank within the nominal pressure. GH_2 vented during flight is released in a lightning-protected overboard vent in the vertical tail. A back-pressure valve is placed at the end to keep a small positive pressure to keep air from coming into the vent line. There is a secondary overboard vent in the tailcone for redundancy. If the tank pressure decreases towards P_{min}, LH_2 is drawn out of the tank, gasified in a small heat exchanger and returned to the ullage to rebuild pressure to the nominal level [35].

APU

The APU is fuelled with LH_2 from the same tailcone tank. It is supplied through the crossfeed using boost-pump pressure, or just from the nominal pressure from the tank itself during initial start before electric power can supply the boost pumps [35]. Running the APU on boil-off GH_2 has been considered by Brewer, but was found to be impractical because the boil-off rate was too unpredictable. Furthermore, the gas would need significant compression to reach pressure for combustion [35], so the APU is fed with LH_2 from the tank similar to the engines.

Figure 14.5: Fuel System Block Diagram

15

Project future

Author: Toine

After this project, some steps still need to be taken to make this aircraft family a product to sell to clients. To show these steps, a project design and development logic block diagram is made and can be seen in Figure 15.1. The first step is a more detailed design of the system. After this, the subsystem is designed in more detail, which includes the aerodynamics, propulsion, structure, and flight control. The third step is building manufacturing infrastructure, which also includes the assembly lines. Then some testing, redesigning, and validation are done on test articles. After the test articles are validated, a prototype of the aircraft can be made. With this prototype, multiple tests can be performed, such as the control surfaces, flight systems, aerodynamics, and the engine. After the tests are performed successfully, the certification procedure is being finalised. This includes ensuring the airworthiness, ground-based structural tests, and the flight test campaign[1]. When the aircraft is certified, the final steps can be made for delivery. The final manufacturing process can be made to maximise efficiency and minimise the cost. Then the actual manufacturing of the aircraft happens. Then the delivery[2] happens to the clients. While the clients use the aircraft, the maintenance of them needs to be supported until the ultimate end-of-life. The timeline for the first-level blocks can be seen in Figure 19.1.

Before the aircraft can go into service multiple technological risks need to be derisked. The first one is the multi-cycle of the hydrogen tank. This will make sure that the tank will be able to handle multiple cycles without failing. The second one is the strut, mainly the interaction between the strut and the fuselage or the wing. This is to ensure that the airflow is approximately the same as the expected airflow. The third one is the embrittlement of the tank. Lastly, the refueling of the hydrogen needs to be derisked, such that the aircraft can be safely refueled at the airports.

[1] https://www.airbus.com/en/products-services/commercial-aircraft/the-life-cycle-of-an-aircraft/test-and-certification, *Accessed: 17-06-2026*

[2] https://www.airbus.com/en/products-services/commercial-aircraft/the-life-cycle-of-an-aircraft/delivery, *Accessed: 17-06-2026*

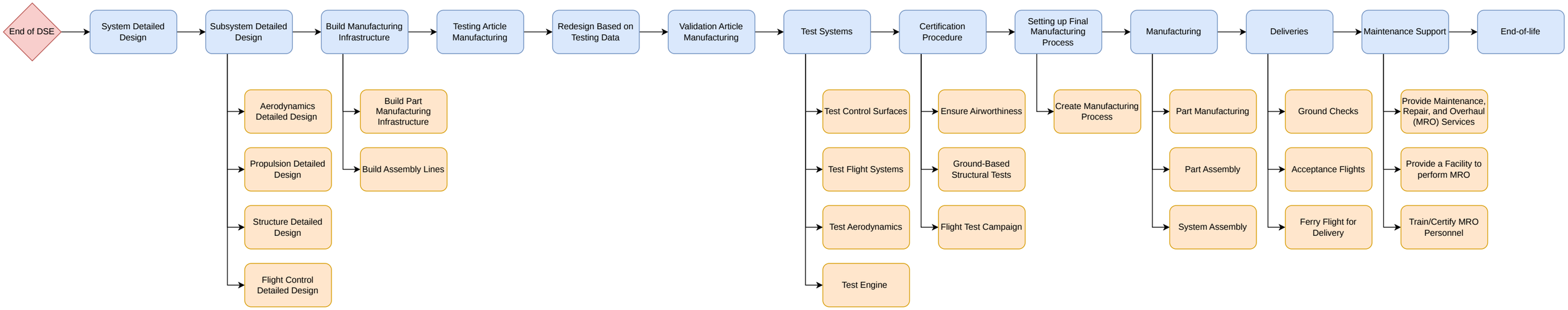

Figure 15.1: Project design and development logic block diagram

16

Sustainability

Author: Daan, Lindsay

16.1. Life cycle analysis

Author: Daan

Many components of aircraft cannot be recycled. The aircraft graveyard in Tucson, Arizona, counts over 3400 aircraft, with almost 300 more arriving yearly[1]. These aircraft are stored, after which some parts can be recycled. For modern aircraft which employ large thermoset composite structures, the recycling rate drops steeply. For that reason, a proper life cycle analysis (LCA) is needed to assess the environmental impact of the aircraft family. In previous chapters, this has already been taken into account by using metallic alloys for various structures, as these can be recycled infinitely.

For this LCA, four stages are considered: manufacturing, operations, maintenance, and end-of-life (EOL). Rahn et al. performed an explicit LCA on both a turboprop and turbojet aircraft, using these four stages [73]. The general methodology for this research is implemented for this assessment. First, manufacturing is taken into account. The EOM of both family members are 12.1 and 10.8 tonnes, respectively. In addition, the manufacturing of the turboprop engine is considered similar to the impact proposed by Rahm et al. The largest difference is the implementation of the hydrogen tank, which requires additional structure and insulation, and the novel wing design. A novelty factor is introduced to account for this. Emissions from the study were taken and normalised for both novel design and the different aircraft configuration, based on the EOM.

Next, operations are defined. According to STKCX08-MIS03-SYS01, the structural lifespan of both family members is at least 75000 FC (Flight Cycles). Using the nominal mission range for both aircraft, this comes to 162750 FH (Flight Hours) for the largest variant, and 141000 FH for the smallest variant. In the midterm report, it was computed that the energy grid produced 10 g/kWh of CO_2[3]. This was made under the assumption that the energy source was completely renewable. This assumption is revisited later. With this assumption made, the operational carbon dioxide emissions have been computed based on the fuel needed for flights. This came to 4.65 gCO_2/(PAX·km) and 3.86 gCO_2/(PAX·km) for member A and B, respectively.

The third form of pollution in the lifetime is maintenance. With the novelty of the concept, the business model will be similar to a low-cost carrier. The maintenance pollution for such a business model of a regional aircraft is $2.42 \cdot 10^{-4}$ $kgCO_2$/ASK [74]. This study analysed kerosene aircraft, whereas the sustainable family flies using liquid hydrogen. Additional maintenance is thus needed for the required hydrogen tank. An estimation for the maintenance time was given by Ramm et al., where tank maintenance was needed every 5600 FH [75]. The hydrogen tank is a safety-critical component, and thus needs shop maintenance. The tank's material is an aluminium alloy, with an emission profile of 18.07 kWh/kg[2]. Using a conversion for safety-critical materials, like the landing gear, the tank inspection yields 59.6 tonnes of CO_2 over the entire lifetime. This was added to the baseline maintenance pollution.

The last potential involves EOL emissions. Since the recyclability is similar to other metallic aircraft, the EOL warming potential is -0.3 gCO_2/ASK. This suggests that the EOL operations have a positive environmental impact, explained by recycling and sustainable disposal. This is then converted to the structural masses of both family members.

[1] https://www.war.gov/Multimedia/Experience/The-Aircraft-Boneyard/, *Accessed: 12-6-2026*

[2] https://www.carbonchain.com/blog/understand-your-aluminum-emissions, *Accessed: 12-6-2026*

With all stages defined, the warming potential of each stage, as well as the total, is computed, as seen in Table 16.1. Several results are of interest. The warming potential of the operations is significantly higher than the other stages, accounting for approximately 91% of total emissions. This mainly comes from fuel production. Furthermore, aircraft A has significantly more emissions than member B. For manufacturing, this is explained by the difference in structural mass. The additional structural mass also causes the operations potential to be higher, as more fuel is needed. Additionally, the maintenance emissions are higher. As there is more material to recycle, however, the EOL impact is better for member A than B. Comparing these results to the baseline of the E175, the family decreases the warming potential by approximately 95%, showing much promise for a sustainable aviation future.

Table 16.1: Warming potential of both family members in gCO_2/PAXkm

	Aircraft A	**Aircraft B**
Manufacturing	0.0588	0.0358
Operations	4.65	3.86
Maintenance	0.326	0.317
End-of-life	-0.0100	-0.00700
Total warming potential	5.02	4.21

With the warming potential for both family members defined, the energy grid assumption is revisited. While this assumption still holds for 2045, an analysis is performed to determine carbon dioxide emissions if a renewable energy grid is not reached. To reach an 80% CO_2 emissions reduction, a warming potential of 15 gCO_2/PAXkm is required. This can be achieved with a greenhouse intensity of 32.13 gCO_{2e}/kWh electricity produced. Several scenarios are provided in Table 16.2 showing LCA emissions with respect to the baseline. It can be seen that both the current world grid and the 2050 pledges fail in meeting the CO_2 requirements. This means that, to achieve compliance with the requirements and a more sustainable future for aviation, a significant improvement in a renewable energy grid has to be made.

Table 16.2: Analysis of warming potential as a function of electricity grid emission assumptions

Scenario	**Carbon emissions w.r.t. baseline [%]**	**Emissions [g CO_2e/ pax-km]**	**LH_2 Carbon Intensity [kg CO_2e/ kg LH_2]**[a]	**Energy grid intensity [g CO_2/ kWh]**[a]
2026 world energy grid[b]	242.1%	182	23.00	416
2050 world energy grid pledges filled[c]	25.7%	19.3	2.40	41
Compliance with STKCX12 (80% reduction)	20.0%	15	1.90	32
Best case (Used in this report)	6.2%	5.02	0.58	5

[a] `hypec.gti.energy`, (*Accessed: 18/06/2026*)
[b] `https://www.iea.org/reports/electricity-2026/emissions`, *(Accessed: 18/06/2026)*
[c] `https://eneroutlook.enerdata.net/forecast-world-co2-intensity-of-electricity-generation.html`, *(Accessed: 18/06/2026)*

16.2. Nitrogen oxide emissions

Author: Daan

Similar to the required reduction in carbon dioxide emissions, system requirements exist aiming to reduce carbon emissions by 30 %. In the midterm report, the overall methodology for determining nitrogen oxide (NO_x) emissions is defined in ICAO Annex 16 [3, 76]. Again, the ATR72-600 is taken as baseline, with 32 gNO_x/(LTO· PAX). For the designed aircraft system, engine emissions per fuel flow are multiplied by the time in the particular flight condition of the LTO cycle.

As mentioned, the nitrogen oxide emissions depend on the fuel mass flow. This value is multiplied by the time in each mode, defined by ICAO, and normalized for the number of passengers. This resulted in nitrogen oxide emissions of 9.47 gNO_x/(LTO·PAX) (Landing Takeoff Cycle passenger) for aircraft member A, and 13.1 gNO_x/(LTO·PAX) for member B. This is a reduction of 70.4% and 59.1% in NO_x emissions for both members, respectively. This is comparable to the results from the midterm, where at most a decrease of 60% was expected. Interestingly, member B has a higher relative emission than A. The LTO mass flow was quite similar, and the difference is thus explained by normalizing for PAXkm, which is lower for member B.

The large reduction in these emissions is explained in part by the decrease in fuel mass flow. This decreased by over 80%. The fuel flow is directly proportional to the nitrogen oxide pollution. Hence, a large decrease in fuel flow results in a large decrease in emissions. Additionally, using pure hydrogen also decreased the nitrogen pollution significantly. This decrease suggests the NO_x requirement has been met.

16.3. Recyclability

Author: Daan. Lindsay

With the life cycle analysis performed, the recyclability of the aircraft can be assessed. As set by the requirements, all family variants must be recyclable for at least 30% of the aircraft empty operating weight. Recycling can be divided into two different sectors: material recycling and product recycling. Both of these options are assessed in order to find the final recyclability percentages of the aircraft. This percentage is based on the weight of a certain component or subsystem, normalised with respect to the operative empty mass of the aircraft.

In order to recycle an aircraft, it is required to dismantle it entirely. The dismantling for a regional jet is estimated as 57000 USD, and the engine 26000 USD per engine [77]. This shows that in order to recycle parts of the aircraft, it is necessary to have a precise plan on the application after dismantling it.

First, the material recycling is looked at. With the fact that aircraft panels have a lot of stringers and rivets, which makes it harder to take apart everything in it [78]. The fuselage material is specified as an aluminium-2050 alloy, and is recyclable. The fuselage itself is about 15 percent of the EOM, which, as mentioned, can be recycled. Besides this, the hydrogen tank can also be recycled, which accounts for 3% of EOM.

Secondly, the product recycling can be assessed. This means that after dismantling the aircraft parts, the separate products can be sold to original equipment manufacturers (OEM). The OEM can use these spare parts for aircraft, in order not to have to rebuild, for example, the engines and landing gear.[3] The engine (propulsion system and nacelle) is 7% of EOM that is assumed to be able to be recycled this way. Alternatively, parts of the engine, such as the blades, can also be used for material recycling. Besides this, another product recycling part is the furnishings of the aircraft. They account for 7 percent of the weight compared to the EOM. A recent study by Nikou shows that it is possible to recycle the cabin interior as well [79]. Nikou states it is both feasible and beneficial, as it is a more novel concept in aircraft circular economies.

Some subsystems are made from composites. As a recommendation for recycling, these composite structures can be recycled. Thermoplastic materials can be reheated and shaped again. For epoxies, this process does not work. Heavy chemical processes are needed to recycle thermoset materials. The environmental impact of these has to be studied if the recyclability of the composite structures is to be implemented.

With all the recyclability strategies proposed, a final of 32% is mentioned here to be able to be recycled. This complies with the requirement of at least 30% of the EOM. Some other part of the aircraft that can potentially also be recycled, but are not identified as detailed yet are the empennage and the wingbox. These are likely also recyclable, and will increase the percentage of recyclability even more.

[3] `https://www.easa.europa.eu/en/light/topics/sustainability-end-life-phase-aircraft`, *Accessed: 12-06-2026*

17

RAMS study

Author: Daan, Lisa, Lindsay

Now the reliability, availability, maintainability, and safety (RAMS) characteristics can be investigated. This focuses on the functions as presented in Section 2.3. The reliability of these functions will have to be assessed, which together with the maintainability of the aircraft systems leads to an availability. Lastly, the safety of the system can be analysed.

First, reliability will be assessed, with a minimum requirement of 95%. This was set to fail when maintenance at the airports occurred, which holds the aircraft there for longer than 15 minutes beyond original planned departure.

For the calculation of the dispatch reliability (DR), the number of delays, cancellations, and services is necessary. It is a simple percentage of the total services. However, the dispatch reliability is partly subject to how the aircraft are operated. The more often an aircraft is well-maintained and inspected, the more likely it is to be dispatched on time. The DR is also affected by the amount of spare parts available. If the aircraft is operated at the airline's hub, and there are many parts available, then some fixes could potentially still occur within the fifteen-minute window. Other times, the necessary parts will have to be shipped in from other places, and ordering might take time as well.

As estimated by Feng et al., the dispatch reliability for a civil aircraft is between 99.7% and 100% [80]. The dispatch reliability of the ATR-72 freighter is 99.7%[1]. For this reason, it can be assumed that the LEAF family variants will have a dispatch reliability close to this one (99.7%). As long as the airline manages the aircraft well, a dispatch reliability of at least 95% can be reached.

The second aspect of the RAMS study is maintenance. The schedule for maintaining aircraft components is given by Rahn et al. [74]. In this study, a distinction is made between line, base, and shop maintenance. Line maintenance involves regular tasks, such as inspections. Base maintenance often takes place in hangars, usually for a longer period of time compared to line maintenance. Shop maintenance takes longer and is usually reserved for safety-critical systems.

In Table 17.1, the maintenance time of several checks is shown. This includes the quick daily checks, as well as slightly more thorough weekly checks. The A-checks take more time and are used for mechanical checks, verifying safety equipment, and inspecting filters and fluid systems, such as the hydraulic system. C-checks are much more extensive and involve opening fuselage panels, cabling, and piping. D-checks are the most extensive of the maintenance. The aircraft is almost completely disassembled, and subsystems such as the engines and landing gear are sent to shop maintenance.

The final aspect of the RAMS study is safety. For this report, safety is defined as the mitigation of product risks. Each risk has an associated likelihood and consequences of it happening, and a mitigation strategy is proposed with its revised risk and consequences. Table 17.2 shows the likelihood scale for each of the defined risks.

[1] `https://www.atr-aircraft.com/wp-content/uploads/2022/06/ATR_Fiche72-600F-3.pdf`, *Accessed: 16-06-2026*

Table 17.1: Duration and time intervals for maintenance checks, based on Rahn et al. and Ramm et al. [74, 75].

Check	Duration	Interval
Daily	2 h	1 day
Weekly	3 h	7 days
A-Check	10 h	450 FH
C-Check	168 h	5,000 FH
D-Check	672 h	6 years
Engine shop	672 h	9,000 FH
APU shop	336 h	7,000 FH
Landing gear shop	1,009 h	10 years
Hydrogen tank shop	960 h	5600 FH

Table 17.2: Likelihood scale for organisational risks.

Level	Label	Definition
L1	Very unlikely	Not expected to occur ($p < 3\%$).
L2	Unlikely	May occur once during the project ($3\% \leq p < 25\%$).
L3	Possible	Realistic chance of occurring ($25\% \leq p < 50\%$).
L4	Likely	High risk of occurring ($50\% \leq p < 75\%$).
L5	Very likely	Extremely high risk of occurring ($p \geq 75\%$).

Once these likelihoods have been declared, the consequences are defined from negligible to critical, as shown in Table 17.3.

Table 17.3: Consequence scale for organisational risks.

Level	Label	Definition
C1	Negligible	Very small effect on the development of the project, near-zero impact on the schedule, and cost of development.
C2	Minor	Minimal effect on the development of the project, hardly any impact on the schedule, and cost of development.
C3	Moderate	Moderate effect on the development of the project, worrying impact on the schedule, and cost of development.
C4	Major	Large effect on the development of the project, extreme impact on the schedule, and cost of development.
C5	Critical	Extreme effect on the development, most likely halting development, exceeding impact on the schedule, and cost of development.

In Table 17.4 the identified risks are displayed with their associated risk probability and consequence evaluation in addition a mitigation strategy is proposed and a revised risk probability and consequence evaluation; finally a member of the team is assigned to track this risk during the project duration. The final risk map pre- and post-mitigation is seen in Figure 17.1 and Figure 17.2 respectively.

Table 17.4: Technical Risk Assessment [P - Probability, I - Impact]

ID	Risk	I	P	Mitigation	I	P	Member assigned
R-01	Ground operations safety can not be ensured (refuelling operations-fire)	C5: The aircraft type certificate is pulled by the regulatory agency or the airports refuse to allow the aircraft to operate.	L2	Provide training to aircraft operators and ensure with inspections that correct refuelling protocols are being followed at airport, including safety zones. Add equipment that forces aircraft to be grounded(electrically) during refuelling operations (both described in Chapter 13).	C5	L1	Carlos
R-02	The refuelling process leaks cryogenic liquids onto refuelling personnel	C3: The aircraft is not refuelled by airports	L3	As defined in the logistical flow diagram, crew will wear personal protective equipment (PPE).	C1	L3	Viktor
R-03	Tail striking can cause the tail cone hydrogen tank to explode, bringing crashworthiness at risk.	C5: The aircraft can not be certified if it cannot be proven that the hydrogen tank in the tail can survive a tailstrike without detonating	L3	Integrate crashworthiness of fuel infrastructure onboard aircraft, as well as increasing the scrape angle of the tail.	C5	L2	Toine
R-04	Fatigue failure of strut brace	C4: If the aircraft truss fails during flight, the type certificate could be pulled; if damage is revealed during inspection, massive recalls for fixes could be necessary.	L3	Frequent inspections for cracks, as defined in Table 17.1. If cracks are found, the aircraft cannot fly until the strut has been repaired.	C4	L1	Seán
R-05	Fatigue failure of fuel tanks due to cyclic cryogenic loading.	C5: If aircraft tanks fail because of repeated thermal cycling the plane could catch fire.	L2	Frequent inspections for cracks, as defined in Table 17.1. If cracks are found, the aircraft cannot fly until the strut has been repaired.	C5	L1	Nathan
R-06	Hydrogen leakage out of tanks	C4: Hydrogen tanks may leak hydrogen due to the size of the molecule. This could accumulate and could ignite.	L3	As described in Section 14.4, the fuel system has a vapour recovery adapter used during refueling and defueling, and has a venting system when the hydrogen reaches P_{vent}.	C4	L1	Marius
R-07	Not meeting noise requirements at takeoff	C2: Airports and operators might be fined by regulatory agencies.	L3	Reduce takeoff power, design for a longer runway	C1	L3	Lindsay

Continued on next page

ID	Risk	I	P	Mitigation	I	P	Member assigned
R-08	Hydrogen leakage within the tailcone possibly damaging avionics, hydraulics, or the composite tailcone structure.	C4: causing damage to these systems can lead to critical failure of the aircraft if it happens during flight.	L2	Fuel lines are insulated, and protected with another outer steel tube to prevent leakage as described in Section 14.4. The tank itself is insulated and routinely checked as described in R-05.	C4	L1	Daan
R-09	Fuel injected at a temperature too low causes freezing issues around the fuel types and gas path in the combustor.	C4: The fuel is not injected properly, and the engine will either fail or efficiency is reduced massively.	L2	The fuel must be injected at a sufficient temperature[42]. This is performed by adding a heat exchanger. In case of failure of the heat exchanger, energy from the engine is directed to heating the fuel.	C4	L1	Toine
R-10	Environmental and price targets for hydrogen production are not met.	C4: Might not make financial sense to operator and might not meet environmental targets	L3	Track progress and be involved in the development of hydrogen production technology.	C4	L1	Daan
R-11	In-flight hydrogen venting creates a flammable cloud near the aircraft.	C4: Ignition of the vented hydrogen cloud due to proximity of a hot surface can cause an explosion during flight	L2	The venting outlet is positioned at the very aft of the aircraft, far away from hot surfaces and engine exhausts. Furthermore, venting is reserved only for extended missions (beginning of loiter) as described in Chapter 6	C4	L1	Lisa

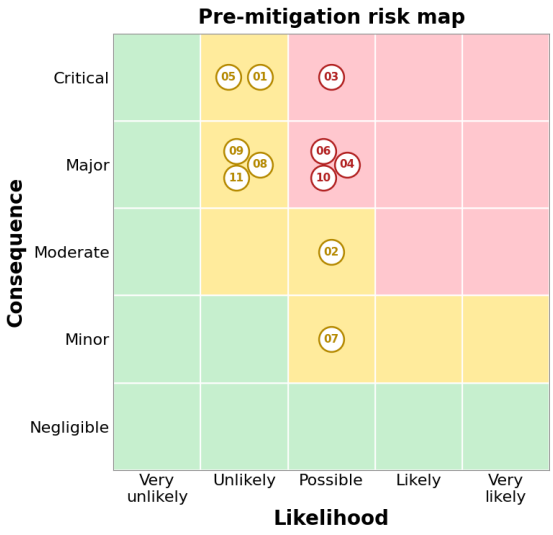

Figure 17.1: Pre-mitigation risk map

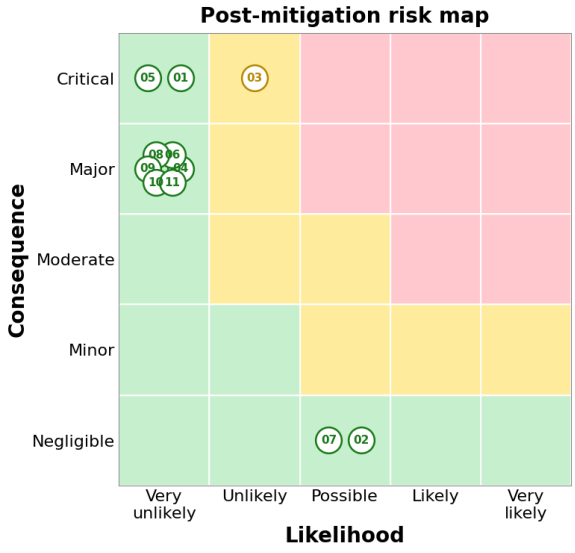

Figure 17.2: Post-mitigation risk map

18

Compliance matrix

Author: Lindsay, Daan

This chapter focuses on the different requirements set, and whether or not the design complies with these requirements. The different requirements will be analysed: stakeholder requirements, mission requirements, then system and subsystem requirements.

18.1. Stakeholder requirements

First, the stakeholder requirements will be assessed. There were 28 requirements set by the customer. Each time ”The family” or ”The aircraft” is used, the requirement refers to all family members. ”At least one family member” refers to individual aircraft. The family members that will meet each mission requirement, as specified by STKCX05, STKCX06 and STKCX07, are referred to as ”Family member A, B or C”. Here, ”A”, ”B” or ”C” does not necessarily refer to a different aircraft, but simply refers to the family member which will satisfy that requirement. ”Family member A” refers to the aircraft with the largest range (1500 km, 78 passengers), ”Family member B” refers to the aircraft with the middle range (1300 km, 58 passengers), and ”Family member C” refers to the smallest range aircraft (1000 km, 84 passengers).

Some other stakeholders were defined, for which the requirements were assessed, including the passengers (PAX), airlines (AIR), airports (APT), certification authorities, residents, and the manufacturer and supply chain.

The stakeholder requirements can be seen in Table 18.1, where the ID and requirement description is given. After this, with the design finalised, the final value for the respective component is given. After this, a check is given when the requirement is met, and the verification method is shown.

There are multiple verification ways, one is testing. For testing, the requirement will undergo actual testing to decide whether or not it complies. For analysis, there will be computations done, where possible, to check compliance. Inspection will be looking at the design to decide compliance. Finally, the demonstration will be more of an informal testing to check compliance. If requirements are not met at this stage, they have been marked with an asterisk.

Table 18.1: Stakeholder requirements derived from the customer-provided top-level aircraft requirements.

ID	Requirement description	Final Value	Check	Verification
STKCX01	The aircraft shall have a minimum cruise Mach number of 0.6.	0.62	✓	Test/Analysis
STKCX02	The aircraft shall be able to achieve an cruise altitude of at least 25000 ft (7620 m).	25000	✓	Test/Analysis
STKCX03	The aircraft shall require an aerodrome reference field length smaller than 1800 m (ICAO code number $\leq$ 3).	1750 m	✓	Test/Analysis
STKCX04	The aircraft shall have an approach speed of at least 110 kts (56.6 m/s).	126	✓	Test/Analysis
STKCX05	At least one family member shall have a cruise range of at least 1500 km with 78 PAX at 100 kg/PAX.	LEAF-A	✓	Test/Analysis

continued on next page

ID	Requirement description	Final Value	Check	Verification
STKCX06	At least one family member shall have a cruise range at least 1300 km with 58 PAX at 100 kg/-PAX.	LEAF-B	✓	Test/Analysis
STKCX07	At least one family member shall have a cruise range at least 1000 km with 84 PAX at 100 kg/-PAX.	LEAF-B	✓	Test/Analysis
STKCX08	The aircraft shall comply with CS-25, or with the certification appropriate to the selected concept [7].	Complies	✓.	Analysis
STKCX09	The aircraft shall have a minimum dispatch reliability of 95%.	SAF		Analysis
STKCX10	The aircraft shall be controllable by a human crew.	2 pilots	✓	Test
STKCX11	All critical energy storage and distribution systems shall incorporate redundancy to ensure safe continuation of flight after single-point failures.	at least double redundancy	✓	Analysis
STKCX12	The aircraft shall reduce well-to-wake CO_2 emissions by 80% versus an Embraer 175 (or similar) on nominal missions, for equal payload/range combinations.	95%	✓	Analysis
STKCX13	The aircraft systems shall emit no more than 561.01 g of NO_x per hour during ground operations[1].	168.30	✓	Test/Analysis
STKCX14	The aircraft shall emit no more than 238.73 mg of non-volatile particulate (nvPM) mass per hour during ground operations.	0	✓	Test/Analysis
STKCX15	The aircraft shall meet the ICAO Annex 16, Volume I, Chapter 14 noise standard [81].		$*$	Test/Analysis
STKCX16	At least 30% of components or component materials, by mass percentage of OEM, shall be recyclable.	32%	✓	Analysis
STKCX17	All family members shall have a commonality index of at least 65%.	75.6%	✓	Analysis
STKCX18	All family members shall be producible with the same toolset.		$*$	Analysis
STKCX19	All family members shall be maintainable with the same toolset.		$*$	Analysis
STKCX20	The largest aircraft variant shall have a maximum cargo volume of at least 15 m^3.	28 m^3	✓	Analysis/Inspection
STKCX21	All family members shall have a maximum cargo volume of at least 12 m^3.	18 m^3	✓	Analysis/Inspection
STKCX22	The direct operating CASK of aircraft A shall be no more than $15.18 \frac{USDcent}{ASK}$.	10.10	✓	Analysis
STKCX23	The direct operating CASK of aircraft B shall be no more than $14.61 \frac{USDcent}{ASK}$.	14.40	✓	Analysis

continued on next page

[1] https://blog.zhaw.ch/metenvia/2023/02/16/aircraft-engines-idle-taxi-gaseous-emissions/ *(Accessed: 26/04/2026)*

ID	Requirement description	Final Value	Check	Verification
STKCX24	The operating cost per block hour of the smaller variant shall be at least 5% lower than that of the larger variant.	23.5% lower	✓	Analysis
STKCX25	The development cost of the family shall not exceed 150% of the development cost of a single equivalent baseline variant.	150%	✓	Analysis
STKCX26	The aircraft shall have a wingspan smaller than 36 m on the ground (ICAO code letter A, B, and C [82]).	36m	✓	Analysis
STKCX27	The aircraft shall enter into service no later than 2045.	2045	✓	Demonstration/Analysis
STKCX28	The aircraft shall have a maximum turnaround time of 1 hour at 100% load factor.	56 min	✓	Analysis/Demonstration
STKPAX01	The aircraft shall be comfortable.	Yes	✓	Demonstration
STKAPT01	The aircraft shall not require costly redo of the existing infrastructure.	Yes	✓	Analysis
STKAPT02	The ground service of the aircraft shall use the same ground equipment as current generation aircraft for payload and handling.		*	Demonstration
STKAIR01	The aircraft shall have acquisition costs no higher than **TBD**			
STKAIR03	The aircraft shall allow onboard product customisation of the cabin layout.	Yes	✓	Demonstration
STKAIR04	All family members shall have the same type rating.	Yes	✓	Analysis

18.2. Mission requirements

With the stakeholder requirements set, the mission requirements are focused on what the system must do. These flow down from the stakeholder requirements, and it can be seen in Table 18.2.

ID	Requirement description	Final Value	Check	Verification
STKCX01-MIS01	The aircraft shall sustain cruise at at least Mach 0.6 at the initial cruise altitude specified by STKCX02-MIS01.	0.62	✓	Analysis/Simulation
STKCX02-MIS01	The aircraft shall be able to achieve a cruise altitude of at least 25000 ft (7620 m) under standard ISA atmosphere at the MTOM.	25000	✓	Analysis
STKCX03-MIS01	The aircraft shall have an aeroplane reference field length of less than 1800 m computed per the ICAO Annex 14 (minimum field length for take-off at MTOM, sea level ISA, still air, zero runway slope) [82].	1750 m	✓	Analysis/Simulation
STKCX04-MIS01	The aircraft shall have an approach speed of at least 110 kts (56.6 m/s) at MLM in the landing configuration.	126	✓	Analysis/Simulation

continued on next page

ID	Requirement description	Final Value	Check	Verification
STKCX05-MIS01	At least one family member shall be capable of carrying 78 passengers at 100 kg/PAX over a cruise range of at least 1500 km.	LEAF A	✓	Analysis/Simulation.
STKCX06-MIS01	At least one family member shall be capable of carrying 58 passengers at 100 kg/PAX over a cruise range of at least 1300 km.	LEAF-B	✓	Analysis/Simulation.
STKCX07-MIS01	At least one family member shall be capable of carrying 84 passengers at 100 kg/PAX over a cruise range of at least 1000 km.	LEAF-A	✓	Analysis/Simulation.
STKCX08-MIS01	The aircraft shall be certifiable per CS-25 (or equivalent Part 25 Special Conditions) [7].		$*$	Analysis
STKCX08-MIS02	The aircraft shall carry 5% extra fuel/energy compared to the mission fuel/energy for each mission as a reserve (alternate, hold, contingency).	At least 7.5%	✓	Analysis
STKCX08-MIS03	The aircraft shall be designed to maintain continued airworthiness per CS-25 Subpart H over a service life of at least 75000 flight cycles[2].	Designed for at least 75000 FC	✓	Analysis
STKCX09-MIS01	The aircraft shall achieve a minimum scheduled-service dispatch reliability of 95% (failure is a delay more than 15 minutes or cancellation).	99.7%	✓	Analysis
STKCX09-MIS02	The aircraft shall limit the contribution of any single subsystem to the dispatch-reliability budget to at most 15%.		$*$	Analysis
STKCX10-MIS01	The aircraft shall be operable by a flight crew of at most 2.	Only 2 pilots could fly the aircraft	✓	Inspection
STKCX11-MIS01	The aircraft shall tolerate any single failure in the energy storage without loss of controlled flight.		$*$	Analysis
STKCX11-MIS02	The aircraft shall tolerate any single failure in the energy distribution without loss of controlled flight.		$*$	Analysis
STKCX12-MIS01	Family variant A shall emit no more than 3214.68 kg of well-to-wake CO_2 on the 1500 km/78 PAX design mission, equal to 20% of the well-to-wake CO_2 emissions of a reference Embraer 175 on the same mission.	640.08 kg	✓	Analysis
STKCX12-MIS02	Family variant B shall emit no more than 2786.06 kg of well-to-wake CO_2 on the 1300 km/58 PAX design mission, equal to 20% of the well-to-wake CO_2 emissions of a reference Embraer 175 on the same mission.	298.35 kg	✓	Analysis
STKCX12-MIS03	Family variant C shall emit no more than 2143.12 kg of well-to-wake CO_2 on the 1000 km/84 PAX design mission, equal to 20% of the well-to-wake CO_2 emissions of a reference Embraer 175 on the same mission.	See LEAF A	✓	Analysis

continued on next page

[2] https://airguide.info/how-long-does-a-boeing-plane-stay-in-service-before-retirement/ *(Accessed: 26/04/2026)*

ID	Requirement description	Final Value	Check	Verification
STKCX12-MIS04	The aircraft shall accept an energy source or energy-source mix consistent with the well-to-wake CO_2 reduction target.	LH_2	✓	Analysis
STKCX13-MIS01	The aircraft systems shall emit no more than 561.01 g of NO_x per hour during ground operations [3].	168.303	✓	Test/Analysis
STKCX14-MIS01	The aircraft shall emit no more than 238.73 mg of non-volatile particulate (nvPM) mass per hour during ground operations.	0	✓	Test/Analysis
STKCX15-MIS01	The aircraft shall meet the cumulative noise margin of ICAO Annex 16, Volume I, Chapter 14 at the three certification points (lateral, flyover, approach)[81].		$*$	Test/Analysis
STKCX15-MIS02	The aircraft shall maintain the Chapter 14 noise margin across the full payload/range spread.		$*$	Test/Analysis
STKCX16-MIS01	At least 30% of family OEM shall consist of components or materials classified as recyclable.	32%	✓	Analysis
STKCX16-MIS02	The family shall be designed for disassembly at end of life such that the recyclable OEM mass fraction of STKCX16-MIS01 is achievable in practice.	Has been designed for	✓	Analysis
STKCX17-MIS01	The family shall achieve a commonality index of at least 65%.	75.6%	✓	Analysis
STKCX17-MIS02	The cockpit, avionics, propulsion, and fuselage cross-section shall have commonality across all family variants.	Has been designed for	✓	Analysis
STKCX17-MIS03	The 65% commonality index shall be quantified using a defined *Aircraft Component Commonality Index* normalised with respect to component weight instead of cost [64].	Has been designed for	✓	Analysis/Demonstration
STKCX18-MIS01	All family variants shall be producible on a single final-assembly line using a shared production toolset.	Taken into account in production plan	✓	Analysis
STKCX19-MIS01	All family variants shall be maintainable using a shared maintenance toolset.		$*$	Analysis
STKCX20-MIS01	The largest family variant shall provide at least 15 m^3 of usable cargo-hold volume, separate from the passenger cabin.	25 m^3	✓	Analysis/Inspection
STKCX21-MIS01	All family members except the largest variant shall provide at least 12 m^3 of usable cargo-hold volume, separate from the passenger cabin.	18 m^3	✓	Analysis/Inspection
STKCX22-MIS01	The direct operating CASK of aircraft A shall be no more than $15.18 \frac{USDcent}{ASK}$.	10.20	✓	Analysis
STKCX23-MIS01	The direct operating CASK of aircraft B shall be no more than $14.60 \frac{USDcent}{ASK}$.	14.40	✓	Analysis

continued on next page

[3] https://blog.zhaw.ch/metenvia/2023/02/16/aircraft-engines-idle-taxi-gaseous-emissions/ *(Accessed: 26/04/2026)*

ID	Requirement description	Final Value	Check	Verification
STKCX24-MIS01	The operating cost per block hour of the smallest family variant shall be at most 95% of that of the largest variant.	76.5%	✓	Analysis
STKCX25-MIS01	The total non-recurring development cost of the family shall not exceed 150% of the development cost of a single equivalent baseline variant.	Has been designed for	✓	Analysis
STKCX26-MIS01	The aircraft shall have a maximum design wingspan of less than 36 m in all ground configurations, consistent with ICAO Annex 14 code letter A, B, and C [82].	30 m	✓	Inspection
STKCX27-MIS01	All family variants shall be deliverable to launch customers no later than 31 December 2045.		*	Demonstration/Analysis
STKCX27-MIS02	The selected design concepts shall be compatible with the certification request duration required to achieve STKCX26-MIS01.		*	Demonstration
STKCX28-MIS01	The aircraft shall achieve a gate-to-gate turnaround-time of at most 1 hour at 100% load factor, measured from on-block to off-block.	57.6 min	✓	Analysis
STKPAX01-MIS01	The aircraft shall provide a cabin seat pitch of at least 29 inches in standard single configuration[4].	31 in	✓	Inspection
STKPAX01-MIS02	The aircraft shall maintain a cabin altitude of no more than 8000ft, per CS-25 [7].	8000 ft	✓	Test/Analysis
STKPAX01-MIS03	The aircraft shall limit the cabin interior noise level during cruise to at most 75 dB at any passenger seat.		*	Test
STKPAX01-MIS04	The aircraft shall have a passenger aisle width of at least 15 inches less than 25 inches from the floor[7]	20 inches everywhere	✓	Analysis
STKPAX01-MIS05	The aircraft shall have a passenger aisle width of at least 20 inches from 25 inches and up from the floor [7].	Has been designed for	✓	Analysis
STKAPT01-MIS01	The aircraft shall be compatible with ICAO Annex 14 aerodrome infrastructure (runway, taxiway, apron pavement strength and geometry) without requiring a modification of the airport infrastructure [82].		*	Analysis / Inspection
STKAPT02-MIS01	The aircraft shall comply with ICAO Doc 4444 Aircraft Traffic Management [83].		*	Analysis
STKAPT03-MIS01	The aircraft shall be serviceable using existing ground support equipment, including pushback car, GPU, water, lavatory, and catering.		*	Demonstration / Inspection
STKAPT03-MIS02	The aircraft's energy source shall be deliverable through airport infrastructure that exists or is planned to exist by 2045 at code C airports.		*	Analysis
STKAIR01-MIS01	The acquisition cost of the aircraft shall not exceed 150% of the price of an equivalent capacity reference aircraft.		*	Analysis

continued on next page

[4] https://www.airlinequality.com/info/seat-pitch-guide/ *(Accessed: 26/04/2026)*

ID	Requirement description	Final Value	Check	Verification
STKAIR03-MIS01	The aircraft shall allow for multiple interior layout configurations without modification to structural or systems components.	Has been designed for	✓	Analysis / Inspection
STKAIR03-MIS02	The aircraft shall allow for airline-specific exterior and interior livery changes without modification to structural or systems components.	Has been designed for	✓	Demonstration
STKAIR04-MIS01	Crew trained shall be able to obtain a single type rating for all members and variants of the aircraft family.		*	Analysis

18.3. System requirements

From the mission requirement, the following system requirements were set. They are more specified to the systems of the aircraft, and can be seen in Table 18.3.

ID	Requirement description	Final Value	Check	Verification
STKCX01-MIS01-SYS01	The aircraft shall achieve a minimum operating Mach of at least 0.62, for a margin above the cruise Mach of STKCX01-MIS01.	0.62	✓	Analysis
STKCX01-MIS01-SYS02	The aircraft shall produce thrust sufficient for steady level flight at $M \geq 0.6$, at the initial cruise altitude of STKCX02-MIS01 at MTOM.	Has been met	✓	Analysis
STKCX02-MIS01-SYS01	The aircraft shall achieve a cruise ceiling, where the reserve climb rate is at 500 ft/min, at least 1000ft higher than the cruise altitude defined by STKCX02-MIS01 at the cruise speed for the maximum possible aircraft weight at the end of climb [14].	Power requirement has been met	✓	Analysis
STKCX02-MIS01-SYS02	The aircraft shall achieve the cruise altitude of STKCX02-MIS01 within a time of at most 36 min at MTOM in standard ISA.	36	✓	Analysis
STKCX02-MIS01-SYS03	The aircraft shall be able to descend from the cruise altitude of STKCX02-MIS01 within a time of at most 20 min across the range of possible weights in standard ISA.		*	Analysis
STKCX03-MIS01-SYS01	The aircraft shall have a wing loading W/S at MTOM of at most 5000 N/m^2.	4801	✓	Analysis
STKCX03-MIS01-SYS02	The aircraft shall have a power-to-weight ratio P/W at MTOM of at least 45 W/N.	50 W/N	✓	Analysis
STKCX03-MIS01-SYS03	The aircraft shall achieve a maximum lift coefficient $C_{L,max}$ in the take-off configuration of at least 1.30.	1.32	✓	Analysis/Test
STKCX04-MIS01-SYS01	The aircraft shall achieve a maximum lift coefficient $C_{L,max}$ in the landing configuration of at least 2.5 satisfying STKCX04-MIS01 at MLM.	2.83	✓	Analysis/Test

continued on next page

ID	Requirement description	Final Value	Check	Verification
STKCX04-MIS01-SYS02	The aircraft shall have a stall speed in the landing configuration V_{S0} of at most 89.4 kts (46 m/s). $V_{REF} \geq 1.23V_{S0}$, where V_{REF} is the minimal reference landing speed, as per CS-25.125 [7].	44.1 m/s	✓	Analysis
STKCX05-MIS01-SYS01	Family variant A shall have a payload capacity of at least 7800 kg (78 PAX $\times$ 100 kg).	8400 kg	✓	Analysis / Inspection
STKCX05-MIS01-SYS02	Family variant A shall provide an installed energy capacity sufficient for the 1500 km range plus reserves per STKCX08-MIS02.	1500 km with reserves	✓	Analysis
STKCX06-MIS01-SYS01	Family variant B shall have a payload capacity of at least 5800 kg (58 PAX $\times$ 100 kg).	5800	✓	Analysis / Inspection
STKCX06-MIS01-SYS02	Family variant B shall provide an installed energy capacity sufficient for the 1300 km range plus reserves per STKCX08-MIS02	See member A	✓	Analysis
STKCX07-MIS01-SYS01	Family variant C shall have a payload capacity of at least 8400 kg (84 PAX $\times$ 100 kg)	8400	✓	Analysis / Inspection
STKCX07-MIS01-SYS02	Family variant C shall provide an installed energy capacity sufficient for the 1000 km range plus reserves per STKCX08-MIS02.	See member B	✓	Analysis
STKCX08-MIS01-SYS01	The aircraft shall comply with all applicable paragraphs of CS-25 (or equivalent Part 25 Special Conditions for the selected energy concept) [7].	Has been designed for	✓	Analysis
STKCX08-MIS01-SYS02	The family shall have a minimum gradient of climb of 12.7 m/s per CS-25.111 [7].	13.6 m/s	✓	Analysis
STKCX08-MIS01-SYS03	The aircraft shall achieve a probability of catastrophic failure per flight hour consistent with CS-25.1309 (system failures) [7]		$*$	Analysis
STKCX08-MIS01-SYS04	The aircraft shall have a diversion time of at least 60 minutes per CS-25.851(b) [7].	60 minutes	✓	Analysis
STKCX08-MIS01-SYS05	The aircraft shall have a diversion time of less than 180 minutes per AMC 25-24 5c(1) [7].	60 minutes	✓	Analysis
STKCX08-MIS01-SYS06	The aircraft shall demonstrate an evacuation time of at most 90 seconds with maximum seating capacity under simulated emergency conditions per AMC-25.803 [7]	Less than 90 seconds	✓	Analysis, Demonstration.
STKCX08-MIS01-SYS07	The aircraft shall have at least two exits, including at least one exit of at least Type I, for each side of the fuselage as per CS-25.807 [7].	Two type II each side	✓	Analysis
STKCX08-MIS01-SYS08	Family member B shall have at least 2 hand fire extinguishers, at least one located in the pilot compartment[7].	Three	✓	Analysis
STKCX08-MIS01-SYS09	Family members A and C shall have at least 3 hand fire extinguishers, at least one located in the pilot compartment, as per CS-25.851 [7]	Three	✓	Analysis
STKCX08-MIS01-SYS10	The aircraft shall operate at a load factor higher than -1 per CS-25.333 [7].	-1	✓	Analysis

continued on next page

ID	Requirement description	Final Value	Check	Verification
STKCX08-MIS01-SYS11	The aircraft shall operate at a load factor lower than 2.5 per CS-25.333 [7].	Maximum is 2.5	✓	Analysis
STKCX08-MIS01-SYS12	The aircraft shall have a dive speed higher than 1.25 times the design cruise speed per CS25.335 [7].	240 m/s	✓	Analysis
STKCX08-MIS01-SYS13	The aircraft shall maintain static longitudinal stability across the full range of CG locations per CS-25.335 [7].	Has been designed for	✓	Analysis
STKCX08-MIS01-SYS14	The aircraft shall maintain dynamic stability as per CS25.335 [7].		*	Analysis
STKCX08-MIS02-SYS01	The aircraft shall carry reserve energy for each design mission consistent with the operational reserve methodology of EU Regulation 965/2012 Part-CAT.OP.MPA.180-185 amended by Commission Implementing Regulation (EU) 2021/1296 (trip, alternate, contingency, final reserve).	Has been designed for	✓	Analysis
STKCX08-MIS03-SYS01	The aircraft shall be designed for a structural service life of at least 75000 flight cycles [5].	Has been designed for	✓	Analysis
STKCX09-MIS01-SYS01	The mean time to repair (MTTR) of any replaceable unit whose failure would prevent dispatch shall not exceed 75 minutes (turn around time plus technical delay threshold).		*	Analysis / Demonstration
STKCX09-MIS01-SYS02	A dispatch reliability allocation and prediction analysis shall allocate the 95% target across aircraft systems	99.7%	✓	Analysis / Inspection
STKCX09-MIS01-SYS03	The aircraft shall include a Master Minimum Equipment List (MMEL) covering redundant equipment and backup functions that supports the dispatch reliability target.		*	Inspection
STKCX09-MIS02-SYS01	The dispatch-reliability allocation analysis shall demonstrate no subsystem failure-rate contribution exceeds the limit set by STKCX09-MIS02		*	Analysis
STKCX10-MIS01-SYS01	The aircraft shall provide a flight deck accessible to at least two crew members as defined by CS-25.1523 [7].	Two pilots	✓	Inspection
STKCX10-MIS01-SYS02	The aircraft shall provide a flight deck meeting CS-25.1523 workload assessment for two-pilot operation [7].		*	Test / Inspection
STKCX11-MIS01-SYS01	The aircraft energy storage shall be partitioned into at least 1 independent units such that loss of any single unit does not result in loss of controlled flight.	Taken into account	✓	Analysis
STKCX11-MIS02-SYS01	The aircraft energy distribution shall provide at least 2 independent paths such that loss of any single path does not result in loss of controlled flight	Seen in the fuel system	✓	Analysis

continued on next page

[5] https://airguide.info/how-long-does-a-boeing-plane-stay-in-service-before-retirement/ *(Accessed: 26/04/2026)*

ID	Requirement description	Final Value	Check	Verification
STKCX12-MIS01-SYS01	Family variant A shall emit no more than 3214.68 kg of well-to-wake CO_2 on the 1500 km/78 PAX design mission, equal to 20% of the well-to-wake CO_2 emissions of a reference Embraer 175 on the same mission.	640.08 kg	✓	Analysis
STKCX12-MIS02-SYS01	Family variant B shall emit no more than 2786.06 kg of well-to-wake CO_2 on the 1300 km/58 PAX design mission, equal to 20% of the well-to-wake CO_2 emissions of a reference Embraer 175 on the same mission.	298.35 kg	✓	Analysis
STKCX12-MIS03-SYS01	Family variant C shall emit no more than 2143.12 kg of well-to-wake CO_2 on the 1000 km/84 PAX design mission, equal to 20% of the well-to-wake CO_2 emissions of a reference Embraer 175 on the same mission.	See LEAF-A	✓	Analysis
STKCX12-MIS04-SYS01	The family shall accept an energy source or energy-source mix consistent with the well-to-wake CO_2 reduction target.	Has been designed for	✓	Analysis
STKCX13-MIS01-SYS01	The aircraft systems shall emit no more than 561.01 g of NO_x per hour during ground operations [6].	168.303 g	✓	Analysis/Test
STKCX14-MIS01-SYS01	The aircraft systems shall emit no more than 238.73 mg of non-volatile particulate (nvPM) mass per hour during ground operations.	0	✓	Analysis / Test
STKCX15-MIS01-SYS01	The noise generated by the aircraft shall not exceed the level specified in ICAO Annex 16, Volume I, Chapter 14.4.1.1 at the lateral noise measurement point described in Chapter 3.3.1.a [81].		*	Test/Analysis
STKCX15-MIS01-SYS02	The noise generated by the aircraft shall not exceed the level specified in ICAO Annex 16, Volume I, Chapter 14.4.1.2 at the flyover noise measurement point described in Chapter 3.3.1.b [81].		*	Test/Analysis
STKCX15-MIS01-SYS03	The noise generated by the aircraft shall not exceed the level specified in ICAO Annex 16, Volume I, Chapter 14.4.1.3 at the approach noise measurement point described in Chapter 3.3.1.c [81].		*	Test/Analysis
STKCX15-MIS02-SYS01	The aircraft shall maintain the noise margin across the full range of payload and range as stated by ICAO Annex 16 [81].		*	Test/Analysis
STKCX16-MIS02-SYS01	The aircraft shall be designed such that recyclable parts can be removed at the end of life.	Has been designed for	✓	Analysis
STKCX16-MIS02-SYS02	The aircraft shall be designed such that recyclable parts can still be recycled once they are removed at the end of life.	Has been designed for	✓	Analysis
STKCX17-MIS01-SYS01	The aircraft shall share at least 65% of parts across all family variants by part count.	75.6%	✓	Analysis

continued on next page

[6] https://blog.zhaw.ch/metenvia/2023/02/16/aircraft-engines-idle-taxi-gaseous-emissions/ *(Accessed: 26/04/2026)*

ID	Requirement description	Final Value	Check	Verification
STKCX17-MIS01-SYS02	The aircraft shall share at least 65% of structural mass across all family variants.	75.6%	✓	Analysis
STKCX17-MIS02-SYS01	The cockpit layout and avionics shall be identical across all family variants.	Exact same cockpits	✓	Inspection
STKCX17-MIS02-SYS02	The propulsion architecture (engine type, energy source, and placement) shall be identical across all family variants.	Exact same propulsion architecture	✓	Inspection
STKCX18-MIS01-SYS01	Final assembly of all family members shall be possible using a shared toolset.		$*$	Analysis
STKCX18-MIS01-SYS02	All family variants be able to be produced on a single, shared assembly line.	Taken into account in production plan	✓	Analysis
STKCX19-MIS01-SYS01	All replacement parts shall be able to be installed with a shared toolset.		$*$	Analysis
STKCX19-MIS01-SYS02	All repair operations shall be able to performed with a shared toolset.		$*$	Analysis
STKCX20-MIS01-SYS01	The largest family variant shall provide a total of at least 15 m^3 of usable cargo-hold volume across the aircraft, separate from the cabin.	28 m^3	✓	Analysis/Inspection
STKCX20-MIS01-SYS02	The cargo hold volume of the aircraft shall be accessible during ground operations without equipment.	Has been designed for	✓	Analysis/Inspection
STKCX21-MIS01-SYS01	All family members shall provide a total of at least 12 m^3 of usable cargo-hold volume across the aircraft, separate from the cabin.	18 m^3	✓	Analysis/Inspection
STKCX22-MIS01-SYS01	The direct operating CASK of aircraft A shall be no more than $13.34 \frac{USDcent}{ASK}$.	10.20	✓	Analysis
STKCX23-MIS01-SYS01	The direct operating CASK of aircraft B shall be no more than $12.77 \frac{USDcent}{ASK}$.	14.40	✓	Analysis
STKCX24-MIS01-SYS01	The operating cost per block hour of the smallest family variant shall be at most 95% of that of the largest variant.	76.5%	✓	Analysis
STKCX26-MIS01-SYS01	The aircraft shall have a design wingspan less than 36 metres in all ground configurations, as specified by ICAO Annex 14 code letter A, B, and C [82].	30 m	✓	Inspection
STKCX26-MIS01-SYS02	The aircraft shall have a design outer main gear wheel span less than 9 metres, as specified by ICAO Annex 14 code letter A, B, or C.		$*$	Inspection
STKCX27-MIS01-SYS01	The aircraft shall be delivered and enter into service no later than 31 December 2045.		$*$	Demonstration/Analysis
STKCX27-MIS01-SYS02	Production shall be ready to produce the aircraft as is needed to achieve STKCX26-MIS01-SYS01.		$*$	Demonstration/Analysis
STKCX27-MIS02-SYS02	The aircraft shall be compatible with the certification request duration required to achieve STKCX26-MIS01.		$*$	Analysis

continued on next page

ID	Requirement description	Final Value	Check	Verification
STKCX28-MIS01-SYS01	The aircraft shall permit refuelling or energy replenishment within the turnaround cycle of STKCX27-MIS01 without extending the total turnaround time.	Has been accounted for	✓	Analysis
STKCX28-MIS01-SYS02	The aircraft shall permit passenger embarking/disembarking, cargo handling, cabin servicing, and pre-departure safety inspection within the turnaround cycle of STKCX27-MIS01.	Has been accounted for	✓	Analysis
STKPAX01-MIS01-SYS01	The aircraft shall provide a cabin seat pitch of at least 29 inches in standard single configuration [7].	31 inch	✓	Inspection
STKPAX01-MIS02-SYS01	The aircraft shall maintain a cabin altitude of no more than 8000 ft per CS-25[7].	8000 ft	✓	Test / Analysis
STKPAX01-MIS03-SYS01	The aircraft shall limit the cabin interior noise level during cruise to at most 75 dB at any passenger seat.		*	Test
STKPAX01-MIS04-SYS01	The aircraft shall have a passenger aisle width of at least 15 inches at height less than 25 inches from the cabin floor [7].	20 inches	✓	Analysis
STKPAX01-MIS05-SYS01	The aircraft shall have a passenger aisle width of at least 20 inches from the height of 25 inches and up from the cabin floor [7].	20 inches	✓	Analysis
STKAPT01-MIS01-SYS01	The aircraft shall be compatible with ICAO Annex 14 aerodrome infrastructure (runway, taxiway, apron pavement strength and geometry) without requiring a modification of the airport infrastructure[82].		*	Analysis / Inspection
STKAPT02-MIS01-SYS01	The aircraft shall comply with ICAO Doc 4444 Aircraft Traffic Management [83].		*	Analysis
STKAPT03-MIS01-SYS01	The aircraft shall be serviceable using existing ground support equipment, including pushback car, GPU, water, lavatory, and catering.		*	Demonstration / Inspection
STKAPT03-MIS02-SYS01	The aircraft's energy source shall be available in sufficient quantities by 2045 at airports, accommodating aircraft wingspan of ICAO code A, B, and C [82].		*	Analysis
STKAPT03-MIS02-SYS02	The aircraft's energy source shall be able to be replenished at airports, accommodating aircraft wingspan of up to and including ICAO code C, by 2045.	Meets the requirement	✓	Analysis
STKAIR01-MIS01-SYS01	The acquisition cost of the aircraft shall not exceed 150% of the price of an equivalent capacity reference aircraft.		*	Analysis
STKAIR03-MIS01-SYS01	The aircraft shall allow for multiple interior layout configurations without modification to structural or systems components.	Has been designed for	✓	Analysis / Inspection

continued on next page

[7] https://www.airlinequality.com/info/seat-pitch-guide/ *(Accessed: 28/04/2026)*

ID	Requirement description	Final Value	Check	Verification
STKAIR03-MIS02-SYS01	The aircraft shall allow for airline-specific exterior livery changes without modification to structural or systems components.	Painting possible	✓	Demonstration
STKAIR03-MIS02-SYS02	The aircraft shall allow for airline-specific interior livery changes without modification to structural or systems components.	Cabin customisation possible	✓	Demonstration
STKAIR04-MIS01-SYS01	Crew switching between aircraft variants within the family will require no extra training.	Commonality	✓	Inspection

19

Conclusion

Author: Kacper

Aviation is among the hardest industries to decarbonise. Currently available alternatives to conventional JET-A1 fuel do not provide energy density high enough to carry the aircraft over distances served by airline operators. In this report, an innovative liquid hydrogen aircraft family concept is presented, capable of serving regional markets while simultaneously minimising emissions. Two family members were considered, LEAF-A as an 84 passenger plane capable of flying 1500 km and LEAF-B carrying 58 passengers over 1300 km. Technology used in the development is expected to be commercially available before planned aircraft entry into service in 2045.

Over the last ten weeks, extensive literature study was conducted covering possible aircraft configurations and propulsion systems. After careful requirement revision it was concluded that for requested mission distances of below 1500 km at speeds above Mach 0.6, a liquid hydrogen powered propeller aircraft with a strut-braced wing is the most promising solution. Planned entry into service date leaves little time margin for research of numerous unproven technologies, such as an Openfan engine or Lifting Fuselage. Thus, the liquid hydrogen propulsion system was chosen as the main technology driven improvement, together with an aircraft configuration presenting less technological risk.

The costs were also assessed, as cost is one of the main drivers in any project. The LEAF variants ended up meeting the cost requirement with maximum of 104% of the cost per available seat kilometre. This shows that operating the aircraft can be very beneficial for airlines. Besides the operating cost for airlines, also a return on investment study was done, which concluded to a 5% return on investment. This shows it is also beneficial for the aircraft manufacturers.

Throughout the development process an integrated Python sizing algorithm was used, capable of performing iterations for each of the family members. Sizing of the fuselage, empennage and landing gear relied on formulas provided in *Airplane Design* publications authored by Jan Roskam. However, due to the novel, unconventional propulsion system and exceptionally high aspect ratio wing, propulsion, wing and certain subsystems, such as avionics, were sized using modern aircraft examples as reference. Convergence of the optimisation loop is presented for the design, and its results are used as a basis for the more detailed component design.

Development of the chosen concept focused on numerous critical systems. Firstly, static analysis of the wing and supporting structure was performed, calculating internal forces and displacements along the wings span, highlighting benefits of the supporting strut for the bending moment relief. Displacement of the wing tip was reduced from 2.37 m to 0.65 m, preventing efficiency losses while in flight due to reduced effective aspect ratio of the wing. Secondly, a study of the necessary fuel volume was conducted, resulting in 14.01 m^3, followed by liquid hydrogen tank sizing and structure integration.

To better present the results of the research, a detailed CATIA model of the LEAF was made, featuring parametrised fuselage, wing with strut support, landing gear, liquid hydrogen tank and propeller engines. By altering the values of input parameters, the same model can be used for representation of both presented family members.

Recommended next steps include optimising the strut cross-section, twist and pitch to reduce interference drag, and trying to achieve a further reduction in cruise drag, with validation done by CFD. Furthermore, it is recommended to broaden the range of the family design, with a Stretch Variant (SV) for additional capacity and a New Engine Option (NEO), with freighter and longer-range variants as longer-term options.

The LEAF aircraft family offers a realistic solution to the de-carbonisation problem of the modern aerospace industry. Technology implemented in the design has a high chance of reaching operational readiness by 2045 and revolutionise the regional air transport.

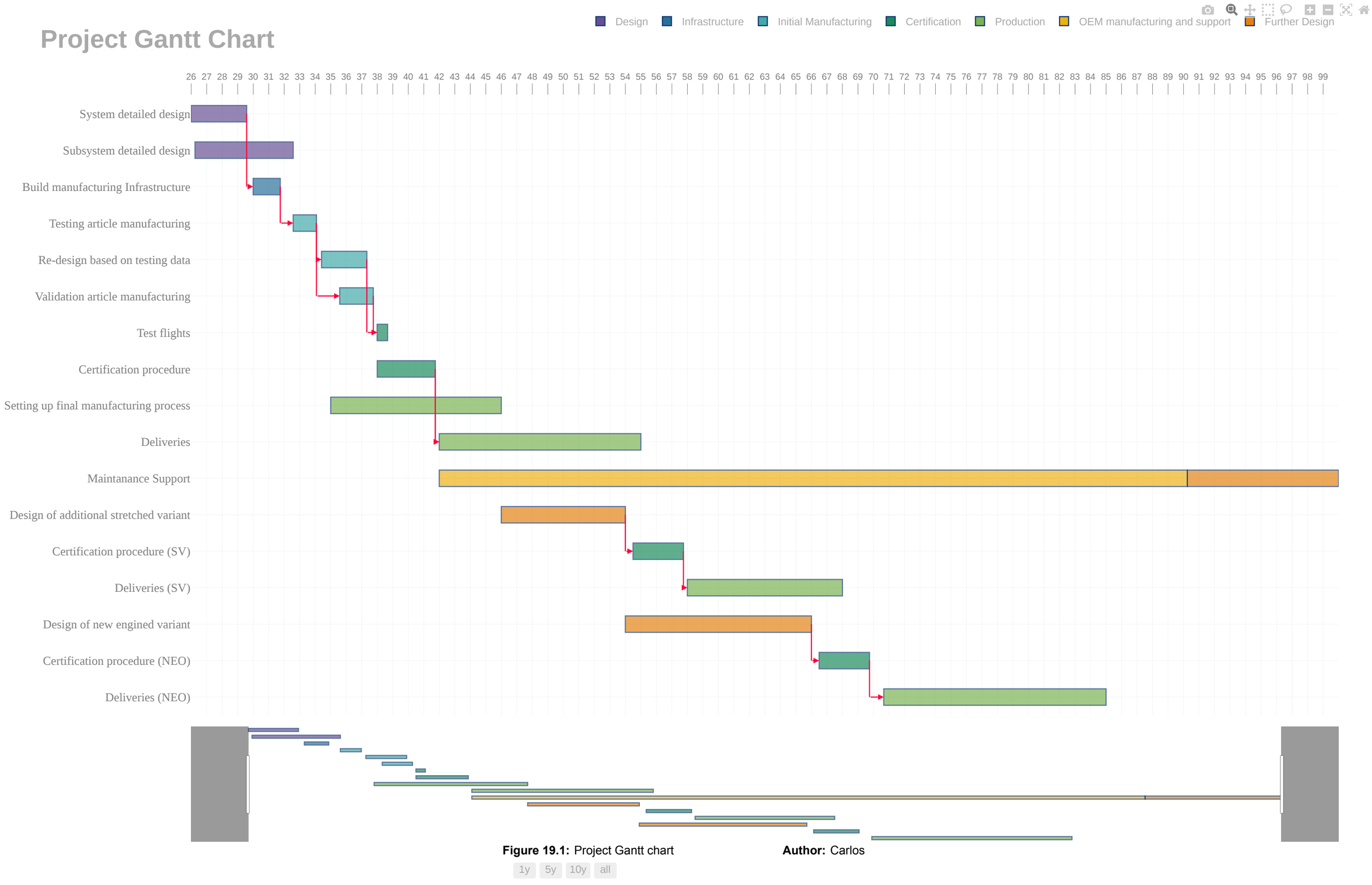

Figure 19.1: Project Gantt chart **Author:** Carlos

References

[1] Klöwer, M., Allen, M., Lee, D., Proud, S., Gallagher, L., and Skowron, A. “Quantifying aviation’s contribution to global warming”. In: *Environmental Research Letters* 16 (Oct. 2021), p. 104027. doi: 10.1088/1748-9326/ac286e.

[2] Klöwer, M., Allen, M., Lee, D., Proud, S., Gallagher, L., and Skowron, A. *Quantifying aviation’s contribution to global warming*. Oct. 2021. doi: 10.1088/1748-9326/ac286e.

[3] Vlasblom, D., van Wassenaar, T., Nikolov, V., Michaud, M., Montewka, K., van den Berg, L., Overvelde, N., Landman, L., Orce López, C., and McCarthy, S. *Midterm Report*. Tech. rep. Delft University of Technology, 2026.

[4] ten Damme, L., van Put, M., Rao, A. G. “Simulation of the refuelling process for an LH2-Powered commercial Aircraft: Part 2 – Refuelling time of the Airbus ZEROe turboprop concept”. In: *International Journal of Hydrogen Energy* 216 (2026), p. 153582. issn: 0360-3199. doi: 10.1016/j.ijhydene.2026.153582.

[5] Johansen, C. S., Skov, I. R., and Mati, A. “Exploring the Potential for Cost-Competitive e-SAF in European Aviation Towards 2050”. In: *Energy Reports* 15 (2026).

[6] Roskam, J. *Roskam 5 - Component Weight Estimation*. Roskam Aviation and Engineering Corporation, 1985.

[7] European Union Aviation Safety Agency. *Certification Specifications and Acceptable Means of Compliance for Large Aeroplanes CS-25, Amendment 28*. Regulation. Cologne, Germany: EASA, 2023.

[8] Roskam, J. *Airplane Design Part V: Component Weight Estimation*. 2nd printing. Lawrence, Kansas: Design, Analysis and Research Corporation (DARcorporation), 1999. isbn: 978-1-884885-50-1.

[9] Onorato, G., Proesmans, P., and Hoogreef, M. F. M. “Assessment of Hydrogen Transport Aircraft: Effects of Fuel Tank Integration”. In: *CEAS Aeronautical Journal* 13.4 (2022), pp. 813–845. doi: 10.1007/s13272-022-00601-6.

[10] Torenbeek, E. *Synthesis of Subsonic Airplane Design*. 1st ed. Dordrecht, The Netherlands: Springer Dordrecht, 1982. isbn: 9789024727247.

[11] Finck, R. D. *USAF Stability and Control DATCOM (Data Compendium)*. Tech. rep. Revised edition. Wright-Patterson Air Force Base, OH: Air Force Flight Dynamics Laboratory, Air Force Wright Aeronautical Laboratories, 1978.

[12] Obert, E. *Aerodynamic Design of Transport Aircraft*. Delft: IOS Press, 2009.

[13] Roskam, J. *Airplane Design Part VI: Preliminary Calculation of Aerodynamic, Thrust and Power Characteristics*. 4th ed. Lawrence, Kansas: DARcorporation, 2004. isbn: 1-884885-52-7.

[14] Roskam, J. *Airplane Design Part II: Preliminary Configuration Design and Integration of the Propulsion System*. Roskam Aviation and Engineering Corporation, 1985.

[15] Gudmundsson, S. *General Aviation Aircraft Design: Applied Methods and Procedures*. 2nd ed. Oxford, United Kingdom: Butterworth-Heinemann, 2022. isbn: 9780128184653.

[16] Hepperle, M. *JAVAFOIL User’s Guide*. MH-AeroTools. Dec. 2017.

[17] Anderson Jr, J. D. *Fundamentals of Aerodynamics - Seventh Edition*. Mc Graw Hill, 2024.

[18] Proesmans, P. J. *Design Synthesis Exercise 2025–2026 Project Guide*. Issue 6. Faculty of Aerospace Engineering, Delft University of Technology. Delft, The Netherlands, Jan. 2026.

[19] Zinjarde, P. “Aerodynamic Design Integration of Strut Braced Wings”. MA thesis. TU Delft, 2023.

[20] El-Sayed, A. F. *Fundamentals of Aircraft and Rocket Propulsion*. Springer London, 2016. isbn: 978-1-4471-6796-9. doi: 10.1007/978-1-4471-6796-9.

[21] Bradley, M. K., Droney, C. K. *Subsonic Ultra Green Aircraft Research: Phase II – Volume II – Hybrid Electric Design Exploration*. Tech. rep. NASA, Boeing Research and Technology, Huntington Beach, California, 2015.

[22] Arslan, S. *Calculating the Wing Lift Distribution with the Diederich Method in Microsoft Excel*. Tech. rep. HAW Hamburg, Apr. 2023.

[23] Newlin, J. A., and Trayer, G. W. *The Design of Airplane Wing Ribs*. Tech. rep. National Advisory Committee for Aeronautics, 1930.

[24] Ma, Y., Karpuk, S., Eliham, A. *Conceptual design and comparative study of strut-braced wing and twin-fuselage aircraft configurations with ultra-high aspect ratio wings*. Tech. rep. Aerospace Science and Technology, Feb. 2022.

[25] Ivaldi, D., Secco, N. R., Chen, S., Hwang, J. T., and Martins, J. R. R. A. "Aerodynamic Shape Optimization of a Truss-Braced-Wing Aircraft". In: *AIAA* (2015).

[26] Droney, C. K., Sclafani, A. J., Harrison, N. A., Grasch, A. D., and Beyar, M. D. "Subsonic Ultra Green Aircraft Research: Phase III – Mach 0.75 Transonic Truss-Braced Wing Design". In: (2020).

[27] Scholz, D. *Aircraft Design: Lecture Notes*. Hamburg University of Applied Sciences. Available at `http://LectureNotes.AircraftDesign.org`. Hamburg, Germany, 2015.

[28] Sadraey, M. H. *Aircraft Design: A Systems Engineering Approach*. Aerospace Series. West Sussex, United Kingdom: John Wiley & Sons, 2012. isbn: 978-1-119-95340-1.

[29] B.L. Stevens and F.L. Lewis. *Aircraft Control and Simulation*. Wiley, 2003. isbn: 9780471371458. url: `https://books.google.nl/books?id=T0Ux6av4btIC`.

[30] *Flying Qualities of Piloted Airplanes*. Military Specification MIL-F-8785C. U.S. Department of Defense, Nov. 1980.

[31] Schmidt, M., Engelmann, M., Rothfeld, R., and Hornung, M. "Boarding Process Assessment of Novel Aircraft Cabin Concepts". In: Munich Aerospace e.V. and Bauhaus Luftfahrt e.V. Munich-Taufkirchen, Germany, 2017.

[32] Megson, T. H. G. *Aircraft Structures for Engineering Students*. 6th ed. Oxford, United Kingdom: Elsevier Ltd., 2017. isbn: 978-0-08-100914-7.

[33] Monteiro, F. A. C., Neto, E. L., and Hernandes, J. A. "LOCAL SKIN BUCKLING OF CYLINDRICAL SHELLS". In: *World Congress on Computational Mechanics* 10 (July 2012). doi: `10.5151/meceng-wccm2012-19895`.

[34] Billaut, F. "Fatigue Behaviour of Drilled T300/Peek Laminated Composites". PhD thesis. Massachusetts Institute of Technology, 1993.

[35] Brewer, G. D. *Hydrogen Aircraft Technology*. Boca Raton, Florida: CRC Press, 1991. isbn: 9780849358388.

[36] Gómez, A., and Smith, H. "Liquid hydrogen fuel tanks for commercial aviation: Structural sizing and stress analysis". In: *Aerospace Science and Technology* 95 (Dec. 2019), p. 105438. issn: 1270-9638. doi: `10.1016/j.ast.2019.105438`.

[37] di Summa, G. J. A. "The Effect of the Internal Layout of Hydrogen Combustion Blended Wing Body Concepts on Performance". MSc thesis. Delft, The Netherlands: Delft University of Technology, 2025.

[38] Lin, C. S., Van Dresar, N. T., and Hasan, M. M. "Pressure Control Analysis of Cryogenic Storage Systems". In: *Journal of Propulsion and Power* 20.3 (2004), pp. 480–485. doi: `10.2514/1.10387`.

[39] Ruijgrok, G. J. J., Voskuijl, M., and Varriale, C. *Elements of Airplane Performance*. 3rd ed. Delft, The Netherlands: TU Delft OPEN Publishing, 2025. isbn: 978-94-6518-164-6. doi: `10.59490/mt.235`.

[40] Saravanamuttoo, H. I. H. "Modern turboprop engines". In: *Progress in Aerospace Sciences* 24 (3 Jan. 1987), pp. 225–248. issn: 0376-0421. doi: `10.1016/0376-0421(87)90008-X`.

[41] Owens, R. E., and Ferguson, W. W. "Some Aspects of Prop-Fan Propulsion Systems Analysis". In: *SAE Technical Papers* (Feb. 1982). issn: 0148-7191. doi: `10.4271/821358`.

[42] Grech, N., and Tacconi, J. "Advanced Hydrogen Cycles To Help Decarbonize The Aviation Industry. Part 2: Hydrogen Fuel Cycles For Aero Gas Turbines". In: *Journal of Engineering for Gas Turbines and Power* 148.6 (June 2025), pp. 1–16. issn: 0742-4795. doi: `10.1115/1.4068606/1217127`. url: `https://dx.doi.org/10.1115/1.4068606`.

[43] Richardson, E. S. *SESA6075 Aircraft Propulsion*. Tech. rep. University of Southampton, 2025.

[44] Liu, B., Zhang, H., Ouyang, T., Chang, R., Xu, M., and Song, Z. "Thermodynamic modelling analysis and characteristics identification for variable cooling air turbine of gas turbine engines". In: *Aerospace Science and Technology* 177 (), p. 112204. issn: 1270-9638. doi: `10.1016/j.ast.2026.112204`.

[45] Acar, H., Arnson, M., Tsai, M., and Cinar, G. "Historical Trends and Future Projections of Key Performance Parameters in Aircraft Design". In: *Journal of Aircraft* (Jan. 2025), pp. 1–23. issn: 0021-8669. doi: `10.2514/1.C038340`.

[46] Tiemstra, F. S., Rao, A. G., Van Oudheusden, B. W., Gallo, M., and Kogenhop, O. "Design of a Semi-Empirical Tool for the Evaluation of Turbine Cooling Requirements in a Preliminary Design Stage". MA thesis. 2014.

[47] Ning, A. “Using blade element momentum methods with gradient-based design optimization”. In: *Journal of the International Society for Structural and Multidisciplinary Optimization* (2021). doi: https://doi.org/10.1007/s00158-021-02883-6.

[48] Chaviaropoulos, P. K., Hansen, M. O. L. “Investigating Three-Dimensional and Rotational Effects on Wind Turbine Blades by Means of a Quasi-3D Navier-Stokes Solver”. In: *Journal of Fluids Engineering* 122 (2 June 2000).

[49] *ICAO Annex 16, Volume I - Aircraft Noise*. Tech. rep. ICAO, 2017.

[50] Y A P Teeuwen. “Propeller Design for Con-ceptual Turboprop Aircraft”. MA thesis. Delft University of Technology, 2017.

[51] Vlasblom, D., van Wassenaar, T., Nikolov, V., Michaud, M., Montewka, K., van den Berg, L., Overvelde, N., Landman, L., Orce López, C., and McCarthy, S. *Baseline Report*. Tech. rep. Delft University of Technology, 2026.

[52] Sarh, B., Buttrick, J., Munk, C., and Bossi, R. “Aircraft Manufacturing and Assembly”. In: *Springer Handbook of Automation* (2009), pp. 893–910. issn: 2522-8706. doi: 10.1007/978-3-540-78831-7_51.

[53] Roskam, J. *Airplane Design Part VIII: Airplane Cost Estimation: Design, Development, Manufacturing and Operating*. DARcorporation, 1990.

[54] Air Products and Chemicals, Inc. *Safetygram 9: Liquid Hydrogen*. Tech. rep. 900-13-082-US. Air Products and Chemicals, Inc., 2014.

[55] Kuhn, M. *Fuel Consumption of the 50 Most Used Passenger Aircraft*. Tech. rep. HAW Hamburg, 2023.

[56] Embraer. *Embraer E190 Financial Forecast*. Exhibit 13: Forecast Financial Information, Draft 4-6-22, Page 1 of 3. 2022.

[57] IATA. *Airline Disclosure Guide Aircraft acquisition cost and depreciation*. Tech. rep. IATA, 2014.

[58] “E-Jets maintenance analysis budget”. In: *Aircraft Commerce* (June 2009).

[59] “ATR 42 72 maintenance analysis budget”. In: *Aircraft Commerce* (Dec. 2006/2007).

[60] DAL MEC. *Delta Pilot Working Agreement*. Jan. 2023.

[61] AircraftCommerce. *AIRCRAFT OWNER’S OPERATOR’S GUIDE: A320 FAMILY*. Issue 44. Mar. 2006.

[62] Airbus. *Aircraft Characteristics Airport and Maintenance Planning*. Tech. rep. Airbus, 2024.

[63] Sanchez, D. R. “Analysis of Ground Handling Characteristics of Innovative Aircraft Configurations”. MA thesis. Hamburg University of Applied Sciences, 2009.

[64] Zhang, Y., Yang, Z., Ma, X., DONG, W., Dong, D., Tan, Z., and Zhang, S. “Exploration and implementation of commonality valuation method in commercial aircraft family design”. In: *Chinese Journal of Aeronautics* 32.8 (Aug. 2019), pp. 1828–1846. issn: 1000-9361. doi: 10.1016/j.cja.2019.05.005.

[65] Gu, Y., Wiedemann, M., Ryley, T., Johnson, M., and Evans, M. “Hydrogen-Powered Aircraft at Airports: A Review of the Infrastructure Requirements and Planning Challenges”. In: *Sustainability* 15 (Nov. 2023), p. 15539. doi: 10.3390/su152115539.

[66] Boeing. *Current Market Outlook*. 2017.

[67] Boeing. *Boeing: Commercial Market Outlook 2025-2044*. 2025.

[68] ATR. *Turboprop Market Forecast 2025-2044*. 2025.

[69] Commission of the European Communities. *Commission Decision of 17/12/2008 Declaring a Concentration to be Compatible with the Common Market and the Functioning of the EEA Agreement (Case No COMP/M.5141 – KLM/Martinair)*. Brussels, Belgium, Dec. 2008.

[70] Boonekamp, T., and Burghouwt, G. “Measuring connectivity in the air freight industry”. In: *Journal of Air Transport Management* 61 (May 2016). doi: 10.1016/j.jairtraman.2016.05.003.

[71] Janssen, G. R. “Exploratory Simulation of Truck-Based Hydrogen Aircraft Refuelling Logistics at an Airport”. MA thesis. Delft University of Technology, 2025.

[72] IATA, Airports Council International, and Airbus. *Concept of Operations of Battery and Hydrogen-Powered Aircraft at Aerodromes*. Tech. rep. Geneva, Switzerland: IATA, 2025.

[73] Rahn, A., Dahlmann, K., Linke, F., Kühlen, M., Sprecher, B., Clemens, D., and Wende, G. “Quantifying climate impacts of flight operations: A discrete-event life cycle assessment approach”. In: *Transportation Research Part D* 141 (2025). doi: 10.1016/j.trd.2025.104646.

[74] Rahn, A., Schuch, M., Linke, F., Wicke, K., Sprecher, B., Clemens, D., and Wende, G. “Beyond flight operations: Assessing the environmental impact of aircraft maintenance through life cycle assessment”. In: *Journal of Cleaner Production* 453 (2024). doi: https://doi.org/10.1016/j.jclepro.2024.142195.

[75] Ramm, J., Pohya, A. A., Wicke, K., and Wende, G. “Uncertainty quantification in hydrogen tank exchange: Estimating maintenance costs for new aircraft concepts”. In: *International Journal of Hydrogen Energy* 68 (2024). doi: https://doi.org/10.1016/j.ijhydene.2024.04.157.

[76] International Civil Aviation Organization. *Annex 16 to the Convention on International Civil Aviation — Environmental Protection, Volume II: Aircraft Engine Emissions*. 2023, July.

[77] Scheelhaase, J., Müller, L., Ennen, D., and Grimme, W. “Economic and Environmental Aspects of Aircraft Recycling”. In: *Transportation Research Procedia* 65 (Nov. 2022), pp. 3–12. doi: 10.1016/j.trpro.2022.11.002.

[78] Rehber, E. “Designing Products Through Structural Reuse of End-of-Life Aircraft Parts”. MA thesis. Delft University of Technology, 2025.

[79] Nikou, S. and Santema, S. “Sustaining aviation: A decision-tree framework for recycling aircraft cabin interior”. In: *Journal of Air Transport Management* (2026).

[80] Chu, S., Liu, F., and Wei, Z. “The Study on Dispatch Reliability Prediction Model of Civil Aircraft”. In: *The Open Mechanical Engineering Journal* 8.1 (2014), pp. 828–832. doi: 10.2174/1874155X01408010828.

[81] International Civil Aviation Organization. *Annex 16 to the Convention on International Civil Aviation — Environmental Protection, Volume I: Aircraft Noise*. 2017.

[82] International Civil Aviation Organization. *Annex 14 to the Convention on International Civil Aviation — Aerodromes, Volume I: Aerodrome Design and Operations*. 2018.

[83] International Civil Aviation Organization. *Procedures for Air Navigation Services: Air Traffic Management (PANS-ATM)*. 16th. ICAO Doc 4444. International Civil Aviation Organization. Montreal, Canada, 2016.

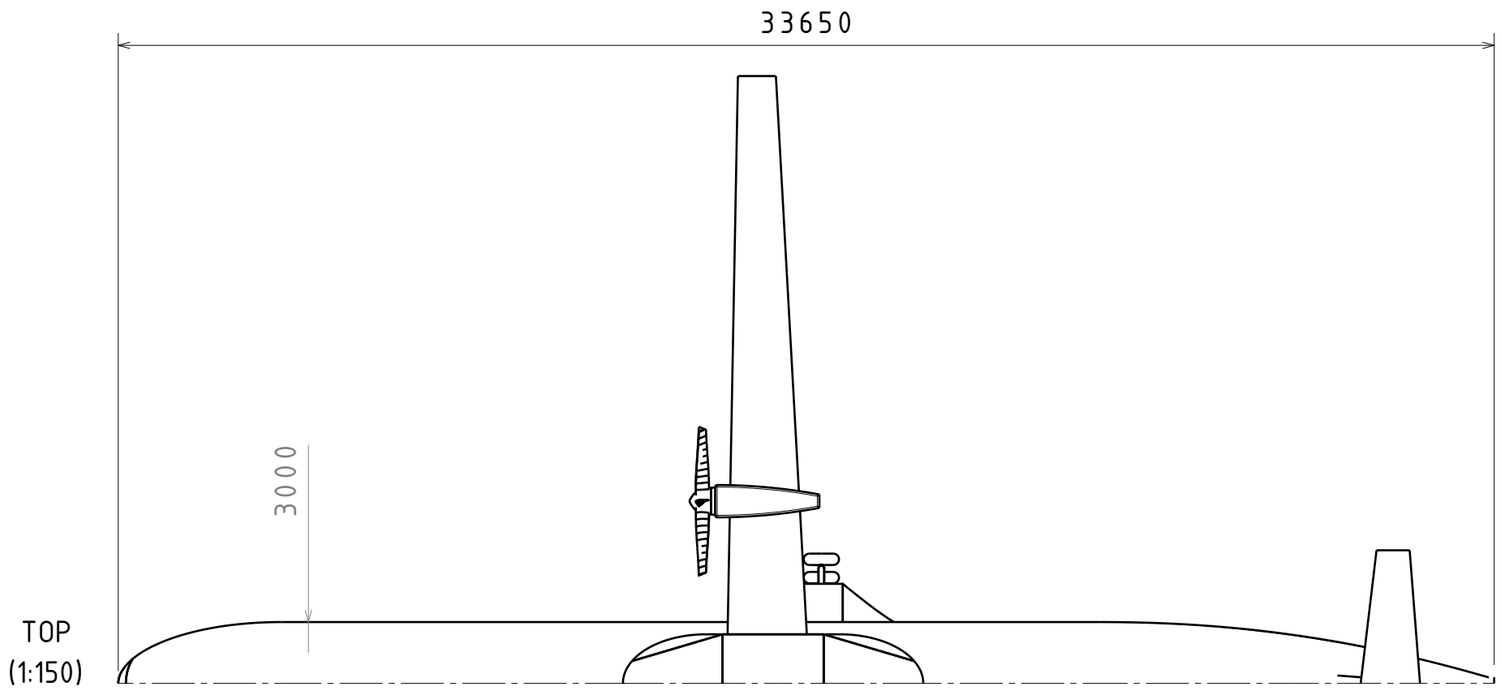

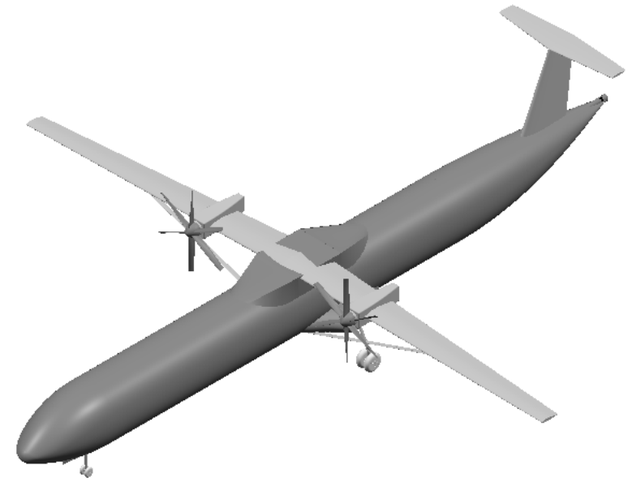

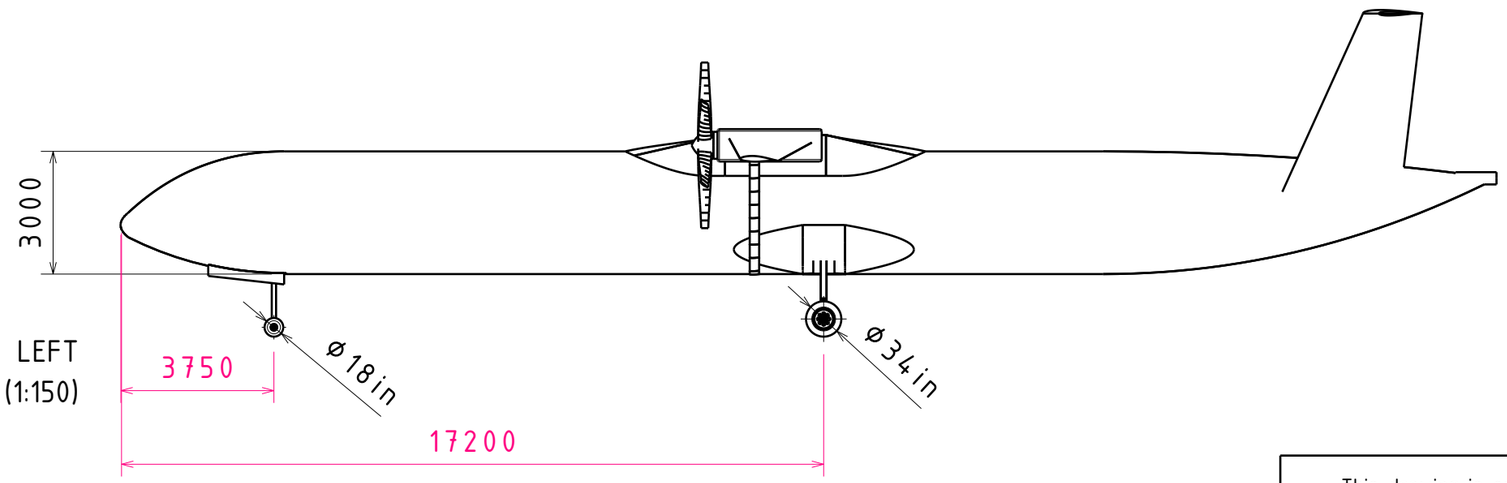

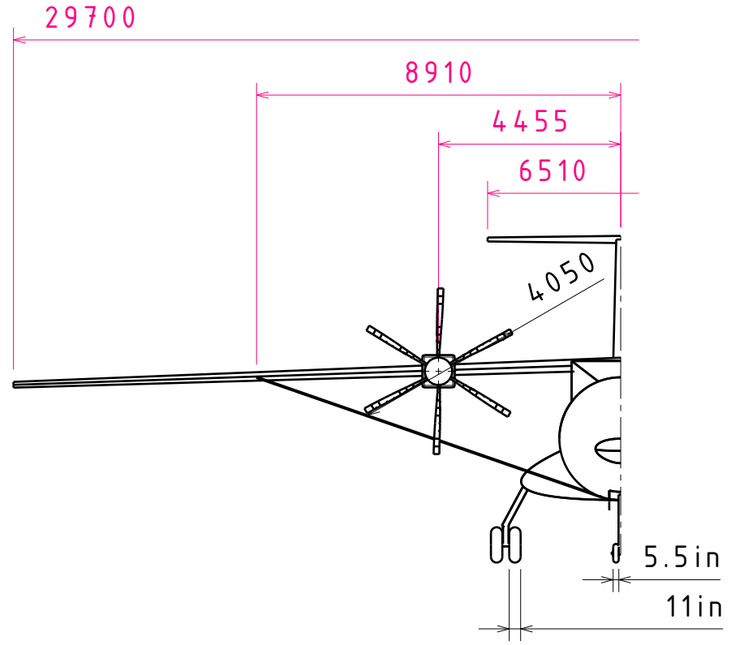

DRAWN BY Kacper Montewka	DATE 18/06/2026	TU DELFT			
CHECKED BY Lindsay Landman	DATE 18/06/2026	DRAWING TITLE DSE26-G14-TBW-MASTER_ASM			
DESIGNED BY Marius Michaud	DATE 18/06/2026	SIZE A3	DRAWING NUMBER LEAF-A THREE VIEW DRAWING		REV X
		SCALE 1:150	WEIGHT(kg) 21810		SHEET 1/1

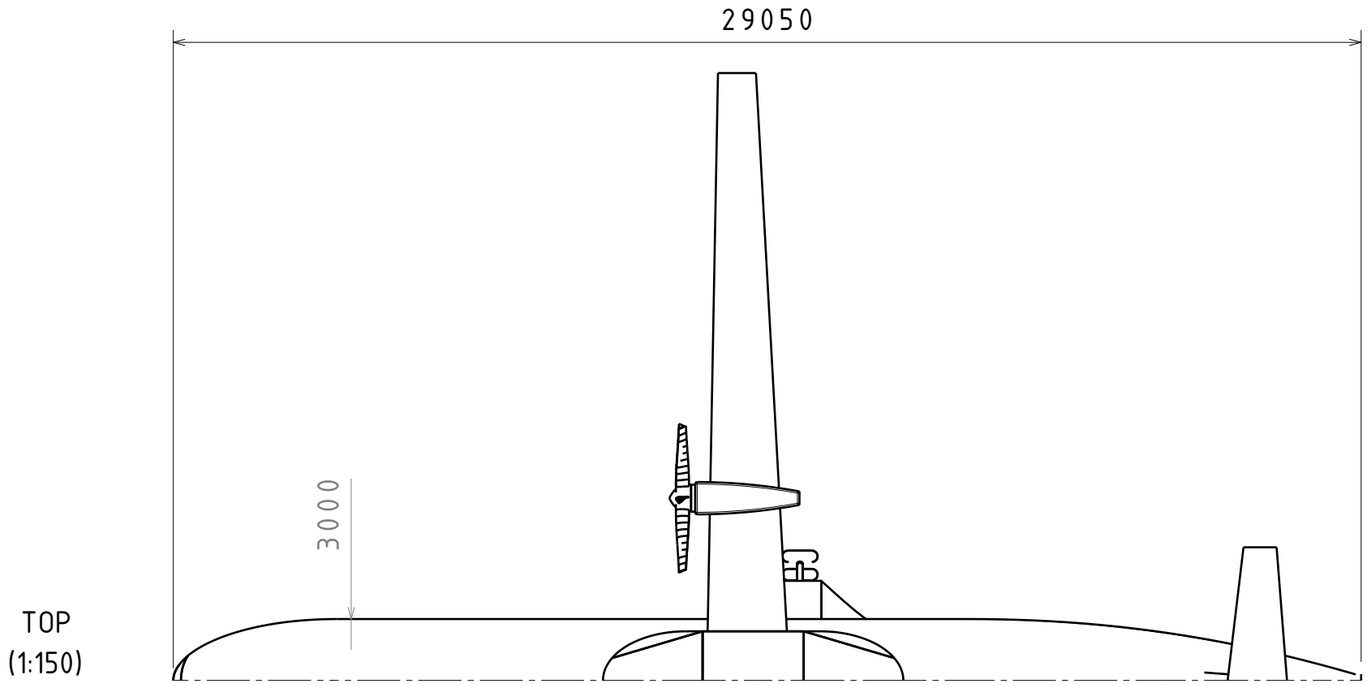

TOP
(1:150)

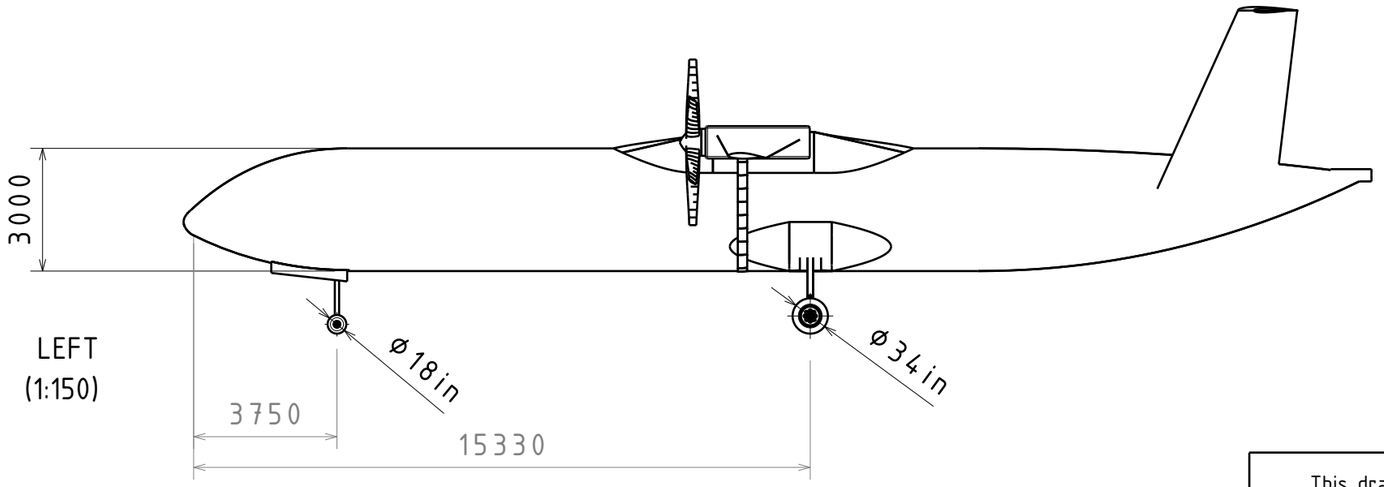

LEFT
(1:150)

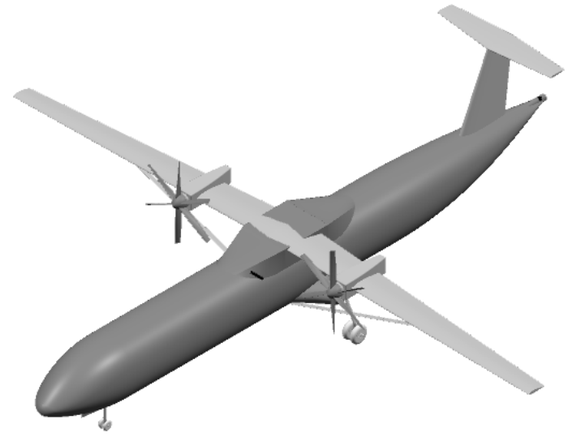

ISO
(1:250)

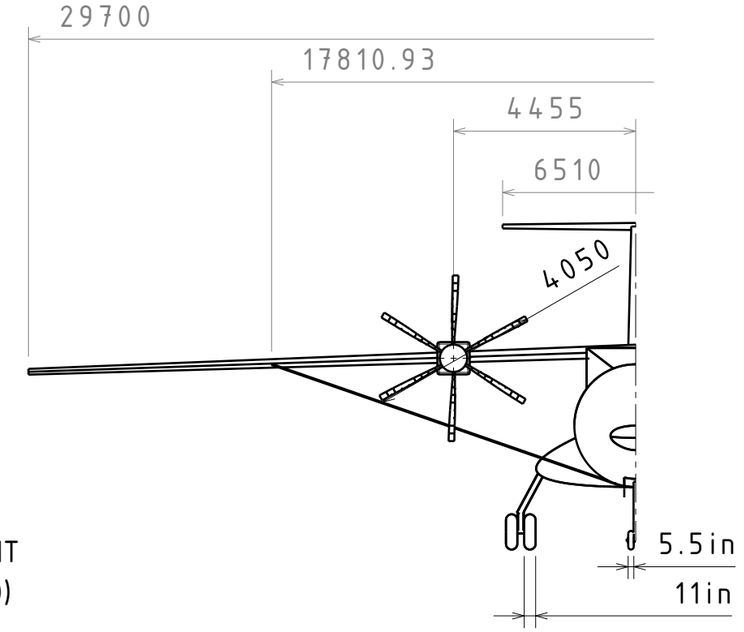

FRONT
(1:150)

DRAWN BY Kacper Montewka	DATE 18/06/2026	
CHECKED BY Lindsay Landman	DATE 18/06/2026	
DESIGNED BY Marius Michaud	DATE 18/06/2026	

TU DELFT

DRAWING TITLE
DSE26-G14-TBW-MASTER_ASM

SIZE	DRAWING NUMBER	REV
A3	LEAF-B THREE VIEW DRAWING	X

SCALE	WEIGHT(kg)		SHEET
1:150	17900		1/1